TESIS DE LA UNIVERSIDAD DE ZARAGOZA

2024

61

Jennifer Riccio

Characterization of Atrial Propagation Patterns and Substrate using Novel Electrogram-Based Approaches in Multielectrode Catheters

Director/es
Laguna Lasaosa, Pablo
Martínez Cortés, Juan Pablo

ISSN 2254-7606

Prensas de la Universidad
Universidad Zaragoza

ISSN 2254-7606

Universidad Zaragoza
1542

Tesis Doctoral

CHARACTERIZATION OF ATRIAL PROPAGATION PATTERNS AND SUBSTRATE USING NOVEL ELECTROGRAM-BASED APPROACHES IN MULTIELECTRODE CATHETERS

Autor

Jennifer Riccio

Director/es

Laguna Lasaosa, Pablo
Martínez Cortés, Juan Pablo

UNIVERSIDAD DE ZARAGOZA
Escuela de Doctorado

Programa de Doctorado en Ingeniería Biomédica

2023

Instituto Universitario de Investigación
en Ingeniería de Aragón
Universidad Zaragoza

Ph.D. Thesis

Characterization of Atrial Propagation Patterns and Substrate using Novel Electrogram-Based Approaches in Multielectrode Catheters

Jennifer Riccio

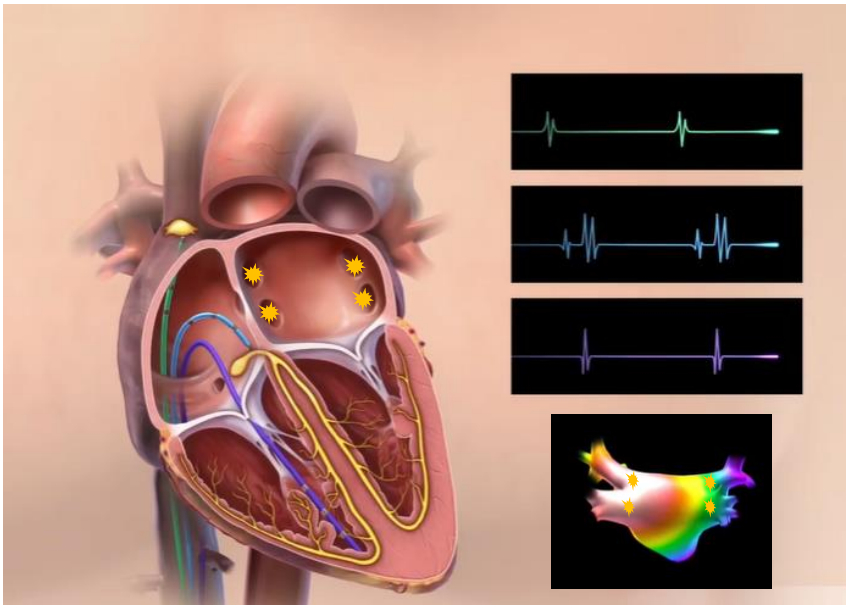

Supervisors: Juan Pablo Martínez Cortés
Pablo Laguna Lasaosa

University of Zaragoza
October 2023

Ph.D. Thesis

Characterization of Atrial Propagation Patterns and Substrate using Novel Electrogram-Based Approaches in Multielectrode Catheters

Jennifer Riccio

I3A Institute, University of Zaragoza, IIS Aragón, Zaragoza, Spain

Supervisors:

Juan Pablo Martínez Cortés

Associate Professor

I3A Institute, University of Zaragoza, IIS Aragón, Zaragoza, Spain

Pablo Laguna Lasaosa

Full Professor

I3A Institute, University of Zaragoza, IIS Aragón, Zaragoza, Spain

October 2023

Characterization of Atrial Propagation Patterns and Substrate using Novel Electrogram-Based Approaches in Multielectrode Catheters

Jennifer Riccio, 2023

This thesis was supported by the European Union's Horizon 2020 (2014-2020) Research and Innovation programme under the Marie Skłodowska-Curie Grant Agreement No.766082: "MultidisciplinarY training network for ATrial fibRillation monItoring, treAtment and progression" (MY-ATRIA), by Ministerio de Ciencia e Innovación through projects PID2019-105674RB-I00 and PID2019-104881RB-I00, and by Government of Aragon through the research project T39-23R (Reference Group BSICoS). Some of the computations and simulations used in this thesis were performed using the ICTS "NANBIOSIS", by means of the High Performance Computing Unit of the CIBER-BBN at Aragón Institute for Engineering Research (I3A).

Cover image reproduced, adapted and modified from www.medmovie.com.

I membri di una famiglia
sono come i rami di un albero,
ognuno prende la propria direzione
pur condividendo le stesse radici.

Abstract

Atrial fibrillation (AF) is the most frequently diagnosed arrhythmia worldwide, representing a significant public health problem with a great impact on the quality of life of patients. Nevertheless, its underlying mechanisms are not completely known. What is established is that both altered electrical impulse propagation and substrate may be involved in the development of the disease. These considerations have led to an increasing interest towards AF treatment, which varies depending on the patient characteristics.

Catheter ablation is a minimally invasive procedure to scar those areas responsible for initiation and/or perpetuation of irregular heartbeats, and is chosen when anti-arrhythmic drugs are not effective. It employs catheters equipped with electrodes which can sense and record the local cardiac electrical signals, known as electrograms (EGMs), or release the energy needed to scar and destroy the arrhythmia triggers when inserted into the cardiac chambers.

This thesis aims to characterize AF dynamics in order to find the most appropriate catheter ablation target and effectively terminate the arrhythmia. To do that, signal processing methodologies have been proposed and investigated, thus extracting EGM characteristics in terms of propagation patterns and substrate.

In chapter 3, the modified omnipolar electrogram (MOP-EGM) method is introduced to overcome limitations affecting current characterization of atrial propagation patterns and substrate. Novel mapping strategies based on conduction velocity (CV) and voltage estimates were evaluated in a simulated bidimensional tissue including a fibrotic patch, and preliminary outcomes were also obtained from real epicardial EGMs. In both cases, multielectrode catheters during the mapping procedure were used, where the plane and homogeneous wave hypothesis into electrode cliques can be assumed. In a simulation context, maps based on the MOP-EGM method were compared with both bipolar electrogram (b-EGM) based approach and the original omnipolar (OP-EGM) one, revealing an improvement of the accuracy and robustness of the CV and voltage estimates and a reduction of the error induced by the b-EGMs dependence on catheter orientation. In a clinical scenario, CV and propagation direction estimates computed with the MOP-EGMs were compared with those derived from manually detected local activation times (LATs). It shows that both approaches were able to reproduce the propagation pattern coherently with the reference one provided by local activation times maps in case of sinus rhythm (SR). However, in case of more complex patterns, like the ones occurring in AF,

the omnipolar estimates show a smoother and more homogeneous behaviour than those based on LATs, especially in areas with reentry circuits and multiple wavelets.

In chapter 4, novel biomarkers of unipolar electrogram (u-EGM) waveform dispersion are proposed, also using multielectrode catheters, to detect fibrotic tissue in the atrium. Those markers are based on the concept of dominant-to-remaining eigenvalue dominance ratio (EIGDR), characterizing the waveform dispersion of u-EGMs in electrode cliques, which are hypothesized to be correlated with the presence of atrial fibrosis. Pixel maps were created for each biomarker computed from synthetic signals in a simulation scenario including a patch of dense fibrosis, with three catheter orientations with respect to the tissue preferential direction and two configurations of electrode cliques. Each map was evaluated in detecting the fibrotic patch assuming different unipolar noise levels and variable electrode-tissue distance and was compared with voltage maps based on the peak-to-peak amplitude of b-EGMs. Results show that the biomarker $\mathcal{R}^{\mathcal{A}}$ based on the time alignment among u-EGMs within the clique provided comparable fibrosis detection accuracy to that of maximum bipolar voltage maps when signals are free from noise, and better performance when high noise levels are present, for both fixed and variable electrode-to-tissue distances. These results open the possibility of an alternative approach for the discrimination of fibrosis, which may overcome limitations affecting the standard approaches, including the one based on bipolar EGM voltage thresholding.

In chapter 5, the EIGDR based markers previously introduced are computed and evaluated in clinical contexts. Mapping data are acquired with two different multipole catheters from patients showing two spatiotemporal patterns. Unipolar waveform dispersion is quantified in atrial depolarization windows following both single-beat and multibeat approaches. The aims of this analysis were to discriminate mapping points clearly belonging to fibrotic (F) and non-fibrotic (NF) areas in the atrium and to evaluate the effect of catheter geometry on the EGM dispersion. Results show that biomarkers based on the previous time alignment of u-EGMs, $\mathcal{R}^{\mathcal{A}}$ and $\Delta\mathcal{R}^{\mathcal{A}}$, are able to identify fibrotic areas, revealing to better accomplish the plane wave hypothesis in grid-shaped mapping catheters. In conclusion, all findings suggest that the MOP-EGM method and the EIGDR approach may be used to reduce estimation errors during electroanatomic mapping (EAM), thus improving the detection of ablation final targets. Therefore, both contributions provided in this thesis may help the physician to guide the ablation procedure, taking into account both complexity of the underlying tissue and of the propagation rhythm.

Keywords: Atrial fibrillation, cardiac arrhythmia, catheter ablation, electrograms, propagation patterns, substrate, omnipolar electrogram, waveform dispersion, eigenvalue dominance ratio.

Resumen y Conclusiones

La fibrilación auricular (AF) es la arritmia cardíaca más frecuente a nivel mundial, y representa un importante problema de salud pública con un gran impacto en la calidad de vida de los pacientes. Sin embargo, sus mecanismos subyacentes no se conocen por completo. Lo que se conoce es que tanto la propagación alterada del impulso eléctrico como el sustrato pueden estar involucrados en el desarrollo de la enfermedad. Estas consideraciones han llevado a un creciente interés por el tratamiento de la AF, que varía según las características del paciente.

La ablación con catéter es un procedimiento mínimamente invasivo para cicatrizar aquellas áreas responsables de la iniciación y/o perpetuación de los latidos cardíacos irregulares, y se elige cuando los medicamentos antiarrítmicos no son efectivos. Emplea catéteres equipados con electrodos que pueden detectar y registrar las señales eléctricas cardíacas locales, conocidas como electrogramas (EGMs), o liberar la energía necesaria para cicatrizar y destruir los desencadenantes de la arritmia cuando se insertan en las cavidades cardíacas.

Esta tesis tiene como objetivo caracterizar la dinámica de la AF con el fin de encontrar el blanco más adecuado de ablación con catéter y terminar con la arritmia de manera efectiva. Para ello, se han propuesto e investigado metodologías de procesamiento de señales, extrayendo así las características de los EGMs en términos de patrones de propagación y sustrato.

En el capítulo 3, se presenta el método de los electrogramas omnipolares modificado (MOP-EGM) para superar las limitaciones que afectan a la caracterización actual de los patrones de propagación auricular y del sustrato. Se han evaluado nuevas estrategias de mapeo basadas en estimaciones de voltaje y velocidad de conducción (CV) en un tejido bidimensional simulado que incluye un parche fibrótico, y también se han obtenido resultados preliminares de EGMs epicárdicos reales. En ambos casos, se han utilizado catéteres de electrodos múltiples durante el procedimiento de mapeo, donde se puede asumir la hipótesis de onda plana y homogénea en *cliques* de electrodos. En el contexto de simulación, los mapas basados en el método MOP-EGM se han comparado con el enfoque basado en electrogramas bipolares (b-EGMs) y el omnipolar original (OP-EGM), revelando que mejoran la precisión y robustez de las estimaciones de CV y voltaje y reducen el error inducido por la dependencia de los b-EGMs en la orientación del catéter. En el escenario clínico, las estimaciones de CV y dirección de propagación calculadas con

los MOP-EGMs se han comparado con aquellas derivadas de los tiempos de activación locales (LATs) detectados manualmente. El estudio muestra que ambos enfoques fueron capaces de reproducir el patrón de propagación de forma coherente con el patrón de referencia proporcionado por los mapas de tiempos de activación local en caso de ritmo sinusal (SR). Sin embargo, en el caso de patrones más complejos, como los que ocurren en la AF, las estimaciones omnipolares muestran un comportamiento más suave y homogéneo que las basadas en LATs, especialmente en áreas con circuitos de reentrada y ondas múltiples (*wavelets*).

En el capítulo 4, se proponen nuevos biomarcadores de dispersión de forma de onda de electrograma unipolar (u-EGM), utilizando también catéteres multielectrodo, para detectar tejido fibrótico en la aurícula. Esos marcadores, basados en el concepto de relación de dominancia de autovalor (EIGDR) dominante al resto de autovalores, caracterizan la dispersión de la forma de onda de los u-EGMs en *cliques* de electrodos, y se hipotetiza que están correlados con la presencia de fibrosis auricular. Se han creado mapas de píxeles para cada biomarcador calculado a partir de señales sintéticas en un escenario de simulación que incluye un parche de fibrosis densa, con tres orientaciones de catéter con respecto a la dirección preferencial del tejido y dos configuraciones de grupos de electrodos. Cada mapa se evaluó para detectar el parche fibrótico asumiendo diferentes niveles de ruido unipolar y una distancia variable entre electrodo y tejido y se han comparado con mapas de voltaje basados en la amplitud pico a pico de los b-EGMs.

Los resultados muestran que el biomarcador $\mathcal{R}^{\mathcal{A}}$ basado en la alineación de tiempo entre los u-EGMs dentro de la clique proporcionan una precisión de detección de fibrosis comparable a la de los mapas de voltaje bipolar máximo cuando las señales están libres de ruido y un mejor rendimiento cuando hay mucho ruido. los niveles están presentes, tanto para distancias fijas como variables de electrodo a tejido. Estos resultados abren la posibilidad de un enfoque alternativo para la discriminación de la fibrosis, que puede superar las limitaciones que afectan a los enfoques estándar, incluido el basado en el umbral de voltaje bipolar.

En el capítulo 5, los marcadores basados en la EIGDR presentados anteriormente se han calculado y evaluado en contextos clínicos. Se han adquirido los datos de mapeo con dos catéteres multipolares diferentes de pacientes que muestran dos patrones espaciotemporales. La dispersión de forma de onda unipolar se cuantifica en ventanas de despolarización auricular siguiendo enfoques de un solo latido y de varios latidos. Los objetivos de este análisis fueron discriminar puntos de mapeo claramente pertenecientes a áreas fibróticas (F) y no fibróticas (NF) en la aurícula y evaluar el efecto de la geometría del catéter en la dispersión del EGM. Los resultados muestran que los biomarcadores basados en el alineamiento temporal previo de los u-EGMs, $\mathcal{R}^{\mathcal{A}}$ y $\Delta\mathcal{R}^{\mathcal{A}}$, pueden identificar áreas fibróticas, cumpliendo mejor la hipótesis de onda plana en catéteres de mapeo en forma de parrilla. En conclusión, todos los hallazgos sugieren que el método MOP-EGM y el método de EIGDR pueden usarse para reducir los errores de estimación durante el mapeo

electroanatómico (EAM), mejorando así la detección de blancos finales de ablación. Por tanto, las dos aportaciones de esta tesis pueden ayudar al médico a orientar el procedimiento de ablación, teniendo en cuenta tanto la complejidad del tejido subyacente como el ritmo de propagación.

Palabras clave: Fibrilación auricular, arritmia cardíaca, ablación por catéter, electroglectrogramas, patrones de propagación, sustrato, electrograma omnipolar, dispersión de forma de onda, relación de dominancia de autovalores.

Acknowledgments

This Ph.D. thesis would not exist without the presence and the involvement of many people, whom I am happy to thank in this section.

First of all, I would like to thank my supervisors, Juan Pablo Martínez and Pablo Laguna, for guiding me with care and dedication during these incredible years. I will always be grateful to you, Pablo and Juan Pablo, for giving me the opportunity to become the researcher I am today, inspiring me every day and instilling all your passion for research. It has been a privilege for me to have been able to learn from you, both about signal processing and daily life. You have been real mentors to me.

A special thanks goes to Alejandro Alcaine, who has supported me with his valuable personal and professional advice over the years. Thank you Alex, for pushing me to be the best version of myself.

I would also like to express my gratitude to all the members of the BSICoS group, who have been a second family to me throughout those years. Special thanks goes to Alba, Alberto, Carlos, Carmen, Cristina, David H., David S., Diego, Esther, Flavio, Hassaan, Javi, Jorge Mario, Konstantinos, Pablo, Saúl, Spyros. Each of you contributed to making my journey to Zaragoza an unforgettable experience and I thank you for that.

Many thanks to the University of Zaragoza, especially the members of I3A, for all the help and support provided.

A special mention goes to the MY-ATRIA consortium, for allowing me to live the most exciting and rewarding experience of my life. I thank the project supervisors and all my ESR colleagues: Jordan, Rebecca, Giorgio, Muhamed, Javier, Ricardo, Hesam, Mostafa, Guadalupe, Luca and Chiara. Every experience we lived together, from the Summer and Winter Schools to conferences and secondments, was full of meaningful and fun moments, making our PhD a real adventure.

I would like to thank Chiara for being the best roommate, colleague and friend I could wish for. It is truly amazing that fate has brought together two people like us, so incredibly similar in many ways, but so geographically distant. I am happy to have shared every moment of this journey with you, I could not have hoped for better.

To my best friend, Tommaso, for always being there, even if only virtually, in every joyful moment of my life, but above all whenever weaknesses were about to take over. You have been one of my few certainties over the years, and for that I will always be grateful.

To Lauren, for her genuine friendship: our conversations are always a source of reflection and serenity for me, and for that I thank you.

Finally, I would like to thank my wonderful family. My aunt, Maria Angela, for always believing in me and in my potential, even and above all when I doubted it. My brother, Joshua, for supporting and enduring me through these difficult years. Thank you for your thoughts and your advice, which were enlightening for me. My mother, for allowing me to achieve my goals with her sacrifices and struggles. Thank you for being my biggest inspiration. I consider myself more than lucky to have you as a mother.

Ringraziamenti

Questa tesi di dottorato di ricerca non esisterebbe senza la presenza ed il coinvolgimento di molte persone, che sono felice di ringraziare in questa sezione.

Prima di tutto, vorrei ringraziare i miei supervisori, Juan Pablo Martínez e Pablo Laguna, per avermi guidata con premura e dedizione in questi anni incredibili. Vi sarò per sempre grata, Pablo e Juan Pablo, per avermi dato l'opportunità di diventare la ricercatrice che sono oggi, ispirandomi ogni giorno e trasmettendomi tutta la vostra passione per la ricerca. E' stato un privilegio per me aver potuto imparare da voi, tanto di elaborazione dei segnali quanto di vita quotidiana. Siete stati dei veri e propri mentori per me.

Un ringraziamento speciale va ad Alejandro Alcaine, che mi ha supportata con i suoi preziosi consigli personali e professionali in questi anni. Grazie Alex, per avermi spinto ad essere la migliore versione di me stessa.

Vorrei poi esprimere la mia gratitudine a tutti i membri del gruppo BSICoS, che sono stati per me una seconda famiglia in questi anni. Un ringraziamento speciale va a Alba, Alberto, Carlos, Carmen, Cristina, David H., David S., Diego, Esther, Flavio, Hassaan, Javi, Jorge Mario, Konstantinos, Pablo, Saúl, Spyros. Ognuno di voi ha contribuito a rendere il mio percorso a Saragozza un'esperienza indimenticabile e per questo vi ringrazio.

Grazie mille all'Università di Saragozza, in particolare ai membri dell'I3A, per tutto l'aiuto e il supporto forniti.

Una menzione speciale va al consorzio MY-ATRIA, per avermi permesso di vivere la più eccitante e gratificante esperienza della mia vita. Ringrazio i supervisori del progetto e tutti miei colleghi ESR: Jordan, Rebecca, Giorgio, Muhamed, Javier, Ricardo, Hesam, Mostafa, Guadalupe, Luca e Chiara. Ogni esperienza vissuta insieme, dalle Summer e Winter School alle conferenze e secondments, è stata ricca di momenti significativi e divertenti, che hanno reso il nostro dottorato di ricerca una vera e propria avventura.

Vorrei ringraziare Chiara, per essere stata la migliore coinquilina, collega e amica che potessi desiderare. E' davvero sorprendente che il destino abbia fatto incontrare due persone come noi, cosí incredibilmente simili sotto molti punti di vista, ma cosí distanti geograficamente. Sono felice di aver condiviso ogni momento di questo percorso con te, non potevo sperare di meglio.

Al mio migliore amico, Tommaso, per esserci stato sempre, anche solo virtualmente, in

ogni momento gioioso della mia vita, ma soprattutto ogni volta che le debolezze stavano per prendere il sopravvento. Sei stato una delle mie poche certezze in questi anni, e per questo ti sarò sempre grata.

A Lauren, per la sua amicizia così autentica: le nostre conversazioni sono sempre fonte di riflessione e serenità per me, e per questo ti ringrazio.

Infine, vorrei rigraziare la mia meravigliosa famiglia. Mia zia, Maria Angela, per aver sempre creduto in me e nelle mie potenzialità, anche e soprattutto quando io ne dubitavo. Mio fratello, Joshua, per avermi supportato e sopportato in questi anni complicati. Grazie per le tue riflessioni e i tuoi consigli, che sono stati per me illuminanti. Mia madre, per avermi permesso di raggiungere i miei obiettivi con i suoi sacrifici e le sue lotte. Ti ringrazio per essere la mia più grande fonte di ispirazione. Mi ritengo più che fortunata ad averti come madre.

Contents

List of Figures

List of Tables

List of Acronyms

ACC detection accuracy

AF atrial fibrillation

AP action potential

AUC area under curve

AVN atrioventricular node

b-EGM bipolar electrogram

CS coronary sinus

CT computed tomography

CV conduction velocity

DE-MRI delayed enhancement magnetic resonance imaging

EAM electroanatomical mapping

ECG electrocardiogram

ECM extracellular matrix

EGM electrogram

EIGDR eigenvalue dominance ratios

F fibrotic

IIR image intensity ratio

IQR interquartile range

LA left atrium

LAT local activation time

LGE-MRI late gadolinium enhanced magnetic resonance imaging

LV left ventricle

MEA multielectrode array

MOP-EGM modified omnipolar electrogram

MRI magnetic resonance image

NF non-fibrotic

OP-EGM omnipolar electrogram

PV pulmonary vein

PVI isolation of pulmonary veins

QCV quartile coeffient of variation

RA right atrium

RMSE root mean square error

ROC receiver operating characteristic

RV right ventricle

SAN sinoatrial node

SD standard deviation

SR sinus rhythm

u-EGM unipolar electrogram

Chapter 1

Introduction

According to the World Health Organisation, cardiovascular diseases represent the main cause of death globally [1]. This trend is estimated to continue over the next years, also due to the increase of elderly population, motivating more and more the interest in improving diagnosis and treatment of these pathologies.
Among them, atrial fibrillation (AF) plays a fundamental role, being the most common heart arrhythmia and affecting 1.5-2% of the general population. This prevalence increases with age and is expected to double in the next fifty years. For this reason, AF represents an important public health problem, which if left untreated can lead to serious and even life-threatening complications.
The main objective of this thesis is to characterize AF dynamics, in order to guide the most suitable therapy and predict its efficacy in terminating the arrhythmia.

1.1 Shape and Structure of the Heart

The heart is a cone-shaped vascular and muscle pump [2], located in the thoracic cavity. Anatomically, its muscular counterpart consists of four chambers, whose contraction and relaxation allow the blood flow: two atria, referred as right atrium (RA) and left atrium (LA), which occupy the upper section of the heart, known as the base, and two ventricles, referred as right ventricle (RV) and left ventricle (LV), occupying the lower section, known as the apex [3], as shown in Fig. 1.1. The RA receives oxygen-poor venous blood returning from the body through the superior and inferior vena cava and pushes it into the RA. From there, blood is pumped via the pulmonary arteries to the lungs, where it is carried back to the LA by the pulmonary veins (PVs). In the posterior surface of the heart, between the LA and LV, is the coronary sinus (CS), the main cardiac vein, which terminates into the RA. The so-oxygenated blood is therefore forced in the LV from where it will be sent to the rest of body regions by the aorta which branches into arteries and arterioles [4]. In the anterior and medial part of the RA, the right atrial appendage is located, overlapping the root of aorta [5]. It is divided from the smooth surface of

RA by a smooth muscular ridge in superior portion of RA referred as crista terminalis. The part of the left border of the heart's anterior surface is the left atrial appendage, which overlaps the root of the pulmonary artery. The right and left atrial appendages are connected by the Bachmann bundle, a bundle of parallel myocardial strands running between the two atria [6]. Two valves, referred as tricuspid valve and mitral valve, are located between RA and RV and between LA and LV, respectively, which open and close in agreement to the chambers contraction (also known as systole) and relaxation (also known as diastole). The CS receives blood during ventricular systole and empties into the RA during atrial systole [7]. Both the inner wall of the heart chambers and the surface of the valves are lined with a layer named endocardium. Then, the central and thicker layer is represented by the myocardium, which is responsible for the contractile activity of the heart. Finally, the heart surface is externally covered by the epicardium.

The human heart is formed by different types of cells including cardiomyocytes and fibroblasts [8]. Cardiomyocytes are responsible for the contractile activity of the cardiac muscle [9] and interact with fibroblasts to regulate the heart function in normal conditions. On the other hand, fibroblasts are involved in the deposition and remodeling of the extracellular matrix (ECM), producing and demolishing its proteins which include collagen and growth factors [10] and thus contributing to replacement of damaged tissue [11], differentiating to myofibroblasts. Loss or changes of the cardiomyocyte-fibroblast communication can be a sign of heart diseases including fibrosis and arrhythmias. In fibrosis, fibroblasts accumulate and production of ECM increases, thus altering their relationship with cardiomyocytes [10]. Arrhythmias derive from decoupling of cardiomyocytes, leading to irregular or slow conduction, among others. Additionally, cardiac fibrosis has been observed to increase the likelihood of the myocardium to become arrhythmic, further pointing out the role of the myocyte-fibroblast communication in heart arrhythmias [12].

1.2 Electrical Conduction System of the Heart

The heart is provided with a system to produce electrical impulses and conduct them from the base to the apex, inducing the rhythmical and sequential contraction of its chambers [4]. This electrical conduction system includes the following structures, also depicted in Fig. 1.2: the sinoatrial node (SAN), the atrioventricular node (AVN), the His bundle, which splits into right and left bundle branches and the Purkinje fibres [13].

1.2.1 Cardiac Action Potential

At the cellular level, the generation and propagation of the electrical impulse throughout the heart define the cardiac action potential (AP) [16]. This results from the selective permeability of the transmembrane proteins of which the membrane of cardiomyocytes is endowed, allowing water-soluble ions, to move across the membrane [17], [4], [18]. The

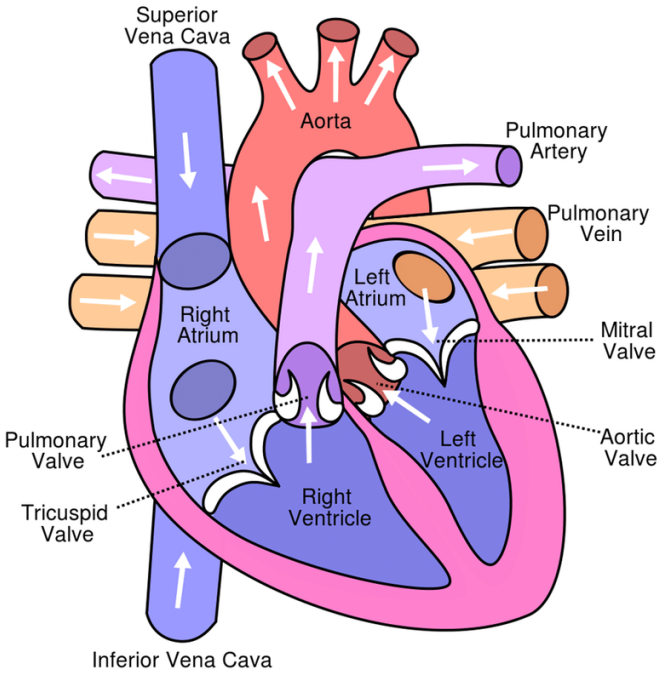

Figure 1.1: Diagram of the anatomy of the heart (anterior view) where cardiac chambers, valves and major vessels are depicted. Blood flow is pointed out by white arrows. Reproduced, adapted and modified from [14].

main ions involved in this process are sodium (Na^+), potassium (K^+), calcium (Ca^{2+}) and chloride (Cl^-). Their movement is forced by an electrochemical gradient from the medium with higher concentration and a certain electrical charge to the medium with lower concentration and the opposite electrical charge, generating a net transmembrane flow of charge (current). When equal concentrations and distribution of charges across the membrane are reached, the electrochemical gradient ends and the transmembrane potential assumes its resting value, which is around -90 mV for cardiomyocytes [4], [17]-[19]. The time variations of the transmembrane potential due to the ion movement across specific ion channels make the cardiomyocytes excitable or not, in five different phases occurring during their AP and reported in Fig. 1.3. The rise of the transmembrane potential over the resting potential is referred as *depolarization*, whereas its return to that value is known as *repolarization*. During diastole, the transmembrane potential remains constant at its resting value (phase 4). In this phase, the Na^+ and Ca^{2+} channels are closed, while the membrane is permeable to K^+. A rapid depolarization (phase 0) caused by an inward flow of Na^+ and Ca^{2+} follows, increasing the transmembrane potential over the threshold potential value (approximately -65 mV). This phase is followed by an equally fast initial repolarization (phase 1), when the Na^+ channels, and consequently currents, inactivate and the transmembrane potential drops to 0 mV, starting a plateau phase (phase 2), when Ca^{2+} enters into the cell. Finally, a rapid repolarization follows (phase 3), mainly due to the outward flow of K^+ and to the deactivation of inward Ca^{2+},

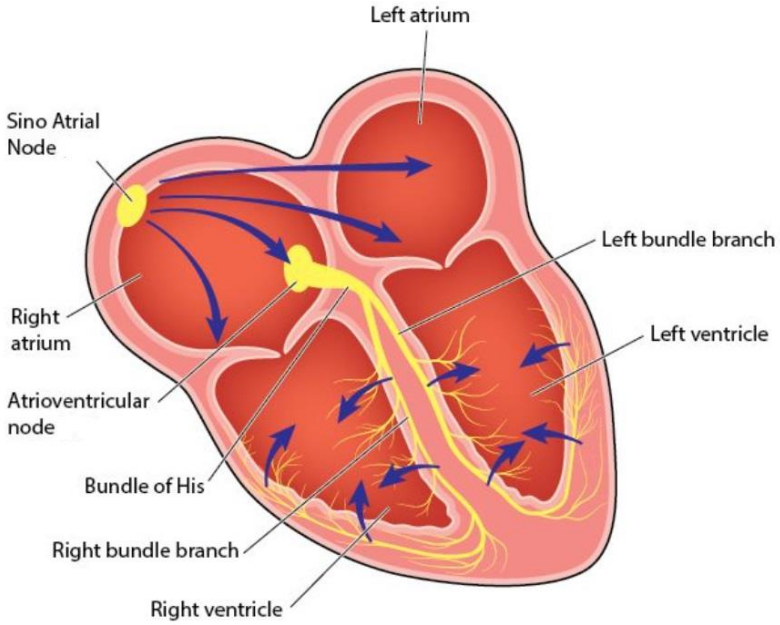

Figure 1.2: Electrical conduction system of the heart. Reproduced, adapted and modified from [15].

bringing back the transmembrane potential to the resting value [17], [18]. During a certain time period along the AP, referred as refractory period, cardiomyocytes are unable to initiate another AP, so as to allow a correct recovery of the cells and prevent multiple APs. Two refractoriness periods are observable during an AP, an absolute refractory period extending 250-300 ms from the AP overshoot, when no further stimuli can excite the cell, followed by a relative refractory period lasting 50 ms, which would require an over-threshold stimulus to generate another AP.
Unlike atrial and ventricular cardiomyocytes, cells in SAN and AVN generate spontaneous AP, not requiring external voltage to stimulate it and producing a slow response because of their slower rate of depolarization [20].
Lastly, a third type of AP characterizes the cells within the conduction His-Purkinje system, which shows a spontaneous depolarization but also producing a fast response.

1.2.2 Electrical Activity in the Heart and Electrocardiography

As mentioned before, in normal conditions, the synchronized contraction of the heart, known as sinus rhythm (SR), starts in the SAN, a group of cells situated in the right atrial wall at the junction of the RA and the superior vena cava [4], which set their

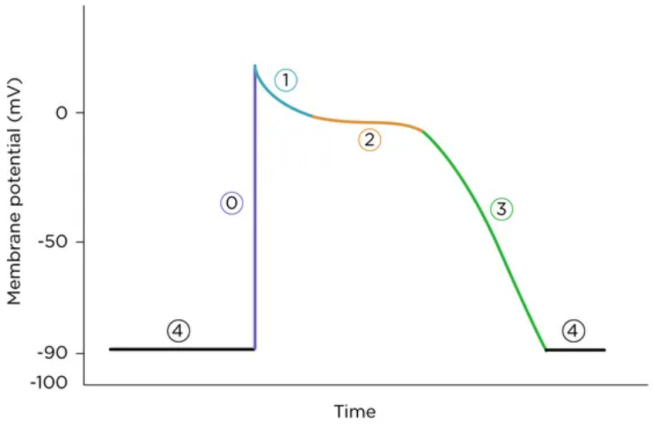

Figure 1.3: Transmembrane AP of a myocardial cell, pointing out its phases. Reproduced, adapted and modified from [21].

frequency for the entire myocardium and therefore act as the dominant pacemaker (see Fig. 1.2). Afterwards, the electrical impulse depolarizes the atrial myocardium in 0.1 s to then converge on the AVN [22]. Due to the slowness of conduction in the AVN, there is a delay of about 0.1 s before the stimulus propagates to the ventricles. This allows the ventricle to fill with blood. The depolarization wave spreads through the left and right bundle branches of the His bundle, and the Purkinje fibers, until it reaches all the parts of the ventricles in 0.08-0.1 s. During this ventricular depolarization, the atrium repolarizes thus reaching its diastole. Finally, ventricles repolarize and reach a relaxation state, thus preparing for a new beat. The heart electrical activity recorded during the cardiac cycle on the torso by different electrodes located at specific leads represents the electrocardiogram (ECG) signal, shown in Fig. 1.4. The P wave is caused by the atrial depolarization and is followed by the so-called QRS complex reflecting the ventricular depolarization. Then, T wave expresses the ventricular repolarization while U wave may depend on the repolarisation of Purkinje fibres, even if the elements that contribute to its formation are not yet defined. The interval spanning from the beginning of the P wave to the start of the QRS complex is referred as PR interval, whereas the segment running from the end of P wave to the beginning of QRS complex, known as PR segment, represents the time elapsed between atrial and ventricular activation. The time from the beginning of the QRS complex to the end of the T wave is named QT interval, while the ST segment from the end of the QRS complex to the start of the T wave represents the time when the ventricles are between depolarization and repolarization. The baseline of the ECG from where the waveforms are measured is called the isoelectric line.

The most used electrode configuration in clinical practise is the 12-lead ECG system, consisting of three bipolar limb leads (denoted as I, II and III), six precordial unipolar leads (indicated with $V_1 - V_6$) and three augmented unipolar limb leads (referred as aVL, aVR and aVF) [23]. Bipolar leads are measured as differences of voltages recorded by electrodes located at the right arm, left arm and left leg. Precordial unipolar leads measure the voltage difference between an electrode located on the chest and an indifferent

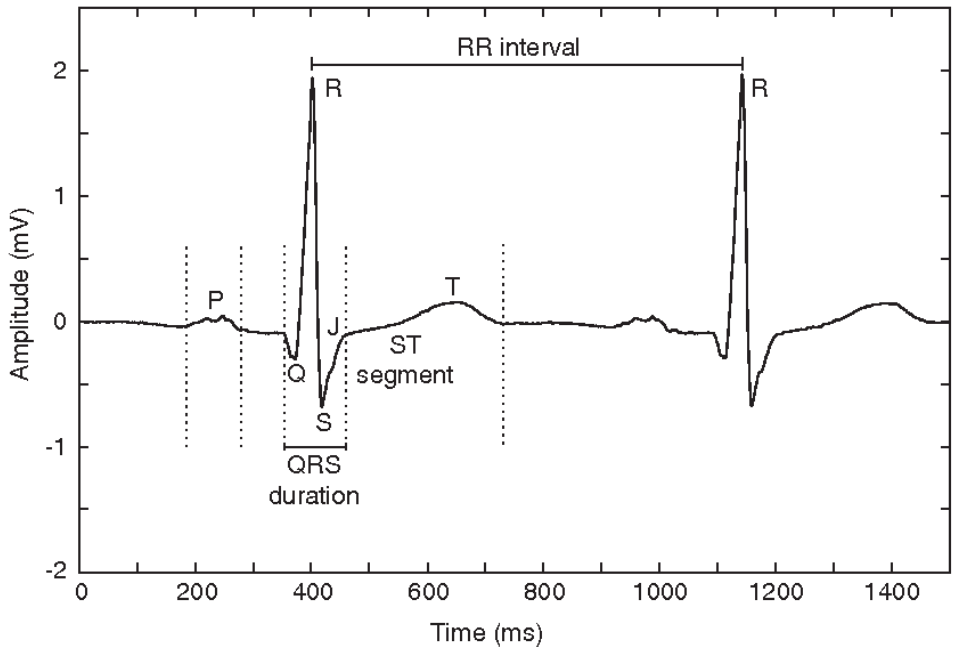

Figure 1.4: Electrocardiografic trace for normal SR, pointing out the different waveforms, segments and intervals that form it. Reproduced, adapted and modified from [23].

electrode (central terminal) obtained by linking the three electrodes positioned at the right arm, left arm and left leg mentioned before. Finally, the augmented unipolar limb leads are the voltage differences between each limb electrode and the average of the other two.

1.2.3 Cardiac Arrhythmias

In normal SR conditions, the number of heart beats per minute, referred as heart rate, is around 70 at resting conditions [22]. Any deviations from the SR, also known as cardiac arrhythmias, manifest as an increase (tachycardias) or decrease (bradycardias) of the normal rate. Bradycardias can be caused by dysfunctions of SAN or other conditions that can require the implantation of a pacemaker to restore the normal SR [24]. Tachycardias can be physiological, due to increased sympathetic activity occurring during exercise, illness or intense emotion, or pathophysiological, due to ischemia or electrolyte disturbances [25]. Electrophysiologically, arrhythmias can be due to alterations in the formation or propagation of the electrical impulse formation, or to a combination of both phenomena. In the first case, any change in the spontaneous depolarization of the cardiac cells in the SAN, referred as automaticity, and/or an enhanced automaticity of different subsidiary atrial or ventricular structures, may promote an arrhythmic event [18], [19]. On the other hand, new activations occurring immediately after an AP, also known as afterdepolarizations, may represent a trigger activity for arrhythmias. In the second case, if

a propagating impulse does not extinguish during the refractoriness period but persists activating excitable tissue, this can generate reentry tachycardias where the activation wave propagates repetitively in circular paths, returning and activating the origin site [17]. For a reentry circuit to be supported, some conditions need to be present, including, among others, an heterogeneous tissue representing the substrate for the circuit, an area of unexcitable tissue where the reentry circuit can spin and a trigger event initiating the reentry path [18], [19]. Two types of reentry are possible: functional, due to heterogeneities in the electrophysiological properties of the cardiac tissue, or anatomical, occurring when the wave finds an anatomical obstacle which determines two pathways [26]. Several scenarios have been labeled as functional reentries. The concept of leading circle was introduced by Allessie and co-workers as the smallest possible reentry wave which can excite the tissue still in its refractory period [27]. Weiner and Rosenblueth introduced the idea of a spiral wave coming out from a rotating source, referred as rotor, related to anatomical reentry [28], which was then applied to functional reentry [29]. By means of the curvature of the spiral wave, the core remains unstimulated, thus reducing conduction velocity (CV) and resulting in conduction block [17]. Two special types of reentry occurring without circular movement are reflection and phase 2 reentry [25]. In the former, the tissue is excited by a wavefront travelling in a forward direction and then is re-excited by a wavefront propagating backward [30]. In the latter, phase 2 plateau of the AP propagates from sites where is maintained to sites where it is abolished, thus producing an extrasystole [31]. Finally, anisotropy refers to the different CV in the transversal and longitudinal directions of the cardiac fibers, which can represent the substrate for a reentry [17].

1.3 Atrial Fibrillation

Currently, AF is the most frequent cardiac arrhythmia, manifesting severe symptoms which cause a high number of hospitalizations [32]. It shows an exponential increase with age, with a prevalence of more than 10% in the population older than 85 years [33]. AF is characterized by an irregular and chaotic activation of the atrium, which does not allow to properly fill the ventricle [34] when the impulse reaches the AVN [4]. The most remarkable features of ECG trace in AF are the absence of visible P waves, replaced by continuous electrical activity referred as f (fibrillatory) waves, and an irregular occurrence of QRS complexes (as shown in Fig. 1.5) [35]. Consequences of AF include heart failure, stroke, dementia and an increased risk of mortality, thus affecting patient's quality of life [36] and making its early diagnosis and treatment extremely important.

1.3.1 Electrophysiological Mechanisms of Atrial Fibrillation

Despite the fact that AF represents the most frequent cardiac arrhythmia and therefore has been studied in great detail, its underlying mechanisms are not yet fully under-

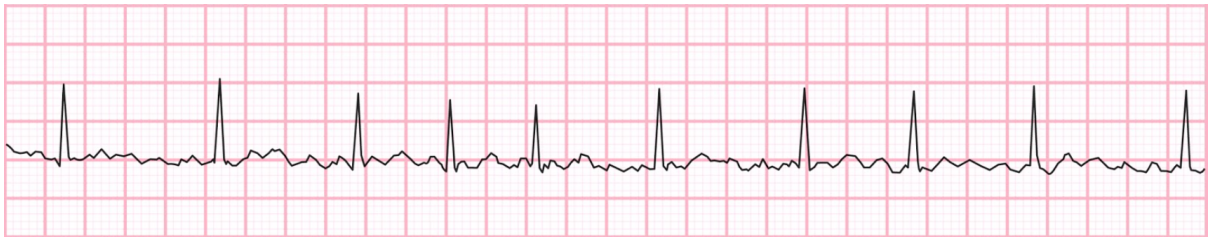

Figure 1.5: Example of ECG trace (lead II) during AF, showing f waves and irregular QRS complexes. Reproduced, adapted and modified from [37].

stood [38], [39]. Over the years, several hypotheses have been proposed to explain the initiation and maintenance of AF, but to date none of them can explain this arrhythmia exhaustively. In 1959, Moe and co-workers introduced the multiple wavelet hypothesis [40], according to which AF is sustained by multiple wavefronts propagating through the atrium, where some of them must always find excitable tissue for the arrhythmia to persist [41]. This hypothesis was experimentally demonstrated later by Allessie and co-workers in isolated canine atria [42] and confirmed in humans with pacing induced AF through maps of the right atria free wall, leading to define breakthrough events as radial propagation patterns spreading in the epi- or endocardium [43]. Another hypothesis was proposed by Haïssaguerre [44], assuming AF as generated and/or sustained by an ectopic focus mainly located in the PVs. The rotor hypothesis was also raised [43], according to which a single or multiple functional reentry may lead to AF by circulating around an excitable but unexcited core [45]. Nevertheless, these mechanisms are not mutually exclusive, as represented in Fig. 1.6, thus complicating even more the disease.

Today, it is widely accepted that AF results from three coexisting factors: 1) a trigger event for the initiation of the arrhythmia, 2) a fibrotic substrate for its maintenance (where atrial fibrosis and its identification are presented in subsection 1.3.5), and 3) several modulators acting by multiple potential mechanisms, summarized by the pathophysiological triangle in Fig. 1.7. As discussed above, triggers are mainly located in the PV ostia, which act as myocardial sleeves and therefore receive ectopic atrial activity, but may also occur in the LA or RA [46]. Secondly, there is a broad consensus that a fibrotic substrate in the atrium derives from a specific disease, referred in literature as fibrotic atrial cardiomyopathy, which may represent the genetic factor of AF [47], [46]. Finally, several risk factors, both modifiable (including obesity, hypertension, diabetes, sleep apnea and lifestyle) and non-modifiable ones (such as age and vascular disease history) have been investigated in their interaction with AF and whose management has been found to be decisive in the reduction of the arrhythmia burden, thus improving catheter ablation treatment outcomes [47], [46] (discussed in subsection 1.3.3).

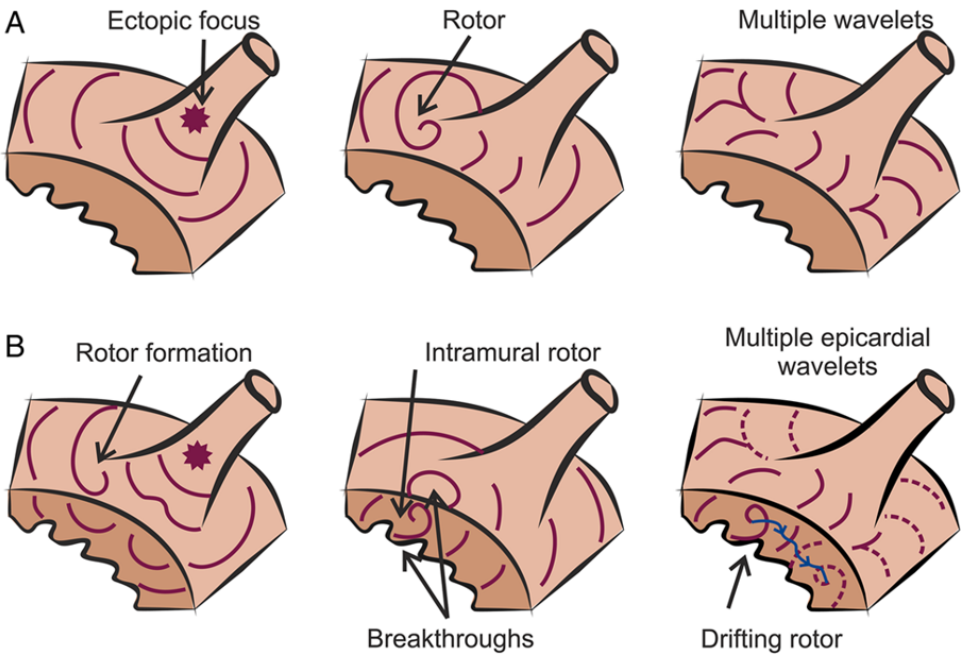

Figure 1.6: Main hypotheses for AF initiation and perpetuation, where propagation patterns are depicted in purple. (A) AF triggered by an ectopic focus located at one of the PV (left), a rotor (middle) or multiple wavelets (right). (B) Coexistence of the different mechanisms explaining AF. Rotor initiated by an ectopic focus at PV (left), coexisting with endo- or epicardial breakthroughs (middle) or driving multiple wavelets (right). Reproduced, adapted and modified from [45].

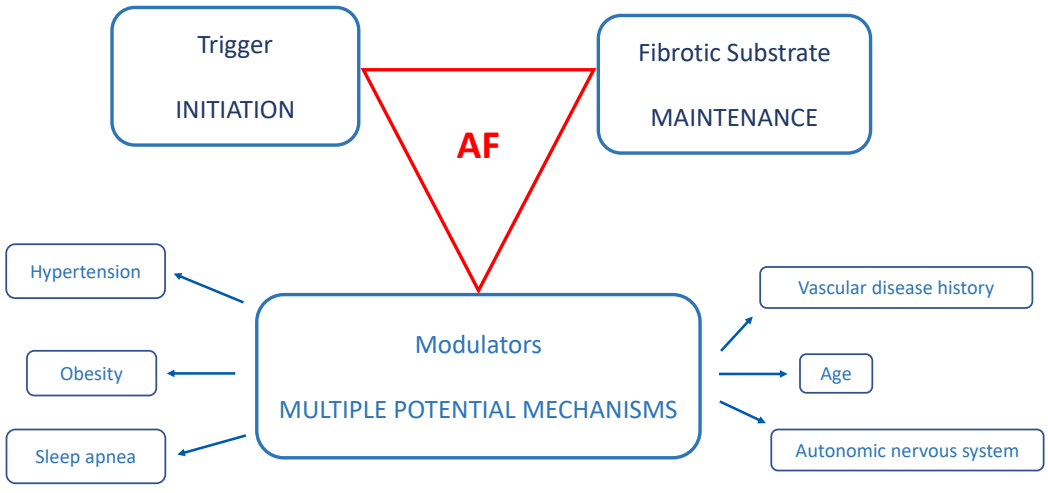

Figure 1.7: The pathophysiological triangle in AF, showing the three main factors characterizing the arrhythmia [47].

1.3.2 Clinical Classification of Atrial Fibrillation

AF is typically classified according to the time duration of the arrhythmogenic episode into the following five categories [35], [48]:

1. First diagnosed AF: this category includes all patients who experience an episode of AF for the first time, regardless of its duration and any associated symptoms.

2. Paroxysmal AF: the episode terminates by itself within 48 hours or by intervention if it continued for up to seven days. Recurrence of the episodes varies and after the threshold of 48 hours, the spontaneous restoration of the rhythm is unlikely.

3. Persistent AF: the recurrent episodes last more than seven days and is not self-terminating, thus requiring cardioversion performance. It can also be referred to as chronic AF (cAF).

4. Long-standing persistent AF: duration of the arrhythmia is greater than twelve months when a rhythm control treatment is considered.

5. Permanent AF: the arrhythmia is accepted by both the patient and the clinician, who decided not to pursue further strategies to restore SR. In this context, the acceptance of the arrhythmia represents a therapeutic approach, which may change both symptoms and the efficacy of the treatment.

The distinction between categories is not absolute and should be understood as flexible, being able to change over time for a given patient [49], allowing to cross from paroxysmal to persistent and from persistent to permanent categories. Patients with paroxysmal AF may have some long-lasting episodes requiring cardioversion. Analogously, the migration from persistent to permanent AF represents one of the most important decisions in the clinical management of a patient with AF.

A further criterion for classifying AF, based on the etiology, distinguishes valvular from nonvalvular AF. Valvular AF is conventionally defined as AF occurring in conjunction with a valve anatomical alteration (for instance, mitral stenosis) or a valve prosthesis. On the contrary, nonvalvular AF does not result from a mechanical heart valve or mitral stenosis.

1.3.3 Treatments for Atrial Fibrillation

Clinical evaluation of AF patients must be done in order to ensure the most appropriate management and treatment, preventing any eventual side effect and associated complications [17]. The first-line treatment for AF, specially in patients with first diagnosed AF, is medical and consists in the administration of drugs for rate or rhythm (anti-arrhythmic) control [50]. The timely administration of the latter, which includes agents like calcium-channel blockers and beta blockers, has proved to be very effective in restoring the normal SR.

In addition to this therapy, anti-coagulants such as warfarin are necessary for preventing stroke in AF patients, since blood clots in the atrium are more likely to form.

As mentioned before, if the AF episode lasts more than seven days (persistent AF), cardioversion is performed since the probability of spontaneous restoration of the SR becomes very low in this case, but also requiring the immediate administration of anti-coagulant medications [50]. Cardioversion consists on the delivery of an electric current during the QRS complex, thus avoiding the depolarization of the myocytes during the ventricular depolarization. In many patients, this electrical shock is combined with an intravenous anti-arrhythmic drug, since their combination was found to increase the probability to restore and maintain the SR. However, a repeated electric shock with increased dose and/or a different drug administration may be necessary if AF recurs within three months of cardioversion.

When anti-arrhythmic drugs are not effective, catheter ablation represents an alternative treatment for rhythm control. It is particularly justified in those patients with persistent AF and systolic dysfunction [50] or when the arrhythmia focus is clearly detectable [17]. Catheter ablation is a minimally invasive procedure consisting on the introduction of catheters within the cardiac chambers to focally burn sites involved into the initiation and/or perpetuation of AF (including fibrotic tissue or areas generating ectopic impulses to trigger the fibrillatory episode). Ablation catheters are able to perform permanent lesions in the cardiac tissue by delivering energy through a generator connected to a metallic tip. They are introduced and visualized through fluoroscopy and specially with contemporary electroanatomical mapping (EAM) systems. As discussed in section 1.4, this technology allows the physician to acquire and visualize electrophysiological information in a 3D space reconstructed from navigation data of the mapping catheters when they are in contact with myocardium, also reducing the exposure time under fluoroscopy and radiation dose. The most common ablation procedure consists of the electrical isolation of pulmonary veins (PVI) (see Fig. 1.8), through linear lesions around the PV ostium [38], where most ectopic foci are known to be located. Based on the energy source used for achieving PVI, two main procedures are distinguished: radiofrequency (RF) ablation and cryoablation. In the first case, a series of RF pulses with a temperature reaching 55°C and energy up to 80 W (solid-tip catheter) or 40 W (irrigated tip catheter) [51] are delivered to create focal RF lesions which encompass the area between PVs and atrium [52]. In the second case, cryothermal energy is delivered to create circumferential transmural lesions through a so-called cryoballoon catheter, consisting of a fixed-expansion outer balloon and a second inner balloon [53], which is cooled to a temperature of –80°C by the injection of a refrigerant medical gas (nitrous oxide). Cryoablation provides a homogeneous freezing area, thus resulting in a non-reversible damage of myocardium with one single application [54]. The two approaches show comparable performance, in terms of maintaining SR [55], AF recurrence [56] and undesirable events [55]. Actually, RF is the prevailing energy source of catheter ablation worldwide, even if cryoablation is shorter, thus reducing procedure duration without compromising its outcomes [56].

In addition to these well-established ablation strategies, a new non-thermal approach referred as *electroporation* has recently been introduced to treat patients with AF [57]. The process consists of creating pores over the cardiomyocyte membrane by means of a strong intensity electric field (E-field). This increases permeability of the membrane, irreversibly destroying its the structure and function and finally carrying to cell death [58]. This procedure revealed to be effective, safe and rapid, reducing PVI duration and avoiding risks and complications of the thermal ablation techniques [57], [58].

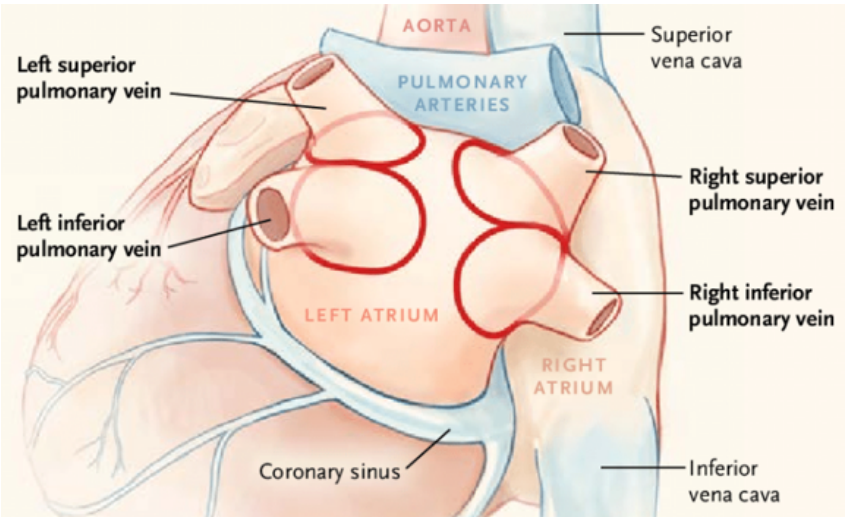

Figure 1.8: PVI where ablation lesions (red circles) encompassing each vein. Reproduced, adapted and modified from [59].

In most of the patients with paroxysmal AF, PVI alone achieves clinically satisfactory results. However, it is not unusual for AF recurrence to occur mainly due to reconnection of the PVs. Higher recurrence rate (of up to 60%) is also observed in the more advanced stages of persistent and long-standing persistent AF, which are associated with atrial remodeling and fibrosis [38], [60]. For this reason, additional radiofrequency ablation strategies beyond PVI have being proposed, including, among others, RF ablation of fibrotic areas, showing reduction in AF recurrence. In patients undergoing AF ablation it was observed that the interface area between fibrosis and more healthy atrium represents an anchor site for rotors [38], thus being responsible of AF maintenance. Hence, the great and growing interest in discriminating fibrotic from non-fibrotic tissue, which is the objective of the method proposed chapter 4 of this thesis.

Surgical interventions represented a well-established option to restore SR for several years [50]. The Cox-Maze III procedure, which represents the improvement of the Cox-Maze introduced by Dr. James L. Cox in 1987 [61], is the *gold standard* treatment for the surgical approach to AF. Performing multiple incisions in the atria, according to *cut and sew* technique, so as to create a series of scars and then force the electrical impulse from the SN to the AVN [50], this approach was used a lot to solve problems affecting function of SN and conduction between right and left atrium occurring with the Cox-Maze I [61]. The Cox-Maze III was then replaced by the latest Cox-Maze IV, which uses

devices delivering RF or cryothermal energy (heating or freezing, respectively) to create scars without cutting the tissue, thus shortening and simplifying the procedure. Unlike catheter ablation, Cox-Maze IV is a (minimally) invasive procedure, performed to specific patients, including those undergoing other cardiac surgical procedures [62].

1.3.4 Electrophysiological Study of Atrial Fibrillation

1.3.4.1 Catheter Technologies

In order to understand the pathophysiologic mechanisms of AF as well as to confirm the diagnosis and identify the most appropriate treatment, recording and processing of the local cardiac electrical activity, referred as electrogram (EGM), is required [63], [17]. These intracardiac signals are acquired with invasive and isolated wires, known as catheters, provided with one or more electrodes, percutaneously guided to be in contact with the cardiac chamber of interest [17]. Because of its large spatiotemporal beat-to-beat variation, AF is better characterized through simultaneous EGMs, recorded by high-density multielectrode catheters (diagnostic catheters) from multiple sites at the same time, rather than by analyzing sequential EGMs, each recorded at a different time [64]. From these signals, meaningful propagation patterns and substrate features may be extracted to provide high-resolution 3D maps of the atrium through a dedicated EAM system, thus allowing the physician to view the sites responsible for starting and/or maintaining the arrhythmia. When these are identified, ablation catheters are used to generate lesions and eliminate AF triggers [63]. The different companies on the market have developed catheters characterized by different shapes, electrode number and interelectrode spacing. Some examples are depicted in Fig. 1.9.

1.3.4.2 Intracardiac Electrogram Recording Modes

Depending on the configuration of the recording electrodes, different types of EGMs may be acquired. They are usually recorded in unipolar or bipolar mode having different characteristics, but providing complementary information. A unipolar electrogram (u-EGM) is recorded as potential difference between a single electrode in direct contact with the myocardium and an *indifferent* electrode, which is at zero potential and placed at distance from the heart (generally on patient's body surface). Since the sensing electrode is typically connected to the positive pole of the amplifier which records the potential difference, a wavefront propagating towards the sensing electrode will generate a positive deflection of the EGM. The signal amplitude is zero when the wavefront is located exactly over the recording electrode. When the wavefront has passed through the sensing electrode and propagates away, the EGM becomes negative [69] and terminates at the baseline, thus producing a deflection similar to an RS complex [70]. The biphasic deflection of the u-EGM generated by this propagation sequence (towards or away from the electrode) is illustrated in Fig. 1.10(a). As a consequence, a u-EGM will reflect the local electrical

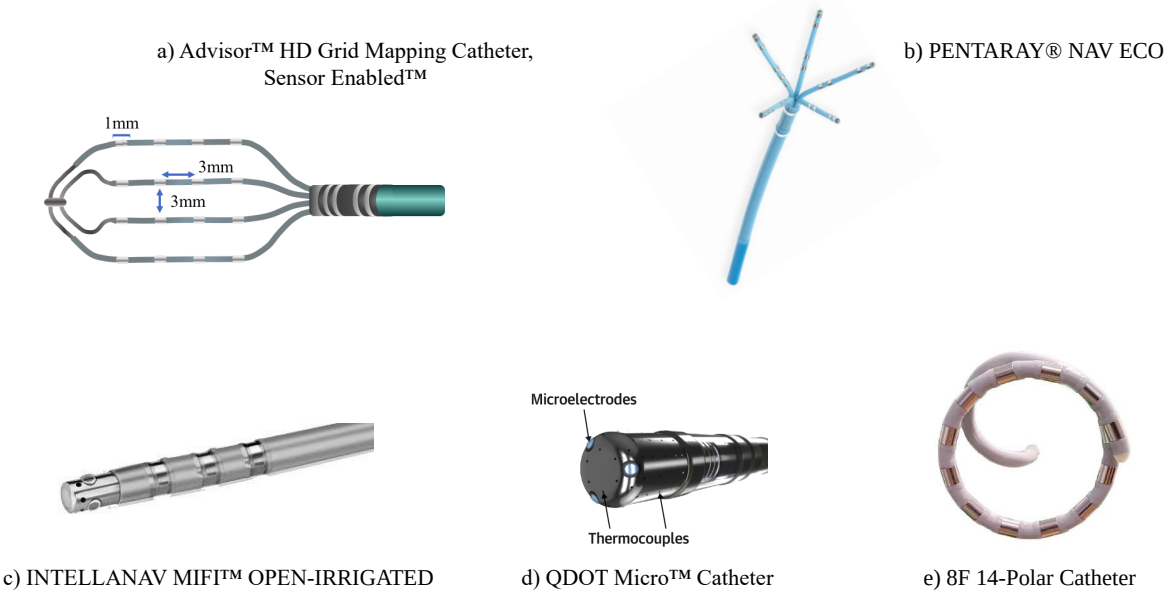

Figure 1.9: Examples of diagnostic (a and b) and ablation (c, d and e) catheters, produced by different companies. Reproduced, adapted and modified from [65] (a), from [66] (b), from [67] (c), from [68] (d) and from [57] (e).

activity, but may also sense remote activity happening far from the recording site (the so-called *far-field* components). In case of an exploring electrode located at the atrial myocardium, resulting u-EGM will also be affected by ventricular depolarization (see the last deflection in Fig. 1.10(a). On the other hand, a bipolar electrogram (b-EGM) is obtained as difference between the two unipolar recordings generated by the passage of the activation wavefront through two closely spaced electrodes located in direct contact with the myocardium in the area of interest [17], [69], [70]. For this reason, b-EGMs are essentially free from far-field effects, thus allowing a more robust detection of local activity than u-EGMs. Nevertheless, unlike unipolar recordings, b-EGM amplitude depends on the relative orientation between the depolarization wavefront and the recording electrodes pair. This effect can be clearly seen in Fig. 1.10(b), where the two different signal amplitudes are due to the different bipole directions. This amplitude would be maximum if the activation front is parallel to the line between the electrodes; it would be close to zero if the wavefront propagates perpendicularly to the recording axis [17]. In addition, further technical aspects including catheter-to-tissue distance, interelectrode spacing, electrode size, signal filtering and sample frequency can influence bipolar amplitude as well [69].

The latest multielectrode catheters allow the possibility to record multiple EGMs simultaneously along orthogonal directions. In this scenario, the recently developed *omnipolar electrogram (OP-EGM)* method [71] aims to propose alternative signals to unipolar and bipolar recordings (see Fig. 1.10(c)), showing to partially overcome their limitations, as extensively discussed in chapter 3.

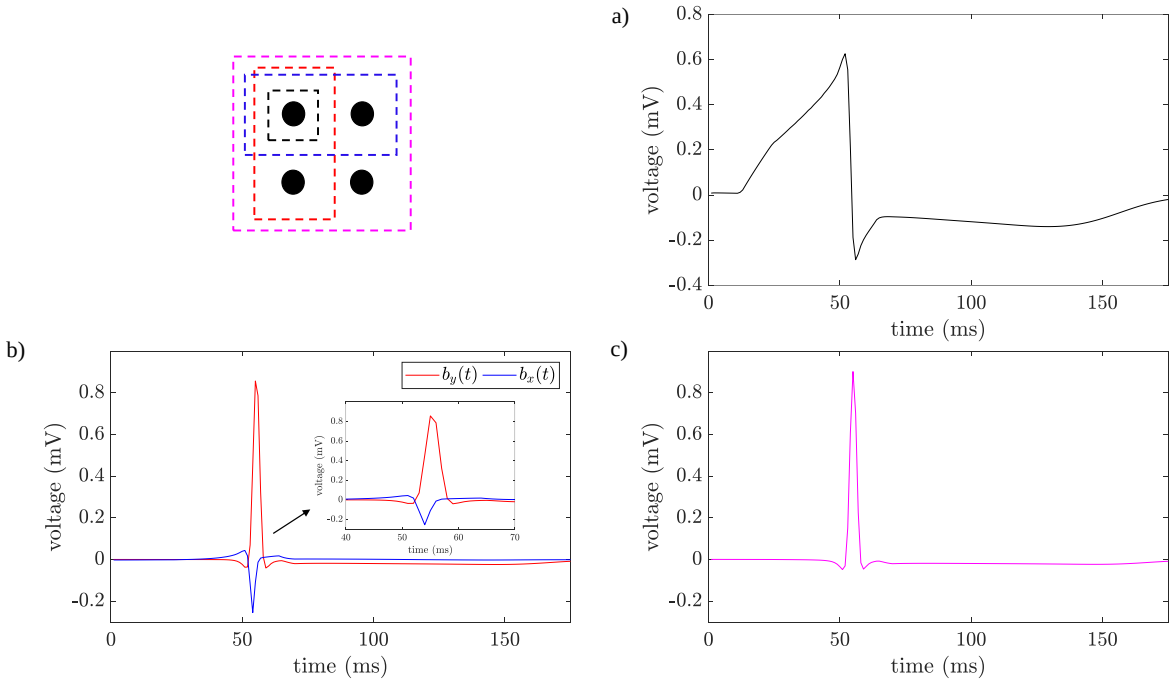

Figure 1.10: Unipolar (a), bipolar (b) (where the amplitudes of signals $b_x(t)$ and $b_y(t)$ are zoomed in) and omnipolar (c) EGM recorded at the atrial myocardium in SR and showing the atrial depolarization (time window of 200 ms). In the same figure, a schematic representation of the recording electrodes (black dots) is also provided.

1.3.5 Fibrosis Identification

During AF, EGMs are characterized by spatiotemporal variations in morphology, due to the depolarization of the atria by multiple activation wavefronts with different interbeat directions [63]. Therefore, meaningful information from fibrillation EGMs can also be used to characterize the underlying electropathological substrate. Many of the patients with persistent AF manifest fibrotic tissue in the atrium. Atrial fibrosis represents a structural anomaly of the atrial myocardium [72]. It is characterized by an altered ECM activity caused by fibroblasts [73], which alters the electrical conduction and excitability of the tissue. Fibroblasts activation and proliferation, as well as their secretion of extracellular matrix proteins, such as collagen, characterize fibrotic tissue [74]. This structural remodeling mainly occurs during the reparative process to replace damaged myocardial parenchyma [75]. In addition to this replacement process, others, as reactive fibrosis to a trigger as inflammation, have been recognized as responsible for fibrosis. This aspect, combined with the structure of the atrial wall, makes detection of fibrotic tissue in the atrium even more challenging (also compared with the identification of ventricular fibrosis) and suggests the need for more specific imaging tools and markers to detect and quantify fibrosis [60], [76].

Atrial fibrosis has been observed to be correlated to AF [77], even if their causal relationship is still challenging [72]. On the one hand, fibrosis can result from the electrical [72] as well as structural [75] atrial remodeling found in AF; on the other hand, remodeling

induced by fibrosis generates a substrate which can promote AF [77], [72] and whose spatial distribution may influence both the location and variability of the fibrillatory wavefronts [78]. This concept is commonly known as "AF begets AF".

As already mentioned in subsection 1.3.3, PVI in patients with persistent AF can eventually show unsatisfactory results for the reconnection of the PVs. This has led to the development of further ablation strategies, including those aiming to ablate scar areas within the atrium [60]. Hence the importance of identifying and quantifying fibrosis in the atrium, with the ultimate goal of improving the ablation outcome. Electrophysiologically, atrial fibrosis areas are characterized by low amplitudes of EGMs and CVs, as well as EGM fractionation, which can be delineated by EAM systems [79], [80]. Several studies conducted over the years have suggested the choice of 0.5 mV as the threshold value of b-EGMs peak-to-peak amplitude to discriminate between fibrotic (F) and non-fibrotic (NF) areas in the atrium during SR [81]. However, this procedure presents limitations, some of which are listed below:

- morphological and temporal information contained in the signal, which reflects the possible presence of underlying abnormalities in the atria, is disregarded by a peak-to-peak voltage measure [82];
- bipolar voltage is influenced by the tissue-electrode contact, whose maintenance cannot be guaranteed in clinical settings and may be challenging in anatomically difficult sites (e.g. the PVs);
- technical factors not related to the substrate, including the relative orientation between the recording electrode pair and wavefront propagation direction, electrode size, interelectrode distance and b-EGMs filtering may affect bipolar voltage measurements, as well [82];
- the voltage threshold used to determine low-voltage areas has never received an histological validation and their definition has not been standardized [82].
- there is no consensus in whether voltage maps (which will be discussed extensively in section 1.4) should be produced in SR or AF.

Clinically, atrial fibrosis corresponding to low-voltage areas is usually delineated by delayed enhancement magnetic resonance imaging (DE-MRI) [79]. This procedure allows the visualization of myocardial scar tissue after the injection of a contrast agent (gadolinium), a paramagnetic metal which is washed out with delay compared to healthy surrounding tissue [78]. Several studies have revealed the utility of gadolinium enhancement to assess LA myocardial tissue in patients with AF [78], [83]. Evaluating pre-existing fibrosis before ablation can help the prediction of procedure outcome and the eventual recurrence of the arrhythmia [78]. The amount of fibrotic tissue can be calculated as the percentage of the total LA volume and categorized according to a well-established Utah

classification [84], [83]. This classification allows the quantification of the extent of atrial fibrosis, by establishing four increasing stages as severity of fibrosis raises: stage I (10% of fibrosis), stage II (10–20% of fibrosis), stage III (20–30% of fibrosis) and stage IV (30% or greater of fibrosis) [85], [86]. Percentage of fibrotic tissue has been shown to affect success of ablation procedure [87], increasing AF recurrence with higher stage of fibrosis. Similarly, post-ablation DE-MRI allows the evaluation of the total scar amount, as well as of residual fibrosis, which can be used as predictors of AF recurrence [84].

Despite the widespread use of DE-MRI in visualization and quantification of atrial fibrosis in patients with AF, some drawbacks affecting both acquisition and processing of images must be pointed out [85]:

- None of the approaches used for fibrosis definition have been standardized [85]. These involve the following main steps [86]:

  1. manual or semi-manual segmentation of the atrial myocardium to delimit the region of interest (atrial wall) from magnetic resonance image (MRI). This is a time-consuming step and may misclassify external tissues, which have been included in the myocardium segmentation, as fibrosis;

  2. detection of fibrotic tissue within the atrial myocardium by thresholding techniques, consisting on the application of cut-off values to distinguish between NF and F tissue. The most suitable threshold value is chosen by an expert, affecting accuracy of the techniques and limiting their interpatient and inter-operator reproducibility.
     Nevertheless, the image intensity ratio (IIR) was introduced in [88] as a normalized measurement for fibrosis assessment, computed as the ratio between the LA wall intensity and the mean blood pool intensity, as described in [89]. Following this approach, the atrium can be segmented in the MRI using an image post-processing software like ADAS 3D® (Galgo medical SL, Barcelona, Spain) and a color-coded 3D mesh can be automatically generated by projecting IIR values over the 3D atrial shell, showing the healthy tissue (IIR ≤ 1.2) in blue, the dense fibrosis (IIR > 1.32) in red and the interstitial fibrosis as a transition area. A representative example of IIR distribution over MRI shell of a LA is shown in Fig. 1.11.

- DE-MRI is a well-established procedure to characterize fibrosis in ventricles, but not in the atria, whose reconstruction is limited by the challenging spatial resolution of atrial wall [78].

- Atrial fibrosis assessment is affected by quality of MRI, which depends on the aforementioned spatial resolution, the gadolinium dose, physiological characteristics of the patient, magnetic field strength, lower sensitivity and artifacts with elevated heart rates [85].

- The use of the DE-MRI has not received histological validation in detecting atrial fibrosis [80].

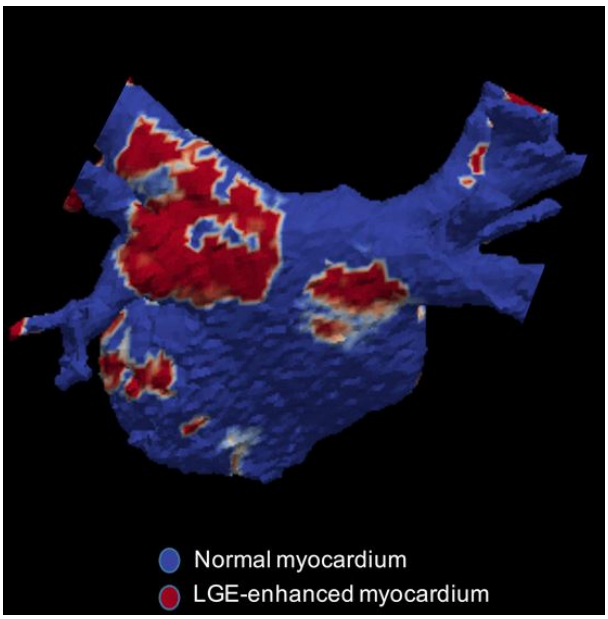

Figure 1.11: Representation of fibrotic and non-fibrotic tissue (in red and blue, respectively) based on the IIR distribution over the 3D LA shell. Reproduced, adapted and modified from [90].

Another non-invasive approach to detect fibrotic tissue in the atrium considers as a fibrosis surrogate the loss of LA function [85], which has been shown to be associated with increased risk of AF [91]. Left atrial strain represents a measure of myocardial deformation [92] and can be derived by the image modality of two-dimensional speckle tracking echocardiography [93]. LA strain are used in diagnosis, prognosis and management of patients with different pathological conditions of the heart [94]. A lower LA strain turned out to be related to higher fibrosis at LA wall detected by DE-MRI in patients with AF [95]. However, this indirect approach is affected, among others, by the following limitations [85]:

- an established and accepted range of average reference values for LA strain is missing;
- a standard technique to measure LA strain is missing;
- LA strain values are highly variable among different echocardiography tools;
- acquisition of LA images may be affected by technical aspects, including PVs;
- tracking of LA wall is influenced by its thickness.

Despite atrial fibrosis detection methods presented above are well-established, novel approaches trying to overcome their limitations should be introduced and their application in clinical practise should be encouraged.

1.4 Atrial Mapping Strategies

Cardiac mapping consists of the visualization and interpretation of the myocardium spatiotemporal electrical characteristics during a certain heart rhythm [17], helping to understand the mechanisms of arrhythmias. This process is mandatory to localize AF triggers so that the ablation strategy can be performed in an effective and safe manner [60], limiting radiation exposure and procedure time.

Atrial mapping procedure is performed under the guidance of EAM systems [96]. Electrical information at each mapping point is recorded in real time with a dedicated catheter and is displayed on a computer screen, resulting in a 3D color-coded reconstruction of the surface of the atrial chamber [97]. Each mapping point of this anatomical reconstruction of the atrium is marked with local electrophysiological information [98]. Based on that, different mapping approaches are distinguished. The main ones are presented below:

- Activation mapping: results from the display of the activation sequences of the myocytes, each of which is referred to as local activation time (LAT), by the depolarization wavefront on the anatomical surface [98]. LATs may be estimated as the maximum negative slope of the u-EGMs or as the maximal peak, the maximal slope and the activation onset of the b-EGMs [17], [99], [66], even if none of them has received an established consensus in clinical settings. In order to perform activation maps, LATs are color-coded, following a continuous color gradient, where each color represents a fixed time frame, typically from red (earlier activation) to purple (later activation). In this way, isochronal areas are shown with the same color on the map and track the whole path of activation on the 3D surface during the whole cardiac cycle. Activation mapping is one of the most frequently used approach for studying cardiac arrhythmias and may be combined with other mapping approaches. Nevertheless, contemporary EAM systems require a manual point-by-point check of LATs during the mapping procedure, making it time-consuming and operator-subject [17], [97].

- Substrate or voltage mapping: consists on the display of amplitude of b-EGMs on the 3D anatomical surface so as to to detect scar/fibrotic tissue, borderline zones and healthy areas [98], [97], [60]. Fibrotic areas are typically characterized by a peak-to-peak voltage value < 0.5 mV and depicted in red, while non-fibrotic tissue, whose delineation threshold classically ranges between 0.5 and 1.5 mV [100], is depicted in violet. Intermediate colors are used for borderline zones, whereas the dense unexcitable tissue without detectable potentials is plotted in in grey. Nevertheless, color code and threshold values adopted depend on the catheter and the EAM system used [98]. Substrate-guided procedures using these low-voltage areas as additional targets to PVs have revealed to improve AF ablation outcomes if compared with PVI alone [101], even though further randomised trials are needed [60], [102].

- Pace mapping: consists of pacing at different endocardial sites in order to reproduce the ECG morphology of the arrhythmia with the aim of identifying the tachycardia origins [17]. For this reason, atrial pace mapping is more useful for studying focal tachycardias than reentrant tachycardias. However, utility of pace mapping in the atrium is limited by the difficulty to accurately match P-wave morphology on ECGs , which results in poor spatial resolution [103].

- Entrainment mapping: results from the display of post-pacing intervals [97] for studying reentrant circuits of complex tachycardias. It is performed by pacing to a specific point with a little higher speed than speed of arrhythmia [104]. If the stimulus site is in the arrhythmia circuit, pacing accelerates the circulation without changing morphology of the P-waves, QRS complexes and EGMs. In case of uninterrupted arrhythmia, we will measure the interval from the last stimulus to the first following signal in the stimulated site, referred to as post pacing interval (PPI). It should be the same cycle length as the tachycardia. The longer PPI is in reference to the cycle length, the farther the stimulated point is from the arrhythmia circuit. In this way, the entrainment method allows the localization of the approximate position of the arrhythmia circuit in few steps. It provides additional information to activation mapping [66] and therefore may be used in conjunction with that approach.

The most common EAM systems used in clinical practise are the CARTO® 3 (Biosense Webster, Baldwin Park, CA, USA), the Ensite™ NavX™ (St. Jude Medical, St. Paul, MN, USA) [97] and the Rhythmia HDx™ (Boston Scientific Inc., Natick, MA, USA) systems. The CARTO® 3 system works with three magnetic fields generated by a location pad situated underneath the patient's thorax [60] and acting as a reference sensor [97]. They are sensed by the tip of the mapping catheter [17], thus computing the exact position of the catheter in relation to the reference sensor in space [60], [98]. The 3D geometry of the cardiac chamber of interest is then reconstructed by dragging the mapping catheter along the endocardial or epicardial surface [98]. In order to create an activation map, LATs at each point are compared with a reference time and are colour coded, thus revealing the reentry circuit or focal sources of the arrhythmia. In case of substrate mapping, the maximum peak-to-peak amplitudes of b-EGMs are depicted with different colours as described above, thus highlighting scar and healthy tissues. In addition, pre-acquired images from computed tomography (CT) imaging or DE-MRI, as well as intraprocedure echocardiography images, can be also merged with the maps created by the EAM system, thus improving the anatomical accuracy of the cardiac chamber under study [97], [98]. An example of voltage map performed with CARTO® 3 system is shown in Fig. 1.12.

The Ensite™ NavX™ system is based on the use of three pairs of patches placed on the patient's skin and a reference patch [66]. The six patches are located along three orthogonal planes and deliver low-power currents in the three directions (X, Y and Z), thus

creating a voltage gradient along each direction [98]. Catheters are equipped with sensing electrodes which measure voltage of each electric field. Their localization in the 3D space is measured based on the impedance variation with respect to the reference patch. Any mapping and ablation catheter can be used and visualized with this system, also allowing the simultaneous recording of anatomical and electrophysiological data from multiple catheters produced by different manufacturers [97]. As for CARTO® 3, this EAM system also allows the fusion of images from CT or MRI with the electroanatomical map, so as to increase the accuracy of geometry [98], [66]. However, a more recent version available, referred to as EnSite Precision™ Cardiac Mapping System, combines the impedance technology with magnetic fields (like the CARTO® 3 system), increasing the navigation accuracy compared to the prior version, especially when gradual changes in impedance occur (for instance, during AF ablation procedures). In addition, a new generation of mapping systems, called EnSite™ X EP, which include Omnipolar Technology, has been introduced, allowing the acquisition of b-EGMs that are less affected by catheter-to-wavefront orientation than conventional signals.

Each 3D mapping system has developed its own multiple electrode catheters. The CARTO® 3 system uses the PentaRay® catheter, having 20 poles arranged in five radiating branches (with an electrode spacing of 4-4–4 or 2-6–2 mm). The EnSite™ Omnipolar Technology can use the Advisor™ HD Grid Mapping Catheter, Sensor Enabled™, consisting on a grid of 4×4 equally-spaced electrodes and two additional electrodes on the shaft, with an interelectrode spacing of 3 mm. Multispline and multielectrode catheters allow a rapid creation of geometry and a simultaneous acquisition of mapping information. This is particularly useful for characterizing irregular arrhythmias like AF, where high diagnostic accuracy can be achieved [66].

The Rhythmia HDx™ system is the first 3D mapping system to allow for automated high-density mapping with a dedicated 64-electrode mini-basket catheter [66], referred to as IntellaMap Orion™. It combines a magnetic-based tracking for a sensor at the catheter tip and impedance-based tracking for all the 64 electrodes, thus allowing the acquisition of thousands of EGMs in a limited time window and consequently a rapid creation of the map with a high spatiotemporal resolution [97].

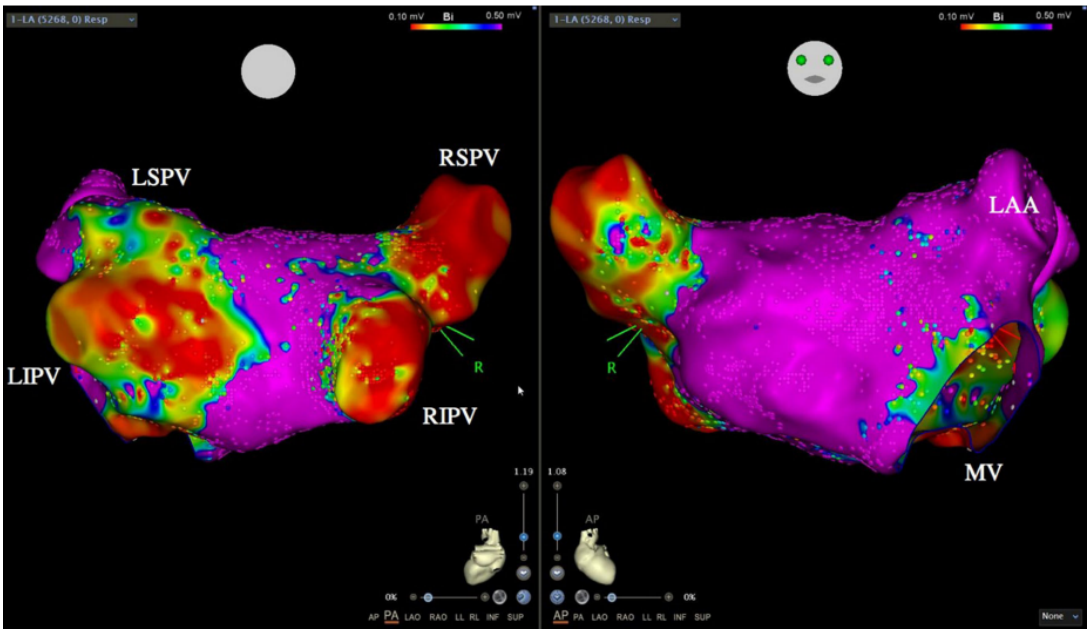

Figure 1.12: Example of a LA substrate map acquired using the CARTO® 3 system in posterior-anterior (left panel) and antero-posterior (right panel) view, for a patient with AF recurrence after PVI. In the same figure, the four PVs are highlighted (left superior pulmonary vein (LSPV), left inferior pulmonary vein (LIPV), right superior pulmonary vein (RSPV) and right inferior pulmonary vein (RIPV)), as well as the left atrial appendage (LAA) and the mitral valve (MV). Reproduced, adapted and modified from [105].

1.5 Objectives of the Thesis

As motivated at the beginning of this chapter, the main objective of the thesis is to characterize AF dynamics, both in terms of propagation patterns and fibrotic atrial substrate, so as to find the most appropriate catheter ablation target and effectively terminate the arrhythmia.
The whole work addresses to identify AF characteristics from EGMs processing. More specifically, the objectives of the different parts of this thesis are:

1. Proposal of mapping strategies based on propagation and substrate characteristics extracted from multisite EGMs and assessment of their ability in characterizing propagation patterns and in detecting fibrotic tissue in the atrium. Atrial propagation patterns are typically characterized by activation mapping, from u-EGMs or b-EGMs. However, u-EGMs are sensitive to electric far-field components due to other large cardiac structures such as the ventricles, b-EGMs depend on the angle between the catheter and wavefront propagation direction and both are sensitive to local recording noise. Atrial substrate is characterized by bipolar voltage mapping, identifying as fibrotic those areas having voltage lower than 0.5 mV. They represent a potential substrate for AF and, consequently, a target for ablation, in combination with PVI. Nevertheless, the dependence of b-EGMs on multiple factors, including

the angle of wavefront propagation relative to electrode pair direction, and the subjectivity of the voltage threshold affect this approach. With the aim of overcoming these limitations, the omnipolar electrogram (OP-EGM) method was recently introduced. In this thesis, performance of different mapping modalities based on the OP-EGM method and on the modified omnipolar electrogram (MOP-EGM) version here introduced, was investigated in characterizing myocardial substrate and propagation patterns. The MOP-EGM was proposed to reduce the residual b-EGMs dependence on catheter orientation of the standard OP-EGM, also improving its accuracy and robustness. These topics are dealt with in chapter 3.

2. Proposal of a strategy based on the u-EGMs morphology to determine the presence of fibrotic areas. Detecting fibrotic tissue by b-EGM thresholding disregards morphological and temporal information contained in the signal, which reflects the possible presence of underlying abnormalities in the atrium. In addition, bipolar voltage mapping may be influenced by technical factors not related to the substrate and the voltage threshold has never been histologically validated. In this thesis, eigenvalue dominance ratios (EIGDR) of neighbor u-EGMs were proposed as a waveform dispersion measure, hypothesizing that it is correlated with the presence of atrial fibrosis. They take into account the spatiotemporal relations of the u-EGM waveforms and overcome the limitations of the use of b-EGM voltage thresholding. These topics are presented in chapter 4.

3. Clinical validation of the methodology based on the EIGDR by means of EGMs provided by Hospital Clínic, (Barcelona, Spain). The strategy is also validated with real recordings acquired with two different types of catheters in order to investigate how their geometry affect fibrosis detection and draw useful conclusions for the application of the proposed biomarkers in clinical settings. This analysis is performed in chapter 5.

1.6 Outline of the Thesis

This document is organized as follows:

- In chapter 1, the anatomy, function and electrophysiology of the heart are introduced. Then, the chapter presents cardiac arrhythmias, focusing on mechanisms and treatment of AF. Next, intracardiac signals used to characterize AF propagation patterns and substrate are presented, pointing out the role of fibrosis in this scenario and also the main mapping strategies used in clinical practise. Finally, the objectives and clinical motivation of the thesis, as well as its outline, are illustrated.

- Chapter 2 describes the general characteristics of the data that have been used in this thesis. In particular, details are provided about the clinical data used in

chapters 3 and 5, as well as the 2D atrial model and the simulated signals used to validate the methods proposed in chapters 3 and 4.

- In chapter 3, the problems affecting current characterization of atrial propagation patterns and substrate are introduced. Therefore, the OP-EGM method introduced to overcome them is presented, together with the here proposed MOP-EGM to improve the accuracy and robustness of the CV and voltage estimates and to reduce the error induced by the b-EGMs dependence on catheter orientation not fully compensated by the original OP-EGM approach. Novel mapping strategies based on these estimates were evaluated in a simulated 2D tissue including a fibrotic patch, and preliminary results were also obtained from real epicardial signals. This chapter is based in the research presented in [64], [106], [107].

- Chapter 4 proposes the novel EIGDR approach to detect atrial fibrosis based on the waveform dispersion of neighbor u-EGMs . The typical procedure to identify fibrotic tissue in the atrium brings along several drawbacks including the lack of spatiotemporal information embedded in the signal, which reflects the possible presence of underlying abnormalities in the atria. In this chapter, eigenvalue-based indices of u-EGMs are proposed as a waveform dispersion measure. Resulting mapping strategies are assessed in detecting fibrosis patch in a simulated scenario including noise and variable electrode-tissue distance. Preliminary results were also achieved by using real u-EGMs and EAM data from individual mapping points belonging to fibrotic or non-fibrotic areas of a single patient. This chapter is based in the research presented in [108] and [109].

- Chapter 5 presents the unpublished research based on the evaluation of the EIGDR method with real EAM data and signals in a database of patients affected by fibrotic tissue at LA. The same chapter also includes a further analysis aiming to compare the values of the EIGDR markers in two different types of catheters used in clinical practice. The final objective is to investigate how the geometry of the catheter affects fibrosis discrimination performed with the proposed methodology, drawing useful conclusions for its application in clinical practise.

- In chapter 6, the main conclusions and limitations of the thesis are presented, together with future research directions.

Chapter 2

Cardiac Electrophysiological Data

In this chapter, characteristics of the electrophysiological data used in the following chapters are described. More in detail, they include clinical data used in chapters 3 and 5 to evaluate the performance of the proposed MOP-EGM with real EGMs and test the dependence of the EIGDR approach on the catheter geometry, respectively, as well as the atrial tissue model used to validate both methodologies proposed in chapters 3 and 4. On the other hand, specific clinical data and simulation scenarios are described in detail in each chapter.

2.1 Clinical Data

2.1.1 Atrial Intracavitary Recordings from PentaRay® Catheter

Intracavitary u-EGMs recorded with a PentaRay® catheter were used in section 5.2 to evaluate performance of EIGDR approach with real signals. They were obtained from fifteen different patients with AF registered at the Hospital Clínic, Barcelona, Spain, for ablation procedure at the time of their LA mapping, which was performed in SR in seven cases and during CS pacing for the other eight patients. The data acquisition protocol was reviewed and approved by the Hospital Clinic Ethical Committee (Ethics approval number: HCB/2019/0881). The patients were informed and signed the consent form. Mapping points (or catheter sites) have been acquired at the anterior, posterior, lateral and septal wall, as well as the left atrial appendage and the PVs of the LA using the CARTO® 3 EAM system, so as to reconstruct a real-time 3D anatomical map before the ablation procedure. EAM data and MRI were co-registered with the ADAS 3D Medical imaging software (*ADAS-3D, Barcelona, Spain*). Resulting views obtained for one of the cases considered are shown in Fig. 2.1. That co-register was performed by manually selecting some landmarks (between six and ten) in specific areas (such as the PVs and the atrial appendage) of the meshes. In order to determine how pathological the tissue is, the methodology described in [89] was used. Following the IIR based thresholding, a color-coded 3D mesh was automatically generated, showing in blue the healthy tissue

(IIR $\leq$ 1.2) and in red the dense fibrosis (IIR $>$ 1.32) (see Fig. 2.1).
Signals were recorded from the 20 poles distributed among the five branches of the catheter, as shown in Fig. 2.2, characterized by consecutive interelectrode spacings d, at each branch of 2, 6 and 2 mm, resulting in 20 u-EGMs associated at each mapping point. They were acquired with a sampling frequency of 1 kHz during 2.5 s (2500 samples) and include two or more activations, each containing the atrial depolarization, followed by the ventricular depolarization and repolarization.
Examples of u-EGM and b-EGM, together with atrial activation segments extracted from them at a single mapping point are shown in Fig. 2.3(a), (b), (c) and (d), respectively.

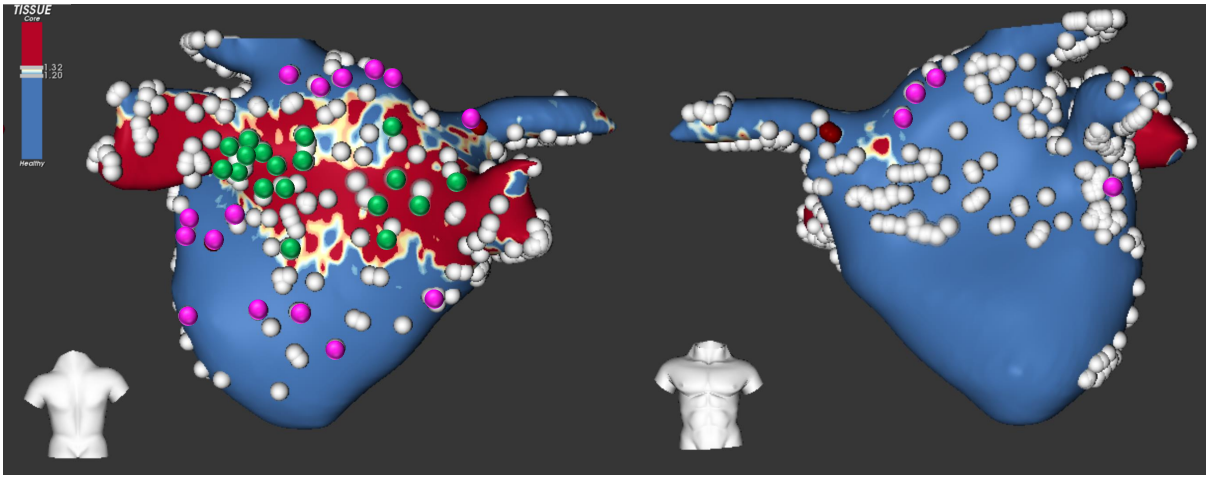

Figure 2.1: Posteroanterior (left) and anteroposterior (right) views of color-coded 3D mesh of MRI (showing dense fibrosis in red and healthy tissue in blue) generated by ADAS 3D co-registered with all EAM mapping points provided by CARTO 3 (grey) for one of the cases considered. The 38 mapping points selected over fibrotic and non fibrotic areas to compute EIGDR and bipolar indices are highlighted in green and magenta, respectively. Colors for fibrotic and healthy tissues are representative of IIR.

2.1.2 Atrial Epicardium Electrograms from Multielectrode Array

Epicardial u-EGMs recorded during SR and electrically induced AF with a 2D high-density multielectrode array (MEA) sensor [110] were used in this thesis. The MEA was positioned on the epicardial wall of the RA of a patient undergoing open-chest surgery coming from the Erasmus Medical Center Rotterdam (Rotterdam, The Netherlands). The MEA sensor was composed by 128 electrodes 2 mm-apart one from each other and organized in an 8 $\times$ 16 rectangular grid. Corner electrodes were not available for recording, so just 124 u-EGMs were available. These signals were recorded with the MEA located at four different positions on the RA, shown in Fig. 2.4: RA1 (cranial), RA2 and RA3 (medial) and RA4 (caudal). The u-EGMs were sampled at 1 kHz and low-pass filtered with 150 Hz cut-off frequency. The recording length was 5 s during SR and 10 s

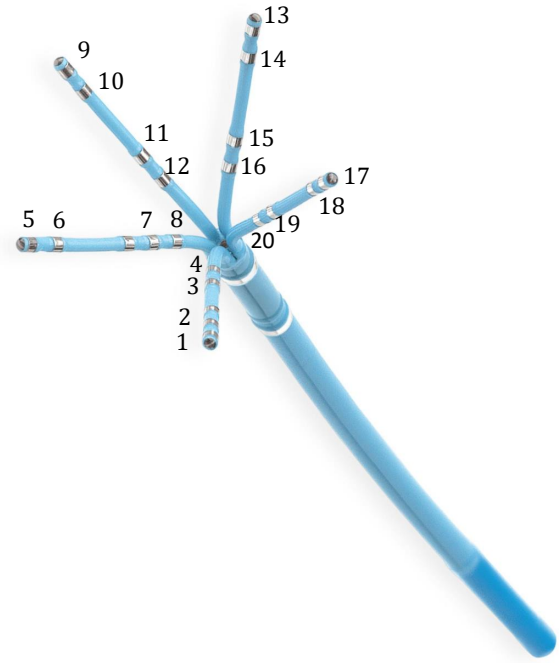

Figure 2.2: The PentaRay® catheter, where the 20 poles are highlighted. This image was modified from the Biosense Webster catalog.

during AF. Examples of u-EGMs recorded with the MEA, both at SR and in AF, are presented in Fig. 2.5. LATs manually detected by an expert electrophysiologist during SR and AF were available for MEA placed on the RA and were used to compute CV, so as to have a manual alternative to automatic estimates based on the MOP-EGM method. For that purpose, the propagation pattern in SR as well as the following representative propagation patterns observed in AF were considered: two different wavefronts colliding and fusing into one, a concentric wavefront whose focus is located within the MEA and a chaotic wavefront with several lines of block. Their respective LATs are visible in Fig. 2.6 (a), (b), (c) and (d), for SR and the three AF propagation patterns with increasing complexity, respectively.

2.1.3 Noise Excerpts from Atrial Intracavitary Recordings

In this thesis, noise segments were extracted from atrial b-EGMs and u-EGMs recorded at Hospital Santa Marta (Lisbon, Portugal). They have been used to corrupt synthetic recordings, so as to assess the sensitivity to noise of the MOP-EGM and the EIGDR methodologies in chapters 3 and 4, respectively. In the first case, six hundred different noise excerpts were extracted from b-EGMs recorded with the PentaRay® catheter (*Biosense-Webster, Inc., Diamond Bar, CA, USA*) in twenty-seven different mapping points from the LA of the same patient at intervals with no visible recorded b-EGMs. All noise excerpts were normalized so as to guarantee the same power level, coinciding with the observed average power. One hundred different realizations of this recorded

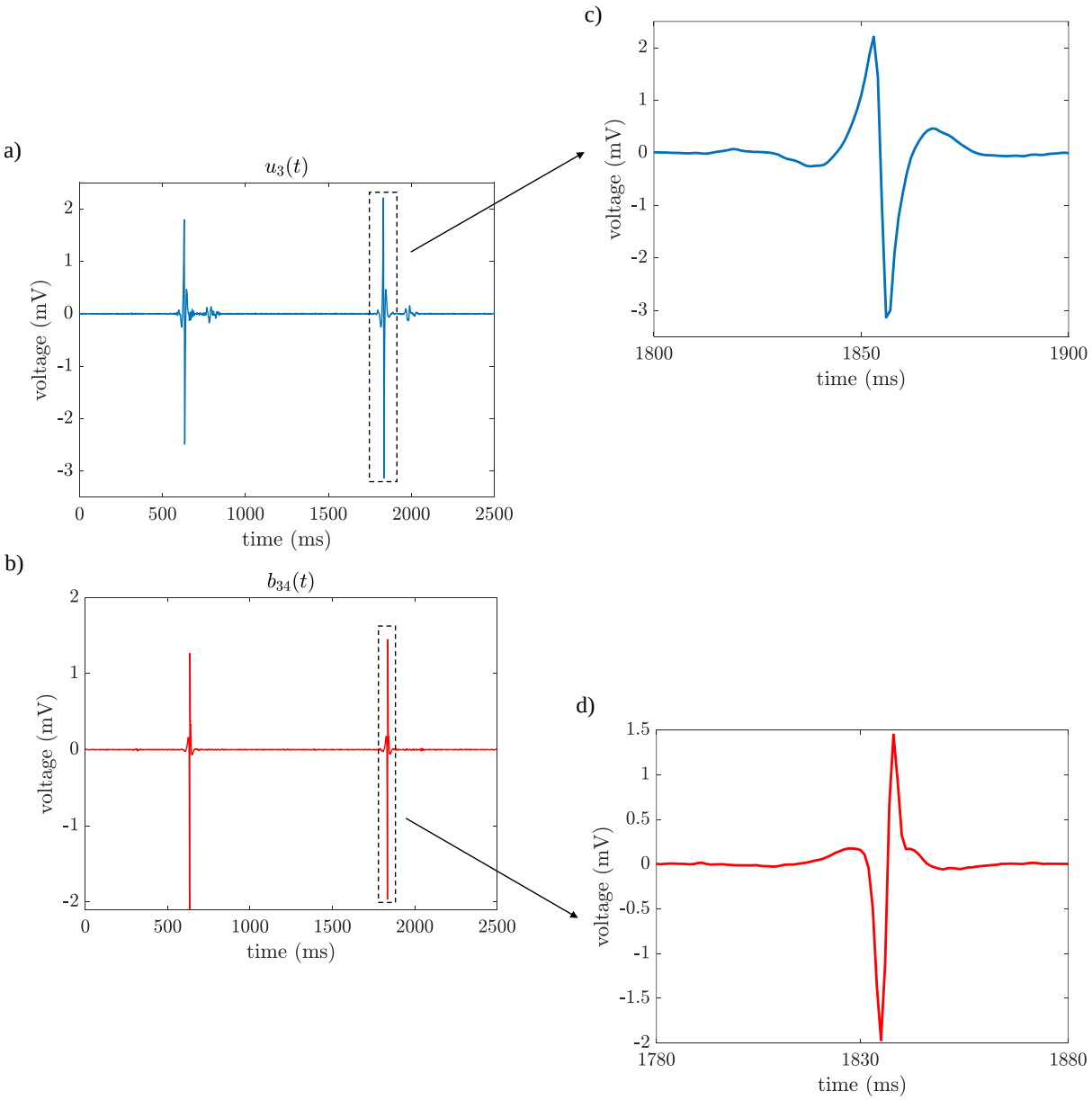

Figure 2.3: Unipolar (a) and bipolar (b) EGMs recorded at a PentaRay® catheter position in non-fibrotic area. In both plots, the atrial activations corresponding to the reference beat (the one occurring at time 2000 ms) and used in section 5.2.1 to evaluate the EIGDR approach and bipolar markers are highlighted and zoomed in panels (c) and (d), respectively. It must be noted that both u-EGMs and b-EGMs have been previously filtered as explained in subsection 2.1.1.

noise were randomly added to each of the simulated bipolar signals introduced in subsection 2.2.2. This procedure was repeated for six different noise levels, scaling the noisy realizations by varying an amplitude factor in the interval {1.0, 2.0, 3.0, 4.0, 5.0} mV, so that they had standard deviations $\sigma_n \in \{3, 6, 14, 28, 42, 55\}$ μV. Analogously, in the second case, two thousand different noise segments were extracted from u-EGMs recorded with the PentaRay® catheter at intervals with no visibly recorded u-EGMs. All noise segments were normalized to have zero mean and standard deviations

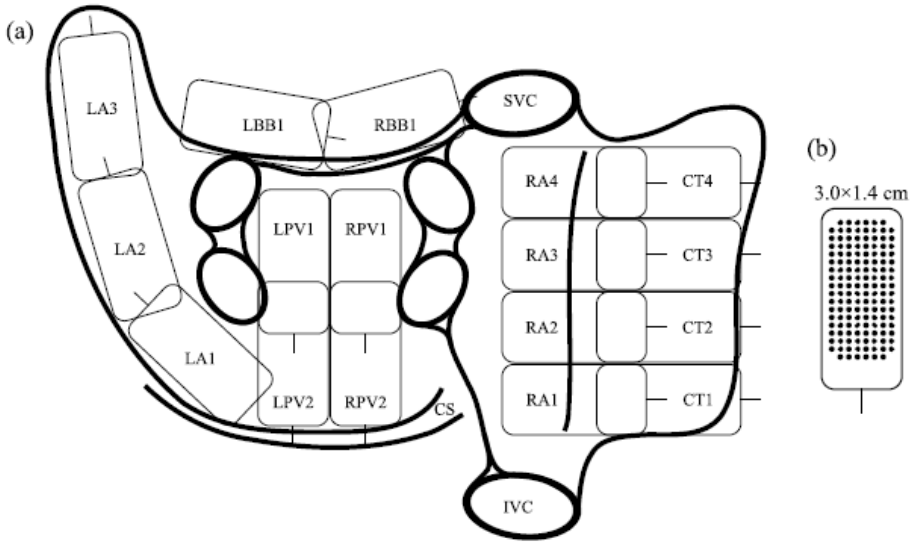

Figure 2.4: (a) Location of the MEA on the atrium during the mapping procedure in posterior view (LA: left appendage, LBB: left Bachmann bundle, LPV: left pulmonary vein, SVC: superior vena cava, RA: right appendage, IVC: inferior vena cava, CS: coronary sinus, CT: crista terminalis) and (b) schematic of the MEA sensor used for mapping.

$\sigma_v \in \{0.0, 5.8, 11.6, 23.2, 46.4\}\ \mu V$, obtained by varying the amplitude factor so as to assume the following values {0.0, 0.125, 0.25, 0.50, 1.0} mV. Resulting standard deviations are concordant with observed average power in unipolar recordings [111] and guarantee a homogeneous power level, yielding the following average peak-to-peak amplitudes of noises $\overline{V}_{pp,v} \in \{0.0, 24.2, 48.4, 96.7, 193.5\}\ \mu V$. Examples of the 20 real u-EGMs acquired by the PentaRay® at a specific mapping point, as well as one of the noise excerpts extracted and two noisy u-EGMs resulting from the corruption of synthetic signals with this excerpt are shown in Fig. 2.7(a), (b) and (c), respectively.

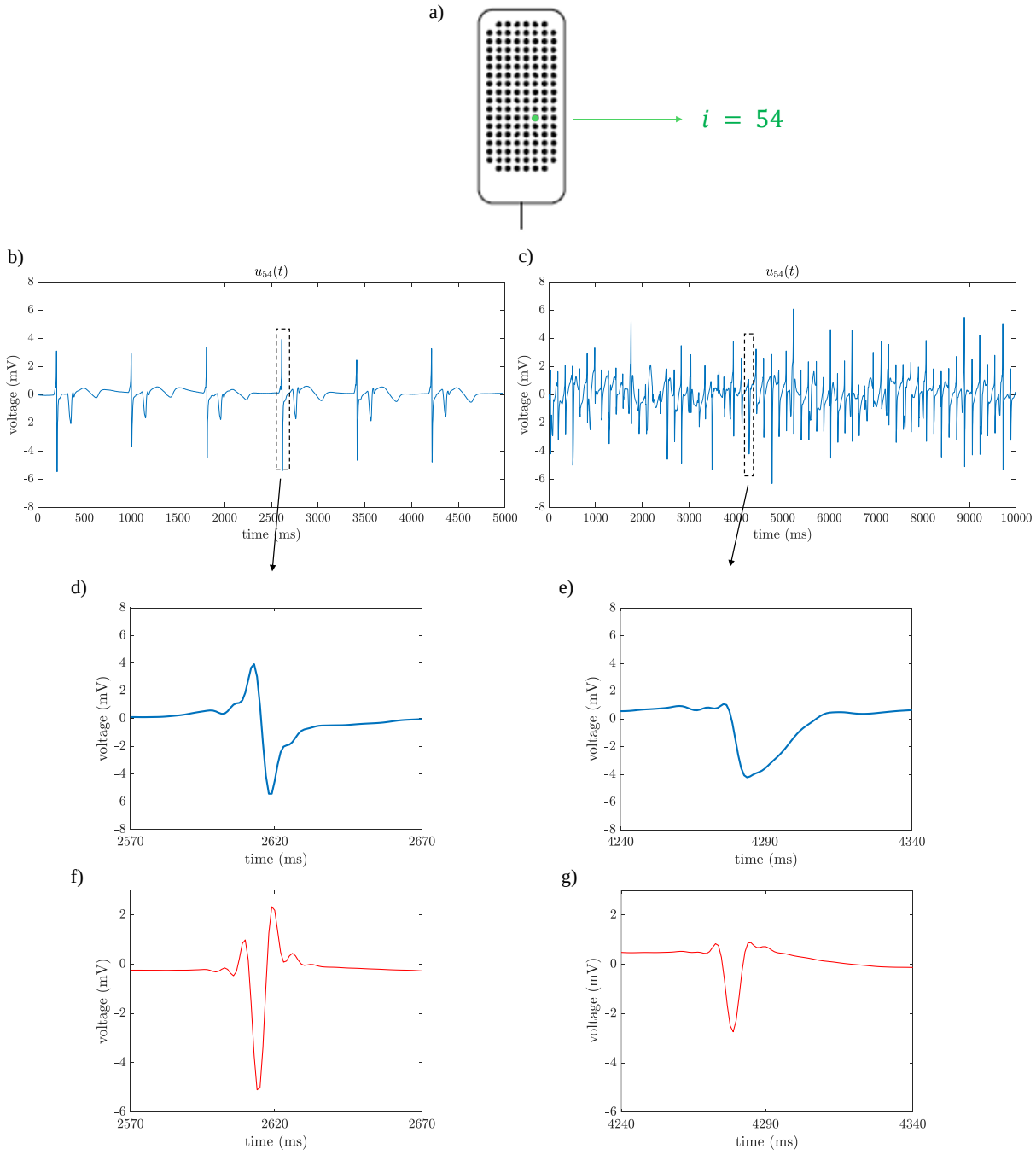

Figure 2.5: From the electrode $i = 54$ of the MEA, depicted in green in (a), u-EGMs were recorded in SR (b) and AF (c) conditions, both at RA2 position of the catheter. The unipolar atrial activations have been depicted in panels (d) and (e) for SR and AF conditions, respectively, whereas atrial depolarizations extracted from the b-EGMs computed between electrodes $i + 1 = 55$ and $i = 54$ have been displayed in panels (f) and (g) for the same rhythms.

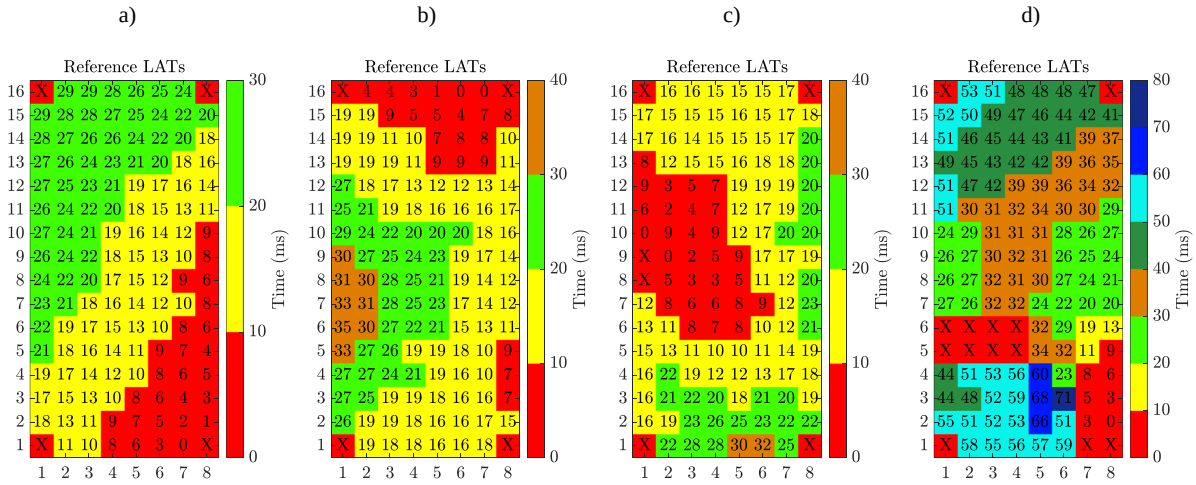

Figure 2.6: LAT maps representative of the atrial propagation patterns in normal SR (a) as well as during three representative propagation patterns in AF characterized by two different wavefronts colliding and fusing into one (b), a concentric wavefront whose focus is located within the MEA (c) and a chaotic wavefront with several lines of block (d).

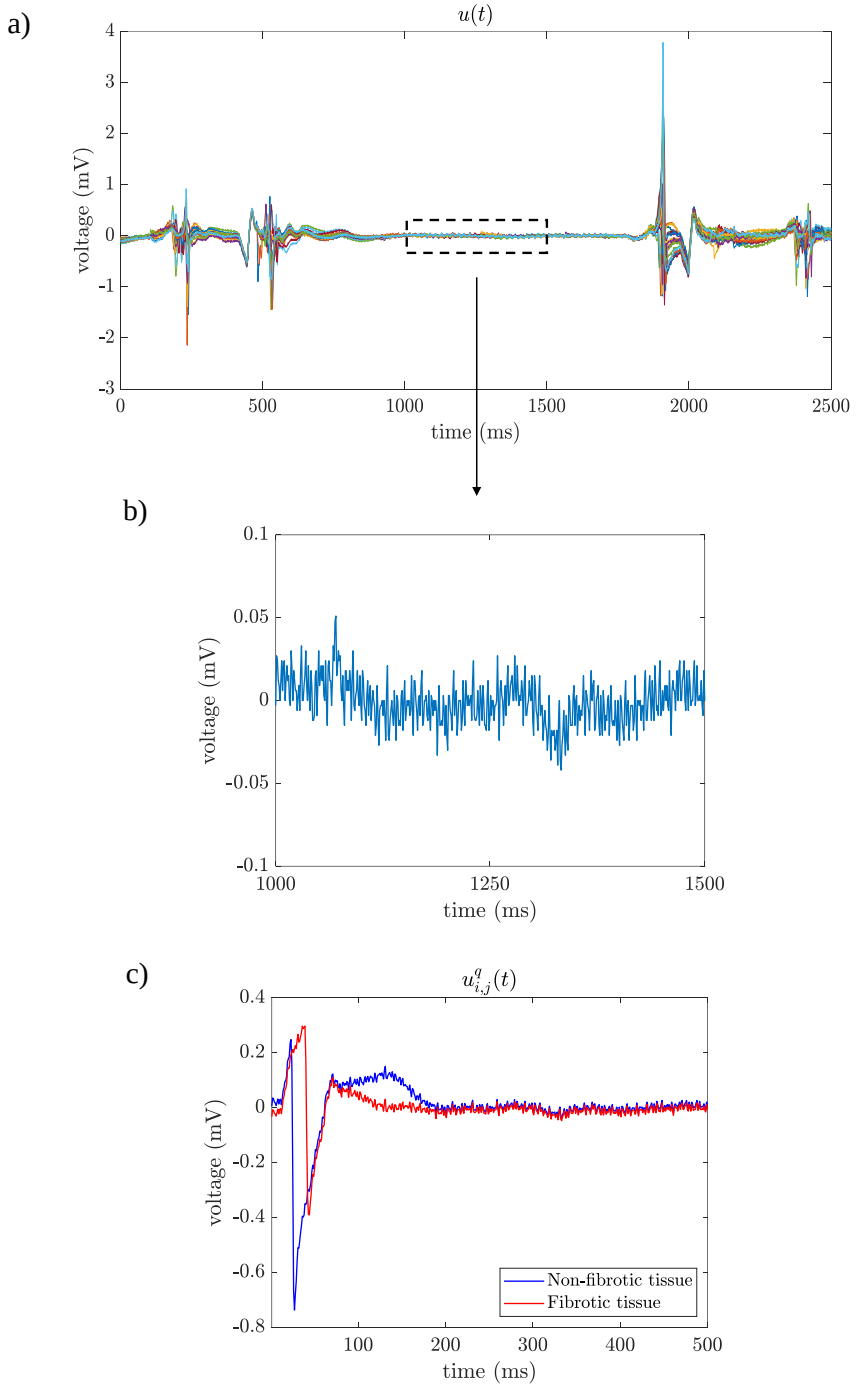

Figure 2.7: (a) Examples of 20 u-EGMs $u(t)$ used to extract noise segments of length 500 ms (highlighted with dashed line) where no activations are present; (b) zoom of one of the noise excerpts extracted and used to corrupt simulated u-EGMs introduced in subsection 2.2.2 (with a noise level $\sigma_v = 46.4\ \mu V$), thus obtaining the noisy signals $u^q_{i,j}(n)$ depicted in (c). From the notation in subsection 2.2.2, $(i, j) = (3, 3)$ corresponds to a non-fibrotic tissue area and $(i, j) = (8, 7)$ to a fibrotic area (blue and red line, respectively).

2.2 Simulated Data

2.2.1 Atrial Recordings from Multielectrode Array in Uniform Double-Layer Model

As a first study for performance assessment of the omnipolar approach, in section 3.2, different propagation patterns were simulated from a single focus in a uniform double-layer model of an atrial tissue planar slice. Tissue slices of 18×34×2 mm were simulated for isotropic and anisotropic tissues (with an anisotropy ratio of 0.5, i.e. double velocity in y-axis than in x-axis or vice versa). In a rectangular 8 × 16 high-density MEA centered in the 2D tissue slice, with an interelectrode distance of 2 mm, u-EGMs were computed. For each set of tissue properties, three different foci were considered for the activation: at the center of the slice, at 30 mm from the left side of the slice and in the right inferior corner of the slice (henceforth referred to as *center*, *side* and *corner*, respectively). The MEA and a schematic representation of the three different propagation patterns simulated are depicted in Fig. 2.8 from (a) to (d), respectively. Each synthetic u-EGM contains a single activation (corresponding to one sinus beat) and was low-pass filtered with 150 Hz cut-off frequency. LATs were computed as the samples where the u-EGMs present their maximum negative slope [17].

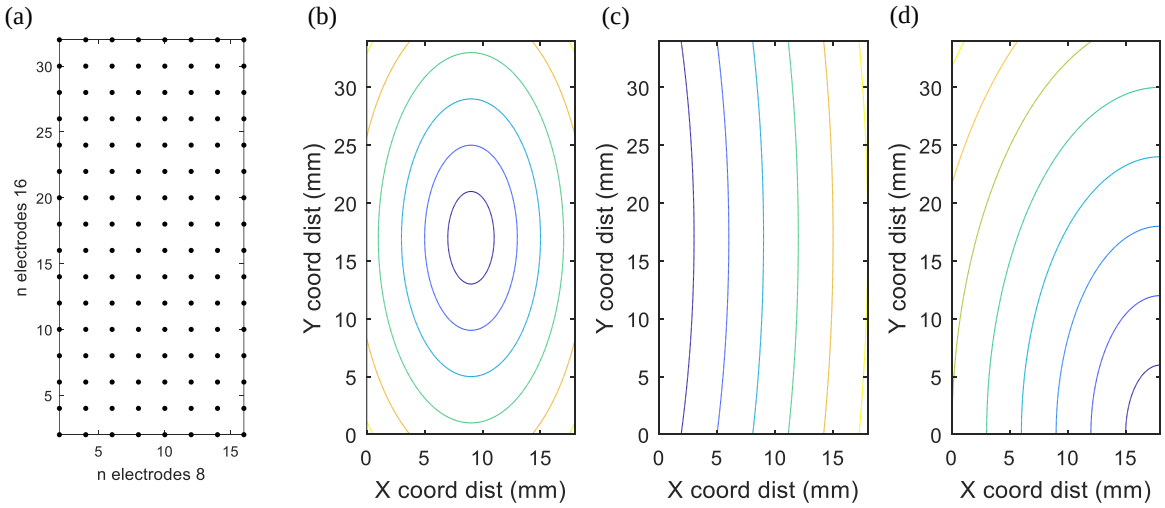

Figure 2.8: Schematic of the 8 × 16 MEA (a) and the focus located at three different positions (at the center (b), at 30 mm from the left side (c) and in the right inferior corner (d) of the slice) considered during the preliminary test of the omnipolar CV and propagation direction.

2.2.2 Atrial Recordings from Multielectrode Array in Two-Dimensional Sheet with Fibrosis

The cellular models developed by Courtemanche *et al.* [112] and Maleckar *et al.* [113] were used as base for generation of the simulation data employed in chapters 3 and 4 of this thesis. They represent two of the main human atrial electrophysiological cell models in literature and will be referred to in the text by the first author's name. The Courtemanche cellular model consists on the development of the human atrial AP based on Na^+, K^+ and Ca^{2+} current data directly recorded from human atrial myocytes [112]. Nevertheless, animal data were also used when human data were not enough to completely characterize a given atrial current. Those experimental data were referred to existing published models of atrial and ventricular APs.
The Maleckar model reproduces the coupling between human atrial myocytes and a variable number of fibroblasts and investigates the role of this cell-to-cell interaction on the myocyte excitability and repolarization [113]. According to this model, the myocyte resting potential and morphology of AP strongly depend on the number and the electrophysiological properties of membrane of coupled fibroblasts, the intercellular coupling conductance and the stimulation frequency.

The atrial model consists of a simplistic 2D finite element mesh of 4×4 cm, simulated under cAF conditions by dividing it into adjacent square elements whose centers were separated 0.1 mm (regular spatial resolution of 100 μm) and provided by Centro de Investigación e Innovación en Bioingeniería at Universitat Politècnica de València (Valencia, Spain). A circular patch having a diameter of 2 cm was defined within the 2D tissue, whose center coincides with that of the tissue slice, as shown in Fig. 2.9 (a). Inside this circular patch, a diffuse fibrosis pattern from endocardium to epicardium was randomly defined following a uniform distribution and the single cardiomyocyte under cAF conditions was coupled with a randomly variable number of fibroblasts within the patch, to reproduce fibrosis effects.

Over the simulated anatomy the electrodes were distributed so as to reproduce a 15×15 high-density MEA, mimicking the Advisor^{TM} HD Grid Mapping Catheter, Sensor Enabled^{TM} shown in Fig. 1.9 (a), with an interelectrode distance $d = 2$ mm. The MEA was located so that its central electrode corresponds to the center of both the tissue slice and the circular patch, and was rotated by an angle Ψ, $\Psi \in \{0°, 30°, 45°\}$, with respect to the tissue fiber direction, so as to simulate three possible catheter positions on the atrial myocardium. Fig. 2.9 (b) shows the three MEA orientations over the tissue geometry.

All the non-fibrotic nodes of the mesh were assigned the properties of a variation of Courtemanche model for the AP morphology of the LA, as fibrosis tends to appear more frequently in that chamber. This modification takes into account the atrial electrophysiological characteristics experimentally observed in the LA and remodeling of atrial cells induced by cAF. In order to reproduce AP morphology of LA, the maximum ionic

conductance of the rapid delayed rectifier potassium current (I_{Kr}) was selected 1.6-fold greater than the original RA model [114], [115]. In addition, electrical remodeling induced by cAF was introduced through the variation of the maximum conductances g of the transient outward potassium current (I_{to}), the L-Type calcium current (I_{CaL}), the inward rectifier potassium current (I_{K1}), the ultrarapid outward potassium current (I_{Kur}) and the slow delayed rectifier potassium current (I_{Ks}), similarly to other computational studies [116], [114]. APs were recorded after 1 minute of stimulation at a basic cycle length of 500 ms. Table 2.1 provides variations of the maximum conductances to reproduce atrial electrical remodeling under cAF conditions.

Within the circular patch, 20% of the nodes were assigned the Maleckar model for the coupling between myocytes and fibroblasts [113]. Fig. 2.10 shows the APs registered in two different cardiomyocytes from the mesh, one outside the fibrotic patch and the other inside the fibrotic patch, where it is coupled with two fibroblasts. Electrical remodeling induced by cAF produces a reduction of 55% in duration measured at 90% of AP repolarization (111 vs. 248 ms), which is consistent with experimental data [117]. Fibroblast coupling with cAF cardiomyocytes makes resting potential less negative (78 vs. 83 mV) and elongates the duration at 90% repolarization (120 vs. 111 ms). The intercellular CV was reduced by 30% in all elements of the patch with at least one fibroblast node [118]. Although atrial fibrosis density depends on the patient, the 20% represents a realistic percentage for the studies conducted in this thesis, representing the threshold value between stage II and stage III of the Utah classification for quantifying fibrosis [83].

The electrical activity was simulated by using the monodomain equation approach [119], [120]. Simulations were run using the ELVIRA software [121], a finite elements code to solve the monodomain equation developed at the Department of Applied mechanics and Bioengineering of the University of Zaragoza. They are characterized by an operator splitting numerical scheme with a constant time step $\delta t = 0.01$ ms and a spatial resolution $\delta x = 0.1$ mm.

Table 2.1: Variation of the maximum conductances g for several ionic channels used to reproduce atrial electrical remodeling under cAF conditions, accordingly to experimental studies reported in literature. As a comparison, g values have also been reported in control conditions.

	g_{to}	g_{CaL}	g_{K1}	g_{Kur}	g_{Ks}
Control	1.00	1.00	1.00	1.00	1.00
cAF	0.25	0.35	2.00	0.55	2.00
References	[122]	[123, 124]	[117, 125, 126]	[122]	[122]

The simulated atrial tissue was excited by a simple propagation pattern consisting of a plane and homogeneous wavefront in the direction of tissue fibers, as indicated by

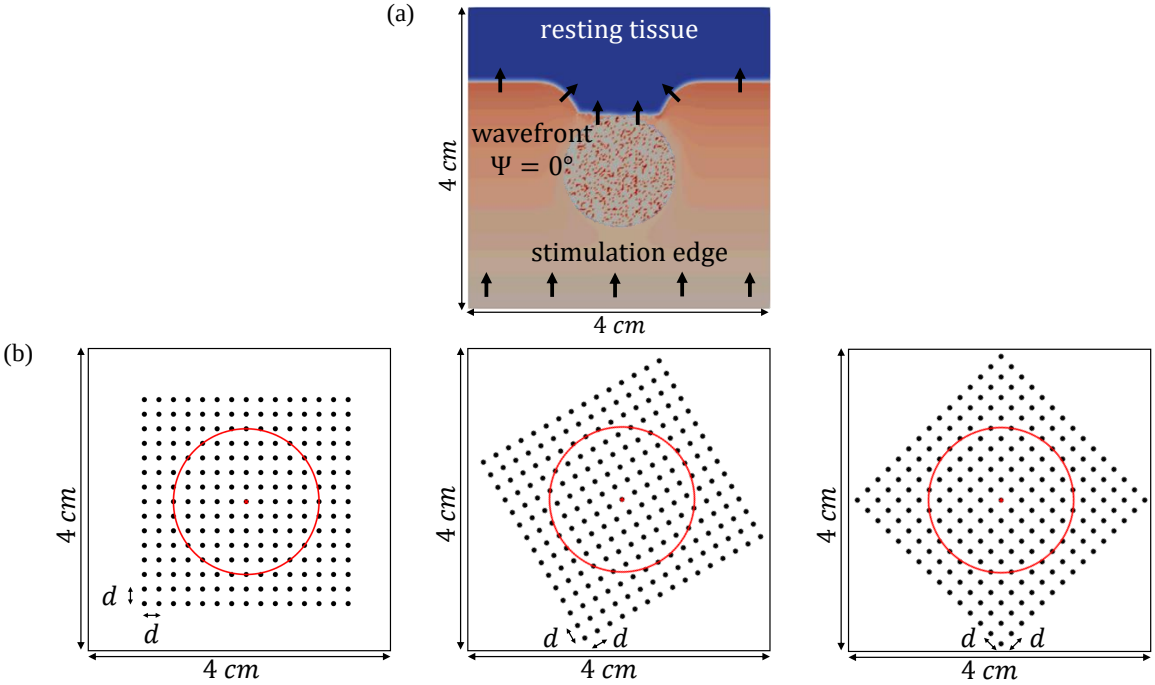

Figure 2.9: (a) Activation distribution at a particular time instant over the 2D tissue used in this work, including the circular fibrotic patch at the center of the tissue marked with a diffuse colored area. Black arrows indicate direction of the plane wave propagation. (b) The three MEA orientations considered in this study, with respect to the tissue: $\Psi = 0°$ (leftmost), $\Psi = 30°$ (middle) and $\Psi = 45°$ (rightmost), where the electrodes are represented as superimposed grid of black dots and the red circle encompasses the fibrotic tissue area. It should be noted that representation in (a) refers to the relative orientation between tissue and propagation direction corresponding to $\Psi = 0°$.

black arrows depicted in Fig. 2.9 (a). Synthetic u-EGMs $u_{i,j}(n)$ were computed as originated by the passage of the propagation wavefront by electrodes located at sites (i, j), $(i \in \{1, ..., N\}, j \in \{1, ..., N\})$, of the MEA. They were computed in a volumetric tissue-blood model with a temporal resolution of 1 ms, as in [127], by using an approximation of the bidomain formulation in two steps [128] implemented in MATLAB (MathWorks, Natick, MA). The detailed calculation can be found in [127]. In summary, the bidomain equations were decoupled assuming equal anisotropy ratios for the intracellular and extracellular conductance tensors, accounting for changes in the transmembrane and extracellular potentials, respectively. In the first step, transmembrane potential was solved by the monodomain approach. Then, in the second step, the already calculated transmembrane potential was used to obtain the extracellular potential, considering the tissue to be immersed in a non-conductive bath. Therefore, unipolar signals were solved in the entire domain by the governing equations for a solid volume conductor and its boundary conditions at the tissue-blood interface.

Simulated u-EGMs were obtained with a sampling frequency of 1 kHz, duration of 0.5 s

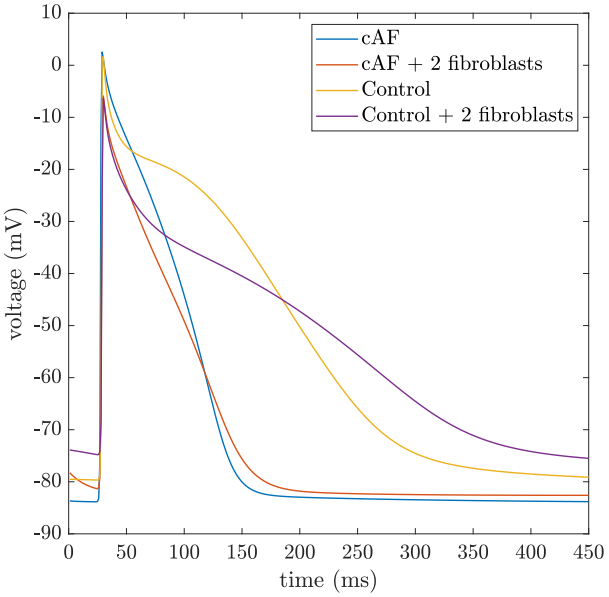

Figure 2.10: APs in cAF registered in two different nodes from the simulation mesh: in a cardiomyocyte outside the fibrotic patch (light blue line) and in a cardiomyocyte inside the fibrotic patch coupled with two fibroblasts (orange line). In order to show the effect of the applied electrical remodeling, APs were also shown in control conditions, from different simulations not including electrophysiological remodeling and not used in works presented in this thesis (yellow and violet lines, for uncoupled and coupled cardiomyocytes, respectively).

($N = 500$ samples), and including one single activation (depolarization plus repolarization).

Synthetic bipolar and unipolar EGMs were corrupted with the noise excerpts introduced in subsection 2.1.3. Resulting noisy recordings have been used to validate the MOP-EGM and the EIGDR methodologies in chapters 3 and 4, respectively, where they have been widely discussed. In the first case (chapter 3), the MEA grid was placed at distance 1 mm from the tissue, representing a plausible compromise between recording realistic amplitude EGMs and the real clinical setting situation where there is no guarantee of maintaining a perfect electrode-tissue contact during the mapping procedure.

From simulated u-EGMs, b-EGMs $b^x_{i,j}(t)$ and $b^y_{i,j}(t)$ were computed along the two main directions x and y of the MEA as follows:

$$\begin{aligned} b^x_{i,j}(t) &= u_{i+1,j}(t) - u_{i,j}(t); \quad i \in \{1, ..., N-1\}, \quad j \in \{1, ..., N\} \\ b^y_{i,j}(t) &= u_{i,j+1}(t) - u_{i,j}(t); \quad i \in \{1, ..., N\}, \quad j \in \{1, ..., N-1\}. \end{aligned} \tag{2.1}$$

One hundred different realizations, indexed by $n \in \{1, \ldots, 100\}$, of the recorded noise introduced in subsection 2.1.3 were randomly added to each of the simulated bipolar signals $b^x_{i,j}(t)$ and $b^y_{i,j}(t)$ of equations (2.1). Consequently, one hundred noisy b-EGMs along each of the two directions, $b^{x,n}_{i,j}(t)$ and $b^{y,n}_{i,j}(t)$, were generated. Fig. 2.11 (a) shows two of the u-EGMs simulated in this study, $u_{14,2}(t)$ and $u_{14,3}(t)$, computed at electrode

sites (14,2) and (14,3) of the MEA, respectively. Resulting b-EGM $b^y_{14,2}(t) = u_{14,3}(t) - u_{14,2}(t)$, derived along y direction of the MEA, is represented in Fig. 2.11 (b). In Fig. 2.11 (c), one of the one hundred noisy b-EGMs corresponding to $b^{y,n}_{14,2}(t)$, obtained by randomly adding one of the one hundred different realizations of the recorded noise to $b^y_{14,2}(t)$ is shown for the noise level $\sigma_n = 14\ \mu V$. In the second case (chapter 4), the distance between each electrode of the MEA and tissue, $\mu_{i,j}$, has been modelled as a random variable following a normal distribution with mean $\overline{\mu} = 1$ mm and standard deviation $\sigma_\mu = 0.1$ mm, so as to take into account a more realistic scenario. Two thousand different random configurations have been simulated, where the distance of each electrode to the tissue was randomly and independently chosen following that distribution. Different realizations, indexed by $q \in \{1, \ldots, 2000\}$, of the recorded noise were randomly added to each one of the two thousand realizations of the simulated u-EGMs $u_{i,j}(n)$ computed with a variable electrode-tissue distance within the MEA, generating as a result noisy unipolar signals $u^q_{i,j}(n)$, $i, j \in \{1, \ldots, 15\}$, $q \in \{1, \ldots, 2000\}$. Noisy u-EGMs examples, in fibrotic and non-fibrotic tissue areas, are shown in Fig. 2.12(a) and (b), at two different electrode-tissue distances, respectively, with noise level corresponding to $\sigma_v = 46.4\ \mu V$.

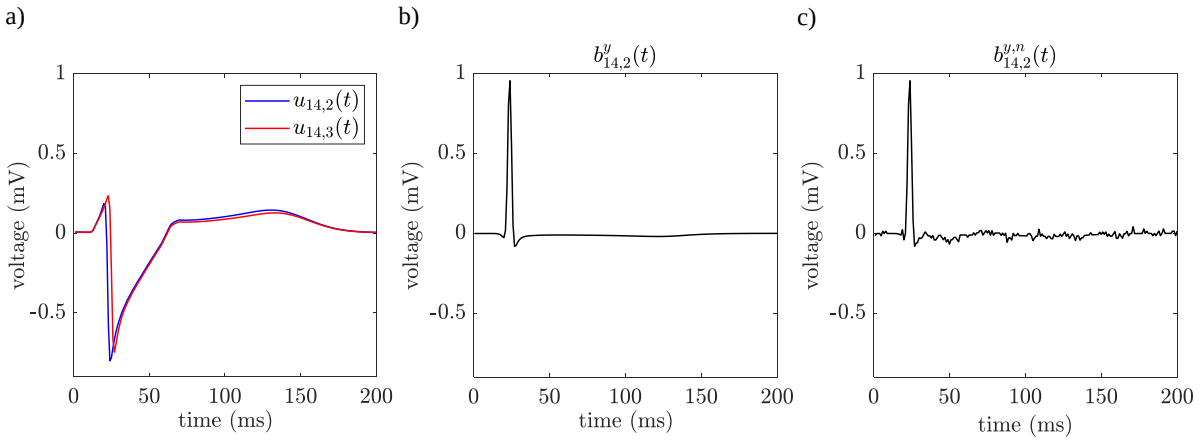

Figure 2.11: (a) Unipolar EGMs $u_{14,2}(t)$ and $u_{14,3}(t)$ and resulting b-EGM $b^y_{14,2}(t) = u_{14,3}(t) - u_{14,2}(t)$, performed without (b) and with (c) added noise.

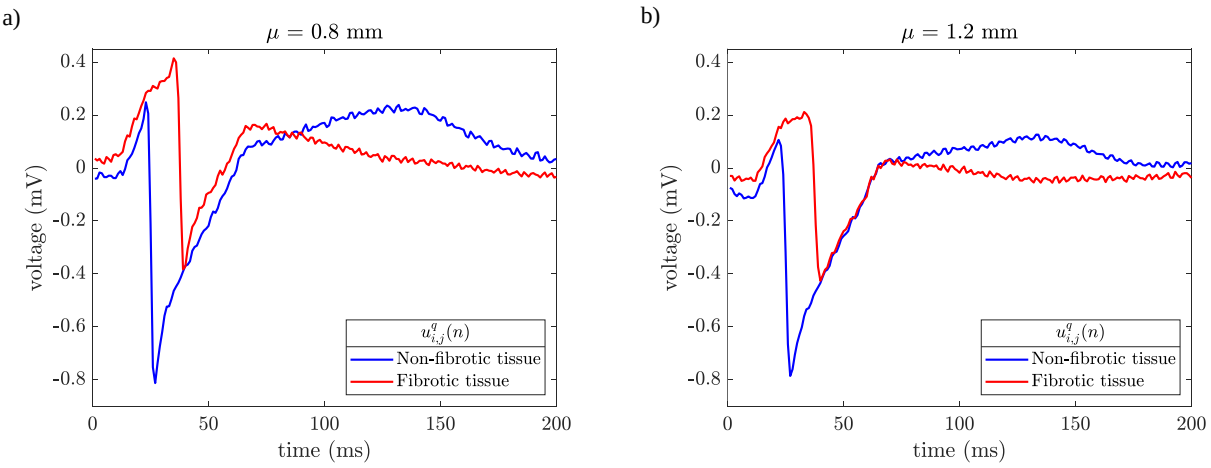

Figure 2.12: Noisy unipolar EGMs $u^q_{i,j}(n)$ ($\sigma_v = 46.4\,\mu V$) recorded in non-fibrotic, $(i,j) = (3,3)$, and fibrotic $(i,j) = (8,7)$ tissue areas, (blue and red line, respectively) at electrode-to-tissue distances of $\mu_{3,3} = \mu_{8,7} = 0.8$ mm (a) and $\mu_{3,3} = \mu_{8,7} = 1.2$ mm (b).

Chapter 3

Voltage and Conduction Velocity Mapping based on a Modified Omnipolar Electrogram Strategy

3.1 Introduction

As introduced in chapter 1, characterization of propagation patterns and substrate is meaningful for diagnosis and treatment of a wide range of atrial arrhythmias, including AF. Clinically, u-EGMs and b-EGMs are used to extract and map meaningful features (such as LATs, CV values and peak-to-peak voltages) through 3D EAM systems, thus helping clinicians to better understand AF trigger and maintenance mechanisms and to guide the ablation procedure [63].

As explained in subsection 1.3.4, AF is better investigated through simultaneous EGMs recorded by high density multielectrode catheters rather than by analyzing sequential EGMs, due to its unstable interbeat nature [64]. However, those approaches are known to have several limitations related to dependence on ventricular far-field disturbances in case of u-EGMs and on catheter-to-wavefront direction in case of b-EGMs. For this reason, the OP-EGM methodology was proposed [71], allowing the generation of voltage and CV maps less affected by u-EGMs and b-EGMs drawbacks.

In this chapter, some modifications over the OP-EGM are introduced, thus leading to the proposal of the MOP-EGM. These modifications are hypothesized to improve the accuracy and robustness of the voltage and CV estimates and to reduce the error induced by the b-EGMs dependence on catheter orientation, which is not fully compensated by the OP-EGM approach. This problem has also been reported and addressed in [129] and [130], by considering the diagonal bipoles in square cliques, in simulation and experimental animal study, respectively. This approach solved the lack of time alignment among electrode pairs, at the cost of larger interelectrode distances, with its potential implications in terms of lower voltages and accomplishment of the planar wave hypothesis.

Therefore, the main objectives of this part of the thesis are to assess the estimates of CV and propagation direction within each clique with the proposed MOP-EGM method and compare them to the ones obtained by the standard OP-EGM; to propose mapping strategies based on omnipolar EGMs estimations to characterize the atrial substrate; to assess the ability of the proposed maps in detecting a fibrotic patch and in reproducing voltage maps based on the u-EGMs. Furthermore, in order to have an alternative estimation of CV, it was also estimated from detected LATs, using a linear model obtained in the least squares (LS) sense, both with real and simulated u-EGMs.

3.2 Testing Datasets

In a first analysis of the omnipolar approach, the accuracy of the CV estimates obtained from EGMs has been assessed by using the simulated propagation patterns introduced in subsection 2.2.1.

Then, in a second analysis, substrate and CV mapping strategies based on bipolar and omnipolar EGMs and measurements have been evaluated using b-EGMs obtained by u-EGMs simulated as described in subsection 2.2.2. In order to assess the sensitivity to noise of voltage and CV maps, these synthetic b-EGMs were also corrupted with noise introduced in subsection 2.1.3. Consequently, one hundred noisy b-EGMs along each of the two directions, $b_{i,j}^{x,n}(t)$ and $b_{i,j}^{y,n}(t)$, were generated. For each realization n, the different modalities of voltage and conduction velocity maps were computed, obtaining one hundred different maps from noisy b-EGMs. These mapping strategies were tested regarding fibrosis detection, as well as voltage map reproducibility. This procedure was repeated for six different noise levels, scaling the noise realizations so that they had standard deviations $\sigma_n \in \{3, 6, 14, 28, 42, 55\}$ μV. Before normalizing the recorded noise excerpts, their standard deviation went from 1.2 μV to 11 μV, with an average value of 2.4 μV. In order to achieve the same range of noise levels reported in [111], an amplitude factor was introduced so as to obtain a range of noise level up to 55 μV, which approximately corresponds to the 95th percentile of the reported bipolar noise levels. With these noise levels, robustness of the mapping strategies can be evaluated.

3.3 Methods

3.3.1 Electrograms Modeling under Plane Wave Assumption

The omnipolar methodology estimates the E-field from the b-EGMs recorded at each set of nearby electrodes, referred as clique, under the assumption of locally plane and homogeneous wave propagation within the same, in multielectrode catheters [71].

Two 2D clique configurations were introduced in literature and considered in this thesis: a) square cliques, which consist of four-electrode sets forming a square, and b)

triangular cliques, which consist of three-electrode sets formed by an electrode and two adjacent ones, one in each direction of the 2D plane. Fig. 3.1 depicts generic square (a) and triangular (b) clique configurations, respectively. The square provides one estimate for each group of four electrodes. In order to keep the same simplified notation in each position within the MEA, its lower left electrode, corresponding to location (i, j) within the MEA, is referred to as electrode 1. The remaining electrodes of the clique are numbered from left to right and bottom to top. Therefore, electrodes 2, 3 and 4 correspond to locations $(i+1, j)$, $(i, j+1)$ and $(i+1, j+1)$, respectively, as shown in Fig. 3.1 (a). The triangular provides four estimates for the same group of four electrodes, corresponding to triangles at bottom left, bottom right, up left and up right and numerated with 1, 2, 3 and 4, respectively, in Fig. 3.1 (b).

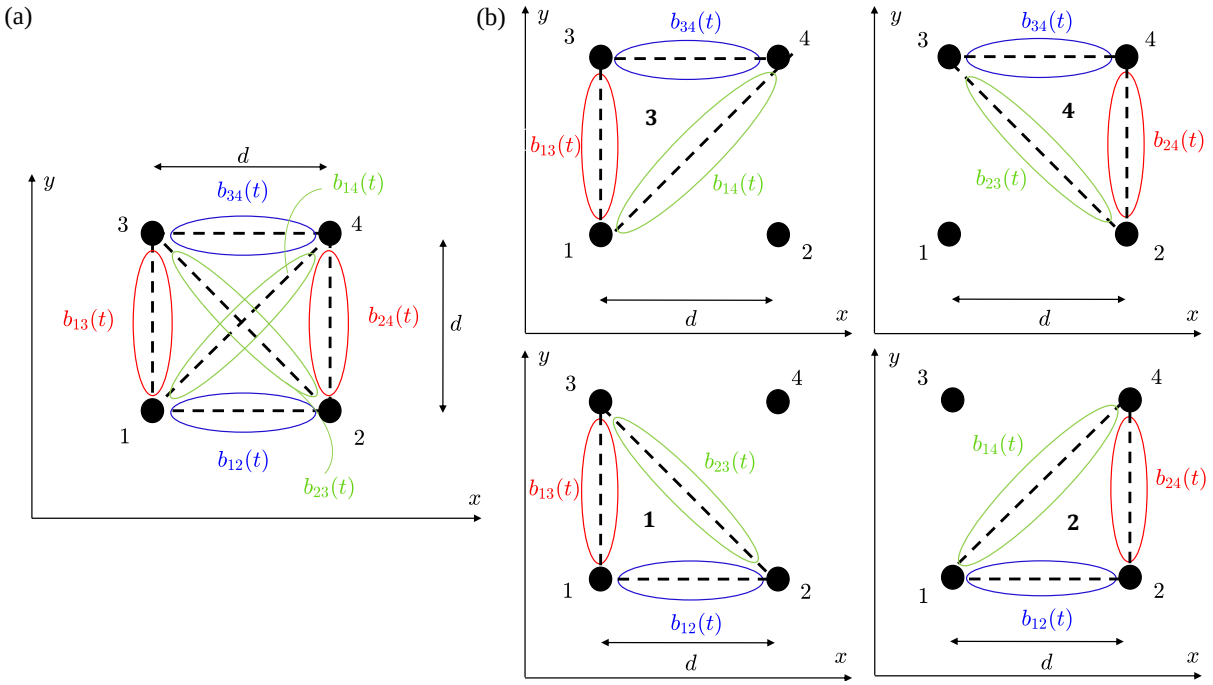

Figure 3.1: (a) Four-electrode clique. (b) Three-electrode cliques.

Let us consider any four-electrode clique within the MEA, like the one in Fig. 3.1(a). Let t_c be the reference time at which the centre of the selected square is activated. Assuming constant velocity within the set, the activation times at the four electrodes

are:

$$t_1 = t_c - \frac{d}{2v}\sin\theta - \frac{d}{2v}\cos\theta; \quad t_2 = t_c + \frac{d}{2v}\sin\theta - \frac{d}{2v}\cos\theta;$$
$$t_3 = t_c - \frac{d}{2v}\sin\theta + \frac{d}{2v}\cos\theta; \quad t_4 = t_c + \frac{d}{2v}\sin\theta + \frac{d}{2v}\cos\theta. \tag{3.1}$$

Let $\phi(t)$ be the unipolar voltage waveform generated by the passage of a plane wave by a given position at time $t = 0$. When one or more electrodes within the square are activated by $\phi(t)$ passage, the following u-EGMs and b-EGMs can be modeled:

$$u_m(t) = \phi(t - t_m),\ m \in \{1, 2, 3, 4\} \tag{3.2}$$
$$b_{mn}(t) = u_n(t) - u_m(t) = \phi(t - t_n) - \phi(t - t_m),\ \ m, n \neq m \in \{1, 2, 3, 4\}. \tag{3.3}$$

It should be noted that bipolar signals in (3.3) are derived within each clique along x direction ($b_{12}(t)$ and $b_{34}(t)$), y direction ($b_{13}(t)$ and $b_{24}(t)$), as well as along the directions of its diagonals ($b_{14}(t)$ and $b_{23}(t)$). Depending on the waveform arrival time to each electrode t_m, the activation time of each b-EGM $b_{mn}(t)$ corresponds to the passage of the wave by the middle point between electrodes m and n. Therefore, relative delays (misalignment) occur between the different $b_{mn}(t)$.

By using the Taylor's series expansion of $u_m(t) = \phi(t - t_m)$ around $t_m = t_c$, we can approximate:

$$u_m(t) \cong \phi(t - t_c) - \Delta t_m\ \phi'(t - t_c) + \frac{1}{2}(\Delta t_m)^2\phi''(t - t_c) \tag{3.4}$$
$$b_{mn}(t) \cong -\Delta t_{mn}\ \phi'(t - t_c) + \frac{1}{2}\left((\Delta t_n)^2 - (\Delta t_m)^2\right)\phi''(t - t_c), \tag{3.5}$$

where $\Delta t_{mn} = t_n - t_m$ are the differences between activation times at electrodes m and n, $m, n \in \{1, 2, 3, 4\}$, and $\Delta t_m = t_m - t_c$ are the differences between activation time at electrode m and the reference activation time of the center of the square. By replacing (3.1) in (3.5) and operating, the following b-EGMs expressions are derived:

$$b_{12}(t) \cong -\frac{d}{v}\sin\theta\ \phi'(t - t_c) - \frac{d^2}{4v^2}\sin(2\theta)\ \phi''(t - t_c) \cong -\frac{d}{v}\sin\theta\ \phi'\left(t - t_c + \frac{d}{2v}\cos(\theta)\right) \tag{3.6}$$
$$b_{34}(t) \cong -\frac{d}{v}\sin\theta\ \phi'(t - t_c) + \frac{d^2}{4v^2}\sin(2\theta)\ \phi''(t - t_c) \cong -\frac{d}{v}\sin\theta\ \phi'\left(t - t_c - \frac{d}{2v}\cos(\theta)\right) \tag{3.7}$$
$$b_{13}(t) \cong -\frac{d}{v}\cos\theta\ \phi'(t - t_c) - \frac{d^2}{4v^2}\sin(2\theta)\ \phi''(t - t_c) \cong -\frac{d}{v}\cos\theta\ \phi'\left(t - t_c + \frac{d}{2v}\sin(\theta)\right) \tag{3.8}$$
$$b_{24}(t) \cong -\frac{d}{v}\cos\theta\ \phi'(t - t_c) + \frac{d^2}{4v^2}\sin(2\theta)\ \phi''(t - t_c) \cong -\frac{d}{v}\cos\theta\ \phi'\left(t - t_c - \frac{d}{2v}\sin(\theta)\right) \tag{3.9}$$
$$b_{14}(t) \cong -\left(\frac{d}{v}\sin\theta + \frac{d}{v}\cos\theta\right)\ \phi'(t - t_c) = -\frac{\sqrt{2}d}{v}\cos(\theta - 45^\circ)\ \phi'(t - t_c) \tag{3.10}$$
$$b_{23}(t) \cong +\left(\frac{d}{v}\sin\theta - \frac{d}{v}\cos\theta\right)\ \phi'(t - t_c) = +\frac{\sqrt{2}d}{v}\sin(\theta - 45^\circ)\ \phi'(t - t_c). \tag{3.11}$$

From these expressions, the second order approximations of the different pairs of b-EGMs $b_{mn}(t)$ can be related, showing the previously mentioned delay between the different b-EGMs. The relationship between $b_{12}(t)$ and $b_{13}(t)$, measured in different x and y directions, is given by:

$$b_{13}(t) \cong -\frac{d}{v}\cos\theta\ \phi'(t-t_c) - \frac{d^2}{4v^2}\sin(2\theta)\ \phi''(t-t_c) \cong \frac{\cos\theta}{\sin\theta}\ b_{12}\left(t - \frac{d}{v}\frac{\sin\left(45^\circ-\theta\right)}{\sqrt{2}}\right). \tag{3.12}$$

Equation (3.12) shows that the b-EGM along y-direction (1-3) is a scaled version of the b-EGM along x-direction (1-2) by a factor $\left(\frac{\cos\theta}{\sin\theta}\right)$ and delayed by a time $\tau = \frac{d}{v}\frac{\sin(45^\circ-\theta)}{\sqrt{2}}$. This corresponds to the delay between the pass of the wave by the middle points of each electrode pair, separated $d/\sqrt{2}$. As expected, for $\theta = 90^\circ$ (propagation in x-direction), $b_{13}(t) = 0$, while for $\theta = 45^\circ$, the delay is $\tau = 0$, meaning that both bipolar EGMs in the x- and y- directions are activated at the same time. Similarly, the relationship between $b_{12}(t)$ with $b_{34}(t)$, both along the x-direction, is given by:

$$b_{34}(t) \cong -\frac{d}{v}\sin\theta\ \phi'(t-t_c) + \frac{d^2}{4v^2}\sin(2\theta)\ \phi''(t-t_c) \cong b_{12}\left(t - \frac{d}{v}\cos\theta\right). \tag{3.13}$$

Equation (3.13) shows that b-EGMs along parallel directions have the same amplitudes (as expected), and the delay $\tau = \frac{d}{v}\cos\theta$ ranges from 0, when the propagation is in the same direction than the electrode pairs ($\theta = 90^\circ$), which are therefore activated at the same time, to a maximum of d/v, when the propagation is orthogonal to the direction of the electrode pairs ($\theta = 0^\circ$).

3.3.2 Omnipolar Electrogram Framework and Electric Field Estimation

The OP-EGM method was introduced with the aim of obtaining EGM amplitude and propagation features which are invariant to the relative orientation between the propagation direction and the catheter [71]. It requires to consider a locally plane myocardial surface, defined by its normal unit vector $\overrightarrow{\mathbf{u}}_n$. At each point of that surface, we can consider the right-handed omnipolar coordinate system defined by the normal unit vector $\overrightarrow{\mathbf{u}}_n$, and the unit vectors in the propagation direction $\overrightarrow{\mathbf{u}}_p$ and in the direction orthogonal to $\overrightarrow{\mathbf{u}}_p$ within the 2D plane, $\overrightarrow{\mathbf{u}}_\perp$ see Fig. 3.2(a). Using this notation, the electric field $\boldsymbol{E}_{3\mathrm{D}}(t)$ at each point of the surface can be described as follows:

$$\boldsymbol{E}_{3\mathrm{D}}(t) = E_n(t)\,\overrightarrow{\mathbf{u}}_n + E_p(t)\,\overrightarrow{\mathbf{u}}_p + E_\perp(t)\,\overrightarrow{\mathbf{u}}_\perp. \tag{3.14}$$

The OP-EGM method is based on the relationship between the spatial gradient of the traveling voltage wave $\phi(x, y, z, t)$ and the E-field at the extracellular-myocardial

interface:

$$\boldsymbol{E}_{3\mathrm{D}}(t) = -\nabla\phi(t - t_c), \tag{3.15}$$

where the explicit dependence on spatial coordinates was suppressed for simplicity, just remaining the delay t_c in $\phi(t)$ associated with the clique center. Since a 2D MEA was used in this thesis, only the electric field components in the plane defined by $\vec{\mathbf{u}}_p$ and $\vec{\mathbf{u}}_\perp$ were estimated: $\boldsymbol{E}_{2\mathrm{D}}(t) = E_p(t)\vec{\mathbf{u}}_p + E_\perp(t)\vec{\mathbf{u}}_\perp$, $\boldsymbol{E}(t) \equiv \boldsymbol{E}_{2\mathrm{D}}(t)$, with $\boldsymbol{E}(t) = \begin{bmatrix} E_x(t) & E_y(t) \end{bmatrix}^T$.

The traveling wave is assumed to be locally plane and homogeneous within each clique of the MEA and to propagate in the same with a velocity vector $\boldsymbol{v} = v\vec{\mathbf{u}}_v$, where the spatial dependence has been omitted for notation simplicity. In the 2D Cartesian coordinate system defined by the unit vectors in the main directions of the MEA ($\vec{\mathbf{u}}_x$ and $\vec{\mathbf{u}}_y$), the local plane wave propagation direction within the clique having electrode (i, j) in its lower left corner, $\vec{\mathbf{u}}_v$, forms an angle $\theta_{(i,j)}$ with the direction of $\vec{\mathbf{u}}_y$, as illustrated in Fig. 3.2(b). It must be noted that the angle Ψ introduced in subsection 2.2.2 and shown in Fig. 2.9(b) is unique for each 2D catheter configuration and should not be mistaken for $\theta_{(i,j)}$, which depends on local propagation at (i, j) electrode position, see black arrows direction variations in Fig. 1.9(a).

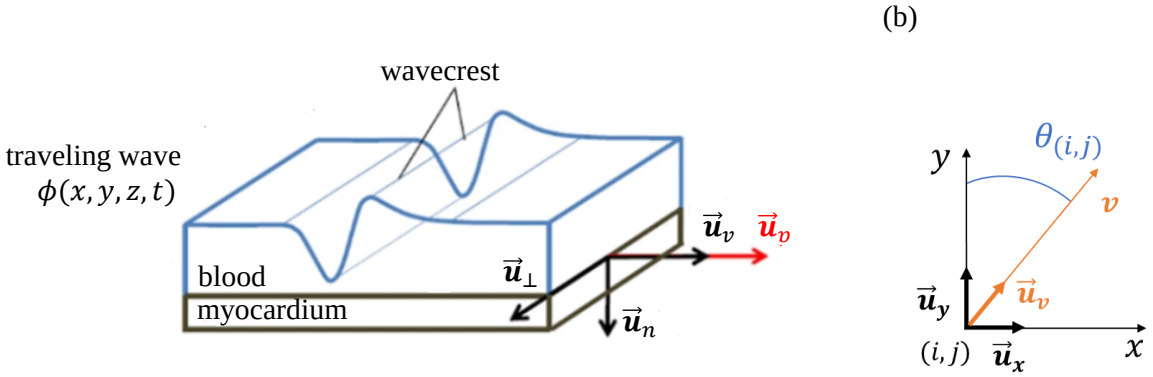

Figure 3.2: (a) The locally plane and homogeneous wave concept over the myocardial surface. In the omnipolar reference system defined by unit vector directions $\vec{\mathbf{u}}_n$, $\vec{\mathbf{u}}_p$ and $\vec{\mathbf{u}}_\perp$, the traveling wave $\phi(x, y, z, t)$ propagates with constant CV along direction detected by $\vec{\mathbf{u}}_v$. Reproduced, adapted and modified from [71]. (b) Local 2D Cartesian coordinate system in the clique defined by unit vectors $\vec{\mathbf{u}}_x$ and $\vec{\mathbf{u}}_y$. It must be pointed out that $\vec{\mathbf{u}}_v$ direction is the same as $\vec{\mathbf{u}}_p$ if CV $\boldsymbol{v}$ is well estimated.

Under that assumption, the relation between the local electric field and the measured b-EGMs is given by the following linear system:

$$\boldsymbol{b}_\varrho(t) = -\mathbf{D}_\varrho^T \boldsymbol{E}(t), \tag{3.16}$$

where $\boldsymbol{b}(t)$ is a vector containing the available b-EGMs affected by measurement errors, $\mathbf{D}$ is a matrix of interelectrode distances, and $\varrho \in \{\square, \triangle\}$ denotes the clique type, square ($\square$) or triangular ($\triangle$), respectively.

In case of square clique, as the one illustrated in Fig. 3.1 (a), $\boldsymbol{b}_{\varrho}(t) \equiv \boldsymbol{b}_{\square}(t)$ contains six b-EGMs, $\boldsymbol{b}_{\square}(t) = \begin{bmatrix} b_{12}(t) & b_{13}(t) & b_{14}(t) & b_{34}(t) & b_{24}(t) & b_{23}(t) \end{bmatrix}^T$ and $\mathbf{D}_{\varrho} \equiv \mathbf{D}_{\square}$ is a 2×6 matrix, reported below. Similarly, in case of triangular configurations, as the clique 1 in Fig. 3.1 (b), $\boldsymbol{b}_{\varrho}(t) \equiv \boldsymbol{b}_{\triangle,1}(t)$ contains three b-EGMs, $\boldsymbol{b}_{\triangle,1}(t) = \begin{bmatrix} b_{12}(t) & b_{13}(t) & b_{23}(t) \end{bmatrix}^T$ and $\mathbf{D}_{\varrho} \equiv \mathbf{D}_{\triangle,1}$ is a 2×3 matrix, also shown below.

$$\mathbf{D}_{\square} = \begin{bmatrix} -d & 0 & -d & -d & 0 & +d \\ 0 & -d & -d & 0 & -d & -d \end{bmatrix}, \quad \mathbf{D}_{\triangle,1} = \begin{bmatrix} -d & 0 & +d \\ 0 & -d & -d \end{bmatrix}. \tag{3.17}$$

Expressions similar to $\mathbf{D}_{\triangle,1}$ were obtained for the other three-electrode configurations of the clique shown in Fig. 3.1 (b). Note that with this formulation, the electric field is taken at the clique center, assuming that there are no delays between b-EGM components.

From equation (3.16) we see that the projection of the E-field along the interelectrode distance results in the corresponding b-EGM. Since measured b-EGMs will be affected by noise and model mismatch errors, we can use the LS criterion to estimate the electric field $\hat{\boldsymbol{E}}_{\varrho}(t)$ at the center of each clique:

$$\hat{\boldsymbol{E}}_{\varrho}(t) = -(\mathbf{D}_{\varrho}\mathbf{D}_{\varrho}^T)^{-1}\mathbf{D}_{\varrho}\boldsymbol{b}_{\varrho}(t). \tag{3.18}$$

The evolution over time of the $\hat{\boldsymbol{E}}_{\varrho}(t)$, estimated at the center c of each ϱ-type clique, describes a loop trajectory in the 2D plane. Under the assumption of locally plane and homogeneous wave, $E_{\perp}(t) \approx 0$ within the clique, so that $\hat{\boldsymbol{E}}_{\varrho}(t)$ should have a dominant direction and the loop should lie on a straight line along the propagation direction $\overrightarrow{\mathbf{u}}_p$ [71]. On the other hand, if the wave is not plane, $\hat{\boldsymbol{E}}_{\varrho}(t)$ will describe a bidimensional loop and propagation cannot be characterized by the projection on a single direction.

If $N \times N$ is the size of the MEA, there will be $(N-1)\times(N-1) = N^2 - 2N + 1$ estimates of $\hat{\boldsymbol{E}}(t)$, in the case of square cliques, and four times this value in the case of triangular configurations. Using (3.18) and the definitions in (3.3) and (3.17), the two components $\hat{E}_x(t)$ and $\hat{E}_y(t)$ of the electric field can be expressed as linear combinations of the two b-EGMs along x- and y- directions, respectively:

$$\hat{\boldsymbol{E}}_{\square}(t): \begin{cases} \hat{E}_x(t) = \frac{1}{2d}(b_{12}(t) + b_{34}(t)) = -\frac{1}{v}\sin\theta\ \phi'(t - t_c) \\ \hat{E}_y(t) = \frac{1}{2d}(b_{13}(t) + b_{24}(t)) = -\frac{1}{v}\cos\theta\ \phi'(t - t_c) \end{cases} \tag{3.19}$$

$$\hat{\boldsymbol{E}}_{\triangle,1}: \begin{cases} \hat{E}_x(t) = \frac{1}{d}b_{12}(t) \cong -\frac{1}{v}\sin\theta\ \phi'\left(t - t_c + \frac{d}{2v}\cos\theta\right) \\ \hat{E}_y(t) = \frac{1}{d}b_{13}(t) \cong -\frac{1}{v}\cos\theta\ \phi'\left(t - t_c + \frac{d}{2v}\sin\theta\right) \end{cases} \tag{3.20}$$

$$\hat{\boldsymbol{E}}_{\triangle,2}: \begin{cases} \hat{E}_x(t) = \frac{1}{d}b_{12}(t) \cong -\frac{1}{v}\sin\theta\ \phi'\left(t - t_c + \frac{d}{2v}\cos\theta\right) \\ \hat{E}_y(t) = \frac{1}{d}b_{24}(t) \cong -\frac{1}{v}\cos\theta\ \phi'\left(t - t_c - \frac{d}{2v}\sin\theta\right) \end{cases} \tag{3.21}$$

$$\hat{\boldsymbol{E}}_{\triangle,3}: \begin{cases} \hat{E}_x(t) = \frac{1}{d} b_{34}(t) \cong -\frac{1}{v} \sin\theta \; \phi'\left(t - t_c - \frac{d}{2v}\cos\theta\right) \\ \hat{E}_y(t) = \frac{1}{d} b_{13}(t) \cong -\frac{1}{v} \cos\theta \; \phi'\left(t - t_c + \frac{d}{2v}\sin\theta\right) \end{cases} \tag{3.22}$$

$$\hat{\boldsymbol{E}}_{\triangle,4}: \begin{cases} \hat{E}_x(t) = \frac{1}{d} b_{34}(t) \cong -\frac{1}{v} \sin\theta \; \phi'\left(t - t_c - \frac{d}{2v}\cos\theta\right) \\ \hat{E}_y(t) = \frac{1}{d} b_{24}(t) \cong -\frac{1}{v} \cos\theta \; \phi'\left(t - t_c - \frac{d}{2v}\sin\theta\right), \end{cases} \tag{3.23}$$

where the approximated terms make use of equations (3.6) to (3.9).

Equations (3.19) and (3.20)–(3.23) show that the two electric field components within each clique have a different amplitude, depending on the propagation angle θ. In addition, for triangular cliques, there is also a delay between both components, which is also a function of the propagation angle θ and the conduction velocity magnitude v. Such delay represents the difference in the wavefront arrival time to the middle point of each bipole.

3.3.2.1 Time Alignment of Bipolar EGMs

In the formulation of equation (3.16), no delay is considered among the b-EGMs. However, when estimating the electric fields making use of measured b-EGMs, the different bipolar signals are activated at their corresponding wavefront arrival times, thus having a delay among them, as expressed in equations (3.6) to (3.11).

For the square cliques, from equation (3.19) we found that there are no delays between $\hat{E}_x(t)$ and $\hat{E}_y(t)$, for plane wave propagation and to that level of approximation. Consequently, the $\hat{\boldsymbol{E}}_{\square}(t)$ loop should lie on a one-dimensional trajectory. However, each component $\hat{E}_x(t)$ and $\hat{E}_y(t)$ in (3.19) is the summation of two terms which have a delay between them: (3.6) and (3.7), and (3.8) and (3.9), respectively. The summation of delayed components results in smoothed estimates [23], which can lead to underestimate $\hat{\boldsymbol{E}}_{\square}(t)$ at the peak of the signal. Therefore, the first-order Taylor series approximation used in this work to arrive to (3.19) no longer applies.

For the triangular cliques, equations (3.20) to (3.23) show that, in general, there is a delay between $\hat{E}_x(t)$ and $\hat{E}_y(t)$ components. This misalignment will be reflected at the $\hat{\boldsymbol{E}}_{\triangle}(t)$ loop trajectory, which thus will lie in a bidimensional plane rather than on the unidimensional line in the wave propagation direction.

To avoid these phenomena and to have well synchronized $\hat{E}_x(t)$ and $\hat{E}_y(t)$, in this study we propose a modified version of the least squares estimator of $\boldsymbol{E}_{\varrho}(t)$, where the b-EMGs in the clique are previously time-aligned. For that purpose, both in square and in triangular configurations, the time delay τ_{mn} between each independent bipolar signal $b_{mn}(t)$, $mn \in \{12, 34, 13, 24\}$ and the b-EGM with the highest amplitude within the clique $b_{max}(t)$ was estimated by maximizing their cross-correlation:

$$\tau_{mn} = \arg\max_{\tau} \int_{-\infty}^{\infty} b_{mn}(t-\tau) \; b_{max}(t) \; dt. \tag{3.24}$$

Each b-EGM $b_{mn}(t)$ was then advanced by τ_{mn} so that it is aligned with $b_{max}(t)$.

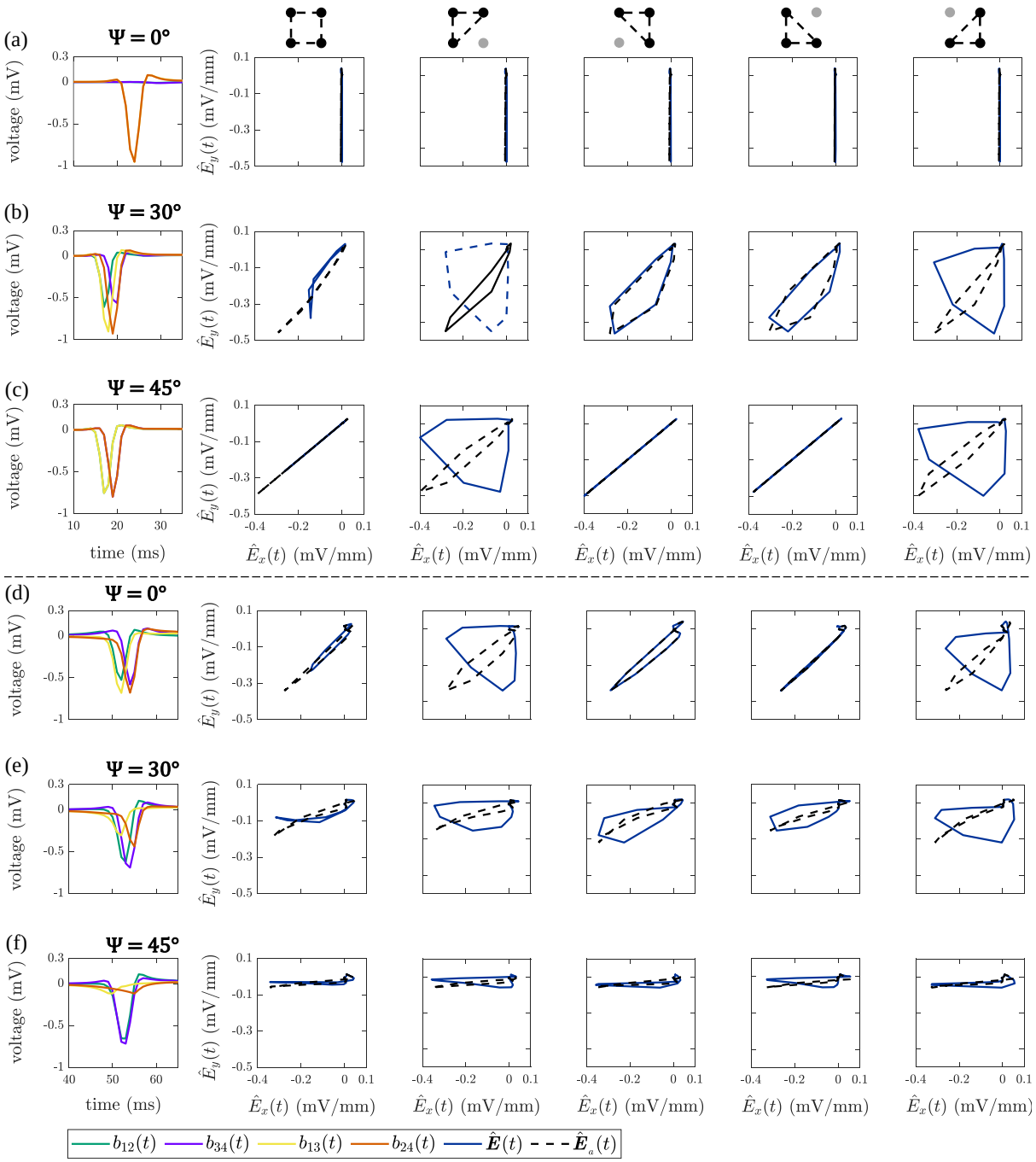

Figure 3.3: Bipolar EGMs (first column) and E-field loops (remaining columns) obtained with (dashed line) and without (solid line) the alignment of b-EGMs, in square and triangular cliques. All the cliques represented are from non-fibrotic areas outside the fibrotic patch. Rows (a) to (c): cliques with plane wavefront, when $\Psi = 0°$, $\Psi = 30°$ and $\Psi = 45°$, respectively. Rows (d) to (f): cliques with curved wavefront, when $\Psi = 0°$, $\Psi = 30°$ and $\Psi = 45°$, respectively.

Fig. 3.3 shows examples of the estimated E-field loops, with ($\boldsymbol{E}_a(t)$) and without ($\boldsymbol{E}(t)$) the previous alignment of bipolar signals (also depicted in the same figure), in both square and triangular cliques, when MEA was oriented with $\Psi = 0°$, $\Psi = 30°$ and $\Psi = 45°$, at different (i, j) electrode positions. This synchronization is similar to what was proposed in [131] to estimate u-EGMs at a desired location by using recordings made

elsewhere, aiming at cardiac mapping. According to this approach, signals measured at neighboring sites are shifted in time according to their estimated LATs; then, these time-aligned signals are spatially interpolated to estimate the unipolar waveform at the desired location. In this case, the basic assumptions on which the technique is based are a smoothly changing CV within a tissue region containing several electrodes and a similar EGM morphology in the neighborhood of each sample point, except for a time delay in the voltage waveforms.

3.3.3 Omnipolar Measurements and Signals

3.3.3.1 Estimation of Local Propagation Direction

OP-EGM approach estimates propagation direction by finding the angle $\hat{\theta}$ which maximizes the cross-correlation between the first time derivative of the unipolar voltage signal $\phi'(t-t_c)$, associated to the clique c, and the projection of the electric field in that direction $\hat{E}_p(t)$. The unipolar voltage signal $\phi'(t-t_c)$ at a given clique corresponds to a locally estimated u-EGM, $u'_c(t)$, eventually delayed by τ_c: $\phi'(t-t_c) = u'_c(t-\tau_c)$. In the latter equation, $u'_c(t)$ must be estimated for each clique as explained later. In the coordinate system depicted in Fig. 3.2 (b), the E-field $\boldsymbol{E}(t)$ is expressed as $\boldsymbol{E}(t) = E_x(t)\overrightarrow{\mathbf{u}}_x + E_y(t)\overrightarrow{\mathbf{u}}_y$. Therefore, the projection of $\boldsymbol{E}(t)$ along the propagation direction is given by:

$$\begin{aligned} E_p(t) &= \boldsymbol{E}(t)\overrightarrow{\mathbf{u}}_p \\ &= E_x(t)\sin(\theta) + E_y(t)\cos(\theta). \end{aligned} \tag{3.25}$$

The estimated conduction angle $\hat{\theta}$ and the possible delay $\hat{\tau}_c$ will be found by replacing the E-field $\boldsymbol{E}(t)$ with its estimate according to (3.19) and (3.20)-(3.23) and solving:

$$[\hat{\theta}, \hat{\tau}_c] = \arg\max_{\theta,\tau_c} \left[\sin(\theta) \int_{-\infty}^{\infty} u'_c(t-\tau_c)\hat{E}_x(t)dt + \cos(\theta) \int_{-\infty}^{\infty} u'_c(t-\tau_c)\hat{E}_y(t)dt \right]. \tag{3.26}$$

If $\hat{\tau}_c$ is the estimated delay τ_c maximizing the previous cross-correlation, the propagation angle estimate is:

$$\hat{\theta} = \arctan \frac{\displaystyle\int_{-\infty}^{\infty} u'_c(t-\hat{\tau}_c)\hat{E}_x(t)dt}{\displaystyle\int_{-\infty}^{\infty} u'_c(t-\hat{\tau}_c)\hat{E}_y(t)dt}. \tag{3.27}$$

For square cliques, considering the estimates of the E-field components for plane wave propagation in (3.19), the expressions in (3.2) and the fact that $u'_c(t-\tau_c) = \phi'(t-t_c)$, we find from (3.27) that $\hat{\theta} = \theta$, i.e., $\hat{\theta}$ is an unbiased estimate.

Using a similar procedure for triangular cliques, as clique 1 in Fig. 3.1 (b), considering the fact that $u'_c(t)$ and $u''_c(t)$ are orthogonal and using the approximation in (3.20), we obtain that the propagation angle estimate when no previous time alignment of b-EGMs

is performed can be expressed as:

$$\hat{\theta} = \arctan \frac{-\frac{1}{v}\sin\theta \int_{-\infty}^{\infty} \phi'(t - t_c + \tau_c - \hat{\tau}_c)\ \phi'\left(t - t_c + \frac{d}{2v}\cos\theta\right) dt}{-\frac{1}{v}\cos\theta \int_{-\infty}^{\infty} \phi'(t - t_c + \tau_c - \hat{\tau}_c)\ \phi'\left(t - t_c + \frac{d}{2v}\sin\theta\right) dt} \neq \theta. \tag{3.28}$$

This result points out that the estimate of θ is biased in general for triangular cliques. Nevertheless, if the electric field components $\hat{E}_x(t)$ and $\hat{E}_y(t)$ are estimated from properly aligned bipolar signals, then we obtain $\hat{\theta} = \theta$. For cliques corresponding to triangles 2, 3 and 4, similar expressions are obtained with only changes in the signs of the $\sin(\theta)$ and $\cos(\theta)$ terms.

In the reference OP-EGM method introduced by [71], it is not specified which of the unipolar signals measured in a clique is used as the $u_c'(t)$ in (3.26). In this thesis, when reproducing the method proposed in literature, we took the signal from lower left corner electrode when using square cliques, so that $u_c(t) = u_1(t)$. For triangular cliques, the signal from the electrode corresponding to the vertex of the right angle was chosen, so that $u_c(t) = u_k(t)$, $k = \{1, 2, 3, 4\}$ for each of the four triangles indicated with the same k-th index, respectively, in Fig. 3.1 (b).

Alternatively, we proposed a more robust approach to find the local propagation direction, where the estimation of $u_c'(t)$ to be included in (3.26) involves all the u-EGMs within the clique. For the case of square clique:

1. each of the four u-EGMs is aligned with respect to the one with the highest amplitude, denoted as $u_{max}(t)$, by computing the maximum cross-correlation between them. In this way, the four aligned u-EGMs $u_k(t-\tau_k), k \in \{1, 2, 3, 4\}$, are obtained;

2. the average signal $\bar{u}(t)$ is calculated by averaging the four aligned u-EGMs $u_k(t-\tau_k)$;

3. the time derivative of $\bar{u}(t)$ is computed and used as estimate of $u_c'(t)$ in (3.26), $u_c'(t) = \partial\bar{u}(t)/\partial t$.

For triangular cliques, steps 1. and 2. are performed by just considering the three u-EGMs at the electrodes forming the clique. Step 3 is the same as for square cliques.

3.3.3.2 Estimation of Local Conduction Velocity

According to the omnipolar method, the conduction velocity v in each clique is estimated by comparing the amplitudes of $\phi'(t - t_c)$ and $\hat{E}_p(t)$, as they are expected to be proportional under the assumption of locally plane wave: $\hat{E}_p(t) = -\phi'(t - t_c)/v$, if the b-EGMs within the clique are aligned (see equations (3.19) and (3.20)-(3.23)). The conduction velocity v can be estimated by computing the ratio of the peak-to-peak (pp) amplitudes

of $\phi'(t-t_c)$ and $\hat{E}_p(t)$, as proposed by [71]:

$$\hat{v} = \frac{[\phi'(t-t_c)]_{\text{PP}}}{[\hat{E}_p(t)]_{\text{PP}}}. \tag{3.29}$$

In order to avoid the large sensitivity to noise that can be expected from an estimation based on peak-to-peak amplitudes, we propose here a more robust estimate of v as the ratio of the standard deviation (SD) of $\phi'(t-t_c)$ and $\hat{E}_p(t)$:

$$\hat{v} = \frac{[\phi'(t-t_c)]_{\text{SD}}}{[\hat{E}_p(t)]_{\text{SD}}}. \tag{3.30}$$

It should be mentioned that the estimate of $\phi'(t-t_c)$ used in (3.29) is the same described in the previous subsection for $u_c'(t)$ ($\phi'(t-t_c) = u_1'(t)$ in square cliques and $\phi'(t-t_c) = u_k'(t)$, where $k \in \{1,2,3,4\}$, in the k-th triangular clique). On the other hand, when using (3.30), $\phi'(t-t_c)$ is estimated as the $u_c'(t)$ described at enumeration points 1 to 3 in the same subsection.

For square cliques, by replacing expressions (3.19) in (3.25) and if the propagation direction is well estimated ($\hat{\theta} = \theta$), simple calculations (including the basic identity $\sin^2\theta + \cos^2\theta = 1$) lead to the expected:

$$\hat{E}_p(t) \;=\; -\frac{1}{v}\phi'(t-t_c). \tag{3.31}$$

For triangular cliques (e.g. clique 1), using the approximations with delays in (3.20) for $\hat{E}_x(t)$ and $\hat{E}_y(t)$ in (3.25), and assuming that the propagation direction is well estimated ($\hat{\theta} = \theta$), we have:

$$\hat{E}_p(t) \cong -\frac{1}{v}\left(\sin^2\theta\ \phi'\left(t - t_c + \frac{d}{2v}\cos\theta\right) + \cos^2\theta\ \phi'\left(t - t_c + \frac{d}{2v}\sin\theta\right)\right). \tag{3.32}$$

This equation shows that the misalignment of $\hat{E}_y(t)$ and $\hat{E}_x(t)$ components in triangular cliques has an effect in the CV estimate, even if propagation direction is estimated without error. Nevertheless, if the b-EGMs are time aligned as proposed in this thesis (i.e. if there are not delays between $\hat{E}_y(t)$ and $\hat{E}_x(t)$), the approximation in (3.32) reduces to an expression analogous to (3.31), allowing a proper estimation of the conduction velocity.

As an alternative, CV was also estimated from detected LATs. For that purpose, a linear model was fitted to the activation times measured from a clique of 4 electrodes, similar to [132]:

$$t(x,y) = a_1 + a_2 x + a_3 y, \tag{3.33}$$

where $t(x,y)$ is the activation time at each electrode site (x,y) and a_1, a_2 and a_3 are the coefficients estimated by LS. Once coefficients are known, the components of CV

vector v_x and v_y can be obtained by partial differentiation of $t(x, y)$ as follows:

$$v_x = \frac{\frac{\partial t}{\partial x}}{(\frac{\partial t}{\partial x})^2 + (\frac{\partial t}{\partial y})^2} = \frac{a_2}{a_2^2 + a_3^2} \tag{3.34}$$

$$v_y = \frac{\frac{\partial t}{\partial y}}{(\frac{\partial t}{\partial x})^2 + (\frac{\partial t}{\partial y})^2} = \frac{a_3}{a_2^2 + a_3^2}. \tag{3.35}$$

3.3.3.3 Omnipolar Electrogram Signals

In this thesis, OP-EGM signals $\varphi_{i,j,(q)}(t)$, where $q \in \{1, 2, 3, 4\}$ refers to each of the four possible triangles when using triangular clique configuration, were defined by projecting $\hat{\boldsymbol{E}}(t)$ within the corresponding clique onto the following directions:

- The direction $\overrightarrow{\mathbf{u}}_{me}$ that maximizes the excursion of the $\hat{\boldsymbol{E}}(t)$ loop within the depolarization interval. In that case, the OP-EGM signal $\varphi^{me}_{i,j,(q)}(t)$ along the loop maximal excursion (me) direction was derived as: $\varphi^{me}_{i,j,(q)}(t) = d \cdot \hat{\boldsymbol{E}}(t) \cdot \overrightarrow{\mathbf{u}}_{me}$. It should be noted that the peak-to-peak amplitude of $\varphi^{me}_{i,j,(q)}(t)$ is equivalent to the peak-to-peak amplitude E_{max} of the electric field, proposed by [71], multiplied by the interelectrode distance d within the clique.
- The principal direction $\overrightarrow{\mathbf{u}}_{\nu}$ obtained by the principal component analysis (pca) of the loop described by $\hat{\boldsymbol{E}}(t)$ within the depolarization interval. The resulting OP-EGM signal $\varphi^{pca}_{i,j,(q)}(t)$ was derived as: $\varphi^{pca}_{i,j,(q)}(t) = d \cdot \hat{\boldsymbol{E}}(t) \cdot \overrightarrow{\mathbf{u}}_{\nu}$. In this approach, we also obtained the voltage projected in the orthogonal direction $\overrightarrow{\mathbf{u}}^{\perp}_{\nu}$ (corresponding to the second principal component): $\varphi^{pca\perp}_{i,j,(q)}(t) = d \cdot \hat{\boldsymbol{E}}(t) \cdot \overrightarrow{\mathbf{u}}^{\perp}_{\nu}$.

Let us consider $\varphi^{me}_{i,j,(q)}(t)$ under the plane wave assumption. For square cliques, if maximal excursion occurs in the propagation direction and conduction angle is well estimated, by using (3.31), we will have:

$$\varphi^{me}_{i,j}(t) = -\frac{d}{v}\phi'(t - t_c). \tag{3.36}$$

It should be noted that there are no second-order terms in (3.36), unlike the expressions of b-EGMs (see (3.6)-(3.11)). Again, alignment prevents attenuation at the $\hat{\boldsymbol{E}}(t)$ peaks and consequently yields a better estimate. For triangular cliques under the same assumptions (let us consider clique 1, for instance), there are indeed second order terms in $\varphi^{me}_{i,j,1}(t)$, affecting omnipolar signal amplitude. Nevertheless, expressing $\hat{E}_y(t)$ and $\hat{E}_x(t)$ components with the delay approximation in (3.20) and time aligning them, we obtain the aligned version $\varphi^{me,a}_{i,j,1}(t)$:

$$\varphi^{me,a}_{i,j,1}(t) = -\frac{d}{v}\phi'\left(t - t_c + \frac{d}{2v}\cos\theta\right), \tag{3.37}$$

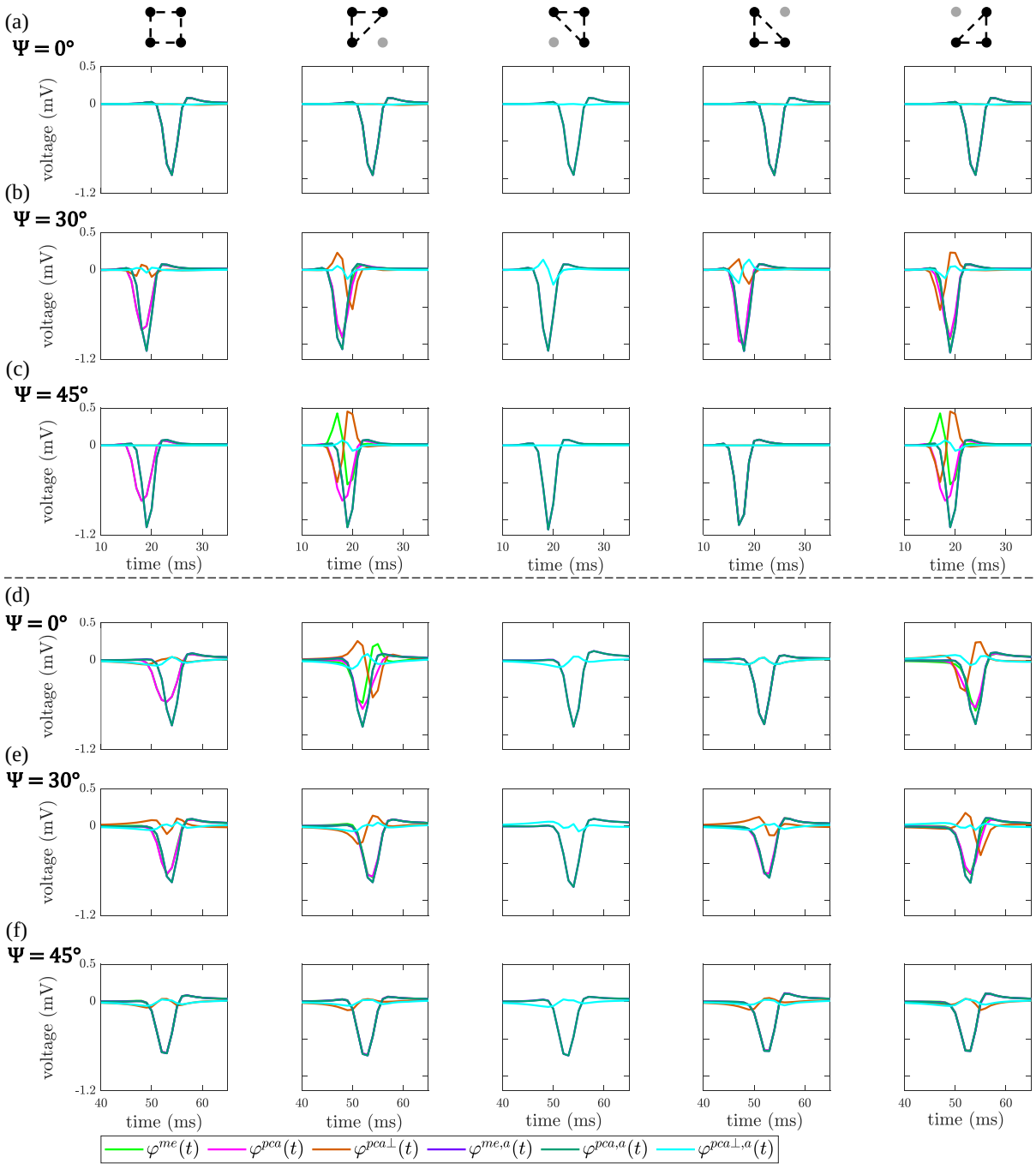

Figure 3.4: OP-EGM signals $\varphi^{s}_{i,j}(t)$, where $s \in \{me, pca, pca\perp\}$, obtained in square and triangular cliques, estimated with (a) and without alignment of b-EGMs. All the cliques represented are from non-fibrotic areas outside the fibrotic patch. Rows **(A)** to **(C)**: cliques with plane wavefront, when $\Psi = 0°$, $\Psi = 30°$ and $\Psi = 45°$, respectively. Rows **(D)** to **(F)**: cliques with curved wavefront, when $\Psi = 0°$, $\Psi = 30°$ and $\Psi = 45°$, respectively.

whose amplitude is properly estimated. Examples of the omnipolar EGM signals $\varphi^{s}_{i,j,(q)}(t)$, where $s \in \{me, pca, pca\perp\}$ here introduced are observed in Fig. 3.4, for both clique configurations and the three MEA orientations, with and without the previous alignment of b-EGMs, at the same electrode positions (i, j) as in Fig. 3.3.

3.3.3.4 Voltage and Conduction Velocity Mapping Strategies

For each OP-EGM signal $\varphi^{s}_{i,j,(q)}(t)$, $s \in \{me, pca, pca\perp\}$ introduced in this subsection, we computed the peak-to-peak amplitude $V^{o\text{-}s}_{i,j,(q)}$, which was used to build voltage maps. In the *pca* approach, we also created maps based on the root sum square of the voltage in the first and second principal components, $V^{o\text{-}pca-r}_{i,j,(q)}$:

$$V^{o\text{-}s}_{i,j,(q)} = \max_t\{\varphi^{s}_{i,j,(q)}(t)\} - \min_t\{\varphi^{s}_{i,j,(q)}(t)\}, \quad i \in \{1,..,N-1\}, j \in \{1,..,N-1\}, \\ s \in \{me, pca, pca\perp\},$$

$$V^{o\text{-}pca\text{-}r}_{i,j,(q)} = \sqrt{\left(V^{o\text{-}pca}_{i,j,(q)}\right)^2 + \left(V^{o\text{-}pca\perp}_{i,j,(q)}\right)^2}, \quad i \in \{1,..,N-1\}, j \in \{1,..,N-1\}. \tag{3.38}$$

We also built bipolar maps based on the peak-to-peak amplitudes $V^{b\text{-}x}_{i,j}$ and $V^{b\text{-}x}_{i,j}$ of the b-EGMs in each of the two catheter directions (i.e. $b^{x}_{i,j}(t)$ and $b^{y}_{i,j}(t)$). The root sum square (r) of both values, as well as their maximum (m) were also considered so as to have a performance reference based on bipolar signals:

$$V^{b\text{-}r}_{i,j} = \sqrt{\left(V^{b\text{-}x}_{i,j}\right)^2 + \left(V^{b\text{-}y}_{i,j}\right)^2}; \quad V^{b\text{-}m}_{i,j} = \max\{V^{b\text{-}x}_{i,j}, V^{b\text{-}y}_{i,j}\}, \quad i \in \{1,..,N-1\}, \\ j \in \{1,..,N-1\}. \tag{3.39}$$

All the voltage maps were computed for each orientation of the MEA, and by using both clique configurations analyzed in this study. Omnipolar voltage maps were also created from aligned b-EGMs. We obtained color-coded maps where a pixel corresponds to a clique (or to an electrode pair, in case of bipolar maps).

Regarding conduction velocity ($\boldsymbol{v} = v\overrightarrow{\mathbf{u}}_v$), maps of estimated CV and propagation directions were created for all propagation patterns with clinical as well as synthetic EGMs. Velocity mapping strategies were created using the omnipolar approaches (both with equation (3.29) proposed by [71] and with equation (3.30) introduced in this thesis) and the LAT-based estimation. Each map consisted of color-coded pixels representing v values and black arrows representing angular direction θ of the estimated velocity vectors $\boldsymbol{v}$ in each clique.

In the first preliminary analysis, in case of simulated patterns, as they were created with known focus, CV and anisotropy ratio, the true conduction velocity was obtained at the center of each clique. This allowed to compute the estimation errors for CV (ϵ^{o}_{CV}, ϵ^{l}_{CV}) and for propagation direction (ϵ^{o}_{θ}, ϵ^{l}_{θ}), obtained with omnipolar and from LATs, respectively, and for each propagation pattern (expressed as mean $\pm$ SD across all the cliques in the MEA). Finally, mean errors were calculated above all the simulated propagation patterns for both approaches.

Then, in the next analysis, CV maps were created for each orientation of the 15 $\times$ 15 MEA, each clique configuration (square and triangular), with and without alignment of

b-EGMs. It should be noted that maps performed with square cliques present the same resolution as bipolar maps, both providing N^2-2N+1 pixels when processing the whole MEA. On the other hand, since triangular cliques result in a total of $4\times(N^2-2N+1)$ measurement configurations (and consequently, pixels) within the MEA, maps performed with this configuration present higher spatial resolution. In addition, in order to assess the sensitivity to noise of voltage and CV maps, simulated b-EGMs $b^x_{i,j}(t)$ and $b^y_{i,j}(t)$ in the 15×15 MEA were also corrupted with noise obtained from real b-EGMs, thus obtaining $b^{x,n}_{i,j}(t)$ and $b^{y,n}_{i,j}(t)$ introduced in subsection 2.2.2. For each realization n, the different voltage and CV mapping strategies were computed from noisy signals, thus obtaining one hundred different maps, which were tested regarding fibrosis detection, as well as voltage map reproducibility.

3.3.3.5 Mapping Performance Evaluation

In order to quantitatively evaluate the ability of the different voltage and CV mapping strategies, computed from the 15×15 MEA, to identify the fibrotic area (i.e. to discriminate pixels within the fibrotic patch from those in the normal tissue), receiver operating characteristic (ROC) curves were used. Two ground-truth masks of fibrosis were created for testing bipolar and omnipolar maps, having the resolution of square and triangular cliques and indicating whether a clique laid within the fibrotic or within the normal tissue. A 14×14 ground-truth mask was used to evaluate bipolar and omnipolar maps with square cliques. A value of 1 was assigned if the four electrodes defining the square clique lay in the F area, and a value of 0 was assigned if all of them lay in the NF area. Cliques with some electrodes inside and some outside the fibrotic patch were not considered in the evaluation. Similarly, a 28×28 ground-truth mask was used to assess omnipolar maps performed with triangular cliques, considering if the three electrodes defining the triangular clique lay in F or NF tissue.

Both ground-truth masks used in this thesis are illustrated in Fig. 4.1 (a) and (b). For each voltage and velocity map, ROC curves relating sensitivity and specificity were obtained by varying the threshold for fibrosis identification [133]. In this analysis, *true positive* denotes the number of cliques correctly identified as F, *false negative* represents the number of missed cliques in the fibrotic area, *true negative* stands for the number of cliques correctly identified as NF and *false positive* is the number of cliques incorrectly detected as F. The detection accuracy (ACC) was defined as the number of cliques correctly identified as F or NF divided by the total number of cliques. The maximum ACC was used as a measure of the overall fibrosis detection ability of a given map. In addition, the sensitivity and specificity with the threshold achieving the maximum ACC were also computed.

The ability of the different tested voltage mapping strategies in reproducing the spatial distribution of reference maps was also evaluated. We created peak-to-peak amplitude maps of u-EGMs, and resampled them to match the spatial resolutions of bipolar and om-

nipolar pixel maps (with both square and triangular cliques). To quantify the agreement of each voltage map with the substrate characterization given by the reference map, we used both Pearson's ρ_p and Spearman's rank ρ_s correlation coefficients. A p-value ≤ 0.05 was required to have statistical significance. Reference voltage maps were obtained by following two sequential steps:

1. A bicubic interpolation of the $N \times N$ peak-to-peak amplitude map of u-EGMs $u_{i,j}(t)$, $(i,j) \in \{1,...,N\}$, was performed placing three interpolated values between any two adjacent electrodes, along both MEA directions, thus increasing the total number of pixels to $(N+3\cdot(N-1)) \times (N+3\cdot(N-1))$. The original and interpolated maps for N=15 are shown in Fig. 4.1 (c) and (d), respectively, when MEA is oriented with $\Psi = 0°$.

2. The interpolated pixel map was later resampled so as to obtain $(N-1) \times (N-1)$ and $2\cdot(N-1) \times 2\cdot(N-1)$ reference maps, matching the dimensions of bipolar and omnipolar maps with square cliques, and omnipolar maps with triangular cliques, respectively. Resulting resampled pixel maps from N=15, for the case when $\Psi = 0°$, are illustrated in Fig. 4.1 (e) and (f).

Additionally, in order to evaluate the effect of noise on voltage and velocity maps, we computed the root mean square error (RMSE) between each noisy map and the respective noise-free map. In case of voltage maps, we calculated:

$$\mathrm{RMSE}(n) = \sqrt{\frac{1}{(N-1)^2}\sum_{i=1}^{N-1}\sum_{j=1}^{N-1}\left(V_{i,j}^{s,n} - V_{i,j}^{s}\right)^2}, \tag{3.40}$$

where $s \in \{b\text{-}m; b\text{-}r; o\text{-}me; o\text{-}me, a; o\text{-}pca\text{-}r; o\text{-}pca\text{-}r, a\}$. Analogously, for velocity maps, we computed:

$$\mathrm{RMSE}(n) = \sqrt{\frac{1}{(N-1)^2}\sum_{i=1}^{N-1}\sum_{j=1}^{N-1}\left(CV_{i,j}^{s,n} - CV_{i,j}^{s}\right)^2}, \tag{3.41}$$

with $s \in \{o; o\text{-}m; o\text{-}m, a\}$.

We also studied the effect of noise on the estimation of the propagation direction with both the original θ^o and the modified $\theta^{o\text{-}m}$ omnipolar method. Angle differences, ϵ_θ, between propagation direction maps obtained from noisy realizations and those obtained from noise-free signals (considered as the reference) were computed for each omnipolar approach and noise level. The mean and SD of the angle differences in each map were obtained and averaged for all noise realizations.

It must be pointed out that at this step of the omnipolar study, all performance measurements were made and reported both separately and jointly for the three MEA

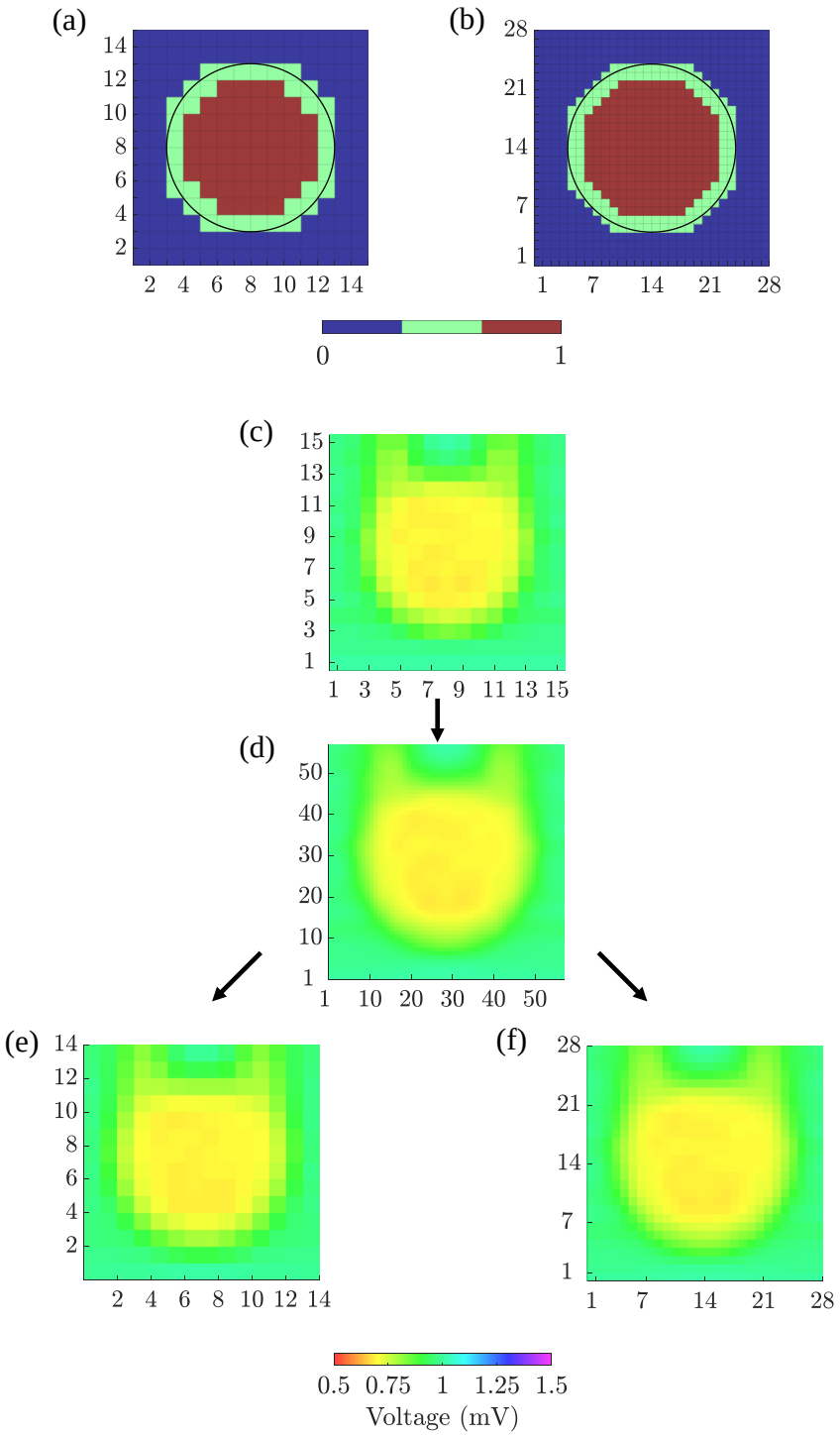

Figure 3.5: (a) 14×14 and (b) 28×28 ground-truth masks for fibrosis detection, for square and triangular cliques, respectively. (c) 15×15 peak-to-peak amplitudes map from u-EGMs and (d) 57×57 map resulting from bi-cubic interpolation of (c). 14×14 (e) and 28×28 (f) amplitude maps for evaluating voltage reproducibility of bipolar and omnipolar maps.

orientations considered. This latter scenario was considered so as to assume that the relative angle of the propagation direction with respect to the catheter is not known a priori, as occurs in clinical settings.

Simulated tissue characteristics	focus	ϵ_{CV}^{o-m} (mm/ms)	ϵ_{CV}^{l} (mm/ms)	ϵ_{θ}^{o-m} (deg)	ϵ_{θ}^{l} (deg)
Isotropic, $v_x = v_y = 0.6$ mm/ms	center	0.155 ± 0.067	0.015 ± 0.057	4.41 ± 3.9	2.35 ± 2.69
	side	0.121 ± 0.074	0.009 ± 0.062	3.78 ± 3.21	3.15 ± 2.86
	corner	0.177 ± 0.071	0.006 ± 0.057	7.28 ± 5.04	4.47 ± 3.27
Isotropic, $v_x = v_y = 1$ mm/ms	center	0.095 ± 0.322	0.045 ± 0.191	11.5 ± 11.8	6.99 ± 6.42
	side	0.053 ± 0.005	0.003 ± 2.11×10^{-5}	6.64 ± 4.3	4.35 ± 2.81
	corner	0.109 ± 0.257	0.016 ± 0.168	12 ± 8.42	7.56 ± 5.1
Anisotropic, $v_x = 1.2$ mm/ms $v_y = 0.6$ mm/ms	center	0.104 ± 0.173	0.013 ± 0.133	4.07 ± 3.32	3.95 ± 2.64
	side	0.117 ± 0.095	0.017 ± 0.075	1.43 ± 1.32	1.49 ± 2.35
	corner	0.118 ± 0.083	0.012 ± 0.071	6.47 ± 4.81	5.16 ± 3.5
Anisotropic, $v_x = 0.6$ mm/ms $v_y = 1.2$ mm/ms	center	0.143 ± 0.351	0.051 ± 0.222	6.3 ± 6.7	4.53 ± 3.61
	side	0.127 ± 0.067	0.012 ± 0.065	2.41 ± 1.95	3.04 ± 2.12
	corner	0.154 ± 0.174	0.017 ± 0.124	8.19 ± 6.82	5.16 ± 4.13
Anisotropic, $v_x = 2$ mm/ms $v_y = 1$ mm/ms	center	-0.049 ± 0.149	-0.019 ± 0.069	8.25 ± 6.13	5.67 ± 3.84
	side	0.056 ± 0.003	0.002 ± 7.7×10^{-4}	1.66 ± 0.974	1.09 ± 0.688
	corner	0.008 ± 0.187	-0.005 ± 0.11	11.8 ± 10.1	7.68 ± 6.59
Anisotropic, $v_x = 1$ mm/ms $v_y = 2$ mm/ms	center	-0.15 ± 0.253	-0.04 ± 0.141	11.7 ± 9	7.28 ± 52.7
	side	0.051 ± 0.008	8.28×10^{-4} ± 0.004	4.24 ± 2.52	2.75 ± 1.66
	corner	0.035 ± 0.382	0.027 ± 0.265	19.7 ± 21.3	10.3 ± 8.25
Mean error		0.08 ± 0.205	0.007 ± 0.13	7.3 ± 8.96	4.86 ± 4.81

Table 3.1: CV and propagation direction angular errors (presented as mean ± SD) calculated with the two different approaches (omnipolar and LAT-based) for the different simulated propagation scenarios considered.

3.4 Results

3.4.1 Analysis of Simulated Recordings

Table 3.1 shows the errors for CV ϵ_{CV}^{o-m} and ϵ_{CV}^{l}, and propagation directions ϵ_{θ}^{o} and ϵ_{θ}^{l}, estimated by the MOP-EGM and from LATs, respectively, with different simulation parameters (velocity components v_x and v_y along the two main directions of the 8 × 16 MEA and focus position). For each simulation scenario, the errors are expressed in mm/ms and degree, for CV and propagation angles, respectively. Even if omnipolar estimation errors are slightly greater than the LAT-based ones in most of the cases, both approaches show lower errors when the plane wave hypothesis is better fulfilled (side focus case). Nevertheless, estimations of CV values and propagation directions based on the MOP-EGM did not require detection or annotation of LATs, which made their computation less time-consuming and demanding.

The effect of the time alignment of b-EGMs computed at the 15 × 15 MEA and proposed in subsection 3.3.2.1 is evident in Fig. 3.3. Rows (a), (b) and (c) correspond to the clique $(i, j) = (2, 2)$ for $\Psi = 0°$, $\Psi = 30°$ and $\Psi = 45°$, respectively. The local propagation angles estimated with the proposed MOP-EGM method were $\hat{\theta}_{2,2}$ = -0.1°, $\hat{\theta}_{2,2}$ = 23.5° and $\hat{\theta}_{2,2}$ = 45.0°, respectively. Lower panels represent cliques from non-fibrotic areas with curved wavefronts: $(i, j) = (4, 12)$ with $\Psi = 0°$ in (d); $(i, j) = (7, 13)$

with $\Psi = 30°$ in (e); and at $(i, j) = (8, 13)$ with $\Psi = 45°$ in (f). The respective estimated local propagation angles were $\hat{\theta}_{4,12} = 34.7°$, $\hat{\theta}_{7,13} = 70.3°$ and $\hat{\theta}_{8,13} = 85.3°$.

The OP-EGM signals $\varphi^{s}_{i,j,(q)}(t)$, where $s \in \{me, pca, pca\perp\}$, estimated with the different approaches proposed in subsection 3.3.3.3 at the same electrode positions (i, j) as in Fig. 3.3, computed with and without alignment of b-EGMs, in square and triangular cliques, are depicted in Figure 3.4. The OP-EGM signals produced by the two modalities *me* and *pca* are quite similar in most of the cases. More in detail, in square cliques $\varphi^{me}_{i,j}(t)$ is equivalent to $\varphi^{pca}_{i,j}(t)$, both when the b-EGMs are aligned and when they are not. In triangular cliques, this is also true in areas where the propagation direction is parallel to one of the main directions of the MEA.

The different bipolar and omnipolar voltage mapping strategies evaluated from the EGMs recorded at the 15 × 15 MEA are illustrated in Fig. 3.6 for $\Psi = 0°$, without noise (left columns) and with a noise level of $\sigma_n = 28\ \mu V$ (right columns), with four (subscripts $_{i,j}$) and three (subscripts $_{i,j,q}$) electrode clique configuration. In the case of noise-corrupted maps, only one of the one hundred noisy realizations is shown. The omnipolar maps are presented without and with the alignment of b-EGMs. These results reveal that combined bipolar maps obtained as the root sum square or the maximum voltage of both MEA directions, $V^{b\text{-}r}$ and $V^{b\text{-}m}$, shown at row (a), present better fibrosis detection performance than omnipolar maps without alignment, illustrated at upper and lower rows in (b) for the two approaches *me* and *pca*, respectively. However, omnipolar maps with previous time alignment of b-EGMs (upper and lower rows in (c) for the same approaches as in (b) show results comparable to combined bipolar maps. Omnipolar mapping strategies also present greater correlation with the reference map when time alignment is applied. When b-EGMs are affected by noise, omnipolar voltage maps are more robust than bipolar maps, improving their performance in fibrosis discrimination and correlation with their reference when previous alignment is performed.

Velocity maps obtained with the reference OP-EGM method (a) and with the proposed approach (without (b) and with (c) alignment of b-EGMs) are presented in Fig. 3.7, at the same MEA orientation and with the same noise level as in Fig. 3.6 and following the same notation for square and triangular clique configurations. For each clique, the CV value was color-coded from red (lowest) to violet (highest), whereas its respective propagation direction is reproduced by a black arrow. These maps reveal better performance of the MOP-EGM method ($CV^{o\text{-}m}$ and $CV^{o\text{-}m,a}$) than the standard approach (CV^{o}). Moreover, the standard approach tends to overestimate CV values, when compared with the MOP-EGM method.

Values of area under curve (AUC), ACC, Pearson ρ_p and Spearman ρ_s correlation coefficients of the proposed mapping strategies for noise-free simulated b-EGMs are shown in Table 3.2, together with the threshold value with maximum fibrosis ACC for each map modality. As mentioned in the previous section, performance was computed by jointly considering the three MEA orientations with respect to the propagation direction.

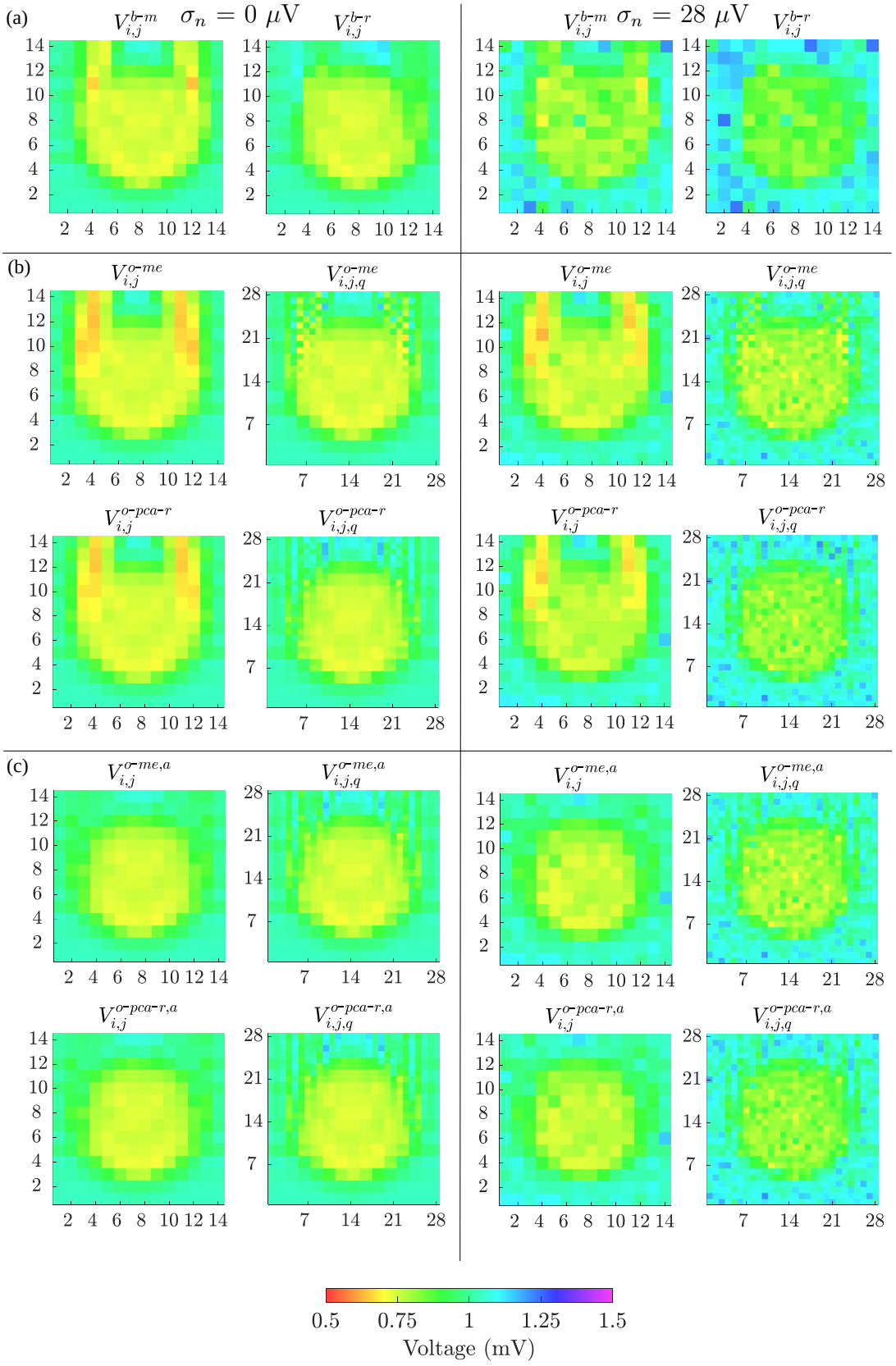

Figure 3.6: Voltage maps when propagation direction is in the main direction of the 15×15 MEA ($\Psi = 0°$). Left columns: noise-free bipolar maps (row (a)) and omnipolar maps without (rows in (b)) and with alignment (rows in (c)) of b-EGMs; right columns: same types of maps performed in left columns, but from noisy b-EGMs (noise level with standard deviation $\sigma = 28$ μV).

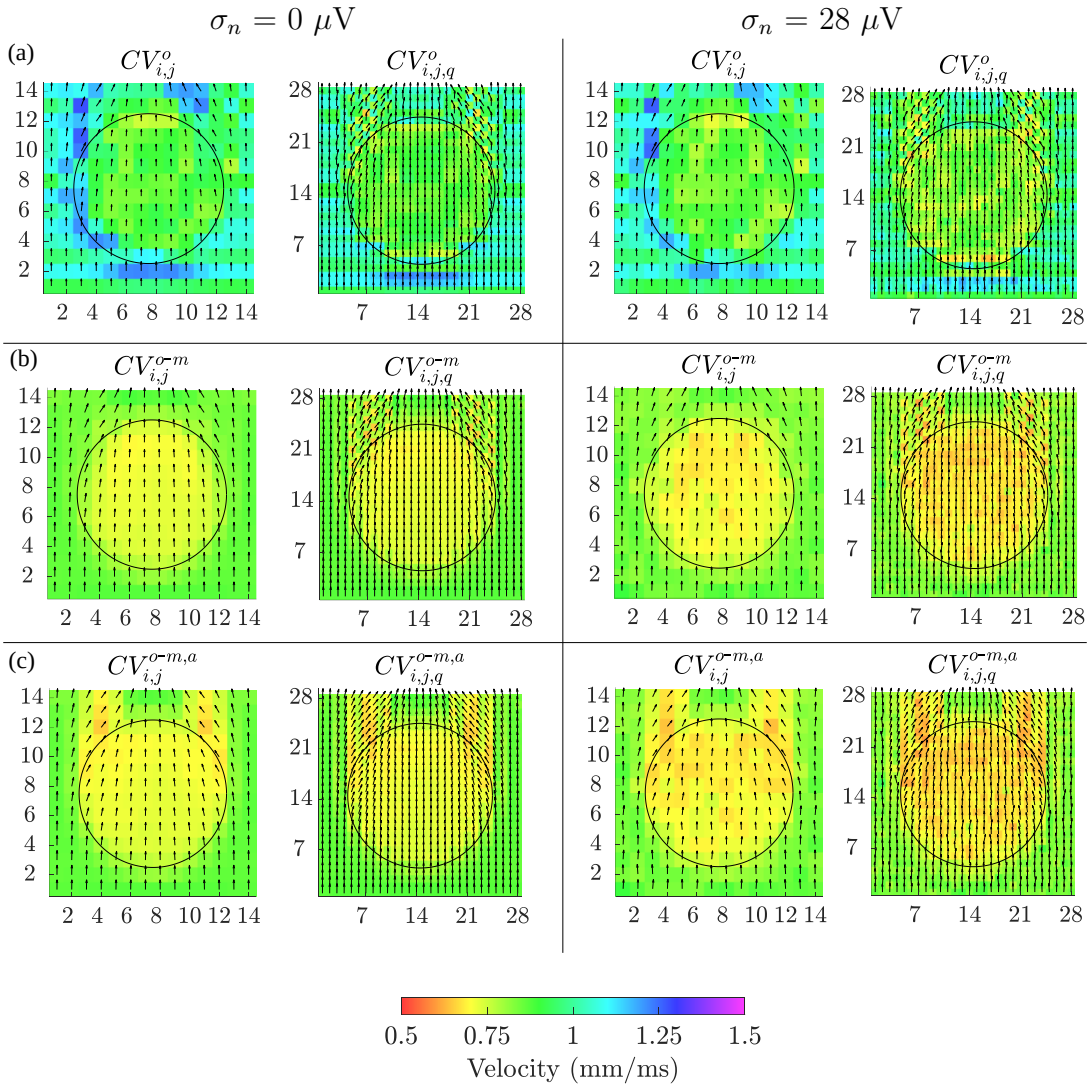

Figure 3.7: Velocity maps when propagation direction is in the main direction of the 15 × 15 MEA ($\Psi = 0°$). Estimated conduction velocities are color-coded and arrows show the estimated propagation direction. Left columns: noise-free velocity maps performed with the reference omnipolar method (a) and with the proposed approach (without (b) and with alignment (c) of b-EGMs). Right columns: same types of maps as in left columns, but performed from noise corrupted b-EGMs for a particular realization and noise level with standard deviation $\sigma = 28$ μV.

Bipolar voltage maps $V^{b\text{-}m}$ and $V^{b\text{-}r}$ identify the fibrotic area with an ACC of 96% and 95%, respectively, whereas the OP-EGM based voltage maps reach a maximum ACC value of 93%, being consistent with results in Fig. 3.6. Regarding correlation of the voltage maps with the reference maps, both omnipolar strategies (*me* and *pca*) achieve values $\rho_p = 0.87$ and $\rho_s = 0.87$ when square cliques are used and b-EGMs alignment

is performed. As a reference, $V^{b\text{-}r}$ and $V^{b\text{-}m}$ present correlations of $\rho_p = 0.86$ and $\rho_p = 0.83$, respectively. Regarding CV maps, the MOP-EGM version proposed in this work (with b-EGMs alignment) presents indeed comparable performance in fibrosis detection to combined bipolar voltage maps (e.g. ACC = 96% for $CV^{o\text{-}m,a}$ with square cliques), and better performance than both omnipolar voltage maps and than the original OP-EGM approach to estimate conduction velocity (CV^o).

Similar results are observed in Fig. 3.8, which shows how fibrosis detection (in terms of the ACC value, (a)) and voltage map fidelity (in terms of Pearson's correlation coefficient ρ_p, (b)) are affected when b-EGMs are corrupted with different noise levels, jointly considering the three MEA orientations. As observed in panel (a), omnipolar voltage and CV maps are less affected by noise than bipolar maps for noise levels greater than or equal to $\sigma_n = 28\ \mu V$. The proposed time alignment of b-EGMs improves fibrosis detection performance and robustness to noise of the MOP-EGM maps, when comparing them to their unaligned versions. The highest ACC was obtained by CV maps computed with the MOP-EGM method in square cliques, including prior alignment of b-EGMs ($CV_{i,j}^{o\text{-}m,a}$), yielding values greater than 90% for all noise levels. On the other hand, CV maps based on the original OP-EGM approach (CV^o) proved to be unstable with noise, both in square and triangular cliques. As shown in panel (b), voltage maps performed with the MOP-EGM method, including b-EGMs alignment, and with square cliques, $V_{i,j}^{o\text{-}me,a}$ and $V_{i,j}^{o\text{-}pca\text{-}r,a}$, are the most robust in reproducing the reference unipolar voltage maps in the presence of noise. They achieve Pearson correlation coefficients greater than 0.80 for all noise levels and present smaller interquartile ranges than bipolar maps. The RMSE between maps computed from noisy b-EGMS and those computed with noise-free b-EGMs are depicted in (a) and (b) panels of Fig. 3.9, respectively, for each noise level. As in previous results, the three MEA orientations are jointly considered. All the omnipolar voltage maps provide RMSE values lower than 0.2 mV, whereas these achieve 0.3 mV in bipolar maps for the highest noise level. As for the CV maps, the MOP-EGM method shows lower RMSE values than the standard OP-EGM approach, in agreement with what was found in Fig. 3.7.

Table 3.3 reports the mean and SD of the error caused by each noise level in the propagation angles estimated with both omnipolar approaches θ^o and $\theta^{o\text{-}m}$ for square and triangular cliques, jointly considering all three MEA orientations. These results show that propagation direction maps performed with square cliques are less affected by noise than those performed with triangular cliques, regardless of the omnipolar approach. However, for noise levels lower than $\sigma_n = 28\mu V$, direction maps with the MOP-EGM approach $\theta^{o\text{-}m}$ exhibit a smaller mean bias than those using the original method θ^o.

Finally, Fig. 3.10 shows the effect of the MEA orientation on omnipolar voltage and velocity maps ($V^{o\text{-}me}$, $V^{o\text{-}pca\text{-}r}$, $V^{o\text{-}me,a}$, $V^{o\text{-}pca\text{-}r,a}$, $CV^{o\text{-}m}$ and $CV^{o\text{-}m,a}$) performed with square cliques. The accuracy in fibrotic patch detection reached the values ACC = 91%, 99% and 100% using $V^{o\text{-}me}$; ACC = 91%, 100% and 100% using $V^{o\text{-}pca\text{-}r}$; and ACC =

Table 3.2: Fibrosis detection performance (voltage threshold, AUC and ACC), Pearson ρ_p and Spearman's ρ_s correlations obtained from clean b-EGMs ($\sigma_n = 0\ \mu V$), by jointly considering the three MEA orientations with respect to the propagation direction. *All the p-values < 0.01.

without —— with b-EGMs alignment						
Map type	Cliques	Threshold (mV)	AUC	ACC (%)	ρ_p^*	ρ_s^*
$V^{b\text{-}m}$	-	0.76	0.98	96	0.83	0.82
$V^{b\text{-}r}$	-	0.88	0.97	95	0.86	0.84
$V^{o\text{-}me}$	□	0.75 —— 0.90	0.97 —— 0.96	92 —— 93	0.77 —— 0.87	0.79 —— 0.87
	△	0.87 —— 0.91	0.96 —— 0.97	88 —— 92	0.83 —— 0.86	0.83 —— 0.85
$V^{o\text{-}pca\text{-}r}$	□	0.75 —— 0.90	0.97 —— 0.96	93 —— 93	0.77 —— 0.87	0.79 —— 0.87
	△	0.93 —— 0.90	0.95 —— 0.96	89 —— 92	0.82 —— 0.86	0.82 —— 0.85
CV^{o}	□	0.90	0.77	70	-	-
	△	0.91	0.80	74	-	-
$CV^{o\text{-}m}$	□	0.82 —— 0.74	0.95 —— 0.98	90 —— 96	-	-
	△	0.74 —— 0.73	0.92 —— 0.97	86 —— 94	-	-

Table 3.3: Expected error ϵ_θ (presented as mean ± SD) estimated globally for all propagation direction maps performed with noisy b-EGMs with respect to clean map.

ϵ_θ (deg) without —— with b-EGMs alignment				
Map type	Cliques	$\sigma_n = 3\mu V$	$\sigma_n = 6\mu V$	$\sigma_n = 14\mu V$
θ^{o}	□	0.00 ± 0.18	-0.01 ± 0.32	-0.01 ± 0.72
	△	-0.02 ± 2.86	-0.03 ± 3.74	-0.03 ± 5.10
$\theta^{o\text{-}m}$	□	$0.00 \pm 0.19 \vert\vert -0.01 \pm 0.41$	$0.01 \pm 0.34 \vert\vert 0 \pm 0.64$	$0.01 \pm 0.72 \vert\vert 0.03 \pm 1.24$
	△	$0.02 \pm 2.76 \vert\vert 0 \pm 0.52$	$0.02 \pm 3.58 \vert\vert 0 \pm 0.76$	$0.08 \pm 4.81 \vert\vert 0.01 \pm 1.65$
Map type	Cliques	$\sigma_n = 28\mu V$	$\sigma_n = 42\mu V$	$\sigma_n = 55\mu V$
θ^{o}	□	0.00 ± 1.38	0.00 ± 2.02	0.00 ± 2.63
	△	-0.05 ± 6.77	0.02 ± 8.14	0.02 ± 9.33
$\theta^{o\text{-}m}$	□	$0.02 \pm 1.35 \vert\vert 0.05 \pm 2.50$	$0.01 \pm 1.99 \vert\vert 0.09 \pm 3.86$	$0.04 \pm 2.60 \vert\vert 0.22 \pm 5.51$
	△	$0.12 \pm 6.31 \vert\vert 0.03 \pm 3.33$	$0.17 \pm 7.54 \vert\vert 0.07 \pm 5.24$	$0.20 \pm 8.75 \vert\vert 0.17 \pm 7.45$

100%, 91 % and 91% using $CV^{o\text{-}m}$, when $\Psi = 0°$, respectively, for MEA orientations $\Psi = 30°$ and $\Psi = 45°$. When previous time alignment of b-EGMs is performed, accuracy achieves values ACC = 100%, 91% and 92% for both $V^{o\text{-}me,a}$ and $V^{o\text{-}pca\text{-}r,a}$, while ACC = 93%, 100% and 100% when using $CV^{o\text{-}m,a}$, for the same catheter orientations.

3.4.2 Analysis of Clinical Recordings

Figure 3.11 shows (from left to right) maps of CV estimated with MOP-EGM ($CV_{i,j}^{o-m}$) and from LATs ($CV_{i,j}^{l}$), and the manually annotated reference LAT maps, respectively,

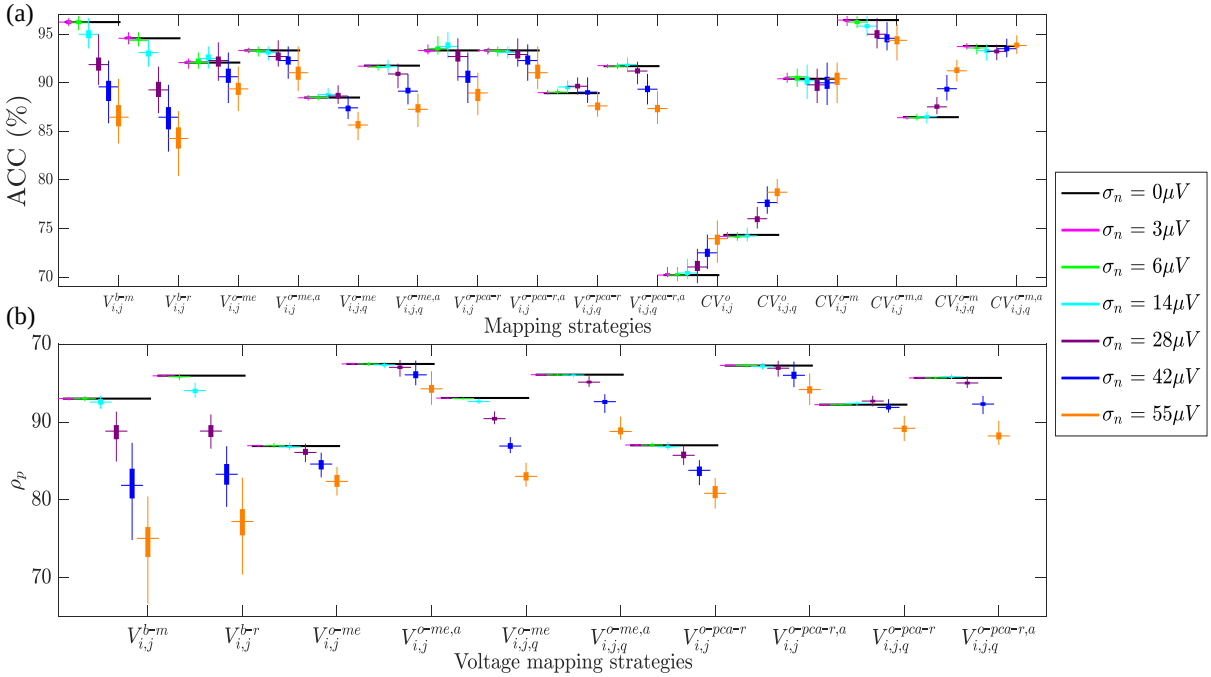

Figure 3.8: (a) Fibrosis ACC of the different mapping strategies. (b) Pearson's correlation coefficient ρ_p of the different voltage mapping strategies. For each noise level, the central mark and the bottom and top edges of each box indicate the median, the first and the third quartile, respectively, whereas the noise-free ACC and ρ_p are depicted as black horizontal lines.

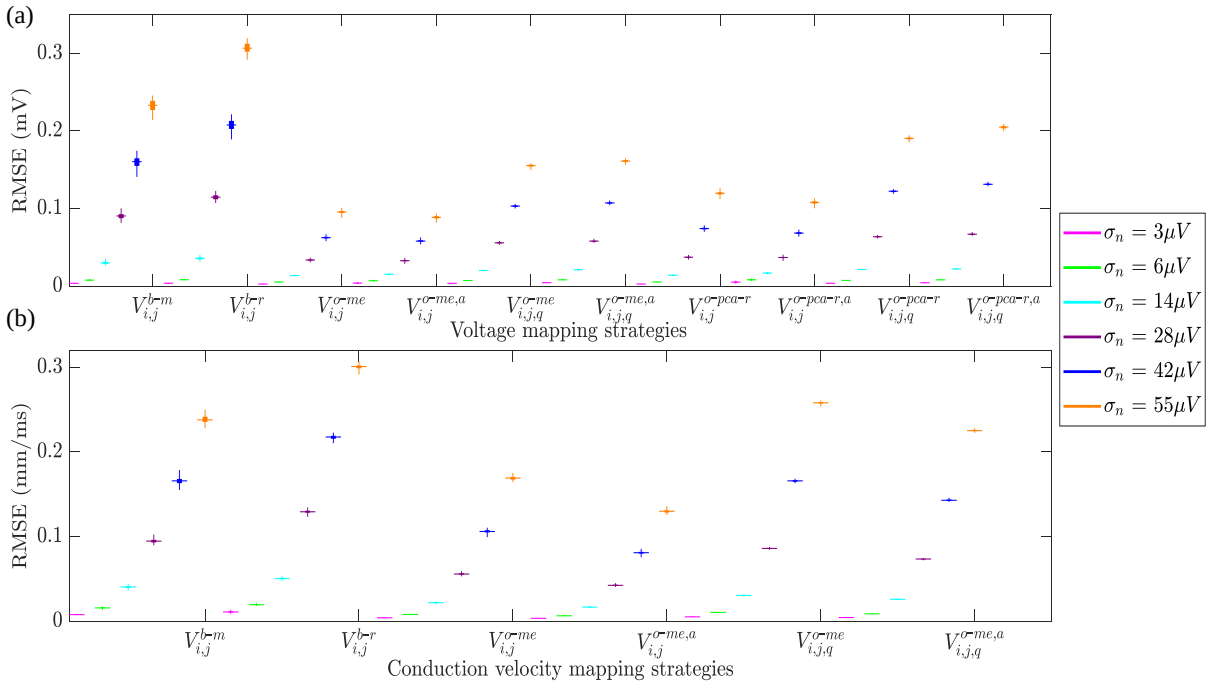

Figure 3.9: (a) RMSE for voltage mapping strategies. (b) RMSE for velocity mapping strategies. For each noise level, the central mark and the bottom and top edges of each box indicate the median, the first and the third quartile, respectively.

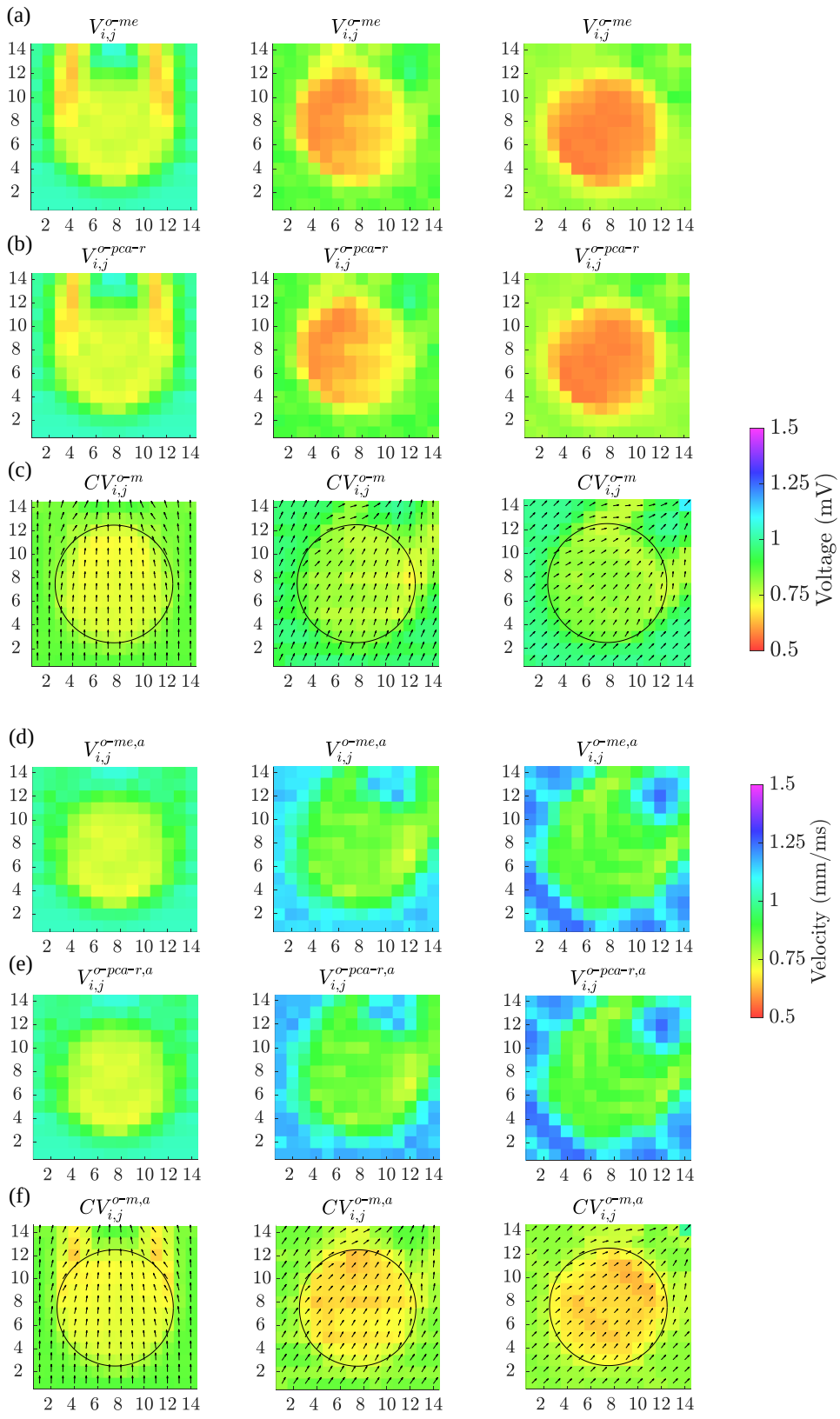

Figure 3.10: Omnipolar voltage maps (panels (a), (b), (d) and (e)) and velocity maps (panels (c) and (f)) performed from clean b-EGMs, without (panels (a), (b) and (c)) and with (panels (d), (e) and (f)) previous time alignment, by using square cliques, when: $\Psi = 0°$ (left column); $\Psi = 30°$ (middle column) and $\Psi = 45°$ (right column).

obtained from the clinical data presented in section 2.1, for some representative propagation patterns. Panel (a) depicts one atrial activation interval during SR, whereas panels (b), (c) and (d) show different patterns observed during AF. For each clique, the CV value was color-coded from blue (lowest) to red (highest), whereas its respective propagation direction is plotted as an arrow whose length is proportional to CV value. When an outlier was obtained (typically due to the non-accomplishment of the planar wave hypothesis), no arrow was plotted for that clique. For both types of estimation (MOP-EGM and LAT-based), any CV greater than 4 mm/ms was considered an outlier and was not represented. It must be pointed out that at this first analysis only square cliques were considered, and that propagation direction and CV were estimated with equations (3.27) and (3.30), respectively, in subsection 3.3.3, without resorting to prior alignment of the b-EGMs. As a reference, LAT maps were also color-coded from red (earliest) to blue (latest) in 10 ms isochrones. When a LAT could not be associated to an electrode within the MEA, a cross appeared in that location [110]. These maps reveal that in case of fibrillatory patterns (see Fig. 3.11 (b) to (c)), CV and propagation direction estimates based on LATs, unlike those obtained from MOP-EGM, yield unpredictable values in cliques characterized by rotors and multiple wavelets sites, where the plane wave hypothesis is not accomplished at all (red pixels with longest arrows).

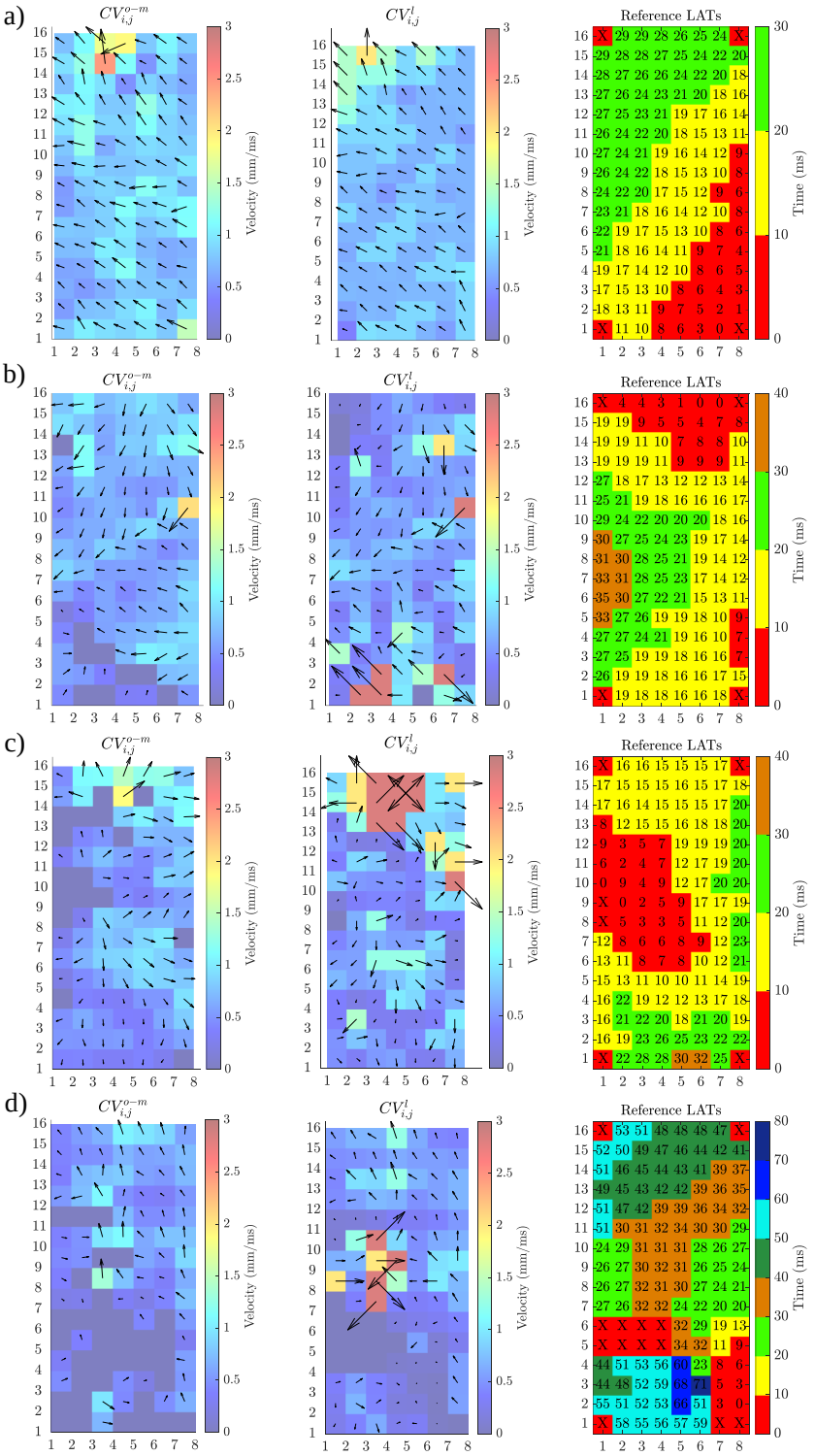

Figure 3.11: Maps of conduction velocities estimated with MOP-EGM method (left column, $CV^{o-m}_{i,j}$) and with LAT-based approach (middle column) and LATs maps used as reference (right column, $CV^{l}_{i,j}$), observed in SR (a) and during some representative propagation patterns in AF: two different wavefronts colliding and fusing into one (b), a concentric wavefront whose focus is located within the MEA (c) and a chaotic wavefront with several lines of block (d).

3.5 Discussion

3.5.1 Clinical Significance of the Work

In this work, we investigated the role of the omnipolar methodology in characterizing atrial propagation patterns and substrate. For that purpose, performance of different propagation estimates, as well as substrate and velocity mapping modalities, based on the standard OP-EGM method and on the MOP-EGM approach proposed in this thesis, is evaluated. The OP-EGM methodology was presented in [71] as a novel approach allowing characterization of myocardial substrate and propagation pattern, making possible real-time high-density maps less sensitive to catheter orientation than current bipolar strategies. It showed to solve complex collision and fractionation wavefront patterns in animal subjects, thus providing coherent voltage maps even during AF [134]. The OP-EGM approach was proposed to surmount the well-known limitations affecting bipolar voltage mapping, which represents the cornerstone for the identification of fibrotic atrial substrate, and consequently for low-voltage-guided catheter ablation strategies in AF [134]. Most studies to detect fibrosis rely on bipolar voltage mapping [81], [79]. Other works demonstrate a high correlation with respect to the use of u-EGMs based maps, suggesting no relevant clinical impact of using b-EGMs over u-EMGs [135]. The efficacy of omnipolar EGMs was also proved in ex vivo [136] and in vivo [137] ventricular mapping, for delineation of both healthy and infarcted areas. OP-EGM approach-based mapping strategies represent an alternative to the more time-consuming LATs mapping, allowing beat-to-beat indication of the wavefront propagation direction [138]. Nevertheless, the unresolved problems concerning directionality of the estimates based on the OP-EGM method, which have been addressed in this chapter, have also been considered in other recent studies, involving both simulation [129] and animal experimental [130] data, and revealing results consistent with those found in this thesis. In these works, an alternative cross-oriented clique configuration, which involves b-EGMs along diagonal directions, was proposed to avoid the time misalignment of bipolar components occurring in triangular cliques, and provide more robust OP-EGM-based estimates, also leading to important conclusions regarding (but not limited to) EGM morphology and interelectrode spacing.

In this chapter, evaluation of the omnipolar approach is conducted by means of two different studies. In the first one, propagation parameters are estimated with a modified version of the OP-EGM method and compared to LAT-based estimations, by using both synthetic and real EGMs in different scenarios including normal SR and fibrillatory patterns. In the second one, further modifications to the standard OP-EGM method are introduced, with the purpose of overcoming the residual dependence of the OP-EGM method on catheter orientation still affecting fibrosis detection, voltage and CV estimations. Resulting mapping strategies were evaluated in a simulation scenario including atrial fibrosis.

3.5.2 Performance Evaluation of the Modified Omnipolar Electrogram Method with Simulated Data

Conduction velocity and propagation direction estimates are initially evaluated in a 8 × 16 MEA within a 2D atrial slice, simulated with different activation patterns, both in SR and in AF, and tissue properties. Results show lower errors in LAT-based estimations than in omnipolar ones, both in terms of CV and of propagation direction. This can be due to the very simple propagation patterns simulated in this study and to the LATs derived from signals which are therefore not affected by detection errors. Anyway, lower errors for both types of estimation are observed when the plane wave hypothesis is better accomplished (*side* cases).

In the second simulation study, a 15 × 15 MEA over a 2D atrial tissue simulated with the Courtemanche cellular model and including fibrosis was considered. To begin with, maps computed from noise-free b-EGMs were analyzed. Results show that the previous alignment of the b-EGMs in each clique, proposed in this part of the thesis for the MOP-EGM method, always improves the fibrosis detection ability of the omnipolar voltage and CV maps. The latter provide a characterization of the atrial substrate comparable to bipolar voltage maps combining b-EGMs along x and y directions. On the other hand, bipolar maps $V^{b\text{-}x}$ and $V^{b\text{-}y}$ in each of the MEA main directions revealed ACC values of 69% and 91%, respectively. Moreover, CV maps computed with the MOP-EGM approach present better performance than both omnipolar voltage maps and CV maps computed with the standard OP-EGM method. It must also be pointed out that, using the omnipolar approaches, conduction velocities are estimated without the need of detecting LATs, thus avoiding the sensitivity to inaccuracies in their determination. In the present study, the sensitivity to noise of the different mapping approaches is also investigated. Results suggest that the voltage and CV maps performed from aligned b-EGMs are more robust against noise than both bipolar voltage maps and their unaligned versions, also showing better performance in detecting fibrosis and in reproducing voltage maps for the same noise level. In addition, the present chapter also addresses the question of the sensitivity of the OP-EGM method to the MEA orientation. Although the fibrotic patch is well discriminated from the healthy tissue by all omnipolar mapping strategies considered in this part of the thesis, both voltage and velocity OP-EGM based estimates are affected by the relative orientation between MEA and tissue fibers. Regarding voltage maps, when the MEA is not oriented in the same direction as tissue fibers ($\Psi \neq 0°$), the omnipolar voltage values are reduced. In addition, in tissue areas where the wavefront propagation is curved, the E-field is overestimated when the local propagation direction becomes parallel to one of the two main directions of the MEA (as when $\Psi = 45°$). As this happens in an area of healthy tissue, it causes a higher overall accuracy in fibrotic patch detection. The reverse occurs when these curved areas are oblique to the MEA (as in $\Psi = 0°$), providing underestimated voltages and a reduction of fibrotic detection

accuracy.

As for the dependence of velocity maps on MEA orientation, the opposite behavior is observed, as CV estimation increases for $\Psi \neq 0°$.

This is explained by the fact that v, in (3.30), has an inverse relationship with the magnitude of the estimated E-field, while in voltage estimation (equations in subsection 3.3.3.3), the dependence is direct. In addition, in those areas where the wave propagation is curved, velocity is overestimated when the MEA is in the same direction as the tissue ($\Psi = 0°$). Therefore, the fibrotic patch is globally better detected for this configuration. On the other hand, if MEA becomes oblique to the tissue ($\Psi \neq 0°$), areas of curved propagation appear underestimated, thus reducing the overall fibrosis detection performance for those configurations. When b-EGMs are time-aligned, both MOP-EGM based voltage and velocity maps continue to be sensitive to the orientation between MEA and tissue, but to a lesser extent if compared to their unaligned versions. As a result, improved fibrosis detection, better voltage estimations and less degradation by noise are observed in average when using the MOP-EGM approach. The remaining dependence with Ψ is not predicted by the mathematical model based on the plane-wave assumption, but the sampling frequency of the b-EGMs (1 kHz) could be behind this observation.

3.5.3 Preliminary Performance Evaluation of the Modified Omnipolar Electrogram Method with Clinical Data

In this thesis, omnipolar estimates were also assessed in clinical data, by using epicardial EGMS recorded with a 8×16 MEA in some representative propagation patterns. As for the simulated data, velocity was also derived from LATs, manually reported by an electrophysiologist. These preliminary results reveal that both MOP-EGM and LAT-based maps are able to reproduce CV and propagation direction estimates coherently with the propagation pattern reference (provided by LATs maps), where the wave plane hypothesis is valid. Nevertheless, when more complex patterns are present, the omnipolar estimates show a smoother and more homogeneous behaviour than LAT-based ones in reentry circuits and multiple wavelets areas. This behaviour can be explained with the fact that CV and propagation direction estimates based on the LATs are affected by the manual detection of the latter, which inevitably adds noise to estimations, making them less predictable.

3.5.4 Limitations

The omnipolar methodology is based on the assumption of plane and homogeneous propagation within each clique, which represents an intrinsic limitation, requiring the use of high spatial resolution multielectrode catheters (like the MEA considered in this study). In addition, the hypothesis of a plane myocardial surface in the area defined by a clique

is not always accomplished, as in non-compacted myocardial regions or in the atrial appendage. In the simulation studies conducted in this thesis, 2D atrial models with very simple propagation patterns are used, which do not perfectly reproduce the real 3D situation. Therefore, the results here obtained should be confronted in future studies with those from other simulation configurations (such as non-plane or wavefronts from multiple foci in AF, as well as patchy fibrosis models). Moreover, results obtained by using the preliminary MOP-EGM over real data need to be integrated with others taking into account the effect of electrode size, interelectrode distance and variable tissue-electrode contact. Nevertheless, the validation of these methods in-vivo is challenging, since late gadolinium enhanced magnetic resonance imaging (LGE-MRI) represents the only non invasive available reference for atrial fibrosis today, and even their utility is under debate [139]. In-vivo/Ex-vivo animal experiments represent an alternative for future works aiming to establish if the simulation-proved superior performance of MOP-EGM translates to clinical counterparts.

3.6 Conclusion

This chapter presents mapping strategies based on the MOP-EGM method (a modification of the OP-EGM method) to characterize atrial substrate and propagation patterns. Conduction velocity amplitude and angle estimates reveal to be able to reproduce propagation patterns both in SR and in AF, also showing lower estimation errors than LAT-based estimations with complex activities. Regarding fibrosis detection, voltage maps are able to discriminate fibrotic from healthy tissue. For low noise levels, they attain comparable performance to maps obtained by combining the b-EGMs amplitudes along the two directions of the catheter, but clearly outperform bipolar maps in the presence of noise. On the other hand, omnipolar CV maps reveal higher fibrosis detection accuracy than voltage maps, specially when the modifications proposed in this chapter are applied. The fibrosis detection performance of voltage and velocity maps benefit from prior intraclique time alignment of b-EGMs as proposed in the MOP-EGM approach. In addition, the use of square cliques outperforms the triangular ones.

As for the different approaches to estimate the omnipolar voltage from the E-field loop, both the one based on maximal excursion (*me*) and the one based on principal component analysis (*pca*) yield similar results, in terms of ACC and correlation with unipolar voltage maps. Similar conclusions are drawn when b-EGMs are affected by noise extracted from real signals.

Both OP-EGM and MOP-EGM strategies considered to estimate the propagation angle revealed smaller sensitivity to noise than methods based on bipolar voltage maps. When compared, the use of square cliques results in lower variance than the use of triangular ones when estimating the propagation direction in noisy situations.

Chapter 4

Atrial Fibrosis Identification by Eigenvalue Dominance Ratio of Multielectrode Electrograms Arrays

4.1 Introduction

As introduced in subsection 1.3.5, detection of fibrotic tissue in the atrium is of considerable importance due to its correlation with AF and its consequent role in the ablation procedures. Electrophysiological and clinical approaches to identify fibrosis present limitations including lack of standardisation and validation, thus requiring the need for objective quantification methodologies.

In recent years, the role of fibrotic tissue has received more attention on the initiation and perpetuation of AF than on its effects on the morphology of the EGMs [140]. In this scenario, only few intracardiac signal processing methods based on EGM features have been proposed to identify fibrotic tissue. Some studies have highlighted the relationship between EGM morphology and tissue alterations, including ablation lesion formation [128]. Others have introduced a method to characterize the different fibrotic textures based on EGM fractionation due to the incidence of wavefront direction [141]. In all these works, *in silico* experiments have been used for validation.

In this chapter, the waveform dispersion of u-EGMs in electrode cliques is hypothesized to be correlated with the presence of atrial fibrosis. Therefore, this part of the thesis aims to propose biomarkers of EGM waveform dispersion based on eigenvalue analysis of nearby u-EGMs to detect areas of fibrosis. In particular, the proposed biomarkers are based on the concept of dominant-to-remaining eigenvalue dominance ratio (EIGDR). These markers consider the spatiotemporal relations of the u-EGM waveforms, thus overcoming limitations which affect the standard approaches for the detection of fibrosis (bipolar voltage thresholding, gadolinium enhancement, LA function loss).

Resulting pixel maps, referred as EIGDR maps, were computed with synthetic u-EGMs.

Two sizes of square cliques, (2×2 and 3×3 electrodes configurations) and three catheter orientations with respect to the tissue preferential direction (0°, 30° and 45°), were considered for that purpose. The ability of each map in detecting a simulated fibrosis patch has been evaluated assuming different unipolar noise levels and variable electrode-tissue distance.

4.2 Testing Dataset

The atrial model used to assess the EIGDR approach has been introduced in subsection 2.2.2. In addition, in order to take into account a more realistic scenario, where the distance from the tissue may not be constant through the electrodes in the clique, the electrode-tissue distance has been assumed to be a random variable following a normal distribution. Two thousand different random configurations have been simulated, where the distance of each electrode to the tissue was randomly and independently chosen following that distribution. In addition, in order to evaluate the sensitivity to noise of EIGDR-based maps, synthetic u-EGMs were also corrupted with real noise, as illustrated in subsection 2.1.3 and 2.2.2, thus obtaining noisy realizations $u_{i,j}^{q}(n)$, $i,j \in \{1,\ldots,15\}$, $q \in \{1,\ldots,2000\}$.

4.3 Methods

4.3.1 Eigenvalue Analysis

Unipolar signals in the clique can be compactly represented by the following $N \times K$ matrix, $K \in \{4,9\}$, as in [142]:

$$\mathbf{U} = \Big[\mathbf{u}_1 \quad \ldots \quad \mathbf{u}_K\Big], \tag{4.1}$$

where the k-th column, $\mathbf{u}_k$, contains the samples of the unipolar signal $u_k(n)$, modeled later in subsection 4.3.3:

$$\mathbf{u}_k = \Big[u_k(0) \quad \cdots \quad u_k(N-1)\Big]^T. \tag{4.2}$$

We propose and assess EIGDR values from the clique u-EGMs in (4.1) to detect fibrosis. The N eigenvalues, sorted in descendent order, $\{\lambda_1,\ldots,\lambda_N\}$, of the $N \times N$ intrasignal correlation matrix $\mathbf{R}_u = E[\mathbf{u}_k\mathbf{u}_k^T]$, were obtained from the following correlation matrix estimate within each clique:

$$\hat{\mathbf{R}}_u = \frac{1}{K}\mathbf{U}\mathbf{U}^T. \tag{4.3}$$

The matrix $\mathbf{R}_u$ is the intrasignal sample correlation matrix, whose eigenvalues reflect the degree of morphological variability among the signals in the clique.

For each clique, the ratio $\mathcal{R}$ of the largest (i.e. *dominant*) eigenvalue λ_1 and the remaining ones was estimated:

$$\mathcal{R} = \frac{\lambda_1}{\sum_{n=2}^{N} \lambda_n}. \tag{4.4}$$

By comparing the first eigenvalue to the sum of the others, we are able to quantify the u-EGM energy percentage which can be explained by the shape of the first eigenvector. The ratio $\mathcal{R}$ would be much higher than one if all u-EGMs were essentially identical to each other and all the waveforms can be explained with just the shape of the first eigenvector (i.e., low morphological variability). On the contrary, when waveform dispersion appears, the eigenvalues from λ_2 to λ_N become higher, thus reducing the ratio $\mathcal{R}$.

4.3.2 Time Alignment of Unipolar Electrograms

Eigenvalues of $\hat{\mathbf{R}}_u$ were computed from the original u-EGMs and alternatively after intra-clique time alignment, proposed to compensate the effect that different activation wavefront arrival times have on the EIGDR not related to fibrosis. In this case, unipolar signals were aligned according to Woody's iterative procedure [23, 143]:

1. at first iteration, $l = 0$, the relative time delay $\hat{\tau}_{k,0}$ between each unipolar signal $u_k(n)$ and the u-EGM with the highest peak-to-peak amplitude within the clique $u_{max}(n)$ (assumed as initial reference signal) was estimated by maximizing their cross-correlation:

$$\hat{\tau}_{k,0} = \arg\max_{\tau} \sum_{n=0}^{N-1} u_k\left(n-\tau\right)\ u_{max}(n); \tag{4.5}$$

2. from the relative time delays, the average of the shifted signals $u_k(n - \hat{\tau}_{k,0})$ within the clique was calculated:

$$\bar{u}_0(n) = \frac{1}{K} \sum_{k=1}^{K} u_k\left(n-\hat{\tau}_{k,0}\right); \tag{4.6}$$

3. in each l-th iteration, $l > 0$, the cross-correlation between each $u_k(n)$ and the average signal obtained in the previous iteration $\bar{u}_{l-1}(n)$ (assumed as updated reference signal) is maximized to find the updated relative time delays $\hat{\tau}_{k,l}$:

$$\hat{\tau}_{k,l} = \arg\max_{\tau} \sum_{n=0}^{N-1} u_k\left(n-\tau\right)\ \bar{u}_{l-1}\left(n\right). \tag{4.7}$$

This process is repeated iteratively until the delay estimates no longer change.

Eigenvalues of the intrasignal correlation matrix of the aligned u-EGMs were calculated in the same way as for their non-aligned version, thus leading to the formulation of the ratio $\mathcal{R}^{\mathcal{A}}$ (where the upper index denotes that the ratio comes from aligned u-EGMs within the clique) analogous to (4.4).

4.3.3 Unipolar Signal Modeling

The u-EGMs within a clique located at (i, j) position within the MEA are indexed as $u_k(n),\ k \in \{1, \ldots, K\},\ K \in \{4, 9\}$. Assuming a plane wave propagation, the different electrodes in a clique are activated at different times, and therefore the u-EGMs in the clique $u_k(n)$ can be modelled as delayed versions of a given waveform, plus noise and other non-homogeneous components. Therefore, they can be modeled, analogously to [144] for misaligned signal ensembles, as:

$$u_k(n) = \alpha_k s(n - \tau_k) + f_k(n) + v_k(n) \quad \begin{cases} k = 1, \ldots, K \\ n = 1, \ldots, N \end{cases}, \tag{4.8}$$

where:

- $s(n)$ is the u-EGM activation signal component assumed to be space invariant in the case of a plane wave propagation and homogeneous tissue free of fibrosis. Its energy is denoted as E_s.

- τ_k is the delay of the k-th u-EGM $s(n - \tau_k)$ with respect to a time reference within the clique, introduced later. Delays τ_k are zero-mean and characterized by their variance in the normal tissue σ_τ^2. In fibrotic areas, the reduction in CV with respect to healthy tissue increases the variance of the τ_k up to $\beta^2\sigma_\tau^2$, where the factor $\beta > 1$ in fibrosis and $\beta = 1$ in non-fibrotic tissue.

- α_k is a parameter accounting for u-EGM amplitude reduction between fibrotic, $\alpha_k < 1$, and healthy, $\alpha_k = 1$, tissues. It is modelled as a random variable with mean $\overline{\alpha}$ and variance σ_α^2 ($\overline{\alpha} = 1$, $\sigma_\alpha^2 = 0$ in healthy tissue; $\overline{\alpha} < 1$, $\sigma_\alpha^2 > 0$ in fibrosis).

- $f_k(n)$ is a zero-mean fibrotic signal component across the clique with variance σ_f^2. In healthy tissue $f_k(n) = 0$.

- $v_k(n)$ is the zero-mean, Gaussian, white noise component at the k-th u-EGM, with variance σ_v^2 and uncorrelated with τ_k and $f_k(n)$.

Four different scenarios for each $u_k(n)$ were considered in this study, as already proposed in [109], with/without fibrosis and with/without prior alignment. Their approximate theoretical eigenvalues and EIGDR were derived following parallel methodology to that used in [144] for repetitive signal ensemble alignment, as detailed below.

1. *Prior alignment with no fibrosis*: For perfectly aligned signals without fibrosis, i.e., $u_k(n) = s(n) + v_k(n)$, the intrasignal correlation matrix is given by:

$$\mathbf{R}_u = \mathbf{s}\mathbf{s}^T + \sigma_v^2\mathbf{I}, \tag{4.9}$$

where $\mathbf{I}$ is the $N \times N$ identity matrix and data vector $\mathbf{s}$, $\mathbf{s} = \begin{bmatrix} s(0) & \dots & s(N-1) \end{bmatrix}^T$, is easily shown to be proportional to the first eigenvector of $\mathbf{R}_u$, whereas the remaining eigenvectors are chosen arbitrarily as long as they are orthogonal to the first. The eigenvalues are given by:

$$\lambda_n = \begin{cases} E_s + \sigma_v^2 & n = 1 \\ \sigma_v^2 & n = 2, \dots, N, \end{cases} \tag{4.10}$$

where $E_s = \mathbf{s}^T\mathbf{s}$ is the signal energy. For real u-EGM, signal energy is much larger than noise energy, $E_s >> N\sigma_v^2$, and $N >> 1$, resulting in an EIGDR of:

$$\mathcal{R}^{\mathcal{A}} \approx \frac{E_s}{N\sigma_v^2}. \tag{4.11}$$

2. *No prior alignment and no fibrosis*: We now analyze the case of raw u-EGMs in the clique where misalignment of $s(n)$ is assumed to be present in each k-th u-EGM, $u_k(n) = s(n - \tau_k) + v_k(n)$. Then, to estimate the eigenvalues we can approximate $u_k(n)$, for small τ_k, as [144]:

$$u_k(n) \approx s(n) - \tau_k s'(n) + \frac{1}{2}\tau_k^2 s''(n) + v_k(n), \tag{4.12}$$

where $s'(n)$ and $s''(n)$ denote the first and second derivative of $s(n)$, respectively. The intrasignal correlation matrix can be expressed as:

$$\mathbf{R}_u \approx \left(\mathbf{s}\mathbf{s}^T + \frac{\sigma_\tau^2}{2}(\mathbf{s}\mathbf{s}''^T + \mathbf{s}''\mathbf{s}^T)\right) + \sigma_\tau^2\mathbf{s}'\mathbf{s}'^T + \sigma_v^2\mathbf{I}, \tag{4.13}$$

where $\mathbf{s}'$ and $\mathbf{s}''$ are the vector counterparts of $s'(n)$ and $s''(n)$, respectively. It can be shown that the eigenvalues of $\mathbf{R}_u$ are approximated by [144]:

$$\lambda_n \approx \begin{cases} E_s - \sigma_\tau^2 E_{s'} + \sigma_v^2 & n = 1 \\ \sigma_\tau^2 E_{s'} + \sigma_v^2 & n = 2 \\ \sigma_v^2 & n = 3, \dots, N, \end{cases} \tag{4.14}$$

where $E_{s'} = \mathbf{s}'^T\mathbf{s}'$ is the derivative signal energy. The resulting EIGDR is approximated by:

$$\mathcal{R} \approx \frac{E_s - \sigma_\tau^2 E_{s'}}{\sigma_\tau^2 E_{s'} + N\sigma_v^2}. \tag{4.15}$$

Note that when $\sigma_\tau = 0$ (i.e., perfect alignment) this equation becomes equal to (4.11).

3. *Prior alignment and fibrosis*: When u-EGMs are first aligned in fibrosis zones, each of them can be modelled as $u_k(n) = \alpha_k s(n) + f_k(n) + v_k(n)$. The correlation matrix results in:

$$\mathbf{R}_u = \left(\overline{\alpha}^2 + \sigma_\alpha^2\right) \mathbf{s}\mathbf{s}^T + \sigma_v^2 \mathbf{I} + \sigma_f^2 \mathbf{I}, \tag{4.16}$$

and their corresponding eigenvalues are:

$$\lambda_n \approx \begin{cases} \left(\overline{\alpha}^2 + \sigma_\alpha^2\right) E_s + \sigma_v^2 + \sigma_f^2 & n = 1 \\ \sigma_v^2 + \sigma_f^2 & n = 2, \ldots, N, \end{cases} \tag{4.17}$$

which, assuming that $\sigma_f << E_s$ in addition to the assumptions made in (4.11), leads to:

$$\mathcal{R}_{\mathcal{F}}^{\mathcal{A}} \approx \frac{E_s}{\frac{N(\sigma_v^2+\sigma_f^2)}{\left(\overline{\alpha}^2+\sigma_\alpha^2\right)}}, \tag{4.18}$$

where the parameters used have already been introduced at the beginning of this section and upper $\mathcal{A}$ and lower $\mathcal{F}$ indices in $\mathcal{R}_{\mathcal{F}}^{\mathcal{A}}$ denote that the calculations are obtained from intraclique aligned u-EGMs in fibrotic tissue, respectively.

4. *No prior alignment with fibrosis*: When raw u-EGMs come from fibrotic areas, each of them can be modelled as $u_k(n) = \alpha_k s(n - \tau_k) + f_k(n) + v_k(n)$. In this case, the delay τ_k has larger SD than in non-fibrotic areas, with the extra delay controlled by a multiplicative factor β, thus resulting in the following correlation matrix:

$$\begin{aligned} \mathbf{R}_u \approx & \left(\overline{\alpha}^2 + \sigma_\alpha^2\right) \left[\left(\mathbf{s}\mathbf{s}^T + \frac{\beta^2 \sigma_\tau^2}{2} (\mathbf{s}\mathbf{s}''^T + \mathbf{s}''\mathbf{s}^T) \right) + \beta^2 \sigma_\tau^2 \mathbf{s}'\mathbf{s}'^T \right] \\ & + \sigma_f^2 \mathbf{I} + \sigma_v^2 \mathbf{I}, \end{aligned} \tag{4.19}$$

which is similar to the case without fibrosis in (4.13) but with different proportionality factor and two different random components, corresponding to noise and fibrosis. The eigenvalues will similarly be approximated by:

$$\lambda_n \approx \begin{cases} \left(\overline{\alpha}^2 + \sigma_\alpha^2\right) \left(E_s - \beta^2 \sigma_\tau^2 E_{s'}\right) + \sigma_v^2 + \sigma_f^2 & n = 1 \\ \left(\overline{\alpha}^2 + \sigma_\alpha^2\right) \beta^2 \sigma_\tau^2 E_{s'} + \sigma_v^2 + \sigma_f^2 & n = 2 \\ \sigma_v^2 + \sigma_f^2 & n = 3, \ldots, N. \end{cases} \tag{4.20}$$

The corresponding EIGDR is approximated by:

$$\mathcal{R}_{\mathcal{F}} \approx \frac{E_s - \beta^2 \sigma_\tau^2 E_{s'}}{\beta^2 \sigma_\tau^2 E_{s'} + \frac{N(\sigma_v^2+\sigma_f^2)}{\left(\overline{\alpha}^2+\sigma_\alpha^2\right)}}. \tag{4.21}$$

Table 4.1: Signal models for non-aligned (NA) and aligned (A) u-EGMs at non-fibrotic (NF) and fibrotic (F) areas, with their respective eigenvalues λ_k and EIGDR.

u-EGM	model	λ_n	EIGDR
NA, NF	$u_k(n) = s(n-\tau_k) + v_k(n)$	$\lambda_n \approx \begin{cases} (E_s - \sigma_\tau^2 E_{s'}) + \sigma_v^2, & n=1 \\ \sigma_\tau^2 E_{s'} + \sigma_v^2, & n=2 \\ \sigma_v^2, & n=3,\ldots,N \end{cases}$	$\mathcal{R} \approx \frac{E_s - \sigma_\tau^2 E_{s'}}{\sigma_\tau^2 E_{s'} + N\sigma_v^2}$
A, NF	$u_k(n) = s(n) + v_k(n)$	$\lambda_n \approx \begin{cases} E_s + \sigma_v^2, & n=1 \\ \sigma_v^2, & n=2,\ldots,N \end{cases}$	$\mathcal{R}^{\mathcal{A}} \approx \frac{E_s}{N\sigma_v^2}$
NA, F	$u_k(n) = \alpha_k s(n-\tau_k) + f_k(n) + v_k(n)$	$\lambda_n \approx \begin{cases} (\overline{\alpha}^2 + \sigma_\alpha^2)(E_s - \beta^2\sigma_\tau^2 E_{s'}) + \sigma_v^2 + \sigma_f^2, & n=1 \\ (\overline{\alpha}^2 + \sigma_\alpha^2)\beta^2\sigma_\tau^2 E_{s'} + \sigma_v^2 + \sigma_f^2, & n=2 \\ \sigma_v^2 + \sigma_f^2, & n=3,\ldots,N \end{cases}$	$\mathcal{R}_{\mathcal{F}} \approx \frac{E_s - \beta^2\sigma_\tau^2 E_{s'}}{\beta^2\sigma_\tau^2 E_{s'} + \frac{N(\sigma_v^2+\sigma_f^2)}{(\overline{\alpha}^2+\sigma_\alpha^2)}}$
A, F	$u_k(n) = \alpha_k s(n) + f_k(n) + v_k(n)$	$\lambda_n \approx \begin{cases} (\overline{\alpha}^2 + \sigma_\alpha^2) E_s + \sigma_v^2 + \sigma_f^2, & n=1 \\ \sigma_v^2 + \sigma_f^2, & n=2,\ldots,N \end{cases}$	$\mathcal{R}_{\mathcal{F}}^{\mathcal{A}} \approx \frac{E_s}{\frac{N(\sigma_v^2+\sigma_f^2)}{(\overline{\alpha}^2+\sigma_\alpha^2)}}$

A summary of eigenvalues and the EIGDR are reported in Table 4.1 for the four scenarios.

Note that if the intersignal correlation matrix, $\mathbf{R}_u^{\bullet} = E[\mathbf{u}(n)\mathbf{u}^T(n)]$, with $\mathbf{u}(n) = \begin{bmatrix} u_1(n) & \ldots & u_K(n) \end{bmatrix}^T$, had been computed rather than the intra-signal correlation matrix $\mathbf{R}_u$, for the more general case with fibrosis and misalignment, and following a derivation parallel to the one presented in [144], the eigenvalues would have resulted in:

$$\lambda_n^{\bullet} \approx \begin{cases} \frac{K}{N}(\overline{\alpha}^2 + \sigma_\alpha^2)(E_s - \beta^2\sigma_\tau^2 E_{s'}) + \sigma_v^2 + \sigma_f^2 & n=1 \\ \frac{K}{N}(\overline{\alpha}^2 + \sigma_\alpha^2)\beta^2\sigma_\tau^2 E_{s'} + \sigma_v^2 + \sigma_f^2 & n=2 \\ \sigma_v^2 + \sigma_f^2 & n=3,\ldots,K. \end{cases} \tag{4.22}$$

When computing the EIGDRs for this matrix the results are approximately the same as for $\mathbf{R}_u$.

In practice, the matrix is estimated as:

$$\hat{\mathbf{R}}_u^{\bullet} = \frac{1}{N}\mathbf{U}^T\mathbf{U}, \tag{4.23}$$

rather than with the theoretical expectations. From these estimates we observe that matrix $\hat{\mathbf{R}}_u^{\bullet}$ is full rank while matrix $\hat{\mathbf{R}}_u$ (estimated as in (4.3)) is not ($N > K$). That circumstance does not represent a limitation, since no matrix inversions are required. In addition, as shown in [142], for the data-estimated autocorrelation matrices with $N > K$, $\lambda_i = \frac{N}{K}\lambda_i^{\bullet}$ ($i \leq K$) and $\lambda_i = 0$ ($i > K$), again showing equivalence of the EIGDR ratios for both matrices when estimated from the available data. Therefore just computational considerations can advise to use one or the other.

4.3.4 Eigenvalue Dominance Ratio and Voltage Based Fibrosis Markers

According to the previous models, the following main differential effects on shape, amplitude and arrival times of the signal are expected to occur in F when compared to NF

tissue:

1. higher morphology dispersion represented by the u-EGM signal component $f_k(n)$ and quantified by σ_f^2;

2. lower and less homogeneous signal amplitudes represented by α_k and quantified by $\overline{\alpha} < 1$ and σ_α^2 $((\overline{\alpha}^2 + \sigma_\alpha^2) < 1)$;

3. larger intersignal misalignment within the clique as a result of slowed conduction and represented by delays τ_k with enlarged variance $(\beta^2\sigma_\tau^2, \beta > 1)$ relative to healthy tissue (σ_τ^2).

In order to establish a suitable index to be used for the discrimination of F and NF tissues, firstly the EIGDR computed with no prior alignment of u-EGMs and no fibrosis, $\mathcal{R}$, was compared with the ratio with fibrotic tissue, $\mathcal{R}_\mathcal{F}$, see Table 4.1. Since the numerator in $\mathcal{R}_\mathcal{F}$ is smaller than in $\mathcal{R}$, being $\beta > 1$, while the denominator is larger, as a combination of the three effects introduced by fibrosis, $\beta^2 > 1$, $\sigma_f^2 > 0$ and $(\overline{\alpha}^2 + \sigma_\alpha^2) < 1$, it results that $\mathcal{R}_\mathcal{F} < \mathcal{R}$. This suggests to use the ratio $\mathcal{R}$ as a thresholding strategy to distinguish if the clique is at fibrotic or healthy tissue.

The same analysis can be performed by comparing the EIGDR with prior alignment of u-EGMs and fibrosis, $\mathcal{R}_\mathcal{F}^\mathcal{A}$, with respect to its counterpart without fibrosis, $\mathcal{R}^\mathcal{A}$. In this case, only the terms $\sigma_f^2 > 0$ and $(\overline{\alpha}^2 + \sigma_\alpha^2) < 1$ are responsible for the difference, since σ_τ^2 has already been compensated for by alignment, resulting in $\mathcal{R}_\mathcal{F}^\mathcal{A} < \mathcal{R}^\mathcal{A}$. This suggests that $\mathcal{R}^\mathcal{A}$ may also be a useful strategy for discriminating fibrotic from healthy tissue.

In order to study which of the two proposals, $\mathcal{R}$ or $\mathcal{R}^\mathcal{A}$, is more sensitive to fibrotic tissue features, we computed the ratio $\Delta\mathcal{R}_\mathcal{F}$ between $\mathcal{R}$ and $\mathcal{R}_\mathcal{F}$ and studied how it changes by varying σ_τ^2. Under the proposed signal model, $\Delta\mathcal{R}_\mathcal{F}$ can be approximated by:

$$\Delta\mathcal{R}_\mathcal{F} = \frac{\mathcal{R}}{\mathcal{R}_\mathcal{F}} \approx \frac{\beta^2\sigma_\tau^2 E_{s'} + \frac{N(\sigma_v^2+\sigma_f^2)}{(\overline{\alpha}^2+\sigma_\alpha^2)}}{\sigma_\tau^2 E_{s'} + N\sigma_v^2}. \tag{4.24}$$

Computing its partial derivative with respect to σ_τ^2, we have:

$$\frac{\partial\Delta\mathcal{R}_\mathcal{F}}{\partial\sigma_\tau^2} \approx \frac{-E_{s'}N\left(\sigma_f^2 + \sigma_v^2\left(1 - \beta^2\left(\overline{\alpha}^2 + \sigma_\alpha^2\right)\right)\right)}{\left(\overline{\alpha}^2 + \sigma_\alpha^2\right)\left(\sigma_\tau^2 E_{s'} + N\sigma_v^2\right)^2}. \tag{4.25}$$

Typically, in fibrosis $(1 - \beta^2\left(\overline{\alpha}^2 + \sigma_\alpha^2\right)) > 0$, since CV reduction is less marked ($\beta \approx 2$ for high fibrosis, [145], [146]) than voltage attenuation ($\overline{\alpha} \approx 0.3$ [82]) and consequently the product $\beta^2\overline{\alpha}^2 < 1$. This results in $\frac{\partial\Delta\mathcal{R}_\mathcal{F}}{\partial\sigma_\tau^2} < 0$, meaning that the lower the misalignment σ_τ^2 the larger $\Delta\mathcal{R}_\mathcal{F}$, which implies higher EIGDR differences between fibrotic, $\mathcal{R}_\mathcal{F}$, and healthy, $\mathcal{R}$, tissue. This justifies the advantage of pre-aligning u-EGMs in the cliques before EIGDR computations, since the higher the misalignment σ_τ^2, the lower $\Delta\mathcal{R}_\mathcal{F}$ and consequently the capacity of $\mathcal{R}$ to discriminate between fibrosis and non-fibrosis, suggesting that $\mathcal{R}^\mathcal{A}$ is better suited fibrosis marker than $\mathcal{R}$.

Alternatively, the ratio $\Delta\mathcal{R}^{\mathcal{A}}$ between $\mathcal{R}_{\mathcal{F}}^{\mathcal{A}}$ and $\mathcal{R}_{\mathcal{F}}$, computed in fibrosis from perfectly aligned and misaligned original u-EGMs, respectively, representing the gain in eigenvalue concentration produced by alignment, was also considered:

$$\Delta\mathcal{R}^{\mathcal{A}} = \frac{\mathcal{R}_{\mathcal{F}}^{\mathcal{A}}}{\mathcal{R}_{\mathcal{F}}} \approx \frac{E_s\left(\beta^2\sigma_\tau^2\left(\overline{\alpha}^2+\sigma_\alpha^2\right)E_{s'}+N(\sigma_v^2+\sigma_f^2)\right)}{\left(N(\sigma_v^2+\sigma_f^2)\right)\left(E_s-\beta^2\sigma_\tau^2E_{s'}\right)}. \tag{4.26}$$

This expression has been estimated for the more general case including fibrosis ($\sigma_f^2 > 0$). Nevertheless, it may be computed at cliques on any tissue and its theoretical value when no fibrosis is present can be obtained from (4.26) by setting $\sigma_f = 0$, $\beta = 1$, $\overline{\alpha} = 1$ and $\sigma_\alpha = 0$.

We studied sensitivity of $\Delta\mathcal{R}^{\mathcal{A}}$ to fibrosis by computing the partial derivative of (4.26) with respect to the fibrosis-dependent parameters. Deriving $\Delta\mathcal{R}^{\mathcal{A}}$ with respect to σ_f^2 to see how it evolves with the level of fibrosis, we obtain:

$$\frac{\partial\Delta\mathcal{R}^{\mathcal{A}}}{\partial\sigma_f^2} \approx \frac{-E_sN\beta^2\sigma_\tau^2\left(\overline{\alpha}^2+\sigma_\alpha^2\right)E_{s'}}{\left(N(\sigma_v^2+\sigma_f^2)\right)^2\left(E_s-\beta^2\sigma_\tau^2E_{s'}\right)}. \tag{4.27}$$

For small delays τ_k, $E_s \gg \beta^2\sigma_\tau^2E_{s'}$, thus resulting in $\frac{\partial\Delta\mathcal{R}^{\mathcal{A}}}{\partial\sigma_f^2} < 0$. This implies that $\Delta\mathcal{R}^{\mathcal{A}}$ decreases if fibrosis (expressed by component σ_f^2) increases and suggests that $\Delta\mathcal{R}^{\mathcal{A}}$ can be used as a fibrosis marker, like $\mathcal{R}$ and $\mathcal{R}^{\mathcal{A}}$. This behaviour is also supported by taking into account the u-EGM amplitude reduction occurring in fibrosis, computing the derivative of $\Delta\mathcal{R}^{\mathcal{A}}$ with respect to $\overline{\alpha}^2$:

$$\frac{\partial\Delta\mathcal{R}^{\mathcal{A}}}{\partial\overline{\alpha}^2} = \frac{E_s\beta^2\sigma_\tau^2E_{s'}}{\left(N(\sigma_v^2+\sigma_f^2)\right)\left(E_s-\beta^2\sigma_\tau^2E_{s'}\right)}. \tag{4.28}$$

For small delays τ_k, this expression is > 0, confirming that the larger the fibrosis, (i.e., the smaller $\overline{\alpha}^2$), the smaller $\Delta\mathcal{R}^{\mathcal{A}}$.

However, when computing the derivative of $\Delta\mathcal{R}^{\mathcal{A}}$ with respect to β^2, we obtain:

$$\frac{\partial\Delta\mathcal{R}^{\mathcal{A}}}{\partial\beta^2} \approx \frac{E_s\sigma_\tau^2E_{s'}}{\left(E_s-\beta^2\sigma_\tau^2E_{s'}\right)^2}\left(1+\frac{E_s(\overline{\alpha}^2+\sigma_\alpha^2)}{N(\sigma_v^2+\sigma_f^2)}\right), \tag{4.29}$$

which is > 0 under the same assumptions. This means that the larger the velocity reduction due to fibrosis (i.e., the higher β), the greater $\Delta\mathcal{R}^{\mathcal{A}}$, thus showing an opposite effect.

Nevertheless, as already mentioned before, fibrosis effects on u-EGM amplitude and morphology, expressed by $\overline{\alpha}^2$ and σ_f^2, respectively, are expected to be much more marked than those on conduction velocity conveyed by β^2 [147]. Therefore, we expect the marker $\Delta\mathcal{R}^{\mathcal{A}}$ to get reduced when fibrosis increases.

Following this analysis, three different EIGDR-based markers are sensitive to the presence of fibrosis and therefore eligible to discriminate between F and NF areas: $\mathcal{R}$, $\mathcal{R}^{\mathcal{A}}$, which may be interpreted as measurements of the shape homogeneity of the u-EGMs

before and after time alignment, respectively, and the ratio between them, $\Delta\mathcal{R}^{\mathcal{A}}$.

We computed maps of $\mathcal{R}$, $\mathcal{R}^{\mathcal{A}}$ and $\Delta\mathcal{R}^{\mathcal{A}}$ by processing the complete MEA with two clique sizes (2×2 and 3×3). Each map consists of color-coded pixels, each representing the EIGDR ratio value at each clique. The 2×2 configuration provides one EIGDR value for each square group of four electrodes numbered like (i,j), $(i+1,j)$, $(i,j+1)$ and $(i+1,j+1), i,j \in \{1,\ldots,14\}$, from left to right and from bottom to top, as already done in chapter 3, and resulting in 14×14 pixel maps for $\mathcal{R}$, $\mathcal{R}^{\mathcal{A}}$ and $\Delta\mathcal{R}^{\mathcal{A}}$. The 3×3 configuration provides one EIGDR value at each squared group of nine electrodes with diagonal vertices at (i,j) and $(i+2,j+2)$, $i,j \in \{1,\ldots,13\}$, resulting in maps of 13×13 pixels, for each proposed marker.
Voltage maps based on the peak-to-peak amplitudes $V_{i,j}^{b\text{-}x}$ and $V_{i,j}^{b\text{-}y}$ of the b-EGMs in each of the two MEA directions, $b_{i,j}^{x}(n)$, $i \in \{1,\ldots,14\}$, $j \in \{1,\ldots,15\}$, and $b_{i,j}^{y}(n)$, $i \in \{1,\ldots,15\}$, $j \in \{1,\ldots,14\}$, as well as on their maximum $V_{i,j}^{b\text{-}m} = \max\{V_{i,j}^{b\text{-}x}, V_{i,j}^{b\text{-}y}\}$, $i \in \{1,\ldots,14\}$, $j \in \{1,\ldots,14\}$, were also computed and considered for fibrosis detection, comparing their performance to EIGDR maps. Each bipolar map shows the same resolution as 2×2 cliques EIGDR maps, providing 14×14 color-coded pixels, representing peak-to-peak amplitude values, when processing the whole MEA.

4.3.5 Effect of Variable Electrode-to-Tissue Distance

In order to introduce the effect of variable electrode-to-tissue distance, the signal model in (4.8) has to be modified by replacing $s(n)$ with $\mu_k s(n)$, where μ_k is a random variable having mean $\overline{\mu}=1$ and variance σ_μ^2 indexing all the $\mu_{i,j}$ within the clique. Similar analysis as in previous subsections led to:

$$\mathcal{R}^{\mathcal{A}} \approx \frac{E_s(1+\sigma_\mu^2)}{N\sigma_v^2} \quad , \quad \mathcal{R}_{\mathcal{F}}^{\mathcal{A}} \approx \frac{E_s(1+\sigma_\mu^2)}{\frac{N(\sigma_v^2+\sigma_f^2)}{\left(\overline{\alpha}^2+\sigma_\alpha^2\right)}}, \tag{4.30}$$

which differ from the ratios in (4.11) and (4.18) only for the multiplying factor, $(1+\sigma_\mu^2)$, equal in both equations. Therefore, the fibrosis identification ability of $\mathcal{R}^{\mathcal{A}}$ biomarker is preserved. This occurs in contrast to b-EGM peak-to-peak marker, $V_{i,j}^{b}$, which is greatly and randomly modified by the variable electrode-to-tissue distance at each electrode, thus reducing its ability as a stratification marker.

Analogously, in case of not previously aligned u-EGMs:

$$\mathcal{R} \approx \frac{(E_s-\sigma_\tau^2 E_{s'})(1+\sigma_\mu^2)}{\sigma_\tau^2 E_{s'}(1+\sigma_\mu^2)+N\sigma_v^2}, \tag{4.31}$$

$$\mathcal{R}_{\mathcal{F}} \approx \frac{(E_s-\beta^2\sigma_\tau^2 E_{s'})(1+\sigma_\mu^2)}{\beta^2\sigma_\tau^2 E_{s'}(1+\sigma_\mu^2)+\frac{N(\sigma_v^2+\sigma_f^2)}{\left(\overline{\alpha}^2+\sigma_\alpha^2\right)}}, \tag{4.32}$$

which approximately result in the same multiplying factor $(1+\sigma_\mu^2)$ if compared to ratios (4.15) and (4.21). For small σ_τ, $N\sigma_v^2 >> \sigma_\tau^2 E_{s'}$ and then the approximation of a multiplying factor relating fixed with variable electrode-to-tissue distance holds. This also shows that $\mathcal{R}$ is expected to maintain the fibrosis identification ability in situations where electrode-to-tissue distance may vary. The same analysis also applies to the ratio $\Delta\mathcal{R}^{\mathcal{A}}$.

It should also be noted that in presence of more complex fibrillatory propagation patterns, electrode-to-electrode changes occurring in the u-EGM morphology can initially be thought of as due to a planar wave propagating in different directions. This can be expressed by introducing a k-dependent signal, $s_k(n-\tau_k)$, where $k \in \{1,\ldots,K\}$, $K \in \{4,9\}$, in the model of (4.8), which depending on the angle of the planar wave, again would not largely affect the EIGDR strategy.

4.3.6 Evaluation of Atrial Fibrosis Discrimination Performance

In order to assess the noise sensitivity and atrial fibrosis identification performance of both EIGDR and bipolar mapping strategies considered in this study, the three different simulated MEA orientations have been aggregated. By doing that, the assessment takes into account that, in a realistic scenario, the relative angle of the propagation direction with respect to the catheter is not known a priori.

We used ROC curves to quantitatively assess the ability of the different maps in discriminating pixels associated to the fibrotic patch from those related to non-fibrotic tissue, as performed in chapter 3 for bipolar and omnipolar maps. For that purpose, we created two ground-truth masks, with the resolution of 14×14 and 13×13 maps, following two different approaches. In the first analysis, they were obtained by labeling whether a clique (or an electrode pair in case of bipolar maps) lies within the F or the NF area. The 14×14 ground-truth mask was created by assigning value 1 if the four electrodes within a 2×2 clique lie in the fibrotic area, and value 0 if the four electrodes lie in the non-fibrotic area. In a similar way, the 13×13 ground-truth mask was created by considering if the nine electrodes within a 3×3 clique fully lie or not in fibrotic/non-fibrotic tissue. Cliques with some electrodes inside and some outside the fibrotic patch were not classified and therefore not taken into account in the evaluation. These two ground-truth masks are shown in Fig. 4.1 (a) and (b), for evaluating 14×14 maps (both EIGDR and bipolar) and 13×13 maps, respectively.

Then, in a further analysis, two binary 14×14 and 13×13 ground-truth masks including those mixed cliques with electrodes inside and outside fibrotic tissue were considered for the evaluation. In this case, we labelled as F those cliques whose central point laid within the fibrotic patch. On the contrary, cliques were classified as NF when their centers were outside the fibrotic patch. For each EIGDR and b-EGM based mapping strategy, ROC curves were computed by varying the threshold for fibrosis identification, obtaining sensitivity and specificity in the detection of the fibrotic area [133], see subsection 3.3.3.5.

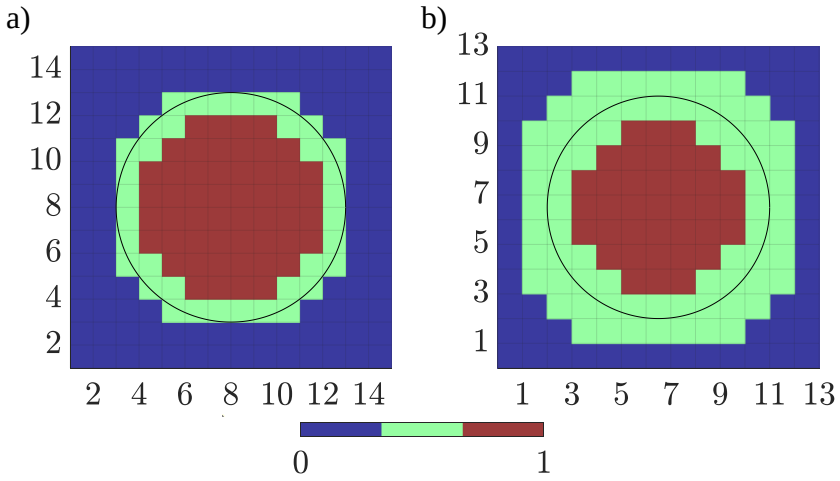

Figure 4.1: (a) 14×14 and (b) 13×13 ground-truth masks for evaluating fibrosis detection ability of maps performed with 2×2 and 3×3 cliques, respectively. Green squares represent the pixels corresponding to cliques with some electrodes inside and some outside the fibrotic patch, i.e. those cliques lying in the border separating the fibrotic patch from non-fibrotic tissue, which were excluded from the evaluation.

In this context, as already done with bipolar and omnipolar maps, *true positive* denotes the number of cliques correctly identified as F, *false negative* represents the number of missed cliques in the F area, *true negative* stands for the number of cliques correctly identified as NF and *false positive* is the number of cliques incorrectly detected as F. The maximum ACC, defined as the highest number of correctly identified cliques (fibrosis or non-fibrosis) divided by the total number of assessed cliques, was used as a measure of the overall fibrosis detection ability of each map. Values of ACC as well as of the threshold corresponding to the maximum ACC (considering the aggregation of the three simulated propagation directions), were computed for each map evaluated in this work. Averaged results over the noisy realizations were then computed and evaluated for performance measurements.

4.4 Results

An example of the mapping strategies (computed with 3×3 cliques) when $\Psi = 45°$, with variable electrode-to-tissue distance and without noise, is shown at upper panels of Fig. 4.2 (a) and (b), for EIGDR ($\mathcal{R}$, $\mathcal{R}^{\mathcal{A}}$, $\Delta\mathcal{R}^{\mathcal{A}}$) and bipolar ($V^{b\text{-}x}$, $V^{b\text{-}y}$, $V^{b\text{-}m}$) maps, respectively. One of the two thousand noisy realizations for noise level of $\sigma_v = 46.4\ \mu V$ is presented at Fig. 4.2 (c) and (d), for the same kind of maps. The fibrotic area which came out by using the threshold that maximizes the ACC for each mapping strategy is displayed in the corresponding lower panels. Blue (brown) pixels inside the circle encompassing fibrotic patch denote false negative (true positive) values, while outside denote true negative (false positive) detection, respectively.

Values of $\mathcal{R}$, $\mathcal{R}^{\mathcal{A}}$ and $\Delta\mathcal{R}^{\mathcal{A}}$ computed from noisy ($\sigma_v = 46.4\ \mu V$) u-EGMs in the non-

fibrotic clique $(i, j) = (3, 3)$ have been included: $\mathcal{R} = 3.39$, $\mathcal{R}^{\mathcal{A}} = 7.76$ and $\Delta\mathcal{R}^{\mathcal{A}} = 2.29$, as well as in the fibrotic clique $(i, j) = (8, 7)$: $\mathcal{R} = 1.36$, $\mathcal{R}^{\mathcal{A}} = 2.44$ and $\Delta\mathcal{R}^{\mathcal{A}} = 1.79$, showing to be consistent with the models presented in subsection 4.3.4.

These illustrative results revealed that EIGDR maps performed from noise-free and time-aligned u-EGMs, $\mathcal{R}^{\mathcal{A}}$ and $\Delta\mathcal{R}^{\mathcal{A}}$, plotted at central and rightmost columns in Fig. 4.2 (a), respectively, present fibrosis detection performance comparable to bipolar maps obtained as the maximum voltage of both MEA directions, $V^{b\text{-}m}$, shown at rightmost column in Fig. 4.2 (b). Nevertheless, when u-EGMs are affected by noise, EIGDR based maps (upper row at Fig. 4.2 (c)) are more robust than b-EGMs maps (upper row at Fig. 4.2 (d)), with $\mathcal{R}^{\mathcal{A}}$ showing the best fibrosis discrimination performance.

Table 4.2 summarizes ACC values of all mapping strategies considered in this study, assuming fixed or variable distance between MEA and tissue, and five different noise levels (reported as both SD values σ_v and average peak-to-peak amplitudes $\overline{V}_{pp,v}$). Thresholds having these maximum ACC values were reported for each map in Table 4.3, where they were given in voltage units in case of b-EGM amplitude based maps. Both ACC and threshold values reported in tables were computed by assuming as ground truth masks the ones which exclude borderline cliques. Moreover, these values were computed and reported by aggregating the three MEA orientations with respect to the propagation direction. Despite this, bipolar voltage maps performance strongly depend on the relative orientation between catheter and propagation direction (e.g., ACC = 68.7% and ACC = 90.8% for $V^{b\text{-}x}$ and $V^{b\text{-}y}$, respectively, for fixed catheter-to-tissue distance and $\sigma_v = 0.0$ μV). For $\sigma_v = 46.4$ μV, $V^{b\text{-}y}$ and $V^{b\text{-}m}$ are more affected by noise than EIGDR maps, both for fixed and variable electrode-to-tissue distance.

The selection of the thresholds for the EIGDR maps requires the following observation. Values reached by $\mathcal{R}^{\mathcal{A}}$ at healthy tissue (4.11) can be obtained as the ratio between the estimated energy $\hat{E}_s$ and N times the estimate of the noise variance $\hat{\sigma}_v^2$, $\hat{\mathcal{R}}^{\mathcal{A}} = \hat{E}_s/(N\hat{\sigma}_v^2)$. The value of $\hat{E}_s$ can be estimated from the data (e.g. by averaging the energy of the u-EGMs in the clique), while the noise variance $\hat{\sigma}_v^2$ can be estimated as the u-EGM variance in areas electrically silent. According to the model, the threshold, $\mathcal{T}$, could be fixed to a value $\mathcal{T} = \hat{E}_s/(N\hat{\sigma}_v^2) - \Delta$, where Δ will control the relationship between required sensitivity and specificity: small Δ will provide high sensitivity and low specificity, while large Δ will provide the reverse. Note that from results reported above and referring to Fig. 4.2, for a NF site such as $(i, j) = (3, 3)$ with noise $\sigma_v = 46.4\mu V$, we measured $\hat{\mathcal{R}}^{\mathcal{A}} = 7.76$, while the optimum threshold reported in Table 4.3 for this noise level is 3.5, corresponding to a $\hat{\Delta} = 4.26$, which can be taken as a reference value. Similar analysis for the same noise level gives Δ values estimates of 1.7 for $\mathcal{R}$ and 0.39 for $\Delta\mathcal{R}^{\mathcal{A}}$, as quantities to subtract to the estimates of $\hat{\mathcal{R}}$ and $\hat{\Delta}\mathcal{R}^{\mathcal{A}}$ at NF areas to derive usable threshold values in real clinical settings. These estimates will require additional estimates of the $\hat{\sigma}_\tau$ and $\hat{E}_{s'}$, see equations (4.15) and (4.26), which can be computed e.g. from the SD of estimated delays in a clique and from the derivative of the aligned and averaged u-EGMs

in the clique, respectively.

Bipolar voltage map $V^{b\text{-}m}$ identifies the fibrotic area with a maximum ACC of 96.2% when distance between MEA and tissue is fixed and u-EGMs are not affected by noise ($\sigma_v = 0.0\ \mu V$). However, this performance decreases to ACC = $92.5 \pm 1.1\%$ when the electrode-to-tissue distance is variable, and further when noise is added, reaching values $86.9 \pm 1.1\%$ and $86.1 \pm 1.2\%$ for the highest noise level ($\sigma_v = 46.4\ \mu V$), in case of fixed and variable electrode-to-tissue distance, respectively. On the other hand, $\mathcal{R}^{\mathcal{A}}$ performed with 3×3 cliques is more robust to the effect of variable distance than $V^{b\text{-}m}$, presenting ACC = 92.1% and ACC = $92.3 \pm 0.8\%$ for fixed and variable catheter-to-tissue distance, respectively. In addition, it achieves ACC = $94.2 \pm 1.6\%$ when $\sigma_v = 46.4\ \mu V$, for both fixed and variable distance scenarios, being consistent with example in Fig. 4.2. The same behaviour has been observed when studying the three MEA orientations separately. For the highest noise level under test, and with 3×3 cliques, $\mathcal{R}^{\mathcal{A}}$ achieves greater ACC values than $V^{b\text{-}m}$. In detail, $\mathcal{R}^{\mathcal{A}}$ reaches 95 ± 2%, 95 ± 3%, and 95 ± 3% for $\Psi = 0°$, 30°, and 45°, respectively, both with fixed and variable electrode-to-tissue distances, while $V^{b\text{-}m}$ reaches 88 ± 2%, 89 ± 2%, and 90 ± 2% with fixed distance, and 87 ± 2%, 88 ± 2% and 89 ± 2%, with variable distance, for $\Psi = 0°$, 30°, and 45°, respectively. If the evaluation is performed without exclusion of cliques which have electrodes inside and outside the fibrotic patch, $\mathcal{R}^{\mathcal{A}}$ still provides higher ACC (83.0 ± 1.5%) than $V^{b\text{-}m}$ (81.2 ± 1.21%), in the case of the highest noise level and with variable electrode-to-tissue distance. Moreover, in a noiseless setting, maximum ACC of $\mathcal{R}^{\mathcal{A}}$ goes from 80.2 % to 80.1 ± 0.6 % when variable instead of fixed electrode-to-tissue distance is considered, while ACC of $V^{b\text{-}m}$ reduces from 90.8 % to 87.2 ± 1.0 % in the same situation.

Table 4.2: Maximum ACC of EIGDR and bipolar amplitude maps, reported jointly for the three MEA orientations and different scenarios, with fixed (FD) or variable (VD) electrode-to-tissue distance, corrupting u-EGMs with noise levels $\sigma_v \in \{0.0, 5.8, 11.6, 23.2, 46.4\}\ \mu V$ ($\overline{V}_{pp,v} \in \{0.0, 24.2, 48.4, 96.7, 193.5\}\ \mu V$). ACC values are presented as mean ± SD except for fixed electrode-to-noise distance and $\sigma_v = 0.0\ \mu V$ ($\overline{V}_{pp,v} = 0.0\ \mu V$).

Fibrosis marker	Map	ACC (%)									
		Fixed electrode-to-tissue distance (FD)					Variable electrode-to-tissue distance (VD)				
		Noise level σ_v ($\overline{V}_{pp,v}$) μV					Noise level σ_v ($\overline{V}_{pp,v}$) μV				
		0.0 (0.0)	5.8 (24.2)	11.6 (48.4)	23.2 (96.7)	46.4 (193.5)	0.0 (0.0)	5.8 (24.2)	11.6 (48.4)	23.2 (96.7)	46.4 (193.5)
u-EGM EIGDR 2 × 2 clique	$\mathcal{R}$	74.0	74.7±0.7	77.0 ± 0.9	81.1±1.2	83.3±1.6	73.2±1.0	74.1±1.0	76.4±1.1	80.9±1.2	83.3 ± 1.6
	$\mathcal{R}^{\mathcal{A}}$	86.2	85.2±0.9	85.7±1.2	87.2±1.3	86.3±1.6	85.0±0.8	84.5±1.0	85.4±1.2	87.1±1.3	86.2±1.6
	$\Delta\mathcal{R}^{\mathcal{A}}$	76.8	79.8±1.0	82.7±1.3	84.4±1.5	79.4±1.8	75.5±1.0	78.9±1.2	82.0±1.3	83.7±1.6	78.7±1.9
u-EGM EIGDR 3 × 3 clique	$\mathcal{R}$	78.4	78.4±0.2	78.5±0.4	82.7±1.4	87.9±2.1	78.1±0.4	78.1±0.4	78.4±0.6	82.6±1.4	87.9±2.1
	$\mathcal{R}^{\mathcal{A}}$	92.1	91.8±1.2	92.2±1.4	94.0±1.4	94.2±1.6	92.3±0.8	91.9±1.2	92.3±1.4	94.0±1.4	94.2±1.6
	$\Delta\mathcal{R}^{\mathcal{A}}$	93.1	91.8±1.3	91.4±1.6	91.2±1.8	84.0±2.5	93.0±0.9	91.6±1.4	91.2±1.7	90.8±1.9	83.6±2.6
b-EGM amplitude	$V^{b\text{-}x}$	68.7	68.8±0.1	68.8±0.1	68.8±0.1	68.8±0.2	68.7±0.0	68.8±0.1	68.8±0.2	68.8±0.2	68.9±0.2
	$V^{b\text{-}y}$	90.8	90.9±0.3	90.9±0.4	88.7±0.7	82.5±1.0	86.8±1.0	86.9±1.0	87.3±1.0	86.5±1.0	81.6±1.1
	$V^{b\text{-}m}$	96.2	96.2±0.3	96.1±0.4	93.4±0.7	86.9±1.1	92.5±1.1	92.6±1.1	92.8±1.0	91.6±1.0	86.1±1.2

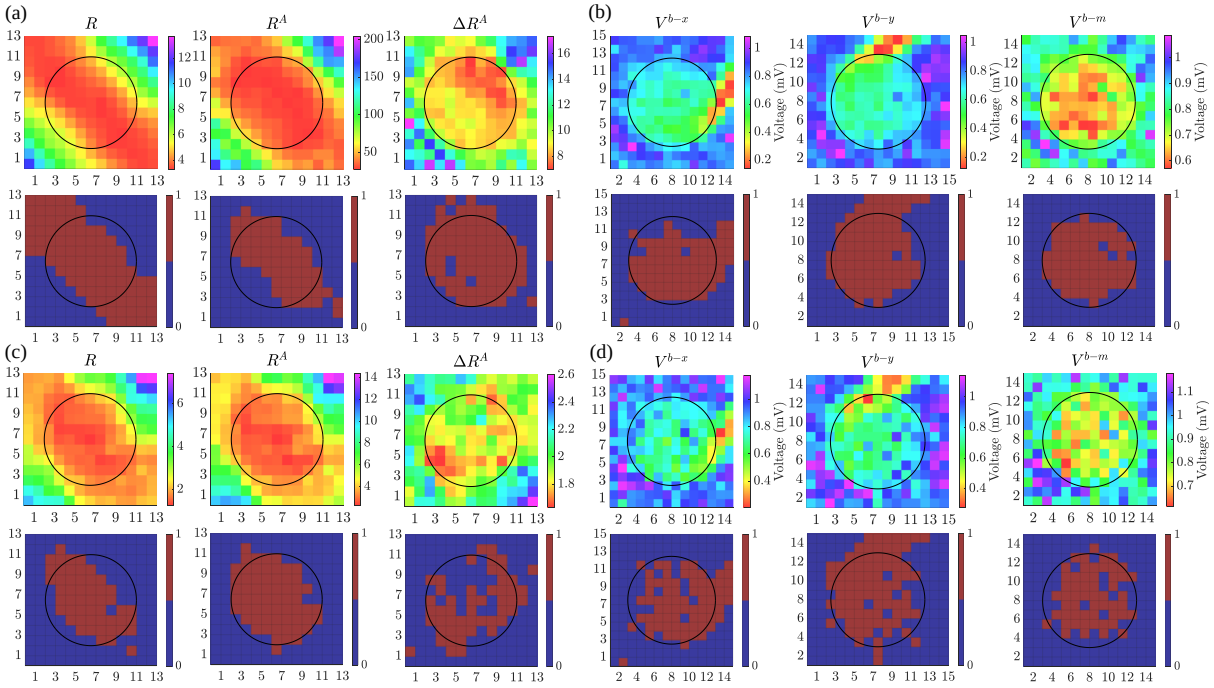

Figure 4.2: Upper panels: maps of $\mathcal{R}$, $\mathcal{R}^{\mathcal{A}}$, $\Delta\mathcal{R}^{\mathcal{A}}$ from 3×3 cliques and bipolar voltage maps $V^{b\text{-}x}$, $V^{b\text{-}y}$, $V^{b\text{-}m}$, for $\Psi = 45°$, performed assuming a variable electrode-to-tissue distance and noise free ((a) and (b)) and noisy ((c) and (d), with noise level $\sigma_v = 46.4$ μV) u-EGMs. Lower panels: detected fibrotic areas (brown), using the thresholds that maximize detection accuracy of each map.

Table 4.3: Thresholds corresponding to the ACC values reported in Table 4.2, presented as mean ± SD except for fixed electrode-to-noise distance and $\sigma_v = 0.0$ μV ($\overline{V}_{pp,v} = 0.0$ μV). Note that thresholds are expressed in adimensional units (a.u.) for $\mathcal{R}$, $\mathcal{R}^{\mathcal{A}}$ and $\Delta\mathcal{R}^{\mathcal{A}}$ and in mV for $V^{b\text{-}x}$, $V^{b\text{-}y}$ and $V^{b\text{-}m}$.

Fibrosis marker	Map	Threshold									
		Fix electrode-to-tissue distance (FD)					Variable electrode-to-tissue distance (VD)				
		Noise level σ_v ($\overline{V}_{pp,v}$) μV					Noise level σ_v ($\overline{V}_{pp,v}$) μV				
		0.0 (0.0)	5.8 (24.2)	11.6 (48.4)	23.2 (96.7)	46.4 (193.5)	0.0 (0.0)	5.8 (24.2)	11.6 (48.4)	23.2 (96.7)	46.4 (193.5)
u-EGM EIGDR 2 × 2 clique (a.u.)	$\mathcal{R}$	7.5	7.3±0.1	6.7±0.2	5.1±0.2	2.7±0.1	7.8 ± 0.5	7.5±0.4	6.8±0.2	5.1±0.2	2.7±0.1
	$\mathcal{R}^{\mathcal{A}}$	86.8	69.1±3.3	39.3±2.1	14.5±0.7	4.3±0.2	87.3±2.9	67.7±3.4	38.7±2.1	14.4±0.7	4.3±0.2
	$\Delta\mathcal{R}^{\mathcal{A}}$	9.1	7.5±0.3	4.9±0.2	2.5±0.1	1.5±0.0	9.1±0.7	7.4±0.3	4.9±0.2	2.5±0.1	1.5±0.0
u-EGM EIGDR 3 × 3 clique (a.u.)	$\mathcal{R}$	4.7	4.7±0.1	4.2±0.3	2.8±0.1	1.7±0.1	4.7±0.1	4.6±0.1	4.1±0.4	2.8 ± 0.2	1.7±0.1
	$\mathcal{R}^{\mathcal{A}}$	36.9	32.1±1.0	23.1±0.8	10.7±0.4	3.5±0.1	36.1±0.6	31.8±1.0	22.9±0.8	10.7±0.4	3.5±0.1
	$\Delta\mathcal{R}^{\mathcal{A}}$	9.8	8.6±0.2	6.4±0.1	3.5±0.1	1.9±0.0	9.7±0.2	8.6±0.2	6.4±0.1	3.5±0.1	1.9±0.0
b-EGM amplitude (mV)	$V^{b\text{-}x}$	0.01	0.02±0.00	0.03±0.01	0.05±0.02	0.11±0.05	0.01±0.00	0.02±0.01	0.04±0.01	0.07±0.02	0.12±0.05
	$V^{b\text{-}y}$	0.76	0.76±0.00	0.76±0.00	0.79±0.01	0.84±0.02	0.76±0.01	0.76±0.01	0.77±0.01	0.79±0.01	0.84±0.02
	$V^{b\text{-}m}$	0.76	0.76±0.00	0.76±0.00	0.79±0.01	0.86±0.02	0.76±0.01	0.76±0.01	0.77±0.01	0.79±0.01	0.86±0.02

4.5 Discussion

4.5.1 Clinical Significance of the Work

As widely discussed in chapter 1 and repeatedly taken up in the course of this thesis, atrial fibrosis detection is capital to guide catheter ablation strategies in AF. The typical atrial fibrosis assessment based on bipolar voltage thresholding presents well-established limitations due to catheter-wavefront orientation, catheter-tissue contact, electrodes size

and interelectrode spacing, thus limiting its reliability as surrogate of fibrosis. Besides this, it is well-known that when using this kind of approach, information about EGM morphology and time relationship among adjacent electrodes are missing. In addition, despite the fact that LGE-MRI is the only non-invasive technique to diagnose atrial fibrosis, its reproducibility is still a matter of debate [148], as well as its utility in clinical practise [139].

In this chapter, we proposed u-EGMs eigenvalue dominance ratios (EIGDR) to quantify dispersion of voltage waveform and investigated their performance as markers in discriminating between F and NF areas, by using a 2D simulated tissue including diffuse fibrosis. The hypothesis behind this approach is that underlying fibrosis in the atrium is reflected not only in the decrease of the waveform amplitude but also in the increased intersignal dispersion in cliques of nearby electrodes, and that this dispersion is essentially insensitive to electrode-to-tissue distance unlike b-EGM amplitudes.

4.5.2 Performance Evaluation of Fibrosis Markers

We considered maps computed both from noise-free u-EGMs and from u-EGMs corrupted by homogeneous noise levels. At first, the distance between each electrode of a square MEA and tissue was assumed to be fixed at 1 mm. Then, in a second step, that distance was assumed to be variable following a normal distribution among the electrodes of catheter, so as to better approach the real situation where the perfect contact cannot be guaranteed during the mapping procedure.

Results obtained have revealed that reducing the time misalignment among u-EGMs within the clique improves fibrosis detection ability of the proposed EIGDR-based marker. This is consistent with other studies where time alignment of b-EGMs has shown to be advantageous for electroanatomical mapping strategies robustness [64]. The biomarker $\mathcal{R}^{\mathcal{A}}$ has provided comparable fibrosis detection accuracy to that of maximum bipolar voltage maps when u-EGMs are free from noise, and better performance when high noise levels are present ($\sigma_v \geq 23.2\ \mu V$), for both fixed and variable electrode-to-tissue distances, if cliques having some electrodes inside and some outside the fibrosis patch are excluded from the evaluation.

Mapping strategies have been evaluated by considering the three MEA orientations separately and also by joining them to better reproduce a real clinical scenario, returning consistent results in both situations. They reinforce the choice of $\mathcal{R}^{\mathcal{A}}$ as an index to be analyzed in extended future studies using clinical signals, for discriminating between F and NF areas. Moreover, the analysis conducted by considering separately the three different catheter orientations has also pointed out the greater impact of MEA orientation on bipolar amplitudes than on EIGDR based measurements.

If the evaluation is performed by including those cliques with electrodes inside and outside the fibrotic patch, similar conclusions, although with reduced difference ranges,

can be drawn. The ratio $\mathcal{R}^{\mathcal{A}}$ still shows higher ACC in the situation with the largest noise and with variable electrode-to-tissue distance. In addition, EIGDR-based markers revealed to be more robust to the variable distance effect than b-EGMs based maps, particularly when u-EGMs are not corrupted by noise.

Our findings also revealed that the threshold values needed to maximize accuracy of bipolar maps $V^{b\text{-}y}$ and $V^{b\text{-}m}$ are greater than the one typically used in clinical settings (0.5 mV), whereas $V^{b\text{-}x}$ presents lower voltage threshold. This is explained by the absence of wavefront propagation projection along the x-axis of the MEA when propagation orientation is $\Psi = 0°$.

4.6 Limitations

In this chapter, a single scenario reproducing a simple propagation pattern in a 2D atrial model has been simulated, which greatly simplifies the real 3D anatomical and electrophysiological situations.

Although a single plane wavefront that propagates in a homogeneous tissue lends itself well to approximating the propagation during pacing, these considerations do not allow to extend quantitatively the results to other propagation patterns (including circular waves, wave collisions, reentrant wave fronts, among others) and model conditions (including conduction anisotropy or patchy fibrosis).

However, despite the fact that the underlying propagation pattern strongly influences EGMs morphology and their spatiotemporal information, we expect that it does not largely affect the local EIGDR computation. This is because we hypothesize that the correlation between the presence of fibrosis and the signal morphology dispersion in electrode cliques is well modeled by a waveform assumed to be locally plane and homogeneous, independently from the global waveform distribution across the entire tissue. For the same reasons, we hypothesized that the EIGDR approach would not be largely affected by the shape and size of the fibrotic patch. In addition, the proposed intraclique time alignment of the u-EGMs compensates the effect of different u-EGM arrival times on EIGDR, leaving the EIGDR to mostly represent spatial relationships differences among u-EGMs within each clique.

In this work, only the effect of broad-band noise affecting u-EGMs was considered, while specific periodic types of noise were not discussed. It must be noted that far-field disturbances due to ventricular depolarization do not occur during atrial activation in SR.

4.7 Conclusion

In this chapter, we demonstrated that mapping strategies based on the EIGDR method are able to discriminate F from NF tissue. For low noise levels and assuming both fixed

and variable distance between the electrode grid and the tissue, they attain comparable performance to map obtained by combining the b-EGMs amplitudes along the two directions of the MEA. Nevertheless, they outperform bipolar maps when facing higher noise levels. In addition, maps of 3×3 electrode cliques outperform the ones with 2×2 cliques and fibrosis detection benefits from the previous time-alignment of u-EGMs, leading us to suggest $\mathcal{R}^{\mathcal{A}}$ as EIGDR biomarker for fibrosis discrimination in similar cases.

Chapter 5

Clinical Impact of the Eigenvalue Dominance Ratio Method for Fibrosis Identification

5.1 Introduction

In chapter 4, three atrial fibrosis markers based on u-EGM eigenvalue dispersion were introduced, with the aim of overtaking limitations affecting the standard fibrosis detection. Resulting maps have been tested in simulation scenarios including noise and variable electrode-tissue distance, showing better performance than that of bipolar voltage maps when u-EGMs are previously time-aligned. In this chapter, the proposed strategy has been tested with real data from different clinical settings, so as to further support the ability of the EIGDRs as fibrosis markers. It has been initially tested in u-EGMs recorded with the multielectrode PentaRay® catheter, at fibrotic and non-fibrotic areas over 3D electroanatomical maps of several patients. Then, the effect of catheter geometry on the resulting EIGDR values has been assessed by using the PentaRay® catheter and the MEA sensor at specific positions in non-fibrotic tissue from a single patient. Finally, single-beat and multibeat analysis based on the EIGDR methodology were conducted in a MEA catheter.

5.2 Discrimination of Fibrotic from Non-Fibrotic Tissue Areas Based on the EIGDR Method

5.2.1 Methods

In a first analysis, the ability of the EIGDR methodology in distinguishing F from NF areas has been assessed by using the intracavitary u-EGMs recorded with the PentaRay® catheter and introduced in subsection 2.1.1. In the same subsection, the signal acquisition

and co-register of EAM data and MRI have been described in detail. Performance of the EIGDR-based markers was evaluated selecting 38 catheter positions by an operator-dependent visual approach in each case. Specifically, nineteen points clearly assignable to F and another nineteen points to NF areas have been visually identified and manually annotated on the anatomic map of each patient. In order to guide this decision, the corresponding MRI has been used as reference.

Unipolar signals were high-pass filtered with 30 Hz cut-off frequency, using a third order Butterworth infinite impulse response filter, so as to reduce artefacts and emphasize more rapid components. An example of filtered u-EGMs at two different mapping points marked on the anatomical 3D mesh of the LA of one of the considered cases is presented in Fig. 5.1, where the atrial activation was plotted.

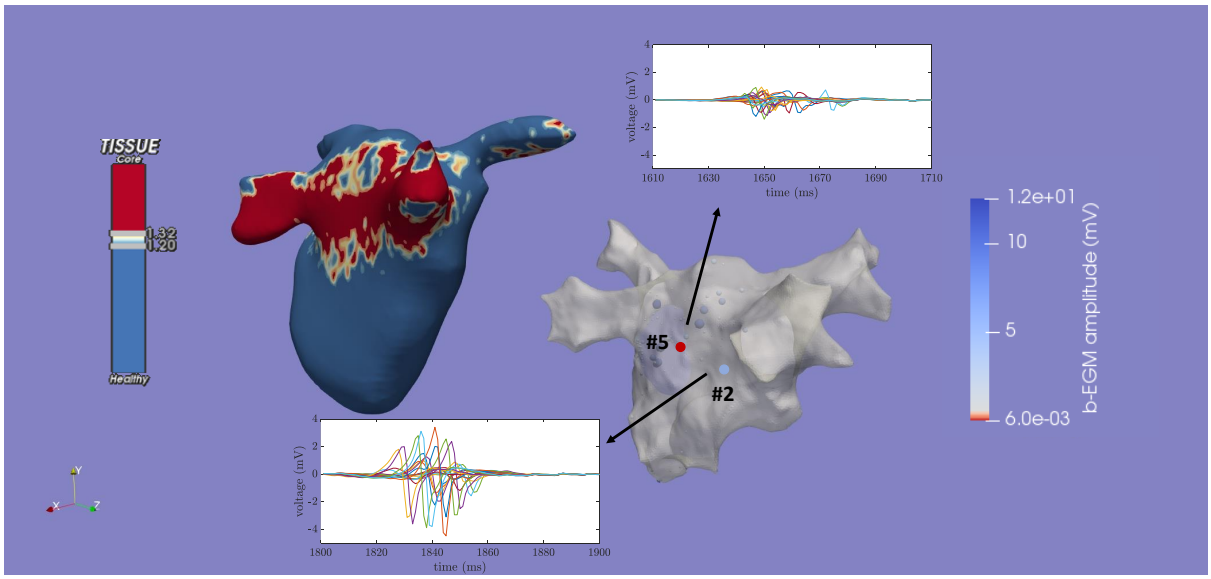

Figure 5.1: 3D reconstruction of the LA geometry (grey mesh) of one of the cases considered and corresponding co-registered MRI, showing the different regional distribution patterns of gadolinium (red areas: latest contrast enhancement, blue areas: absence of latest contrast enhancement). In the geometrical mesh, two of the mapping points acquired and considered in the analysis (point #5 at fibrosis, point #2 at non-fibrosis) are marked and color-coded according to their corresponding bipolar peak-to-peak amplitude. For each of them, the atrial activation windows extracted from the twenty filtered u-EGMs recorded with the PentaRay® catheter are also displayed.

At each catheter position, u-EGMs were considered in the following five four-electrode cliques, according to the pole numbering in Fig. 5.2: (3,4,7,8), (7,8,11,12), (11,12,15,16), (15,16,19,20), (19,20,3,4) and the central five-electrode clique (4,8,12,16,20), for their smaller interelectrode spacing, so as to compute resulting values of $\mathcal{R}$, $\mathcal{R}^{\mathcal{A}}$ and $\Delta\mathcal{R}^{\mathcal{A}}$. As example, cliques (3,4,7,8) and (4,8,12,16,20) are depicted in blue and orange in Fig. 5.2. In order to quantify the atrial activity related dispersion, an atrial depolarization window

of 100 ms fixed length ($N = 100$ samples) was extracted from the u-EGM at each recording site. Therefore, the proposed EIGDR-based markers were calculated using windowed signals within each clique, aligning them when required as explained in subsection 4.3.2.

In a second analysis, the same u-EGMs recorded with the PentaRay® catheter from fourteen out of the fifteen patients were used to quantitatively evaluate the overall ability of the different EIGDR and bipolar amplitude based indices to discriminate F and NF areas. More in detail, markers maps were created by computing $\mathcal{R}$, $\mathcal{R}^{\mathcal{A}}$, $\Delta\mathcal{R}^{\mathcal{A}}$, V^b and V^{b-m} at each clique (with four electrodes) of each available catheter position (see Fig. 5.2), where V^b and V^{b-m} represent the mean and the maximum peak-to-peak amplitude between the two b-EGMs available along the catheter splines in the clique, respectively. These b-EGMs recorded along the longitudinal directions of the PentaRay® are the only ones recorded by the catheter and saved by the CARTO® 3 system, and therefore they are the only b-EGMs considered to compute V^b and V^{b-m}. For each patient, mapping points whose recorded u-EGMs presented an activation duration greater than or equal to 30 ms were discarded from the analysis since they were assumed to correspond to ventricular far-field components. In addition, only catheter positions included in a sphere whose center was manually selected near the center of each atrial electroanatomical map were considered for the evaluation, so as to exclude those ones located at the PVs. The latter were not suitable for the analysis since tissue is mainly electrically inactive at PVs, thus acting as far-field component.

Maps obtained for each biomarker in each patient were considered individually in order to assess the discriminant ability of the marker to separate F from NF sites. This assessment was also done jointly for all patients. The five final map types were evaluated with ROC curves computed by varying the threshold for fibrosis identification (where each unique value of the marker was considered as threshold), thus obtaining curves of sensitivity and specificity in the detection of the fibrotic area. For that purpose, ground-truth masks were created with the same resolution as markers maps and where the label of normal or fibrotic tissue was based on the IIR values associated with the electrode pairs highlighted by the CARTO® 3 system. In fact, it must be pointed out that even if all the fifteen b-EGMs that can be recorded at a catheter position are always saved by the EAM, the latter highlights only one b-EGM for each mapping point. Therefore, at each quadrangular clique of each mapping point, the IIR value to be used for the comparison was computed as follows:

- if both b-EGMs recorded with the two electrode pairs involved in the clique were highlighted by the EAM system, the resulting IIR was computed by averaging the two IIR values corresponding to the two bipoles;

- if one of the b-EGMs involved in the clique was not highlighted, resulting IIR for that clique was the single IIR value associated with the only bipole considered by the CARTO® 3 system;

- if both b-EGMs were omitted, the corresponding clique was discarded and not included in the computation of the ground-truth mask. As a result, corresponding EIGDR and bipolar amplitude based markers were also removed by the map;
- if all possible cliques were missing at a catheter position, it was discarded, as well as all the EIGDR and bipolar amplitude based markers that could be computed at that point.

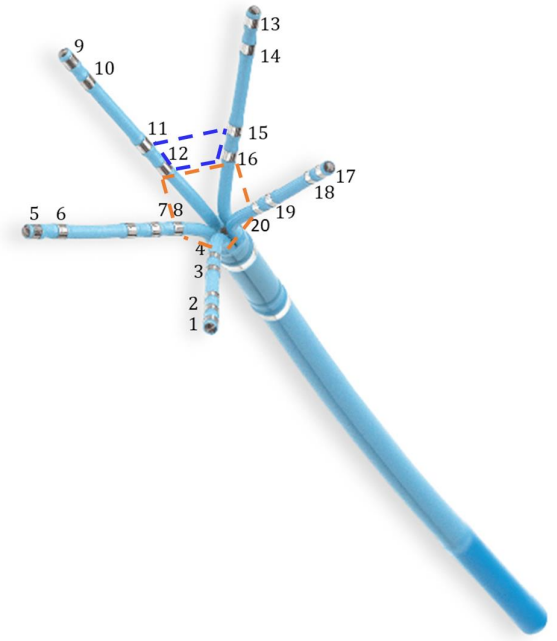

Figure 5.2: The PentaRay® catheter, where the 20 poles are highlighted. Two of the clique distributions considered around each catheter mapping point, with four (dashed blue line) and five (dashed orange line) electrodes, are also pointed out. This image was modified from the Biosense Webster catalog.

A binary ground-truth mask was finally created for each patient by labeling whether the IIR value tells us that the clique lied in F or NF tissue (see also subsection 1.3.5). Value 1 (meaning fibrotic tissue) was assigned to the clique if IIR > 1.20, and value 0 (meaning normal tissue) otherwise. Resulting binary masks were then jointly considered on all patients to evaluate biomarker maps.

In order to compare performance of biomarker maps, specificity was set at 90 % for each of them, and resulting sensitivity (Se) and threshold were calculated, both separately for each patient and also considering all the patients jointly. The biomarkers were computed in EGM windows that completely covered the atrial depolarization for each patient. It should be noted that one of the patients available in the database was not considered in this analysis since it was not possible to select a single time window valid for all mapping points.

In addition, Pearson's ρ_p and Spearman's rank ρ_s correlation coefficients were also computed for each pair of variables studied among IIR, V^{b-m}, $\mathcal{R}$, $\mathcal{R}^{\mathcal{A}}$ and $\Delta\mathcal{R}^{\mathcal{A}}$, so as to

quantify the degree of point-by-point correlation between them, testing the alternative hypothesis of a nonzero correlation. Such analysis was conducted considering biomarker values both on linear and logarithmic scale, as already performed in literature [139] for bipolar voltage values. Two-sided p-values < 0.05 and p-values < 0.001 were considered to indicate statistical significance.

5.2.2 Results

As an illustrative example, table 5.1 shows the median of the different markers $\mathcal{R}$, $\mathcal{R}^{\mathcal{A}}$ and $\Delta\mathcal{R}^{\mathcal{A}}$ computed among the six cliques at nineteen mapping points in F and other nineteen in NF areas for one of the fifteen patients considered in the study. In the same table, median V^b and maximum V^{b-m} bipolar amplitudes among the five innermost bipoles of the PentaRay® are also reported at each catheter site. Medians and interquartile range (IQR) of these values, both for F and NF points, as well as p-values referring to comparison between them, are also shown. Two of the mapping points are depicted in Fig. 5.1. The patient was in cAF, had a slightly dilated LA (26 cm^2), a left ventricular ejection fraction of 58% and was treated with anticoagulation and flecainide. In this case, a total of 758 catheter sites were acquired during SR. It can be observed that median values related to $\mathcal{R}$ and $\mathcal{R}^{\mathcal{A}}$ indices evaluated at NF tissue are greater than their counterparts at F points. When u-EGMs are not previously time aligned, $\mathcal{R}$ shows the following median [IQR] values across sites: 2.45 [0.80] vs. 2.22 [1.47], at NF vs. F points, respectively (Wilcoxon rank-sum test, non-significant). A similar behavior is observed when considering $\mathcal{R}^{\mathcal{A}}$ (7.35 [5.62] vs. 6.18 [4.08]), which revealed to be significantly lower at F than at NF areas (Wilcoxon rank-sum test, p-value < 0.05). Regarding $\Delta\mathcal{R}^{\mathcal{A}}$, median [IQR] values across sites assume greater values at F than at NF areas for this particular case (3.00 [2.78] vs. 2.61 [2.09], Wilcoxon rank-sum test, non-significant). On the other hand, when considering each clique or bipolar measurement independently, without computing the median of indices among cliques or bipoles at each site, as reported in Table 5.2, both EIGDR markers based on the alignment of u-EGMs showed to be significantly greater at NF than their counterparts at F areas, having the following median [IQR] values: 7.42 [6.74] and 2.67 [3.25] vs. 5.85 [5.62] and 2.17 [3.12] for $\mathcal{R}^{\mathcal{A}}$ and $\Delta\mathcal{R}^{\mathcal{A}}$ at NF and F tissue, respectively. These results are consistent with the theoretical model introduced in chapter 4 and overtake fibrosis discrimination performance of V^b (Wilcoxon rank-sum test, p-value < 0.05).

Table 5.3 shows the final median and IQR values of EIGDR markers $\mathcal{R}$, $\mathcal{R}^{\mathcal{A}}$ and $\Delta\mathcal{R}^{\mathcal{A}}$, as well as of median V^b and maximum V^{b^m} amplitudes of b-EGMs resulting from the 19 catheter positions in fibrosis and 19 in non-fibrotic areas for each of the fifteen patients considered. The same table also reports those patients where discrimination between F and NF mapping points is statistically significant (Wilcoxon rank-sum test, p-value < 0.05 and p-value < 0.001). These results show that the $\mathcal{R}^{\mathcal{A}}$ can significantly discriminate

between F and NF in four cases out of fifteen (#4, #5, #7 and #10), as $\Delta\mathcal{R}^{\mathcal{A}}$ (#4, #5, #6 and #13), whereas $\mathcal{R}$ reveals to be a significant fibrosis biomarker in two cases out of fifteen (#8 and #15). On the other hand, bipolar amplitude markers V^b and V^{b-m} are statistically significant in two (#3 and #5) and three (#5, #6 and #13) cases, respectively.

Overall, EIGDR indices outperform bipolar amplitude markers in five cases (#4, #7, #8, #10 and #15), while V^b and V^{b-m} show better performance only in one case (#3). In two cases, #1 and #6, the markers $\Delta\mathcal{R}^{\mathcal{A}}$, V^b and V^{b-m} reveal a similar discrimination power. Finally, in four patients, #2, #9, #11 and #12, no marker has been able to significantly discriminate between F and NF mapping points.

When statistics of EIGDR and bipolar amplitudes are computed considering individually the cliques and the five innermost bipoles, respectively, of all catheter sites, EIGDR markers were able to better distinguish between F and NF tissue in twelve patients out of fifteen, while the reverse occurs only in one case, as reported by results in Table 5.4. This analysis has also been performed considering the individual cliques and the five innermost electrode pairs for all mapping points jointly for the fifteen patients. Resulting median and IQR are shown in the last row of Table 5.4. These results reveal that EIGDR biomarkers based on previous alignment of u-EGMs and V^b show higher values at NF than at F areas, with $\Delta\mathcal{R}^{\mathcal{A}}$ presenting the lowest p-value and therefore the best discrimination power ($4.3e-8$ vs. $5.7e-4$ for $\Delta\mathcal{R}^{\mathcal{A}}$ and V^b, respectively).

Table 5.5 shows the AUC, as well as threshold and Se values corresponding to a specificity of 90 % for each biomarker and for all patients, considering individually each of them and also jointly, where all the resulting maps have been used at the same time to analyze the discrimination ability of each index. Median and IQR values have also been presented for each parameter computed at each patient. The biomarker $\Delta\mathcal{R}^{\mathcal{A}}$ reveals the highest median AUC and Se values (AUC = 0.61 and Se = 0.15, respectively), meaning that it shows the best discrimination power when all the patients are weighted equally. When all the mapping points are weighted equally, bipolar amplitude based biomarkers V^b and V^{b-m} show the highest global AUC (AUC = 0.69), but without achieving Se of $\Delta\mathcal{R}^{\mathcal{A}}$ in this scenario (Se = 0.25 and 0.24, vs. 0.31, respectively).

Analogously, Pearson and Spearman's rank correlation coefficients between IIR and V^{b-m}, $\mathcal{R}$, $\mathcal{R}^{\mathcal{A}}$ and $\Delta\mathcal{R}^{\mathcal{A}}$, as well as between V^{b-m} and EIGDR based biomarkers, computed by patient and also globally among all of the patients, are reported in Table 5.6. In the same table, fibrosis percentage %F, computed as ratio between number of cliques labelled as fibrotic according to the IIR, and the total number of cliques, is also reported, both individually at each case and also jointly. In this correlation analysis, the only bipolar amplitude based index considered was V^{b-m}, since V^b provided similar results and were not presented.

Table 5.1: Median values of EIGDR indices ($\mathcal{R}$, $\mathcal{R}^{\mathcal{A}}$ and $\Delta\mathcal{R}^{\mathcal{A}}$) computed over the six cliques considered for the PentaRay® catheter, median (V^b) and maximum ($V^{b\text{-}m}$) bipolar amplitude computed over the five innermost electrode pairs along the splines of the catheter, at different mapping points, taken at fibrotic (F) and non-fibrotic (NF) areas, respectively, from a patient in SR during the mapping procedure. Median and IQR were also performed among F and NF points, separately.

	# Catheter site	$\mathcal{R}$	$\mathcal{R}^{\mathcal{A}}$	$\Delta\mathcal{R}^{\mathcal{A}}$	V^b (mV)	$V^{b\text{-}m}$ (mV)
F	1	3.42	4.79	1.04	0.04	0.60
	2	6.18	6.18	1.00	0.90	4.46
	3	2.45	4.75	1.95	1.65	3.61
	4	3.25	8.03	2.18	0.10	2.31
	5	1.47	5.35	3.03	1.46	1.63
	6	2.33	6.46	4.22	1.35	1.42
	7	2.22	2.24	1.02	0.16	0.30
	8	2.42	9.52	4.30	0.39	1.53
	9	2.18	7.24	4.17	1.31	3.06
	10	2.19	8.05	4.31	1.30	1.43
	11	3.40	9.92	3.06	0.25	0.50
	12	1.77	16.2	9.83	1.91	3.52
	13	1.56	2.56	1.57	1.01	2.00
	14	2.60	13.4	3.94	0.44	0.51
	15	0.91	2.27	1.83	0.84	3.73
	16	1.05	1.29	1.38	0.45	1.20
	17	1.18	4.90	4.57	1.46	1.89
	18	6.07	6.31	1.00	0.06	0.09
	19	1.80	3.70	3.00	0.37	5.04
	median/IQR	2.22/1.47	6.18/4.08	3.00/2.78	0.84/1.05	1.63/2.66
NF	1	4.54	8.08	2.44	1.42	2.06
	2	1.47	15.4	12.4	3.45	7.93
	3	2.33	6.46	2.61	1.15	1.72
	4	3.63	7.33	1.81	0.22	0.80
	5	2.06	4.62	1.66	1.36	4.51
	6	2.29	7.51	3.29	0.99	2.51
	7	1.51	16.5	9.97	6.90	10.2
	8	1.92	9.69	5.03	0.24	1.43
	9	1.65	6.51	3.14	0.88	1.39
	10	2.69	14.1	4.90	0.46	0.84
	11	2.45	4.75	1.95	1.65	3.61
	12	2.70	5.10	1.86	0.86	2.03
	13	2.95	6.29	1.75	0.14	0.39
	14	4.31	16.5	2.96	0.21	1.54
	15	2.19	7.61	3.54	0.25	1.36
	16	3.17	6.72	1.76	1.10	1.78
	17	2.72	6.11	1.80	1.05	4.02
	18	2.23	12.5	4.03	0.67	2.20
	19	2.61	5.89	2.22	0.27	1.20
	median/IQR	2.45/0.80	7.33/5.62	2.61/2.09	0.88/1.05	1.72/2.09
	p-value*	0.17	0.03	0.26	0.35	0.32

* refers to the comparison of markers between F and NF areas.

Most of correlation coefficients between V^{b-m} and IIR are negative, as expected, ranging from -0.02 to -0.46 among patients. The global correlation is negative, as well (ρ_p = -0.07, ρ_s = -0.12, p-value < 0.001). The same occurs between $\Delta\mathcal{R}^{\mathcal{A}}$ and IIR, where negative correlation coefficients vary from -0.01 to 0.37 and global ρ_s = -0.05 (p-value $<$ 0.001). Conversely, a positive and significant correlation was found when comparing both EIGDR biomarkers based on the time alignment with V^{b-m}, for most patient considered individually and also globally, where $\rho_p = 0.22$ and $\rho_p = 0.36$, $\rho_s = 0.26$ and $\rho_s = 0.49$, for $\mathcal{R}^{\mathcal{A}}$ and $\Delta\mathcal{R}^{\mathcal{A}}$, respectively ($p$-value < 0.001).

Table 5.7 contains correlation coefficients between IIR and the logarithmic values of V^{b-m}, $\mathcal{R}$, $\mathcal{R}^{\mathcal{A}}$ and $\Delta\mathcal{R}^{\mathcal{A}}$, as well as correlation between log-transformed of V^{b-m} and the EIGDR based biomarkers. These results corroborate those reported in Table 5.6 and are consistent with the existing literature [139]. Negative and statistically significant correlations are globally found between $log_{10}(V^{b-m})$ and IIR (ρ_p = -0.19 and ρ_s = -0.12, p-value < 0.001), and between $log_{10}(\Delta\mathcal{R}^{\mathcal{A}})$ and IIR (ρ_p = -0.06 and ρ_s = -0.05, p-value < 0.001). Moreover, global correlation is positive and significant between $log_{10}(\Delta\mathcal{R}^{\mathcal{A}})$ and $log_{10}(V^{b-m})$, as well as between $log_{10}(\Delta\mathcal{R}^{\mathcal{A}})$ and $log_{10}(V^{b-m})$ ($\rho_p = 0.22$ and $\rho_p = 0.49$, $\rho_s = 0.26$ and $\rho_s = 0.49$, respectively). Table 5.8 contains correlation coefficients between the EIGDR based markers computed on linear scale, and $log_{10}(V^{b-m})$, both individually at the single patient and globally considering all the remaining mapping points, as already done in Tables 5.6 and 5.7. A positive and significant correlation exists in most of patients, especially for $\mathcal{R}^{\mathcal{A}}$ and $\Delta\mathcal{R}^{\mathcal{A}}$, which reaches the maximum value ρ_s = 0.75. The same pattern is found in global correlations for both markers based on the time alignment of u-EGMs ($\rho_p = 0.15$ and $\rho_s = 0.26$, $\rho_p = 0.34$ and $\rho_s = 0.49$, p-value $<$ 0.001, for $\mathcal{R}^{\mathcal{A}}$ and $\Delta\mathcal{R}^{\mathcal{A}}$, respectively).

As an illustrative example, Fig. 5.3 shows point-by-point correlation plots between some of the variables presented in Tables 5.6, 5.7 and 5.8, for case #6. In each scatter plot, Pearson ρ_p and Spearman's rank ρ_s correlation coefficients have also been reported. Negative correlations have been found for V^{b-m} and $log_{10}(V^{b-m})$ with IIR (plots (a) and (b)), where ρ_s assumes the highest absolute value in both cases (ρ_s = -0.27). Conversely, $\mathcal{R}^{\mathcal{A}}$ and $\Delta\mathcal{R}^{\mathcal{A}}$ have a positive correlation with V^{b-m}, both in linear and in logarithmic scale (plots from (c) to (h)), where the highest correlation is achieved by $\Delta\mathcal{R}^{\mathcal{A}}$ (ρ_s = 0.63).

Table 5.2: Median and IQR of the EIGDR indices ($\mathcal{R}$, $\mathcal{R}^{\mathcal{A}}$ and $\Delta\mathcal{R}^{\mathcal{A}}$) computed individually on the six cliques of all catheter sites considered, and of bipolar amplitude values (V^b) computed individually on the five innermost electrode pairs of all catheter sites, at F and NF areas, from a patient mapped during SR.

		$\mathcal{R}$	$\mathcal{R}^{\mathcal{A}}$	$\Delta\mathcal{R}^{\mathcal{A}}$	V^b (mV)
F	median/IQR	2.14/2.13	5.85/5.62	2.17/3.12	0.55/1.26
NF	median/IQR	2.43/2.34	7.42/6.74	2.67/3.25	0.80/1.24
	p-value*	0.08	$4.0e^{-4}$	0.01	0.16

* refers to the comparison of markers between F and NF areas.

Table 5.3: Median and IQR values of EIGDR indices ($\mathcal{R}$, $\mathcal{R}^{\mathcal{A}}$ and $\Delta\mathcal{R}^{\mathcal{A}}$), of the median ($V^b$) and maximum ($V^{b\text{-}m}$) bipolar amplitudes computed over the five innermost electrode pairs along the splines of the catheter, among 38 different mapping points (19 taken at F and 19 at NF areas), for each of the fifteen patients mapped in SR (patients from #1 to #7) and during pacing (patients from #8 to #15).

	$\mathcal{R}$		$\mathcal{R}^{\mathcal{A}}$		$\Delta\mathcal{R}^{\mathcal{A}}$		V^b		$V^{b\text{-}m}$	
	F	NF	F	NF	F	NF	F	NF	F	NF
# Case	Median (IQR)	Median (IQR)	Median (IQR)	Median (IQR)	Median (IQR)	Median (IQR)	Median (IQR)	Median (IQR)	Median (IQR)	Median (IQR)
1	2.93 (3.00)	1.82 (1.16)	4.72 (3.63)	3.84 (2.01)	1.00 (1.16)	1.77 (2.55)	0.15 (0.38)	0.41 (0.59)	0.55 (1.10)	1.25 (1.28)
2	5.58 (16.5)	5.80 (12.8)	10.8 (13.1)	6.49 (10.4)	1.00 (0.36)	1.00 (0.44)	0.49 (0.80)	0.52 (0.59)	1.28 (1.40)	1.60 (1.46)
3	2.68 (1.11)	2.11 (0.98)	4.49 (2.81)	3.64 (3.63)	1.27 (1.21)	1.69 (1.75)	0.08 (0.12)	0.15 (0.25)*	0.41 (0.65)	0.49 (0.60)
4	3.55 (2.21)	3.23 (6.05)	6.03 (2.37)	8.76 (11.3)*	1.06 (0.50)	1.62 (2.50)*	0.11 (0.23)	0.14 (0.15)	0.40 (0.53)	0.65 (0.69)
5	3.50 (1.60)	2.00 (1.14)	4.79 (2.25)	15.6 (18.7)*	1.17 (0.42)	6.90 (7.59)**	0.10 (0.10)	0.91 (0.68)**	0.41 (0.64)	2.60 (1.65)**
6	2.86 (2.39)	2.03 (1.35)	5.68 (5.30)	8.03 (13.5)	1.96 (2.02)	3.06 (9.98)*	0.28 (0.43)	0.45 (0.99)	0.98 (1.57)	1.54 (1.48)*
7	2.22 (1.47)	2.45 (0.80)	6.18 (4.08)	7.33 (5.62)*	3.00 (2.78)	2.61 (2.09)	0.84 (1.05)	0.88 (1.05)	1.63 (2.66)	1.72 (2.09)
8	1.82 (1.34)	2.16 (3.66)*	11.4 (8.80)	7.45 (7.85)	6.23 (6.03)	2.16 (2.70)	1.10 (1.41)	0.19 (0.34)	2.51 (2.55)	1.25 (1.14)
9	2.04 (1.74)	1.93 (0.44)	7.00 (10.3)	4.91 (5.89)	1.48 (2.81)	2.23 (3.25)	0.41 (0.66)	0.36 (0.54)	1.79 (1.08)	1.27 (1.54)
10	2.34 (1.08)	2.50 (5.88)	2.52 (1.09)	2.54 (6.74)**	1.00 (0.02)	1.00 (0.14)	0.03 (0.03)	0.03 (0.05)	0.31 (0.15)	0.12 (0.26)
11	3.11 (4.39)	2.36 (2.28)	13.7 (27.3)	8.58 (10.4)	2.13 (2.26)	2.81 (1.67)	0.34 (0.74)	0.57 (0.94)	1.44 (2.82)	2.17 (2.25)
12	1.76 (1.85)	2.43 (1.25)	6.55 (13.0)	5.42 (3.01)	3.17 (6.20)	1.57 (2.70)	0.36 (0.61)	0.19 (0.65)	1.32 (1.02)	0.69 (1.75)
13	2.23 (1.24)	1.88 (1.03)	4.93 (6.78)	5.41 (8.38)	2.43 (1.59)	3.29 (1.90)*	0.21 (0.32)	0.36 (0.37)	1.09 (1.98)	1.80 (1.13)*
14	1.64 (0.78)	1.68 (0.66)	6.43 (3.88)	7.95 (6.62)	4.19 (3.70)	4.31 (3.66)	0.96 (1.02)	1.28 (1.88)	2.49 (3.75)	2.62 (4.80)
15	1.46 (0.52)	2.01 (0.81)*	5.91 (4.86)	7.24 (6.19)	3.66 (2.05)	3.45 (4.15)	1.22 (1.50)	0.74 (0.90)	2.84 (1.63)	1.63 (1.04)

* and ** refer to the comparison of markers between F and NF areas in each case (p-value < 0.05 and p-value < 0.001, respectively).

Table 5.4: Median and IQR values of EIGDR indices ($\mathcal{R}$, $\mathcal{R}^{\mathcal{A}}$ and $\Delta\mathcal{R}^{\mathcal{A}}$) computed for all six cliques of each considered catheter site, and of bipolar amplitude values (V^b) computed for all five innermost electrode pairs of each catheter site, at F and NF areas, for the same fifteen patients mapped in SR and during pacing considered in Table 5.3.

	$\mathcal{R}$		$\mathcal{R}^{\mathcal{A}}$		$\Delta\mathcal{R}^{\mathcal{A}}$		V^b	
	F	NF	F	NF	F	NF	F	NF
# Case	Median (IQR)	Median (IQR)	Median (IQR)	Median (IQR)	Median (IQR)	Median (IQR)	Median (IQR)	Median (IQR)
1	3.18 (4.25)	2.02 (2.41)	4.61 (6.69)	4.29 (5.28)	1.00 (1.24)	1.46 (2.68)*	0.15 (0.43)	0.29 (0.75)*
2	7.02 (19.9)	7.55 (24.8)	10.5 (19.7)	8.90 (22.6)	1.00 (0.63)	1.00 (0.38)	0.30 (0.96)	0.25 (0.85)
3	2.35 (3.35)	2.04 (2.17)	4.61 (4.69)	4.13 (4.17)	1.22 (1.57)	1.67 (2.15)	0.12 (0.24)	0.16 (0.26)
4	3.70 (4.36)	3.81 (11.9)	4.81 (4.62)	9.14 (22.0)**	1.10 (0.63)	1.62 (2.31)**	0.12 (0.26)	0.13 (0.35)*
5	3.56 (4.75)	1.98 (1.76)	5.07 (6.46)	14.3 (21.7)**	1.22 (0.89)	5.59 (9.85)**	0.09 (0.19)	0.82 (1.27)**
6	2.91 (3.64)	2.12 (3.52)	6.29 (8.20)	9.86 (14.6)*	1.88 (2.43)	3.25 (7.67)**	0.32 (0.58)	0.53 (1.10)*
7	2.14 (2.13)	2.43 (2.34)	5.85 (5.62)	7.42 (6.74)**	2.17 (3.12)	2.67 (3.25)*	0.55 (1.26)	0.80 (1.24)
8	1.83 (2.48)	2.69 (7.18)**	11.1 (14.0)	7.92 (15.1)	5.24 (7.95)	1.93 (2.74)	0.98 (1.72)	0.25 (0.69)
9	2.57 (5.53)	1.83 (1.98)	7.69 (12.0)	5.27 (8.96)	1.52 (2.76)	2.28 (4.13)*	0.27 (0.95)	0.34 (0.65)
10	1.94 (2.58)	2.50 (5.69)*	2.27 (2.84)	3.06 (7.67)**	1.00 (0.18)	1.00 (0.31)	0.04 (0.12)	0.03 (0.08)
11	3.01 (8.82)	2.55 (4.76)	11.4 (24.9)	7.86 (16.9)	1.91 (3.31)	2.48 (2.79)	0.29 (0.84)	0.50 (1.21)*
12	1.75 (3.05)	2.31 (3.28)	8.03 (14.2)	5.18 (6.03)	3.03 (6.12)	1.88 (3.00)	0.46 (0.97)	0.26 (0.55)
13	2.04 (3.51)	1.64 (1.46)	5.44 (11.1)	5.35 (10.3)	2.10 (2.27)	3.15 (3.13)**	0.13 (0.65)	0.33 (0.80)*
14	1.52 (1.40)	1.78 (1.66)	6.00 (11.1)	8.90 (13.2)*	3.40 (4.79)	3.71 (5.15)	0.67 (1.59)	1.33 (2.10)
15	1.56 (1.31)	1.78 (1.67)*	5.87 (5.72)	6.50 (9.95)	3.39 (3.40)	3.24 (4.50)	1.01 (1.99)	0.74 (1.02)
Global	2.36 (3.94)	2.19 (3.40)	6.04 (9.58)	6.71 (11.0)*	1.73 (2.72)	2.21 (3.53)**	0.25 (0.85)	0.34 (0.91)**

* and ** refer to the comparison of markers between F and NF areas in each case (p-value < 0.05 and p-value < 0.001, respectively).

5.2.3 Discussion

In this section, we evaluated the ability of the proposed EIGDR indices to distinguish between F and NF points using signals acquired with a PentaRay® catheter in patients mapped during SR and pacing conditions. The rationale behind this is that fibrotic tissue is better identified by higher morphology dispersion of u-EGMs than by low bipolar voltage, thus supporting the use of EIGDR biomarkers to characterize the arrhythmogenic

Table 5.5: AUC computed for each biomarker studied ($\mathcal{R}$, $\mathcal{R}^{\mathcal{A}}$, $\Delta\mathcal{R}^{\mathcal{A}}$, V^b and V^{b-m}), both individually for each patient (Patients from #1 to #6: SR, patients from #7 to #14: pacing) and also considering them jointly (last row, referring to as Global). For each patient, For each patient, sensitivity (Se) and threshold values evaluated for a specificity value of 90% are also reported for each index. In addition, for each variable, median and IQR values have been computed. Note that thresholds are expressed in mV for V^b and V^{b-m} and in adimensional units (a.u.) for $\mathcal{R}$, $\mathcal{R}^{\mathcal{A}}$, $\Delta\mathcal{R}^{\mathcal{A}}$.

	AUC | Se | Threshold														
# Case	$\mathcal{R}$ (a.u.)			$\mathcal{R}^{\mathcal{A}}$ (a.u.)			$\Delta\mathcal{R}^{\mathcal{A}}$ (a.u.)			V^b (mV)			V^{b-m} (mV)		
1	0.36	0.00	1.03	0.50	0.00	2.54	0.59	0.00	1.00	0.59	0.00	0.13	0.59	0.09	0.19
2	0.17	0.00	1.11	0.36	0.09	4.09	0.81	0.14	1.00	0.82	0.51	0.27	0.80	0.51	0.32
3	0.35	0.03	1.09	0.59	0.32	4.66	0.73	0.49	1.45	0.65	0.23	0.08	0.67	0.19	0.08
4	0.33	0.00	1.13	0.78	0.75	3.07	0.83	0.50	1.05	0.19	0.00	0.10	0.26	0.00	0.10
5	0.32	0.00	0.98	0.35	0.00	2.19	0.50	0.00	0.93	0.73	0.44	0.09	0.82	0.44	0.09
6	0.50	0.03	1.10	0.45	0.00	2.79	0.45	0.06	1.00	0.53	0.10	0.13	0.55	0.10	0.15
7	0.49	0.21	1.12	0.46	0.16	7.33	0.50	0.16	2.62	0.67	0.12	0.60	0.70	0.12	0.60
8	0.41	0.25	1.03	0.39	0.00	2.19	0.52	0.38	1.26	0.73	0.25	0.26	0.77	0.25	0.29
9	0.59	0.17	1.04	0.87	0.50	1.72	0.85	0.17	0.98	0.59	0.00	0.04	0.61	0.00	0.04
10	0.29	0.08	1.20	0.18	0.05	3.10	0.62	0.45	1.00	0.69	0.46	0.11	0.69	0.46	0.11
11	0.52	0.10	1.06	0.49	0.40	3.74	0.48	0.10	1.35	0.27	0.00	0.26	0.24	0.00	0.27
12	0.53	0.03	1.06	0.74	0.29	3.42	0.71	0.14	1.12	0.61	0.06	0.11	0.59	0.06	0.12
13	0.39	0.06	1.20	0.58	0.15	3.82	0.63	0.19	2.20	0.52	0.12	0.49	0.54	0.12	0.49
14	0.69	0.00	1.10	0.74	0.00	2.75	0.52	0.00	1.24	0.43	0.00	0.16	0.43	0.00	0.16
Median	0.40	0.03	1.10	0.50	0.12	3.09	0.61	0.15	1.09	0.60	0.11	0.13	0.60	0.11	0.16
IQR	0.19	0.10	0.08	0.35	0.32	1.28	0.23	0.32	0.35	0.17	0.25	0.16	0.16	0.25	0.19
Global	0.41	0.04	1.10	0.48	0.10	2.84	0.62	0.31	1.08	0.69	0.25	0.14	0.69	0.24	0.15

Table 5.6: Pearson's ρ_p and Spearman's rank ρ_s correlation coefficients between all possible pairs of variables among IIR, V^{b-m}, $\mathcal{R}$, $\mathcal{R}^{\mathcal{A}}$ and $\Delta\mathcal{R}^{\mathcal{A}}$, computed both individually at each patient (Patients from #1 to #6: SR, patients from #7 to #14: pacing) and also considering all of them jointly (last row). The fibrotic tissue percentage %F is also reported for the same cases.

	ρ_p/ρ_s							
# Case	(V^{b-m}, IIR)	($\mathcal{R}$, IIR)	($\mathcal{R}^{\mathcal{A}}$, IIR)	($\Delta\mathcal{R}^{\mathcal{A}}$, IIR)	($\mathcal{R}$, V^{b-m})	($\mathcal{R}^{\mathcal{A}}$, V^{b-m})	($\Delta\mathcal{R}^{\mathcal{A}}$, V^{b-m})	%F
1	0.25*/0.17	0.17/0.16	0.37**/0.41**	0.28*/0.28*	0.07/0.07	0.75**/0.68**	0.55**/0.62**	24.4
2	-0.32**/-0.37**	0.40**/0.40**	0.19*/0.19*	-0.22*/-0.37**	-0.39**/-0.63**	0.17*/0.07	0.63**/0.75**	19.7
3	-0.25**/-0.27**	0.20**/0.17*	0.08/-0.19*	-0.11/-0.34**	-0.33**/-0.43**	0.15*/0.14*	0.43**/0.59**	79.2
4	-0.19*/-0.29**	0.17/0.29**	-0.25*/-0.13	-0.36**/-0.32**	-0.36**/-0.51**	0.19*/0.10	0.55**/0.56**	2.99
5	-0.04/-0.46*	0.11/0.16	0.13/0.29	0.05/0.14	-0.35/-0.59*	-0.23/-0.31	0.63*/0.41	45.0
6	-0.13**/-0.27**	0.10*/0.14**	0.01/0.03	-0.03/-0.10*	-0.20**/-0.32**	0.33**/0.42**	0.50**/0.63**	8.04
7	-0.11/-0.12	0.10/0.01	0.01/-0.04	0.04/-0.09	0.19*/0.21*	-0.05/0.01	-0.24*/-0.13	13.2
8	-0.04/-0.02	0.12*/0.19**	0.10*/0.13**	-0.07/0.02	-0.17**/-0.25**	0.12*/0.19**	0.27**/0.43**	1.16
9	-0.20*/-0.11	-0.37**/-0.19	-0.37**/-0.28*	-0.01/-0.16	-0.10/-0.23*	0.17/0.34**	0.26*/0.62**	5.77
10	-0.03/-0.05	0.33**/-0.02	0.26**/0.10**	0.08*/0.01	-0.19**/-0.29**	0.20**/0.25**	0.45**/0.60**	5.40
11	0.23**/0.25**	-0.02/-0.01	0.14*/0.08	0.12*/0.07	-0.17**/-0.13*	0.33**/0.28**	0.34**/0.35**	2.08
12	-0.18/-0.12	-0.19*/-0.01	-0.33**/-0.30**	-0.21*/-0.30**	-0.11/-0.21*	0.39**/0.39**	0.47**/0.55**	29.7
13	-0.16*/-0.18*	0.21*/0.12	-0.24*/-0.28**	-0.18*/-0.34**	-0.19*/-0.06	0.49**/0.59**	0.50**/0.60**	18.1
14	0.07*/-0.05	0.14**/0.19**	0.00/-0.01	-0.13**/-0.16**	-0.13**/-0.13**	0.11**/0.06	0.17**/0.18**	0.39
Global	-0.07**/-0.12**	0.17**/0.10**	0.10**/0.07**	-0.01/-0.05**	-0.16**/-0.24**	0.22**/0.26**	0.36**/0.49**	9.58

* p-value < 0.05 ** p-value < 0.001.

Table 5.7: Pearson's ρ_p and Spearman's rank ρ_s correlation coefficients between all possible pairs of variables among IIR, $log_{10}(V^{b-m})$, $log_{10}(\mathcal{R})$, $log_{10}(\mathcal{R}^{\mathcal{A}})$ and $log_{10}(\Delta\mathcal{R}^{\mathcal{A}})$, computed both individually at each patient (Patients from #1 to #6: SR, patients from #7 to #14: pacing) and also considering all of them jointly (last row). The fibrotic tissue percentage %F is also reported for the same cases.

	ρ_p/ρ_s							
# Case	($log_{10}(V^{b-m})$, IIR)	($log_{10}(\mathcal{R})$, IIR)	($log_{10}(\mathcal{R}^{\mathcal{A}})$, IIR)	($log_{10}(\Delta\mathcal{R}^{\mathcal{A}})$, IIR)	($log_{10}(\mathcal{R})$, $log_{10}(V^{b-m})$)	($log_{10}(\mathcal{R}^{\mathcal{A}})$, $log_{10}(V^{b-m})$)	($log_{10}(\Delta\mathcal{R}^{\mathcal{A}})$, $log_{10}(V^{b-m})$)	%F
1	0.34**/0.17	0.14/0.16	0.50**/0.41**	0.39**/0.28*	0.01/0.07	0.62**/0.68**	0.59**/0.62**	24.4
2	-0.38**/-0.37**	0.44**/0.40**	0.21*/0.19*	-0.31**/-0.37**	-0.66**/-0.63**	-0.01/0.07	0.69**/0.75**	19.7
3	-0.30**/-0.27**	0.23**/0.17*	-0.12/-0.19*	-0.32**/-0.34**	-0.50**/-0.43**	0.08/0.14*	0.53**/0.59**	79.2
4	-0.22*/-0.29**	0.25*/0.29**	-0.18*/-0.13	-0.38**/-0.32**	-0.52**/-0.51**	0.08/0.10	0.55**/0.56**	2.99
5	-0.24/-0.46*	0.12/0.16	0.17/0.29	0.06/0.14	-0.64*/-0.59*	-0.41/-0.31	0.51*/0.41	45.0
6	-0.22**/-0.27**	0.11*/0.14**	0.04/0.03	-0.05/-0.10*	-0.35**/-0.32**	0.36**/0.42**	0.61**/0.63**	8.04
7	-0.11/-0.12	0.03/0.01	-0.03/-0.04	-0.05/-0.09	0.22*/0.21*	0.02/0.01	-0.15/-0.13	13.2
8	-0.03/-0.02	0.18**/0.19**	0.14**/0.13**	0.00/0.02	-0.24**/-0.25**	0.22**/0.19**	0.44**/0.43**	1.16
9	-0.14/-0.11	-0.31*/-0.19	-0.36**/-0.28*	-0.09/-0.16	-0.23*/-023*	0.32**/0.34**	0.56**/0.62**	5.77
10	-0.10**/-0.05	0.14**/-0.02	0.17**/0.10**	0.02/0.01	-0.37**/-0.29**	0.19**/0.25**	0.55**/0.60**	5.40
11	0.21**/0.25**	0.00/-0.01	0.09/0.08	0.08*/0.07	-0.18**/-0.13*	0.26**/0.28**	0.37**/0.35**	2.08
12	-0.12/-0.12	-0.14/-0.01	-0.35**/-0.30**	-0.25*/-0.30**	-0.24*/-0.21*	0.38**/0.39**	0.55**/0.55**	29.7
13	-0.20*/-0.18*	0.17*/0.12	-0.26**/-0.28**	-0.33**/-0.34**	-0.09/-0.06	0.60**/0.59**	0.59**/0.60**	18.1
14	-0.05/-0.05	0.16**/0.19**	-0.04/-0.01	-0.17**/-0.16**	-0.16**/-0.13**	0.10*/0.06	0.22**/0.18**	0.39
Global	-0.19**/-0.12**	0.14**/0.10**	0.07**/0.07**	-0.06**/-0.05**	-0.32**/-0.24**	0.22**/0.26**	0.49**/0.49**	9.58

* p-value < 0.05 ** p-value < 0.001.

Table 5.8: Pearson's ρ_p and Spearman's rank ρ_s correlation coefficients between EIGDR based markers, $\mathcal{R}$, $\mathcal{R}^{\mathcal{A}}$ and $\Delta\mathcal{R}^{\mathcal{A}}$, and logarithmic values of bipolar voltage amplitudes, $log_{10}(V^{b-m})$, computed both individually at each patient (Patients from #1 to #6: SR, patients from #7 to #14: pacing) and also considering all of them jointly (last row). The fibrotic tissue percentage %F is also reported for the same cases.

	ρ_p/ρ_s			
# Case	($\mathcal{R}$, $log_{10}(V^{b-m})$)	($\mathcal{R}^{\mathcal{A}}$, $log_{10}(V^{b-m})$)	($\Delta\mathcal{R}^{\mathcal{A}}$, $log_{10}(V^{b-m})$)	%F
1	0.00/0.07	0.61**/0.68**	0.50**/0.62**	24.4
2	-0.59**/0.63**	-0.09/0.07	0.54**/0.75**	19.7
3	-0.39**/0.43**	0.05/0.14*	0.36**/0.59**	79.2
4	-0.48**/-0.51**	0.08/0.10	0.45**/0.56**	2.99
5	-0.53*/-0.59*	-0.42/-0.31	0.53*/0.41	45.0
6	-0.29**/-0.32**	0.28**/0.42**	0.47**/0.63**	8.04
7	0.17*/0.21*	-0.03/0.01	-0.21*/-0.13	13.2
8	-0.16**/-0.25**	0.16**/0.19**	0.29**/0.43**	1.16
9	-0.13/0.23*	0.30*/0.34**	0.42**/0.62**	5.77
10	-0.37**/0.29**	0.06*/0.25**	0.36**/0.60**	5.40
11	-0.22**/-0.13*	0.29**/0.28**	0.31**/0.35**	2.08
12	-0.15/-0.21*	0.38**/0.39**	0.41**/0.55**	29.7
13	-0.19*/-0.06	0.49**/0.59**	0.47**/0.60**	18.1
14	-0.12**/-0.13**	0.15**/0.06	0.22**/0.18**	0.39
Global	-0.29**/-0.24**	0.15**/0.26**	0.34**/0.49**	9.58

* p-value < 0.05 ** p-value < 0.001.

substrate in the atrium.

To start with, we tested the ability of $\mathcal{R}$, $\mathcal{R}^{\mathcal{A}}$ and $\Delta\mathcal{R}^{\mathcal{A}}$ to distinguish between well established F and NF points, according to LGE-MRI, by using signals acquired with a PentaRay® catheter in patients mapped during SR and pacing conditions. These were evaluated in six electrode cliques (five quadrangular and one pentagonal), individually at each mapping point and also considering them jointly, both on the single patient and on all of them at the same time. Resulting statistics were used to compare EIGDR markers with bipolar peak-to-peak amplitudes, considered as the milestone approach in detecting atrial fibrosis during EAM procedures.

The proposed method revealed not to show statistically significant differences for all the cases considered. The reason why this occurs may be its lack of standardization. In addition, despite the fact that LGE-MRI gives important information regarding the presence of atrial fibrosis which may be used to improve catheter ablation of AF patients, it may not represent a reliable reference for fibrosis detection in the atrium, thus pushing the interest in the research of more innovative approaches.

However, results reveal that $\Delta\mathcal{R}^{\mathcal{A}}$ is the most suitable biomarker for the detection of atrial fibrosis when considering mapping points of all of the patients jointly, showing to improve its performance when the sample number of cliques increases. This paves the way for the use of the EIGDR method even with the most modern higher density catheters, where $\Delta\mathcal{R}^{\mathcal{A}}$ performance is expected to improve on the analysis conducted in this paragraph. Therefore, only further future studies will be able to elucidate this.

Additionally, we computed high-density EIGDR and bipolar voltage maps, so as to evaluate their overall fibrosis discrimination power and a point-by-point correlation between surrogate fibrosis parameters. Our findings show a significant and inverse but weak correlation between bipolar voltage and IIR, as already found in [139], revealing that the latter cannot be considered a *gold standard*. Nevertheless, results have provided higher correlation between EIGDR markers based on the previous time alignment and bipolar voltage maps, suggesting that $\mathcal{R}^{\mathcal{A}}$ and $\Delta\mathcal{R}^{\mathcal{A}}$ might be valid techniques to characterize atrial fibrosis. Nonetheless, results also suggest that bipolar voltage might be more sensitive to fibrotic tissue percentage than EIGDR biomarkers, with lower fibrosis identification performance associated to lower percentage of fibrosis.

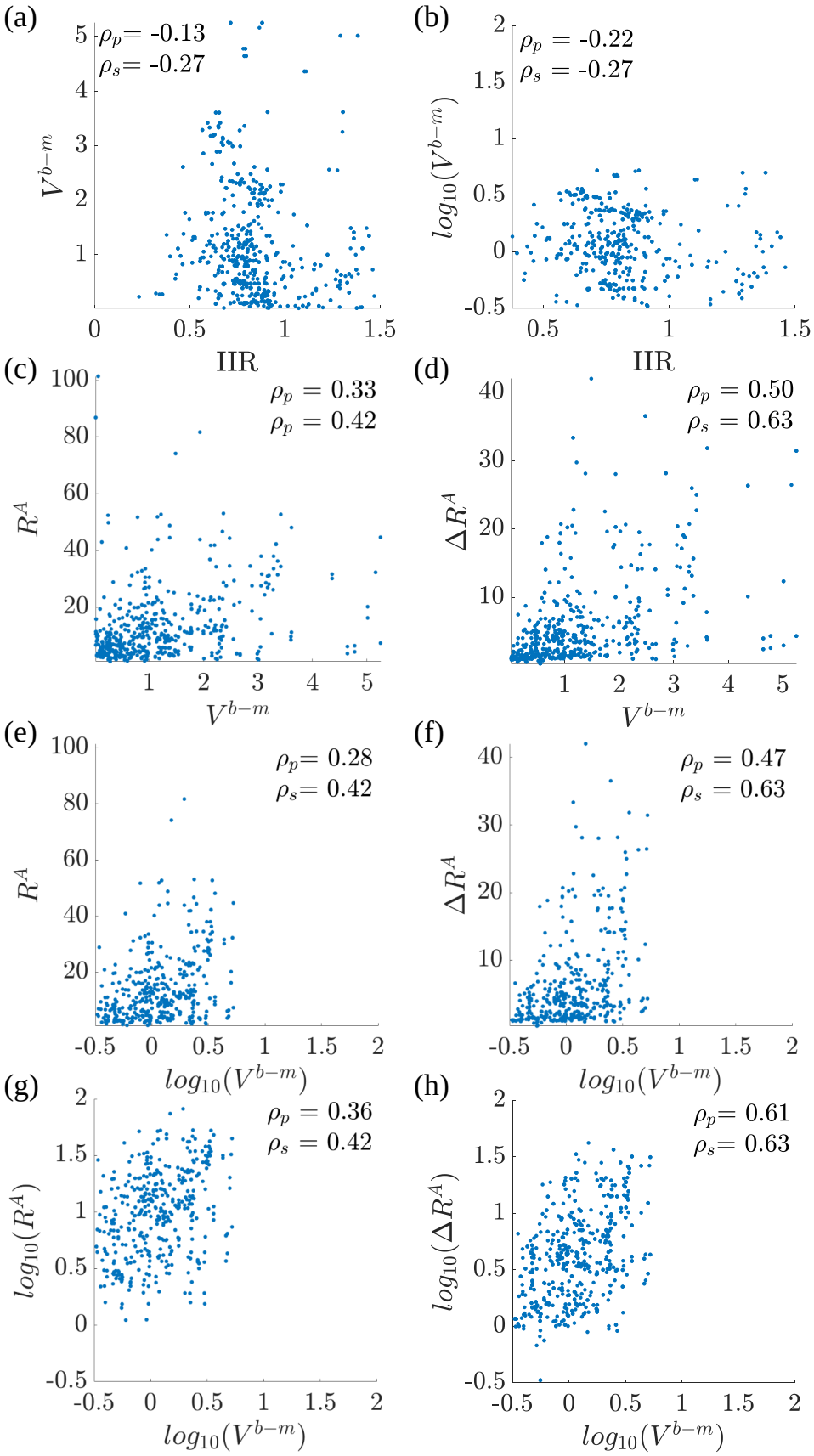

Figure 5.3: Scatter plots between V^{b-m} and IIR values (a), $log_{10}(V^{b-m})$ and IIR values (b), $\mathcal{R}^{\mathcal{A}}$ and V^{b-m} (c), $\Delta\mathcal{R}^{\mathcal{A}}$ and V^{b-m} (d), $\mathcal{R}^{\mathcal{A}}$ and $log_{10}(V^{b-m})$ (e), $\Delta\mathcal{R}^{\mathcal{A}}$ and $log_{10}(V^{b-m})$ (f), $log_{10}(\mathcal{R}^{\mathcal{A}})$ and $log_{10}(V^{b-m})$ (g), $log_{10}(\Delta\mathcal{R}^{\mathcal{A}})$ and $log_{10}(V^{b-m})$ (h), for patient #6 of Tables 5.5, 5.6, 5.7 and 5.8. In each subplot, correlation coefficients have also been reported.

5.3 Effect of Multielectrode Mapping Catheter Geometry on the Unipolar Electrogram Eigenvalue Dispersion

The EIGDR method is based on the hypothesis of local plane wave propagation within the considered cliques. However, this hypothesis could be compromised when applied to the PentaRay® catheter, due to its dimensions and geometry, which could affect the interpretation of the results. In this section, we compared the values and interelectrode variability observed for the EIGDR indices as well as bipolar amplitudes in the PentaRay® catheter with those obtained in epicardial EGMs recorded with the rectangular MEA sensor introduced in subsection 2.1.2. In the MEA, the plane wave hypothesis is expected to be better accomplished than in a PentaRay®, where electrodes can be at a distance of the order of centimeters in the transversal direction, like the physiological dimensions of the atrium.

5.3.1 Materials and Methods

In order to make the comparison between catheters, a total of 124 u-EGMs with recording length of 5 s, acquired in SR with the MEA introduced in subsection 2.1.2, located at the medial position of the RA of a patient with no fibrosis (RA2 in Fig. 2.4) and the 20 u-EGMs recorded at a single PentaRay® position (or mapping point) in NF area (according to its IIR value), from a case in SR, were considered. The comparison has been conducted following three complementary approaches so as to make it more robust. In the first one, only the atrial depolarization corresponding to the beat occurring at $t = 2000$ ms was considered for computing EIGDR markers and bipolar peak-to-peak amplitudes. Figures 5.4 and 5.5 show the whole-length u-EGMs recorded with both catheters, where the signal windows used, having length $T = 100$ ms, have been highlighted. Mean and maximum bipolar amplitudes, V^b and V^{b-m}, respectively, have also been computed for performance comparison. In PentaRay®, V^b represents the average value between bipolar peak-to-peak amplitudes computed along the two splines involved in each clique, whereas V^{b-m} is the maximum value between them. In the MEA, V^b represents the mean between the bipolar peak-to-peak amplitudes computed along two orthogonal splines at each 2×2 clique configuration available in the catheter, while V^{b-m} is the maximum value between them.

In order to make the comparison between the catheters consistent, two scenarios were followed in the MEA. In the first one, EIGDR and bipolar amplitude based indices were computed at five 2×2 cliques chosen at five different electrode locations within the MEA, as depicted in Fig. 5.6. In the same figure, u-EGMs at each clique are also shown with different colors for each pole.

In the subsequent case, those markers were computed at all the available 2×2 cliques

within the MEA at RA2.

In both cases, median and IQR values, as well as the resulting quartile coeffient of variation (QCV), defined as the ratio between IQR and median values, were calculated for $\mathcal{R}$, $\mathcal{R}^{\mathcal{A}}$, $\Delta\mathcal{R}^{\mathcal{A}}$, V^b and V^{b-m} and compared with statistics of the markers computed at the five cliques of the PentaRay® pointed out in Fig. 5.7.

After that, two different multibeat approaches were followed. In the first one, for each of the 8 × 16 electrodes of the MEA, six atrial depolarization windows corresponding to the six beats available have been considered and time-aligned, in order to average them and obtain 128 average u-EGMs. Markers based on the EIGDR method and bipolar peak-to-peak amplitude have thus been computed in 2×2 cliques all over the MEA, providing summary statistics (median, IQR and QCV values) for resulting 7×15 maps. The same procedure has been performed at each of the 10 innermost poles of the PentaRay®, averaging in this case two atrial activation windows corresponding to the two recorded beats. EIGDR values and bipolar amplitudes have been computed in the five 4-electrode cliques and median, IQR and QCV values have been provided. In the second approach, 7×15 EIGDR and bipolar amplitude maps have been created for each of the six MEA-registered beats with 2×2 cliques. The median of the six resulting maps has been computed for each marker, and median, IQR and QCV values have been computed over the median maps. With PentaRay®, the median of markers calculated in the five 4-electrode cliques between beats has been obtained, also providing median, IQR and QCV values of median markers as summary statistics.

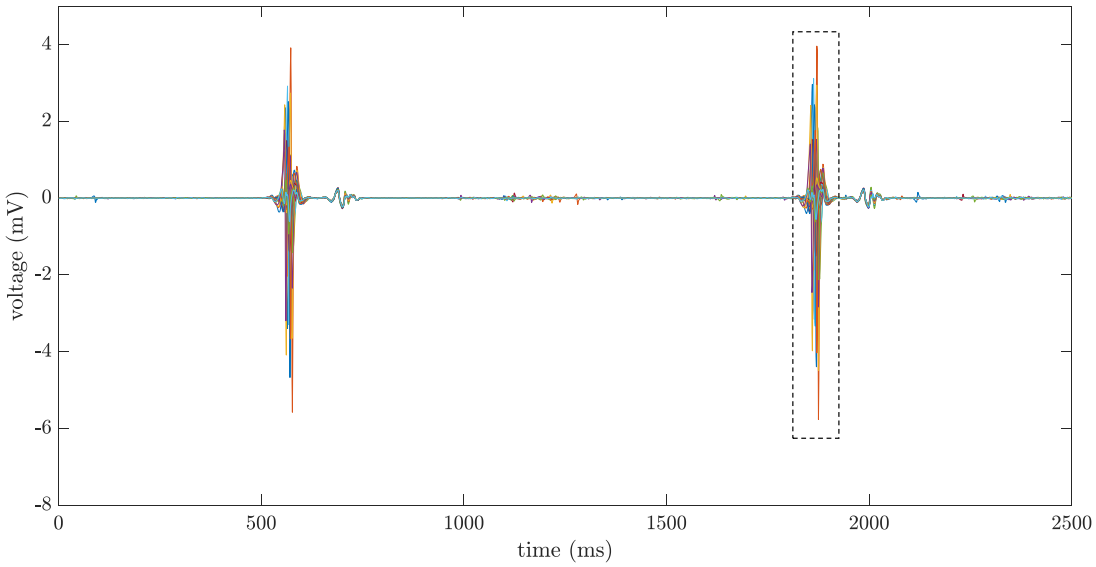

Figure 5.4: The 20 u-EGMs, previously filtered as described in 2.1.1, acquired by the PentaRay® at a single mapping point at NF tissue of a patient during SR. In the same plot, the atrial depolarization window used is highlighted with dashed line.

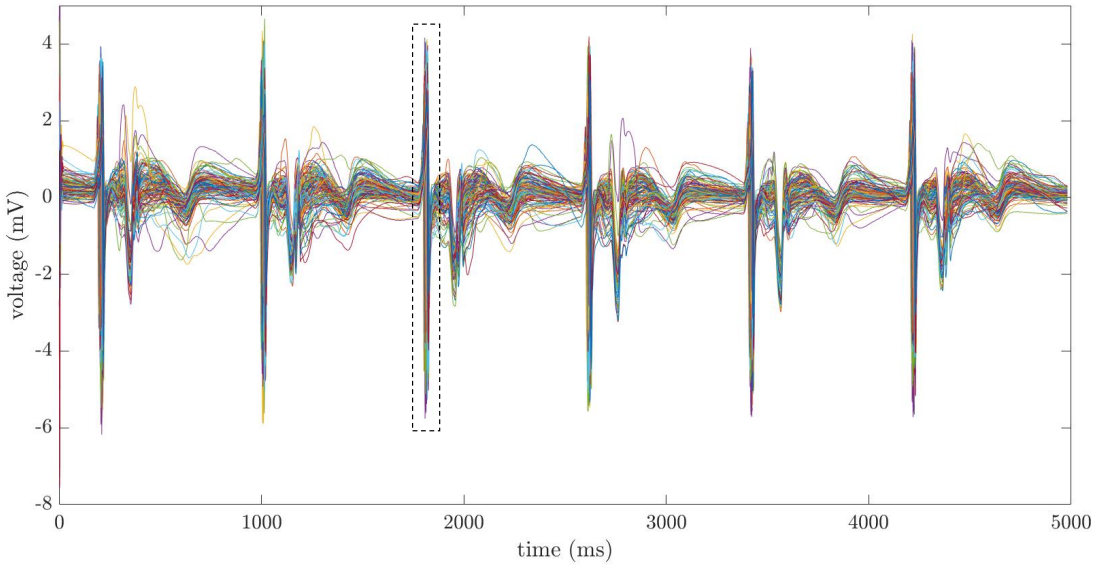

Figure 5.5: The 124 u-EGMs, previously filtered as described in 2.1.2, acquired by the MEA at a single medial position in a patient during SR. In the same plot, the atrial depolarization window considered is highlighted with dashed line.

5.3.2 Results

Table 5.9 reports median, IQR and QCV values of EIGDR based markers and of the bipolar amplitudes computed among the five cliques depicted in Fig. 5.6 and Fig. 5.7 for the MEA and PentaRay® catheters, respectively. These results reveal that median and IQR values for $\mathcal{R}$, $\mathcal{R}^{\mathcal{A}}$ and $\Delta\mathcal{R}^{\mathcal{A}}$ are greater when computed in MEA than in PentaRay®, as expected. This is clearly visible in Fig. 5.6 and Fig. 5.7, where interclique and intraclique waveform dispersion is higher in PentaRay® than in the MEA. On the other hand, the reverse occurs for IQR values of bipolar amplitudes, which are higher in the star-shaped catheter than in the grid-shaped one (2.95 mV and 5.19 mV vs. 2.46 mV and 3.42 mV for V^b and V^{b-m}, respectively). This greater dispersion can be explained with the dependence of voltage measurements on distance between catheter and tissue, which is more variable in PentaRay® than in MEA for their own structure, also corroborating a higher sensitivity of bipolar voltage amplitudes than EIGDR markers to electrode-to-tissue distance.

The most stable performance for the EIGDR based markers in both catheters are obtained by using $\mathcal{R}^{\mathcal{A}}$, whose QCV values suggest a lower degree of variability among the cliques considered in both catheters. Similar results can be observed in Table 5.10, which contains statistics of markers computed among all the available cliques in the catheters. Note that for PentaRay®, results are the same as those shown in Table 5.9 (see bottom row in both tables). This is due to the fact that, in our analyses, one PentaRay® catheter position consists of only the five innermost cliques of four electrodes, which were therefore

used for comparison both with the five cliques chosen from the MEA and with the entire clique set available within the same. Even in this case, median (IQR) values of EIGDR based indices are greater in the grid-shaped catheter than in the star-shaped one (e. g. 93.6 (72.2) vs. 4.37 (4.11) for $\mathcal{R}^{\mathcal{A}}$). The opposite occurs for the bipolar amplitude based markers for the reason explained above (1.37 and 2.65 vs. 2.95 and 5.19 for V^b and V^{b-m} in MEA and PentaRay®, respectively). The best quantification performance is given again by $\mathcal{R}^{\mathcal{A}}$ over $\mathcal{R}$ and $\Delta\mathcal{R}^{\mathcal{A}}$, reinforcing the use of time-alignment based biomarkers in the identification of atrial fibrosis.

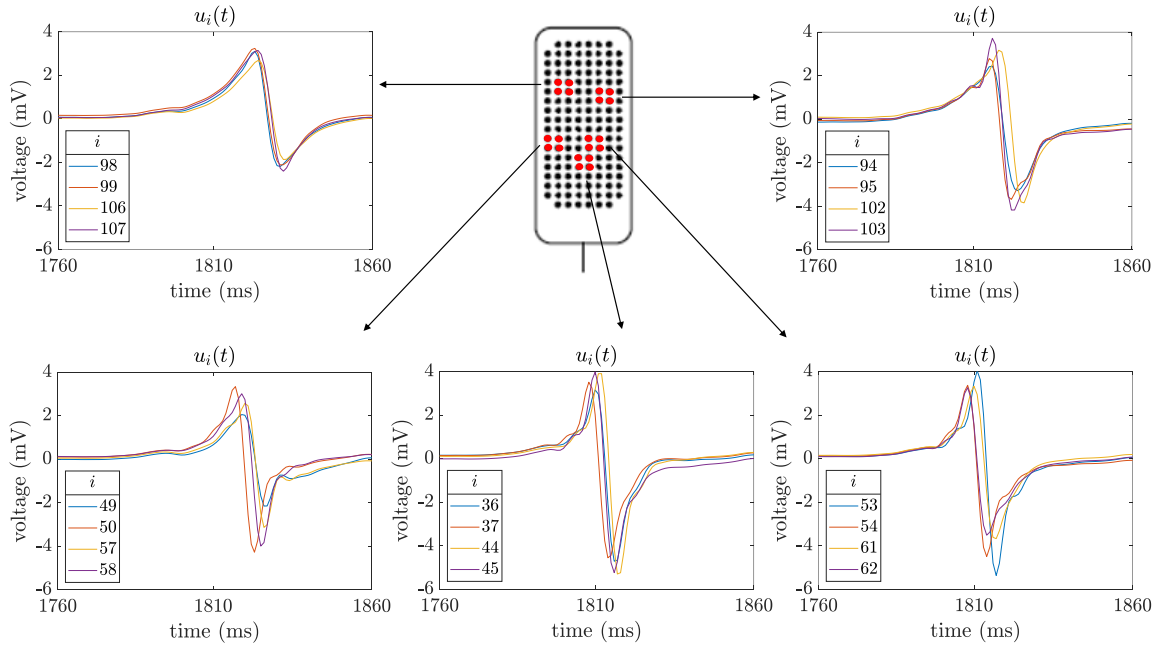

Figure 5.6: Unipolar EGMs $u_i(t)$, $i \in \{1, \ldots, 124\}$, plotted at each of the five 2×2 cliques (highlighted in red over the MEA) considered within the catheter at RA2 position. At each plot, u-EGMs have been displayed in blue, orange, yellow and violet, at lower left, lower right, upper left and upper right electrodes, respectively.

Table 5.9: Median, IQR values and QCV values of EIGDR indices ($\mathcal{R}$, $\mathcal{R}^{\mathcal{A}}$ and $\Delta\mathcal{R}^{\mathcal{A}}$), and of the mean ($V^b$) and maximum ($V^{b\text{-}m}$) bipolar amplitudes computed among the five cliques depicted in Fig. 5.6 and Fig. 5.7 in both catheters.

	$\mathcal{R}$	$\mathcal{R}^{\mathcal{A}}$	$\Delta\mathcal{R}^{\mathcal{A}}$	V^b (mV)	$V^{b\text{-}m}$ (mV)
# Catheter	Median (IQR) [QCV]	Median (IQR) [QCV]	Median (IQR) [QCV]	Median (IQR) [QCV]	Median (IQR) [QCV]
MEA	6.88 (15.2) [2.20]	99.6 (67.5) [0.68]	9.59 (11.2) [1.17]	4.13 (2.46) [0.59]	5.70 (3.42) [0.60]
PentaRay®	1.57 (1.71) [1.08]	4.37 (4.11) [0.94]	2.61 (4.78) [1.83]	1.05 (2.95) [2.81]	1.85 (5.19) [2.81]

Tables 5.11 and 5.12 show statistics of the EIGDR and bipolar amplitude based indices, in case of multibeat average analysis of biomarkers. As already found in single-beat analysis, median and IQR values of $\mathcal{R}$, $\mathcal{R}^{\mathcal{A}}$ and $\Delta\mathcal{R}^{\mathcal{A}}$ are higher in MEA than in PentaRay®, confirming a higher dispersion of the u-EGMs morphology, not related to presence of fibrosis, in the latter. When averaging in time the available atrial depolar-

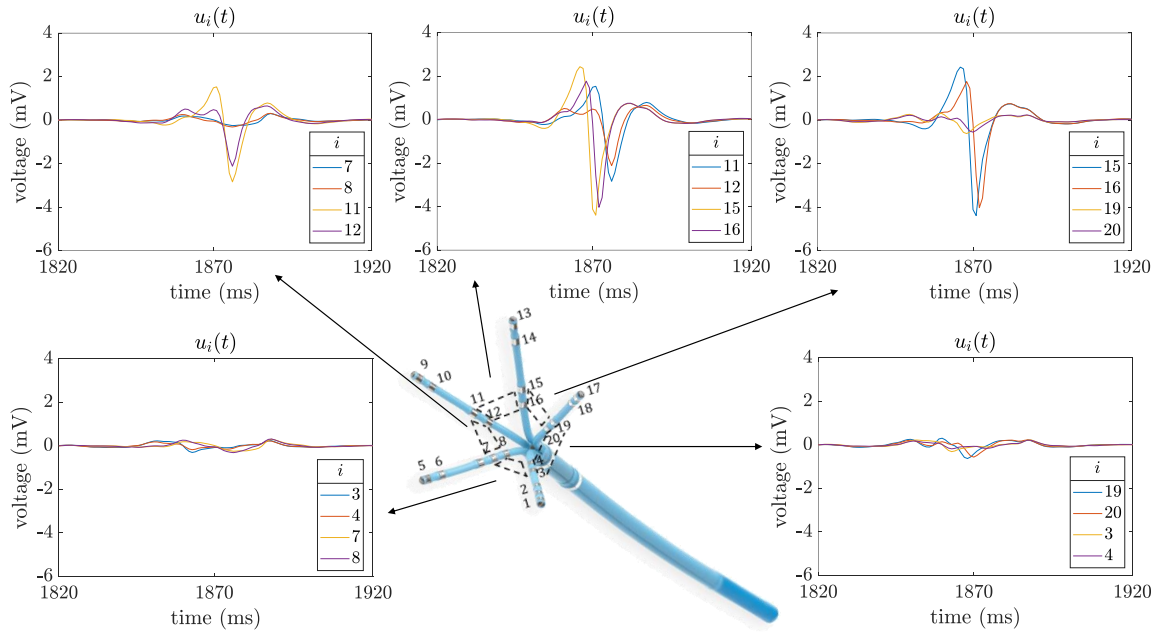

Figure 5.7: Unipolar EGMs $u_i(t)$, $i \in \{1, \ldots, 20\}$, plotted at each of the five 4-electrode cliques (highlighted with black dashed lines over the PentaRay®) considered at one position. At each plot, legend show electrodes as numbered in the catheter figure.

Table 5.10: Median, IQR values and QCV values of EIGDR indices ($\mathcal{R}$, $\mathcal{R}^{\mathcal{A}}$ and $\Delta\mathcal{R}^{\mathcal{A}}$), and of the mean ($V^b$) and maximum ($V^{b\text{-}m}$) bipolar amplitudes computed among all the available cliques in both catheters.

	$\mathcal{R}$	$\mathcal{R}^{\mathcal{A}}$	$\Delta\mathcal{R}^{\mathcal{A}}$	V^b (mV)	$V^{b\text{-}m}$ (mV)
# Catheter	Median (IQR) [QCV]	Median (IQR) [QCV]	Median (IQR) [QCV]	Median (IQR) [QCV]	Median (IQR) [QCV]
MEA	6.78 (4.19) [0.62]	93.6 (72.2) [0.77]	11.7 (13.5) [1.16]	4.05 (1.37) [0.34]	4.81 (2.65) [0.55]
PentaRay®	1.57 (1.71) [1.08]	4.37 (4.11) [0.94]	2.61 (4.78) [1.83]	1.05 (2.95) [2.81]	1.85 (5.19) [2.81]

ization windows (see Table 5.11), $\mathcal{R}^{\mathcal{A}}$ achieves the following median (IQR) values: 118 (94.2) vs. 3.43 (5.19) in MEA and PentaRay® catheters, respectively. Similar results were obtained when computing median of markers at different catheter positions, each resulting from a different beat (see Table 5.12). As example, median and IQR of $\mathcal{R}^{\mathcal{A}}$ assume values 37.6 and 22.4 vs. 3.39 and 5.13 in MEA and in PentaRay®, respectively. An exception is represented by IQR value of $\Delta\mathcal{R}^{\mathcal{A}}$, which is greater in PentaRay® than in MEA (5.45 vs. 2.80), showing higher spatial variability.

The higher variability of electrode-to-tissue distance which characterizes the PentaRay® at each position is reflected by higher IQR values than in the MEA for bipolar voltage based markers, with both multibeat approaches (e.g. 4.76 mV vs 2.53 mV and 4.96 mV vs. 1.68 mV for V^{b-m} in PentaRay® vs. MEA, respectively, in both scenarios), which is consistent with our findings in single-beat analysis (see Tables 5.9 and 5.10).

Table 5.11: Median, IQR values and QCV values of EIGDR indices ($\mathcal{R}$, $\mathcal{R}^{\mathcal{A}}$ and $\Delta\mathcal{R}^{\mathcal{A}}$), and of the mean ($V^b$) and maximum ($V^{b\text{-}m}$) bipolar amplitudes computed among all the cliques of the MEA and the five cliques of PentaRay® depicted in Fig. 5.7, considering average u-EGMs over available beats.

	$\mathcal{R}$	$\mathcal{R}^{\mathcal{A}}$	$\Delta\mathcal{R}^{\mathcal{A}}$	V^b (mV)	$V^{b\text{-}m}$ (mV)
# Catheter	Median (IQR) [QCV]	Median (IQR) [QCV]	Median (IQR) [QCV]	Median (IQR) [QCV]	Median (IQR) [QCV]
MEA	6.33 (4.47) [0.71]	118 (94.2) [0.80]	16.1 (13.4) [0.83]	3.86 (1.44) [0.37]	4.84 (2.53) [0.52]
PentaRay®	1.29 (1.25) [0.97]	3.43 (5.19) [1.52]	2.94 (5.39) [1.83]	1.14 (2.82) [2.48]	2.04 (4.76) [2.34]

Table 5.12: Median, IQR values and QCV of median maps of EIGDR indices ($\mathcal{R}$, $\mathcal{R}^{\mathcal{A}}$ and $\Delta\mathcal{R}^{\mathcal{A}}$), and of the mean ($V^b$) and maximum ($V^{b\text{-}m}$) bipolar amplitudes, computed among the six available beats, considering all the cliques of the MEA and the five cliques of PentaRay® depicted in Fig. 5.7. Note that in case of PentaRay®, with only two beats, resulting median position coincides with the average value.

	$\mathcal{R}$	$\mathcal{R}^{\mathcal{A}}$	$\Delta\mathcal{R}^{\mathcal{A}}$	V^b (mV)	$V^{b\text{-}m}$ (mV)
# Catheter	Median (IQR) [QCV]	Median (IQR) [QCV]	Median (IQR) [QCV]	Median (IQR) [QCV]	Median (IQR) [QCV]
MEA	10.8 (9.38) [0.87]	37.6 (22.4) [0.60]	3.05 (2.80) [0.92]	2.45 (1.66) [0.68]	2.25 (1.68) [0.75]
PentaRay®	1.32 (1.34) [1.02]	3.39 (5.13) [1.51]	1.99 (5.45) [2.74]	1.14 (2.93) [2.58]	2.04 (4.96) [2.43]

5.3.3 Discussion

In this section, the effect of catheter geometry on the performance of the EIGDR methodology in quantifying voltage waveform dispersion has been tested. The assumption behind this is that the plane wave hypothesis within the electrode cliques, on which u-EGM spatiotemporal relations depend, is better accomplished in grid-patterned configurations than in star-shaped ones, where the interelectrode spacing may also achieve values higher than physiological dimensions of the atrium. In order to achieve this purpose, the 20-pole PentaRay® catheter has been compared to the 8×16 MEA, considering one single atrial activation and also including averaging of atrial depolarization windows of u-EGMs, for the quantification of signal dispersion within the cliques. Our findings revealed that median and IQR values of EIGDR based markers computed over the MEA are greater than their counterparts calculated in the PentaRay®. This means that signal morphology is significantly influenced by catheter geometry and dimensions, with grid-shaped catheters implying a lower signal waveform dispersion and therefore lending themselves better to identifying atrial fibrosis with EIGDR based approach. These results have also been corroborated by a more robust multibeat approach, which has revealed that the closest distribution of electrodes in MEA over PentaRay® and the consequent better accomplishment of the plane wave hypothesis in nearby cliques implies a more clear eigenvalue concentration in this kind of catheter. However, they should be interpreted with the care that recordings come from different patients.

5.4 Limitations

In this chapter, some clinical applications of the three atrial fibrosis biomarkers of u-EGM waveform dispersion proposed in chapter 4 have been covered. They are based on the concept of dominant-to-remaining eigenvalue dominance ratio (EIGDR), which requires the assumption of plane and homogeneous propagation within each clique of electrodes. This may represent an intrinsic restriction, forcing to use high spatial resolution multielectrode mapping catheters, like the MEA and the PentaRay® used in this study. Nevertheless, our findings have revealed that the plane wave hypothesis may not be satisfied in the latter and more generally in asymmetric shaped catheters having dimensions comparable to those of the atrium, where intraclique signal waveform dispersion (not related to atrial fibrosis) occurs. Another intrinsic limitation of the EIGDR approach is represented by mapping points availability. When one or more electrode pairs are discarded by the EAM system at a certain catheter position, mainly due to lack of catheter-to-tissue contact, localization for cliques involving those electrodes is missing. Therefore, even if signals are available since they are saved several times by the EAM system, those incomplete cliques are discarded from the analysis. As a consequence, if so many electrode pairs were missing that not even a clique could be formed, the whole mapping point would be discarded from the analysis. In these studies, atrial fibrosis markers based on EIGDR and bipolar voltage amplitude have been computed and evaluated in a small sample of patients, whose size should be acknowledged as a limiting factor, who were in SR at the time of their mapping or during CS pacing. Therefore, these results should be integrated with others found during fibrillatory propagation patterns. In addition, in section 5.3, a single PentaRay® position coming from a single patient was considered for the comparison with MEA sensor to be consistent. This may have affected resulting statistics, having included only five electrode cliques in the analysis. However, performance of biomarkers may also have been influenced by interpatient variability (both in anatomical and electrophysiological terms), data acquisition errors and the fact that some of the procedures followed in these analyses are manual and operator-dependent. Last but not least, the LGE-MRI used as reference for the location of fibrotic tissue is not the *gold standard* for atrial fibrosis assessment, which is instead represented by histological assessment (not achievable in healthy individuals).

5.5 Conclusions

In this chapter, we tested the ability of EIGDR methodology in the discrimination between F and NF tissue in the atrium, in clinical conditions where multipole catheters are employed for EAM. Atrial fibrosis markers based on EIGDR have revealed to be able to significantly discriminate fibrosis in most of the cases considered and mapped with the PentaRay®, especially after performing the time alignment of the signals within the

clique. Results also reveal that EIGDR markers can eventually be more beneficial when applied on EGMs acquired with high density grid-shaped catheters, for the better accomplishment of the plane wave hypothesis, indicating that catheter geometry and size plays a key role for this kind of approach. Therefore, these outcomes open the possibility to create high-density maps based on the EGM dispersion, useful to detect fibrotic substrate and therefore successfully guide ablation procedures towards it.

Chapter 6

Final Discussion and Conclusions

6.1 Summary and Discussion

This thesis aims to propose mapping strategies based on intracardiac electrogram (EGM) signal processing techniques, to characterize atrial propagation patterns and fibrotic substrate. The results presented can improve the understanding of the mechanisms underlying atrial fibrillation (AF) and support decision process of physicians and companion technicians during ablation procedures. This chapter summarizes the analyses conducted in the course of the thesis and contains the specific conclusions found at the end of each chapter.

6.1.1 Characterization of Atrial Propagation Patterns and Fibrotic Substrate with Modified Omnipolar Electrogram Methodology

Characterization of propagation patterns and substrate is remarkable to diagnose and treat a wide range of cardiac arrhythmias, including AF. The clinical current strategies use simultaneous unipolar and bipolar EGMs (u-EGMs and b-EGMs, respectively), recorded with multielectrode catheters for the irregular interbeat nature of AF, to extract and map useful features including, among all, conduction velocity (CV) and peak-to-peak voltage values, through dedicated electroanatomic mapping (EAM) systems, but are affected by practical limitations like the relative catheter-to-wavefront orientation. In chapter 3, we evaluated performance of the omnipolar electrogram (OP-EGM) method, which was proposed to generate mapping strategies less affected by u-EGMs and b-EGMs drawbacks. However, in the same chapter, we introduced a modified omnipolar electrogram (MOP-EGM) approach with the aim of reducing the residual b-EGMs dependence on catheter orientation of the standard OP-EGM. Validation has been conducted in two different scenarios. In simulation, voltage and CV mapping modalities based on the MOP-EGM were compared with both bipolar EGM and the original OP-EGM based

maps, also evaluating their accuracy in the detection of a fibrotic patch included in the atrial tissue and their robustness against noise of different levels. The MOP-EGM revealed better performance for the CV and voltage estimates and lower error induced by the b-EGMs dependence on catheter orientation. In clinical scenario, CV and propagation direction estimates computed with the MOP-EGM were compared with those derived from manually detected local activation times (LATs), assuming LATs maps as reference. Results showed consistent behaviour of both types of approaches in reproducing sinus rhythm (SR), but a more coherent behaviour of the omnipolar based maps in presence of complex propagation patterns.

The proposed MOP-EGM method provides more accurate and robust high-density voltage and CV mapping strategies if compared to standard OP-EGM approach and the b-EGM based maps. Therefore, it can be used to successfully map the atrial chambers during electrophysiological studies and finally detect the appropriate targets of catheter ablation.

6.1.2 Atrial Fibrosis Discrimination with Eigenvalue Dominance Analysis of Unipolar Electrograms

Initiation and perpetuation of AF are known to be associated with the presence of atrial fibrosis, although their cause and effect relationship is not yet clear. For this reason, detection of atrial fibrosis assumes great importance in identifying the ablation target. The current approach to discriminate fibrotic tissue from healthy tissue relies on b-EGM voltage thresholding, which can be affected by different factors other than the presence of fibrosis and also disregards the spatiotemporal details of the signal. Chapter 4 introduces novel biomarkers based on the dominant-to-remaining eigenvalue dominance ratio (EIGDR) of u-EGMs in electrode cliques, which are proposed as a waveform dispersion measure, hypothesizing that it reflects the presence of atrial fibrosis. Biomarker maps were evaluated in the same simulation context used to evaluate the MOP-EGM, where u-EGMs have also been corrupted with noise of increasing level. In addition, distance between each electrode and tissue has been assumed to be fixed and also variable following a normal distribution. Results obtained have revealed that mapping modalities based on the EIGDR allow the detection of fibrotic patch from non-fibrotic tissue. For low noise levels and with both fixed and variable electrode-to-tissue distance, they attain comparable discrimination performance to b-EGMs amplitudes based maps. Nevertheless, biomarkers based on the previous time-alignment of u-EGMs outperform bipolar maps when facing higher noise levels, suggesting that the proposed timing is beneficial for fibrosis identification.

6.1.3 Preliminary Clinical Applications of Eigenvalue Dominance Ratio Approach for the Detection of Atrial Fibrosis

The quantitative EIGDR based markers have been introduced in chapter 4 to overcome limitations affecting clinical tools for mapping AF substrate using EAM systems. Therefore, chapter 5 is focused on testing the spatiotemporal approach in clinical scenarios, thus creating high-density mapping strategies using the well-known multielectrode catheters. Evaluation was conducted using EGMs acquired with the PentaRay® catheter and a MEA sensor, to test the ability of the EIGDR based indices to quantify signal morphology dispersion and their discrimination power as fibrosis markers, assuming LGE-MRI as reference. Our findings revealed that EIGDRs based on the time alignment of u-EGMs may be used as biomarkers to discriminate F from NF tissue in the atrium, although it is not clear that they outperform bipolar amplitude based markers. These results have been reinforced by a significant correlation with both bipolar voltage amplitude and IIR values derived by the MRI. This may actually pave the way to a new type of mapping strategies, which take into consideration signal spatiotemporal information (and consequently the complexity of the arrhythmia, not necessarily AF) and are less sensitive to technical issues affecting substrate maps.

6.2 Main Limitations

One of the main limitations encountered during the development of this thesis has been the relatively small size of patients sample used for the validation of the EIGDR based markers in chapter 5, who were heterogeneous with regard to atrial anatomy and electrophysiology. Therefore, further evaluation in more populous and homogeneous datasets is needed. The absence of a *gold standard* for the atrial fibrosis assessment represented another inevitable limitation of this work. In addition, most of the procedures that led to the results presented in this thesis were performed manually, and therefore may be acknowledged as a limiting factor affecting their reproducibility.

On the other hand, it was not possible to use the automatic selection of the atrial depolarization windows, performed in chapter 5 over mapping points of patients, in case of atrioventricular conduction disturbances (such as the atrioventricular block), since the relationship between P wave and QRS complex is altered.

As a final remark, the differences in catheter dispositions and mapping density, both among patients and between catheters, could have made results of the studies not perfectly comparable.

6.3 Main Conclusions

This thesis aims to propose quantitative approaches based on EGM characteristics to improve the outcome of AF catheter ablation, so as to reduce the most common technical and clinical issues in the field of EAM of the arrhythmia. The two signal processing techniques studied have provided comparable or better performance than the standard approaches commonly used in clinical setup, but with the advantage of taking into consideration both the underlying tissue characteristics and spatiotemporal information embedded in the signals. For these reasons, they may potentially have a direct impact in helping physicians and technicians during daily electrophysiology procedures.

6.4 Future Work

Some of the possible future lines unearthed by this thesis are:

1. The study of the MOP-EGM methodology with more complex atrial simulation configurations (including models of patchy fibrosis) and propagation patterns (including non-plane or multiple wavefronts in AF).

2. The assessment of the effect of clinical and technical factors, such as electrode size, interelectrode distance and variable tissue-electrode contact, on the MOP-EGM based mapping strategies.

3. The use of the MOP-EGM methodology to characterize arrhythmias other than AF in clinical scenarios, also employing mapping catheters of different configurations.

4. The use of MOP-EGM based maps and EIGDR based biomarkers for the detection of ventricular fibrosis.

Bibliography

[1] H. Ritchie, F. Spooner and M. Roser, "Causes of death," *Our World in Data*, 2018. [Online]. Available: https://ourworldindata.org/causes-of-death.

[2] R. H. Whitaker, "Anatomy of the heart," *Medicine*, vol. 38, no. 7, pp. 333–335, 2010.

[3] F. Shaffer, R. McCraty and C. L. Zerr, "A healthy heart is not a metronome: an integrative review of the heart's anatomy and heart rate variability," *Frontiers in Psychology*, vol. 5, no. 1040, pp. 1–19, 2014.

[4] A. C. Guyton and J. E. Hall, *Textbook of Medical Physiology*, 13th ed. W. B. Saunders, 2016.

[5] P. A. Iaizzo. Atlas of human cardiac anatomy. [Online]. Available: http://www.pathophys.org/physiology-of-cardiac-conduction-and-contractility/#Electrophysiology

[6] N. Naksuk, D. Padmanabhan, B. Yogeswaran and S. J. Asirvatham, "Cardiac anatomy for catheter mapping and ablation of arrhythmias," in *Catheter Ablation of Cardiac Arrhythmias*, Elsevier, Ed. Shoei K. Stephen Huang and John M. Miller, 2019, vol. 4, pp. 54–74.

[7] A. Habib, N. Lachman, K. N. Christensen and S. J. Asirvatham, "The anatomy of the coronary sinus venous system for the cardiac electrophysiologist," *Europace*, vol. 11, no. suppl 5, pp. v15–v21, 2009.

[8] C. Hall, K. Gehmlich, C. Denning and D. Pavlovic, "Complex relationship between cardiac fibroblasts and cardiomyocytes in health and disease," *Journal of the American Heart Association*, vol. 10, no. 5, p. e019338, 2021.

[9] E. A. Woodcock and S. J. Matkovich, "Cardiomyocytes structure, function and associated pathologies," *The International Journal of Biochemistry & Cell Biology*, vol. 37, no. 9, pp. 1746–1751, 2005.

[10] J. Pellman, J. Zhang and F. Sheikh, "Myocyte-fibroblast communication in cardiac fibrosisand arrhythmias: Mechanisms and model systems," *Journal of Molecular and Cellular Cardiology*, vol. 94, pp. 22–31, 2016.

[11] S. W. van den Borne, J. Diez, W. M. Blankesteijn, J. Verjans, L. Hofstra and J. Narula, "Myocardial remodeling after infarction: the role of myofibroblasts," *Nature Reviews Cardiology*, vol. 7, pp. 30–37, 2010.

[12] K. H. Ten Tusscher and A. V. Panfilov, "Influence of diffuse fibrosis on wave propagation in human ventricular tissue," *EP Europace*, vol. 9, no. suppl 6, p. vi38–vi45, 2007.

[13] J. Boullin and J. M. Morgan, "The development of cardiac rhythm," *Heart*, vol. 91, no. 7, p. 874–875, 2005.

[14] Wapcaplet, "Diagram of the human heart," *Wikimedia Commons*, 2003. [Online]. Available: https://commons.wikimedia.org/wiki/File:Diagram_of_the_human_heart.svg

[15] R. Chaudhary and S. Kumar, "Comparison on time basis of atrial fibrillation with normal sinus rhythm ECG on MATLAB," *International Journal of Electronics and Computer Science Engineering*, vol. 2, no. 3, pp. 1042–1049, 2019.

[16] A. O. Grant, "Cardiac ion channels," *Circulation: Arrhythmia and Electrophysiology*, vol. 2, no. 2, pp. 185–194, 2009.

[17] A. Alcaine, "Intracardiac signal processing for mapping and characterising cardiac arrhythmias," Ph.D. dissertation, Instituto Universitario de Investigación en Ingeniería de Aragón, Universidad de Zaragoza, 2016.

[18] Z. F. Issa, J. M. Miller and D. P. Zipes, *Clinical Arrhythmology, Electrophysiology: A Companion to Braunwald's Heart Disease*, 2nd ed. Elsevier, 2012.

[19] L. Gaztañaga, F. E. Marchlinski and B. P. Betensky, "Mechanisms of cardiac arrhythmias," *Revista Española de Cardiología (English Edition)*, vol. 65, no. 2, pp. 174–185, 2012.

[20] R. E. Klabunde, *Cardiovascular Physiology Concepts*, 3rd ed. Wolters Kluwer, 2021.

[21] G. Ikonnikov and D. Yelle. Physiology of cardiac conduction and contractility. [Online]. Available: http://www.pathophys.org/physiology-of-cardiac-conduction-and-contractility/#Electrophysiology

[22] K. E. Barrett, S. M. Barman, S. Boitano and H. L. Brooks, *Fisiologia medica di Ganong* , 13 ed. ed. Piccin, 2017.

[23] L. Sörnmo and P. Laguna, *Bioelectrical Signal Processing in Cardiac and Neurological Applications*. Amsterdam: Elsevier (Academic Press), 2005.

[24] A. E. Epstein *et al.*, "ACC/AHA/HRS 2008 guidelines for device-based therapy of cardiac rhythm abnormalities," *Circulation*, vol. 117, no. 21, pp. e350–e408, 2008.

[25] G. Tse, "Mechanisms of cardiac arrhythmias," *Journal of Arrhythmia*, vol. 32, no. 2, pp. 75–81, 2016.

[26] W. E. Garrey, "The nature of fibrillary contraction of the heart - its relation to tissue mass and form," *American Journal of Physiology - Heart and Circulatory Physiology*, vol. 33, p. 397–414, 1914.

[27] M. A. Allessie, F. I. M. Bonke and F. J. Schopman, "Circus movement in rabbit atrial muscle as a mechanism of tachycardia. III. the Leading Circle concept: A new model of circus movement in cardiac tissue without the involvement of an anatomical obstacle," *Circulation Research*, vol. 41, no. 1, pp. 9–18, 1977.

[28] N. Wiener and A. Rosenblueth, "The mathematical formulation of the problem of conduction of impulses in a network of connected excitable elements, specifically in cardiac muscle," *Archivos del Instituto de Cardiologia de Mexico*, vol. 16, no. 3, pp. 205–265, 1946.

[29] J. Jalife, O. Berenfeld and M. Mansour, "Mother rotors and fibrillatory conduction: a mechanism of atrial fibrillation," *Cardiovascular Research*, vol. 54, no. 2, pp. 204–216, 2002.

[30] S. M. Kandel and B. J. Roth, "The mechanism of reflection type reentry: A simulation study," *Journal of Cardiovascular Electrophysiology.*, vol. 26, no. 12, pp. 1370–1375, 2015.

[31] A. Lukas and C. Antzelevitch, "Phase 2 reentry as a mechanism of initiation of circus movement reentry in canine epicardium exposed to simulated ischemia," *Cardiovascular Research*, vol. 32, no. 3, pp. 593–603, 1996.

[32] A. Bhat, S. Khanna, H. H. L. Chen, G. C. H. Gan, C. R. MacIntyre and T. C. Tan, "Drivers of hospitalization in atrial fibrillation: A contemporary review," *Heart Rhythm*, vol. 17, no. 11, pp. 1991–1999, 2020.

[33] G. Lip *et al.*, "Atrial fibrillation," *Nature Reviews Disease Primers*, vol. 2, no. 16016, 2016.

[34] J. B. Shea and S. F. Sears, "A patient's guide to living with atrial fibrillation," *Circulation*, vol. 117, no. 20, pp. e340–e343, 2008.

[35] C. T. January *et al.*, "2014 AHA/ACC/HRS guideline for the management of patients with atrial fibrillation: Executive summary a report of the american college of cardiology/american heart association task force on practice guidelines and the

heart rhythm society," *Journal of the American College of Cardiology*, vol. 64, no. 21, pp. 2246–2280, 2014.

[36] V. E. Hagens *et al.*, "Effect of rate or rhythm control on quality of life in persistent atrial fibrillation. Results from the rate control versus electrical cardioversion (RACE) study," *Journal of the American College of Cardiology*, vol. 43, no. 2, pp. 241–247, 2004.

[37] J. Winter. Atrial fibrillation (AF). [Online]. Available: https://ecg-educator.blogspot.com/2016/11/atrial-fibrillation-af.html

[38] H. Calkins *et al.*, "2017 HRS/EHRA/ECAS/APHRS/SOLAECE expert consensus statement on catheter and surgical ablation of atrial fibrillation," *Heart Rhythm*, vol. 14, no. 10, pp. e275–e444, 2017.

[39] S. Nattel, "New ideas about atrial fibrillation 50 years on," *Nature*, vol. 415, no. 6868, pp. 219–226, 20021.

[40] G. K. Moe and J. A. Abildskov, "Atrial fibrillation as a self-sustaining arrhythmia independent of focal discharge," *American Heart Journal*, vol. 58, no. 1, p. 59–70, 1959.

[41] A. Shiroshita-Takeshita, B. J. J .M. Brundel and S. Nattel, "Atrial fibrillation: Basic mechanisms, remodeling and triggers," *Journal of Interventional Cardiac Electrophysiology*, vol. 13, p. 181–193, 2005.

[42] M. A. Allessie, W. J. E. P. Lammers, F. I. M. Bonke and J. Hollen, "Experimental evaluation of Moe's multiple wavelet hypothesis of atrial fibrillation," *Cardiac Electrophysiology, Arrhythmias*, p. 265–276, 1985.

[43] J. Eckstein, M. Kühne, S. Osswald and U. Schotten, "Mapping of atrial fibrillation - basic research and clinical applications," *Swiss medical weekly*, vol. 139, no. 35-36, p. 496–504, 2009.

[44] M. Haïssaguerre *et al.*, "Spontaneous initiation of atrial fibrillation by ectopic beats originating in the pulmonary veins," *The New England Journal of Medicine*, vol. 339, no. 10, p. 659–666, 1998.

[45] M. S. Guillem, A. M. Climent, M. Rodrigo, F. Fernández-Avilés, F. Atienza and O. Berenfeld, "Presence and stability of rotors in atrial fibrillation: evidence and therapeutic implications," *Cardiovascular Research*, vol. 109, no. 4, p. 480–492, 2016.

[46] H. Kottkamp, "On the atrial fibrillation substrate," *Journal of the American College of Cardiology*, vol. 74, no. 10, p. 1348–1351, 2019.

[47] H. Kottkamp and D. Schreiber, "The Substrate in "Early Persistent" Atrial Fibrillation Arrhythmia Induced, Risk Factor Induced, or From a Specific Fibrotic Atrial Cardiomyopathy?" *Journal of the American College of Cardiology: Clinical Electrophysiology*, vol. 2, no. 2, pp. 140–142, 2016.

[48] A. J. Camm *et al.*, "Guidelines for the management of atrial fibrillation: The task force for the management of atrial fibrillation of the european society of cardiology (ESC)," *European Heart Journal*, vol. 31, no. 19, p. 2369–2429, 2010.

[49] M.M. Gallagher and A. J. Camm, "Classification of atrial fibrillation," *Pacing and Clinical Electrophysiology*, vol. 20, no. 6, pp. 1603–1605, 1997.

[50] J. Xu, J. G. Y. Luc and K. Phan , "Atrial fibrillation: review of current treatment strategies," *Journal of Thoracic Disease*, vol. 8, no. 9, pp. E886–E900, 2016.

[51] J. C. Nielsen *et al.*, "Radiofrequency ablation as initial therapy in paroxysmal atrial fibrillation," *The New England Journal of Medicine*, vol. 367, no. 17, pp. 1587–1595, 2012.

[52] G. Katritsis and H. Calkins, "Catheter ablation of atrial fibrillation – techniques and technology," *Arrhythmia & Electrophysiology Review*, vol. 1, no. 1, pp. 29–33, 2012.

[53] M. Kühne and C. Sticherling, "Cryoballoon ablation for pulmonary vein isolation of atrial fibrillation: A better way to complete the circle?" *The Journal of Innovations in Cardiac Rhythm Management*, vol. 2, p. 264–270, 2011.

[54] S. K. Sørensen, A. Johannessen, R. Worck, M. L. Hansen and J. Hansen, "Radiofrequency versus cryoballoon catheter ablation for paroxysmal atrial fibrillation: Durability of pulmonary vein isolation and effect on atrial fibrillation burden: The RACE-AF randomized controlled trial," *Circulation: Arrhythmia and Electrophysiology*, vol. 14, no. 5, p. 2021, 2021.

[55] Y-H Chen, Z-Y Lu, Y-Xiang , J-W Hou, Q. Wang, H Lin and Y-G Li, "Cryoablation vs. radiofrequency ablation for treatment of paroxysmal atrial fibrillation: a systematic reviewand meta-analysis," *Europace*, vol. 19, no. 5, p. 784–794, 2017.

[56] J. G. Andrade *et al.*, "Cryoballoon or radiofrequency ablation for atrial fibrillation assessed by continuous monitoring," *Circulation*, vol. 140, no. 22, pp. 1779–1788, 2019.

[57] P. Loh *et al.*, "Pulmonary vein isolation with single pulse irreversible electroporation," *Circulation: Arrhythmiaand Electrophysiology*, vol. 13, no. 10, p. e008192, 2020.

[58] F. Xie, Y. Chen, X. Chen and Z. Zhao, "Irreversible electroporation ablation for atrial fibrillation: Status and challenges," *Cardiology Discovery*, vol. 2, no. 1, pp. 41–50, 2022.

[59] A. Verma *et al.*, "Approaches to catheter ablation for persistent atrial fibrillation," *The New England Journal of Medicine*, vol. 372, no. 19, pp. 1812–1822, 2015.

[60] M. Andronache, N. Drcaand G. Viola, "High-resolution mapping in patients with persistent AF," *Arrhythmia & Electrophysiology Review*, vol. 8, no. 2, p. 111–5, 2019.

[61] N. Ad *et al.*, "Expert consensus guidelines: Examining surgical ablation for atrial fibrillation," *The Journal of Thoracic and Cardiovascular Surgery*, vol. 153, no. 6, pp. 1330–1354, 2017.

[62] C. Ruaengsri, M. R. Schill, A. J. Khiabani, R. B. Schuessler, S. J. Melby and R.J. Damiano Jr, "The Cox-Maze IV procedure in its second decade: still the gold standard?" *European Journal of Cardio-Thoracic Surgery*, vol. 53, no. *suppl*_1, p. i19–i25, 2018.

[63] R. P. M. Houben and M. A. Allessie, "Processing of intracardiac electrograms in atrial fibrillation - diagnosis of electropothological substrate of AF," *IEEE Engineering in Medicine and Biology Magazine*, vol. 25, no. 6, pp. 40–51, 2006.

[64] J. Riccio *et al.*, "Characterization of atrial propagation patterns and fibrotic substrate with a modified omnipolar electrogram strategy in multi-electrode arrays," *Frontiers in Physiology*, vol. 12, no. 674223, 2021.

[65] K. Okubo *et al.*, "Grid mapping catheter for ventricular tachycardia ablation," *Circulation: Arrhythmia and Electrophysiology*, vol. 12, no. 9, p. e007500, 2019.

[66] Y-H Kim *et al.*, "2019 APHRS expert consensus statement on threedimensional mapping systems for tachycardia developed in collaboration with HRS, EHRA, and LAHRS," *Journal of Arrhythmia*, vol. 36, no. 2, pp. 215–270, 2020.

[67] G. Matsuura *et al.*, "Catheter contact angle influences local impedance drop during radio frequency catheter ablation: Insight from a porcine experimental study with 2 different LI-sensing catheters," *Journal of Cardiovascular Electrophysiology*, vol. 33, p. 380–388, 2022.

[68] V. Y. Reddy *et al.*, "Pulmonary vein isolation with very high power, short duration, temperature-controlled lesions: The QDOT-FAST trial," *Journal of the American College of Cardiology: Clinical Electrophysiology*, vol. 5, no. 7, pp. 778–786, 2019.

[69] J. M. T. de Bakker, "Electrogram recording, analyzing techniques to optimize selection of target sites for ablation of cardiac arrhythmias," *Pacing and Clinical Electrophysiology*, vol. 42, no. 12, p. 1503–1516, 2019.

[70] U. B.Tedrow and W. G. Stevenson, "Recording, interpreting unipolar electrograms to guide catheter ablation," *Heart Rhythm*, vol. 8, no. 5, pp. 791–796, 2011.

[71] D. C. Deno, R. Balachandran, D. Morgan, F. Ahmad, S. Massé and K. Nanthakumar, "Orientation-independent catheter-based characterization of myocardial activation," *IEEE Transactions on Biomedical Engineering*, vol. 64, no. 5, pp. 1067–1077, 2017.

[72] P. G. Platonov, "Atrial fibrosis: an obligatory component of arrhythmia mechanisms in atrial fibrillation?" *Journal of Geriatric Cardiology*, vol. 14, no. 4, pp. 233–237, 2017.

[73] A. Xintarakou, S. Tzeis, S. Psarras, D. Asvestas and P. Vardas, "Atrial fibrosis as a dominant factor for the development of atrial fibrillation: facts and gaps," *EP Europace*, vol. 22, no. 3, pp. 342–351, 2020.

[74] S. Tzeis, D. Asvestas and P. Vardas, "Atrial fibrosis: translational considerations for the management of af patients," *Arrhythmia & Electrophysiology Review*, vol. 8, no. 1, pp. 37–41, 2019.

[75] B. Burstein and S. Nattel, "Atrial fibrosis: mechanisms and clinical relevance in atrial fibrillation," *Journal of the American College of Cardiology*, vol. 51, no. 8, pp. 802–809, 2008.

[76] R. A. de Boer *et al.*, "Towards better definition, quantification and treatment of fibrosis in heart failure. a scientific roadmap by the committee of translational research of the heart failure association (HFA) of the european society of cardiology," *European Journal of Heart Failure*, vol. 21, no. 3, pp. 272–285, 2019.

[77] T. H. Everett 4th and J. E. Olgin, "Atrial fibrosis and the mechanisms of atrial fibrillation," *Heart Rhythm*, vol. 4, no. 3 Suppl, pp. S24–S27, 2007.

[78] R. S. Oakes *et al.*, "Detection and quantification of left atrial structural remodeling using delayed enhancement MRI in patients with atrial fibrillation," *Circulation*, vol. 119, no. 13, p. 1758–1767, 2009.

[79] M. Rodríguez-Mañero *et al.*, "Validating left atrial low voltage areas during atrial fibrillation and atrial flutter using multielectrode automated electroanatomic mapping," *Journal of the American College of Cardiology: Clinical Electrophysiology*, vol. 4, no. 12, pp. 1541–1552, 2018.

[80] B. Yang *et al.*, "STABLE-SR (electrophysiological substrate ablation in the left atrium during sinus rhythm) for the treatment of nonparoxysmal atrial fibrillation: A prospective, multicenter randomized clinical trial," *Circulation: Arrhythmia and Electrophysiology*, vol. 10, no. 11, p. e005405, 2017.

[81] T. Yamaguchi, A. Fukui and K. Node, "Bipolar voltage mapping for the evaluation of atrial substrate: Can we overcome the challenge of directionality?" *Journal of Atrial Fibrillation*, vol. 11, no. 5, 2019.

[82] I. Sim, M. Bishop, M. O'Neill and S. E. Williams, "Left atrial voltage mapping: defining, targeting the atrial fibrillation substrate," *Journal of Interventional Cardiac Electrophysiology*, vol. 56, no. 3, pp. 213–227, 2019.

[83] M. G. Chelu *et al.*, "Atrial fibrosis by late gadolinium enhancement magnetic resonance imaging and catheter ablation of atrial fibrillation: 5-year follow-up data," *Journal of the American Heart Association*, vol. 7, no. 23, p. e006313, 2018.

[84] P. Gal and N. F. Marrouche, "Magnetic resonance imaging of atrial fibrosis: redefining atrial fibrillation to a syndrome," *European Heart Journal*, vol. 38, no. 1, pp. 14–19, 2015.

[85] J. X. Quah *et al.*, "Atrial fibrosis and substrate based characterization in atrial fibrillation: Time to move forwards," *Journal of Cardiovascular Electrophysiology*, vol. 32, no. 4, pp. 1147–1160, 2021.

[86] J. Lacalzada-Almeida and J. García-Niebla, "How to detect atrial fibrosis," *Journal of Geriatric Cardiology*, vol. 14, no. 3, pp. 185–194, 2017.

[87] Marrouche *et al.*, "Association of atrial tissue fibrosis identified by delayed enhancement MRI and atrial fibrillation catheter ablation: the DECAAF study," *Journal of the American Medical Association*, vol. 311, no. 5, pp. 498–506, 2014.

[88] I. M. Khurram *et al.*, "Magnetic resonance image intensity ratio, a normalized measure to enable interpatient comparability of left atrial fibrosis," *Heart Rhythm*, vol. 11, no. 1, pp. 85–92, 2014.

[89] E. M. Benito *et al.*, "Left atrial fibrosis quantification by late gadolinium-enhanced magnetic resonance: a new method to standardize the thresholds for reproducibility," *Europace*, vol. 19, no. 8, pp. 1272–1279, 2017.

[90] T. Zghaib and S. Nazarian, "New insights into the use of cardiac magnetic resonance imaging to guide decision making in atrial fibrillation management," *Canadian Journal of Cardiology*, vol. 34, no. 11, pp. 1461–1470, 2018.

[91] D. J. Lim *et al.*, "Change in left atrial function predicts incident atrial fibrillation: the multi-ethnic study of atherosclerosis," *European Heart Journal - Cardiovascular Imaging*, vol. 20, no. 9, pp. 979–987, 2019.

[92] G. C. H. Gan, A. Ferkh, A. Boyd and L. Thomas, "Left atrial function: evaluation by strain analysis," *Cardiovascular Diagnosis & Therapy*, vol. 8, no. 1, pp. 29–46, 2018.

[93] H. Blessberger and T. Binder, "Two dimensional speckle tracking echocardiography: basic principles," *Heart*, vol. 96, no. 9, pp. 716–722, 2010.

[94] J. Buggey and B. D. Hoit, "Left atrial strain: measurement and clinical application," *Current Opinion in Cardiology*, vol. 33, no. 5, pp. 479–485, 2018.

[95] S. S. Kuppahally *et al.*, "Left atrial strain and strain rate in patients with paroxysmal and persistent atrial fibrillation: relationship to left atrial structural remodeling detected by delayed-enhancement MRI," *Circulation: Cardiovascular Imaging*, vol. 3, no. 3, pp. 231–9, 2010.

[96] S. Rolf *et al.*, "Tailored atrial substrate modification based on low-voltage areas in catheter ablation of atrial fibrillation," *Circulation: Arrhythmia and Electrophysiology*, vol. 7, no. 5, p. 825–833, 2014.

[97] S. Nedios, P. Sommer, A. Bollmann and G. Hindricks, "Advanced mapping systems to guide atrial fibrillation ablation: Electrical information that matters," *Journal of Atrial Fibrillation*, vol. 8, no. 6, p. 1337, 2016.

[98] P. Maury, B. Monteil, L. Marty, A. Duparc, P. Mondoly and A. Rollin, "Three-dimensional mapping in the electrophysiological laboratory," *Archives of Cardiovascular Diseases*, vol. 111, no. 6-7, pp. 456–464, 2018.

[99] C. Weiss, S. Willems and R. Rueppel, M. Hoffmann and T. Meinertz, "Electroanatomical mapping (CARTO®) of ectopic atrial tachycardia: Impact of bipolar and unipolar local electrogram annotation for localization the focal origin," *Journal of Interventional Cardiac Electrophysiology*, vol. 5, no. 1, pp. 101–107, 2001.

[100] S. Knecht, V. Schlageter, P. Badertscher, P. Krisai, F. Jousset, T. Küffer, A. Madaffari, B. Schaer, S. Osswald, C. Sticherling, M. Kühne, "Atrial substrate characterization based on bipolar voltage electrograms acquired with multipolar, focal, mini-electrode catheters," *EP Europace*, vol. 25, no. 5, p. euad127, 2023.

[101] S. Kircher *et al.*, "Individually tailored vs. standardized substrate modification during radiofrequency catheter ablation for atrial fibrillation: a randomized study," *Europace*, vol. 20, no. 11, pp. 1766–1775, 2018.

[102] A. Blandino *et al.*, "Left atrial substrate modification targeting low-voltage areas for catheter ablation of atrial fibrillation: a systematic review and meta-analysis," *Pacing and Clinical Electrophysiology*, vol. 40, no. 2, pp. 199–212, 2017.

[103] R. J. Selvaraj, S. Yerram, P. Kumar, S. Satheesh, A. A. Pillai, M. K. Saktheeswaran, J. Balachander, "Pace mapping in the atrium using bipolar electrograms from widely spaced electrodes," *Journal of Arrhythmia*, vol. 31, no. 5, pp. 274–278, 2015.

[104] T. Skála and M. Táborský, "Electromechanical mapping in electrophysiology and beyond," *Cor et Vasa*, vol. 57, no. 6, pp. e470–e482, 2015.

[105] L. Rottner *et al.*, "Catheter ablation of atrial fibrillation: State of the art and future perspectives," *Cardiology and Therapy*, vol. 9, pp. 45–58, 2020.

[106] J. Riccio, A. Alcaine, S. Rocher, P. Laguna, J. Saiz and J. P. Martínez, "Omnipolar EGM voltage mapping for atrial fibrosis identification evaluated with an electrophysiological model," *2020 28th European Signal Processing Conference*, pp. 920–924, 2021.

[107] J. Riccio, A. Alcaine, N. M. S. de Groot, R. Houben, P. Laguna and J. P. Martínez, "Characterization of propagation patternswith omnipolar EGM in epicardial multielectrode arrays," *2019 Computing in Cardiology*, vol. 46, pp. 1–4, 2019.

[108] J. Riccio *et al.*, "Unipolar electrogram eigenvalue distribution analysis for the identification of atrial fibrosis," *2020 Computing in Cardiology*, vol. 47, pp. 1–4, 2020.

[109] J. Riccio *et al.* , "Atrial fibrosis identification with unipolar electrogram eigenvalue distribution analysis in multi-electrode arrays," *Medical & Biological Engineering & Computing*, vol. 60, no. 11, p. 3091–3112, 2022.

[110] A. Alcaine, N. M. S. de Groot, P. Laguna, J. P. Martínez and R. P. M. Houben, "Spatiotemporal model-based estimation of high-density atrial fibrillation activation maps," *Digital Signal Processing*, vol. 54, pp. 64–74, 2016.

[111] L. A. Unger, T. G. Oesterlein, A. Loewe and O. Dössel, "Noise quantification and noise reduction for unipolar and bipolar electrograms," *2019 Computing in Cardiology*, vol. 46, pp. 1–4, 2019.

[112] M. Courtemanche, R. J. Ramirez and S. Nattel, "Ionic mechanisms underlying human atrial action potential properties: insights from a mathematical model," *The American Journal of Physiology*, vol. 275, no. 1, pp. H301–21, 1998.

[113] M. M. Maleckar, J. L. Greenstein, W. R. Giles and N. A. Trayanova, "Electrotonic coupling between human atrial myocytes and fibroblasts alters myocyte excitability and repolarization," *Biophysical Journal*, vol. 97, no. 8, p. 2179–2190, 2009.

[114] L. Martinez-Mateu *et al.*, "Factors affecting basket catheter detection of real and phantom rotors in the atria: A computational study," *PLoS Computational Biology*, vol. 14, no. 3, p. e1006017, 2018.

[115] D. Li, L. Zhang, J. Kneller and S. Nattel, "Potential ionic mechanism for repolarization differences between canine right and left atrium," *Circulation Research*, vol. 88, no. 11, pp. 1168–1175, 2001.

[116] C. Tobón, C. A. Ruiz Villa, E. Heidenreich, L. Romero, F. Hornero and J. Saiz, "A three-dimensional human atrial model with fiber orientation. electrograms and arrhythmic activation patterns relationship," *PLoS ONE*, vol. 8, no. 2, p. e50883, 2013.

[117] R. F. Bosch, X. Zeng, J. B. Grammer, K. Popovic, C. Mewis and V. Kühlkamp, "Ionic mechanisms of electrical remodeling in human atrial fibrillation," *Cardiovascular Research*, vol. 44, no. 1, pp. 121–131, 1999.

[118] J. Sánchez, J. F. Gomez, L. Martínez-Mateu, L. Romero, J. Saiz and B. Trenor, "Heterogeneous effects of fibroblast-myocyte coupling in different regions of the human atria under conditions of atrial fibrillation," *Frontiers in Physiology*, vol. 10:847, 2019.

[119] J. S. J. P. Keener, *Mathematical Physiology*. Springer, 1998.

[120] J. P. Whiteley, "An efficient numerical technique for the solution of the monodomain and bidomain equations," *IEEE Transactions on Biomedical Engineering*, vol. 53, no. 11, pp. 2139–2147, 2006.

[121] E. A. Heidenreich, J. M. Ferrero, M. Doblaré and J. F. Rodríguez, "Adaptive macro finite elements for the numerical solution of monodomain equations in cardiac electrophysiology," *Annals of Biomedical Engineering*, vol. 38, no. 7, pp. 2331–2345, 2010.

[122] R. Caballero *et al.*, "In humans, chronic atrial fibrillation decreases the transient outward current and ultrarapid component of the delayed rectifier current differentially on each atria and increases the slow component of the delayed rectifier current in both," *Journal of the American College of Cardiology*, vol. 55, no. 21, pp. 2346–54, 2010.

[123] D. R. Van Wagoner, A. Pond, M. Lamorgese, S. Rossie, P. McCarthy, and J. Nerbonne, "Atrial L-type Ca2+ currents and human atrial fibrillation," *Circulation Research*, vol. 85, no. 5, pp. 428–436, 1999.

[124] A. J. Workman , K. Kane and A. Rankin, "The contribution of ionic currents to changes in refractoriness of human atrial myocytes associated with chronic atrial fibrillation," *Cardiovascular Research*, vol. 52, no. 2, p. 226–235, 2001.

[125] D. Dobrev *et al.*, "Molecular basis of downregulation of G-protein-coupled inward rectifying K(+) current (I(K,ACh) in chronic human atrial fibrillation: decrease in GIRK4 mRNA correlates with reduced I(K,ACh) and muscarinic receptor-mediated shortening of action potentials," *Circulation*, vol. 104, no. 21, pp. 2551–7, 2001.

[126] N. Voigt *et al.*, "Left-to-right atrial inward rectifier potassium current gradients in patients with paroxysmal versus chronic atrial fibrillation," *Circulation: Arrhythmia and Electrophysiology*, vol. 3, no. 5, pp. 472–80, 2010.

[127] L. Martinez-Mateu, L. Romero, J. Saiz and O. Berenfeld, "Far-field contributions in multi-electrodes atrial recordings blur distinction between anatomical and functional reentries and may cause imaginary phase singularities – a computational study," *Computers in Biology and Medicine*, vol. 108, pp. 276–287, 2019.

[128] D. U. J. Keller, F. M. Weber, G. Seemann and O. Dössel, "Ranking the influence of tissue conductivities on forward-calculated ECGs," *IEEE Transactions on Biomedical Engineering*, vol. 57, no. 7, pp. 1568–1576, 2010.

[129] F. Castells *et al.*, "Performance assessment of electrode configurations for the estimation of omnipolar electrograms from high density arrays," *Computers in Biology and Medicine*, vol. 154, no. 106604, 2023.

[130] S. Ruipérez-Campillo *et al.*, "Evaluation and assessment of clique arrangements for the estimation of omnipolar electrograms in high density electrode arrays: an experimental animal model study," *Physical and Engineering Sciences in Medicine*, 2023.

[131] Q. Ni, R. S. MacLeod, R. L. Lux and B. Taccardi, "A novel interpolation method for electric potential fields in the heart during excitation," *Annals of Biomedical Engineering*, vol. 26, no. 4, pp. 597–607, 1998.

[132] P. V. Bayly , B. H. KenKnight, J. M. Rogers, R. E. Hillsley, R. E. Ideker and W. M. Smith, "Estimation of conduction velocity vector fields from epicardial mapping data," *IEEE Transactions on Biomedical Engineering*, vol. 45, no. 5, pp. 563–571, 1998.

[133] C. E. Metz, "Basic principles of ROC analysis," *Seminars in Nuclear Medicine*, vol. 8, no. 4, pp. 283–298, 1978.

[134] S. K. Haldar *et al.*, "Resolving bipolar electrogram voltages during atrial fibrillation using omnipolar mapping," *Circulation: Arrhythmia and Electrophysiology*, vol. 10, no. 9, p. e005018, 2017.

[135] D. Nairn *et al.*, "Comparison of unipolar and bipolar voltage mapping for localization of left atrial arrhythmogenic substrate in patients with atrial fibrillation," *Frontiers in Physiology*, vol. 11, no. 575846, pp. 1–13, 2020.

[136] K. Magtibay *et al.*, "Physiological assessment of ventricular myocardial voltage using omnipolar electrograms," *Journal of the American Heart Association*, vol. 6, no. 8, p. e006447, 2017.

[137] A. Porta-Sánchez *et al.*, "Omnipolarity applied to equi-spaced electrode array for ventricular tachycardia substrate mapping," *EP Europace*, vol. 21, no. 5, p. 813–821, 2019.

[138] D. C. Deno *et al.*, "High-resolution, live, directional mapping," *Heart Rhythm*, vol. 17, no. 9, pp. 1621–1628, 2020.

[139] G. Caixal *et al.*, "Accuracy of left atrial fibrosis detection with cardiac magnetic resonance: correlation of late gadolinium enhancement with endocardial voltage and conduction velocity," *EP Europace*, 2020.

[140] J. Sánchez *et al.*, "Using machine learning to characterize atrial fibrotic substrate from intracardiac signals with a hybrid in silico and in vivo dataset," *Frontiers in Physiology*, vol. 12, no. 699291, 2021.

[141] F. O. Campos *et al.*, "Electro-anatomical characterization of atrial microfibrosis in a histologically detailed computer model," *IEEE Transactions on Biomedical Engineering*, vol. 60, no. 8, p. 2339–2349, 2013.

[142] F. Castells, P. Laguna, L. Sörnmo, A. Bollmann and J. M. Roig, "Principal component analysis in ECG signal processing," *EURASIP Journal on Advances in Signal Processing*, vol. 2007, no. 74580,, pp. 1–21, 2006.

[143] C. D. Woody, "Characterization of an adaptive filter for the analysis of variable latency neuroelectric signals," *Medical and biological engineering*, vol. 5, p. 539–554, 1967.

[144] P. Laguna, A. Garde, B. F. Giraldo, O. Meste, R. Jané and L. Sörnmo, "Eigenvalue-based time delay estimation of repetitive biomedical signals," *Digital Signal Processing*, vol. 75, pp. 107–119, 2018.

[145] T. Nezlobinsky, O. Solovyova and A. V. Panfilov, "Anisotropic conduction in the myocardium due to fibrosis: the effect of texture on wave propagation," *Scientific Reports*, vol. 10, no. 764, 2020.

[146] L. C. Palacio, J. P. Ugarte, J. Saiz and C. Tobón, "The effects of fibrotic cell type and its density on atrial fibrillation dynamics: An in silico study," *Cells*, vol. 10, no. 10, 2021.

[147] E. Vigmond, A. Pashaei, S. Amraoui, H. Cochet and M. Hassaguerre, "Percolation as a mechanism to explain atrial fractionated electrograms and reentry in a fibrosis model based on imaging data," *Heart Rhythm*, vol. 13, no. 7, pp. 1536–43, 2016.

[148] D. G. Laţcu *et al.*, "Scar identification, quantification, and characterization in complex atrial tachycardia: a path to targeted ablation?" *Europace*, vol. 21, p. i21–i26, 2019.

Scientific Contributions

- **J. Riccio**, A. Alcaine, S. Rocher, L. Martinez-Mateu, J. Saiz, E. Invers-Rubio, M. S. Guillem, J. P. Martínez, P. Laguna, "Atrial Fibrosis Identification with Unipolar Electrogram Eigenvalue Distribution Analysis in Multi-Electrode Arrays", Medical and Biological Engineering and Computing, vol. 60, no. 11, pp. 3091-3112, 2022. doi:10.1007/s11517-022-02648-3. *Editor's Choice of November 2022 Issue.*

- **J. Riccio**, A. Alcaine, S. Rocher, L. Martinez-Mateu, S. Laranjo, J. Saiz, P. Laguna, J. P. Martínez, "Characterization of Atrial Propagation Patterns and Fibrotic Substrate with Modified Omnipolar Electrograms in Multi-Electrode Arrays", Atrial Fibrillation: Technology for Diagnosis, Monitoring, Eds: Jose F Rodriguez Matas, Omer Berenfeld, Axel Loewe, Valentina Corino, Juan Pablo Martínez, pp. 475-495, Frontiers Research Topics, Frontiers Media SA, ISBN: 978-2-88974-690-3, 2022.

- **J. Riccio**, A. Alcaine, S. Rocher, L. Martinez-Mateu, S. Laranjo, J. Saiz, P. Laguna, J. P. Martínez, "Characterization of Atrial Propagation Patterns and Fibrotic Substrate with Modified Omnipolar Electrograms in Multi-Electrode Arrays", Frontiers in Physiology, vol. 12, p. 674223, 2021. doi:10.3389/fphys.2021.674223.

- **J. Riccio**, A. Alcaine, J. P. Martínez, P. Laguna, "Análisis de dispersión de autovalores de electrogramas unipolares para la detección de fibrosis auricular", Actas de la X Jornada de Jóvenes Investigadores e Investigadoras del I3A, 2021, doi:10.26754/jjii3a.20216003.

- **J. Riccio**, A. Alcaine, S. Rocher, J. Saiz, J. P. Martínez, P. Laguna, "Analysis of Unipolar Electrogram Eigenvalue Dispersion for the Detection of Atrial Fibrosis", Proceedings of Atrial Signals, p. 12, 2021, doi:10.5445/IR/1000138459. *Best Poster Award.*

- **J. Riccio**, A. Alcaine, S. Rocher, P. Laguna, J. Saiz, J. P. Martínez, "Omnipolar EGM Voltage Mapping for Atrial Fibrosis Identification Evaluated with an Electrophysiological Model", Proceedings of the 28th European Signal Processing Conference (EUSIPCO 2020), pp. 920-924, 2021, doi:10.23919/Eusipco47968.2020.9287670.

- **J. Riccio**, S. Rocher, L. Martinez-Mateu, A. Alcaine, J. Saiz, J. P. Martínez, P. Laguna, "Unipolar Electrogram Eigenvalue Distribution Analysis for the Identification of Atrial Fibrosis", Proceedings of Computing in Cardiology 2020, vol. 47, pp. 1-4, 2020, doi:10.22489/CinC.2020.434.

- **J. Riccio**, A. Alcaine, N. M. S. de Groot, R. P. M. Houben, P. Laguna, J. P. Martínez, "Characterization of Propagation Patterns With Omnipolar EGM in Epicardial Multi-Eelectrode Arrays", Proceedings of Computing in Cardiology 2019, vol. 46, pp. 1-4, 2019, doi:10.22489/CinC.2019.340.

Collaborations and Research Stays

All the methods proposed and developed in this dissertation were evaluated in collaboration with researchers and clinicians belonging to other research groups and institutions, who actively contributed with data collection and interpretation:

- Dr. Alejandro Alcaine
  Facultad de Ciencias de la Salud, Universidad San Jorge, Zaragoza, Spain.
- Prof. Dr. Javier Saiz
  Centro de Investigación e Innovación en Bioingeniería, Universitat Politècnica de València, Valencia, Spain.
- Prof. Dr. Sergio Laranjo
  Centro Hospitalar Universitário de Lisboa central, Faculdade de Medicina de Universidade de Lisboa, Lisbon, Portugal.
- Dr. Laura Martinez-Mateu
  Grupo de Investifación de alto rendimiento en Ingeniería Biomédica y Ciencia de Datos. Universidad Rey Juan Carlos, Madrid, Spain.
- Sara Rocher
  Centro de Investigación e Innovación en Bioingeniería, Universitat Politècnica de València, Valencia, Spain.
- Dr. Maria S. Guillem
  ITACA Institute, Universidad Politécnica de València, Valencia, Spain.
- Dr. Lluis Mont Girbau
  Institut Clínic Cardiovascular, Hospital Clínic, Barcelona, Spain.
- Eric Invers-Rubio
  Institut d'Investigacions Biomèdiques August Pi i Sunyer, Hospital Clínic, Barcelona, Spain.

In addition, during my PhD I had the opportunity to benefit from three research stays within the MY-ATRIA consortium:

- Laboratorio de Función Autonómica Cardiovascular, Instituto de Fisiología, Faculdade de Medicina de Lisboa, Universidade de Lisboa, Lisbon, Portugal (6 May 2019 - 31 May 2019).
- Centro de Investigación e Innovación en Bioingeniería, Universitat Politècnica de València, Valencia, Spain (1 June 2021 - 31 July 2022).
- Sección de Arritmias, Servicio de Cardiología, Institut Clínic Cardiovascular, Hospital Clínic de Barcelona, Barcelona, Spain (21 March 2022 - 2 April 2022).

Characterization of Atrial Propagation Patterns and Substrate using Novel Electrogram-Based Approaches in Multielectrode Catheters

Atrial fibrillation (AF) is the most frequently diagnosed arrhythmia worldwide, representing a significant public health problem with a great impact on the quality of life of patients. Nevertheless, its underlying mechanisms are not completely known. What is established is that both altered electrical impulse propagation and substrate may be involved in the development of the disease. These considerations have led to an increasing interest towards AF treatment, which varies depending on the patient characteristics.

Catheter ablation is a minimally invasive procedure to scare those areas responsible for initiation and/or perpetuation of irregular heartbeats, employing catheters equipped with electrodes which can sense and record the local cardiac electrical signals, known as electrograms (EGMs), or release the energy needed to scar and destroy the arrhythmia triggers when inserted into the cardiac chambers.

This thesis aims to characterize AF dynamics in order to find the most appropriate catheter ablation target and effectively terminate the arrhythmia. To do that, signal processing methodologies have been proposed and investigated, thus extracting EGM characteristics in terms of propagation patterns and substrate.

Instituto Universitario de Investigación en Ingeniería de Aragón
Universidad Zaragoza

BSICoS
Biomedical Signal Interpretation & Computational Simulation